FLOW DYNAMICS AND REACTIVITY IN THE TRANSITION ZONE BETWEEN STREAMS AND RIPARIAN AQUIFERS

DISSERTATION

zur Erlangung des akademischen Grades eines Doktors der Naturwissenschaften (Dr. rer. nat.) an der Fakultät für Biologie, Chemie und Geowissenschaften der Universität Bayreuth

vorgelegt von

Guilherme Emídio Horta Nogueira

aus Itajubá, MG - Brasilien

Bayreuth, 2022

Die vorliegende Dissertation wurde im Zeitraum von November/2017 bis Januar/2022 in Leipzig am Helmholtz-Zentrum für Umweltforschung unter Betreuung von Herrn Prof. Dr. Jan H. Fleckenstein angefertigt.

Die Arbeit im Rahmen der Dissertation wurden durch die "**E**uropean training **N**etwork for **I**n situ ima**G**ing of dyna**M**ic processes in heterogeneous subsurf**A**ce environments" (ENIGMA-ITN) gefördert im Rähme des Marie Sklodowska-Curie Grant Agreement n°722028, einem Teilprojekt innerhalb der EU-Horizon 2020 Programme.

Vollständiger Abdruck der von der Fakultät für Biologie, Chemie und Geowissenschaften der Universität Bayreuth genehmigten Dissertation zur Erlangung des akademischen Grades eines Doktors der Naturwissenschaften (Dr. rer. nat.).

Dissertation eingereicht am: 14.02.2022

Zulassung durch die Prüfungskommission: 02.03.2022

Wissenschaftliches Kolloquium: 04.07.2022

Amtierender Dekan: Prof. Dr. Benedikt Westermann

Prüfungsausschuss:

Prof. Dr. Jan H. Fleckenstein	(Gutachter)
PD. Dr. Sven Frei	(Gutachter)
Prof. Dr. Martin Obst	(Vorsitz)
Dr. Benjamin Gilfedder	

Acknowledgements

- Ich möchte Jan H. Fleckenstein für die Betreuung und hilfreiche Beratung in allen Phasen dieser Arbeit danken. Ich möchte auch Christian Schmidt meine Anerkennung aussprechen, der die von mir durchgeführte Arbeit aufmerksam verfolgte und während ihrer Entwicklung brillante Einblicke gab. Ich bin dankbar für alles, was ich während der Zusammenarbeit mit Ihnen gelernt habe. *Tomorrow, training as usual!*

- I would like to extend the acknowledgment to all the other colleagues I was pleased to meet from the HyDroGeology department (UFZ) - especially the ones who were lucky enough to share the room 355 with us! Our discussions and talks over coffee, meals or simply across the tables were on the dot for many times during my work - either for its scientific part, or for its endurance! I would like to especially thank Toralf Keller, who supported me with some core technical skills required for the start and continuation of my work, as well as for the sharpen field work assistance.

- Many other researchers were essential and have collaborated on the carrying out and on the expansion of this work. Especially, I would like to thank Nico Trauth, whose supervision was crucial during the first steps of my work. I also would like to acknowledge Philip Brunner for an accurate guidance and support on the carried out numerical modelling activities of this work - particularly during my staying in Neuchâtel. I also would like to extend the acknowledgment to Peter Engesgaard, who also welcomed me and have greatly supported my work while in Copenhagen. I also would like to express my special gratitude to both Daniel Graeber and Daniel Partington for very enjoyable collaborations and fruitful discussions during parts of my research.

- I thank the ENIGMA-ITN friends and colleagues who provided rich discussions and ideas during all the times we could meet (either in person or virtually) during summer schools, workshops, conferences, and secondments. As in many things in life, only by connecting and sharing can we learn more and go further.

- Ringrazio anche Alessia per essere stata al mio fianco, per la pazienza, il supporto, e per tutto il tempo passato insieme su queste montagne russe. Senza di te questa avventura sarebbe stata molto più difficile (e noiosa).

- Sobretudo, eu gostaria de agradecer minha família, em especial meus pais Fábio e Meiry e minha irmã Thaís que me ajudaram a crescer e fortaleceram-me a todo momento de minha jornada até aqui: *longe ou perto – mas nunca distantes de mim*. Vocês foram (e são) fundamentais para o meu sucesso.

Table of Contents

Abstract

The stream water (SW) and groundwater (GW) domains are two parts of one hydrologic continuum. The riparian zone (RZ) is a transition zone between both domains, which connects the aquatic and terrestrial ecosystems. The RZ has been shown to have a potential for regulating water quality in stream-corridors. This potential is mainly related to SW-GW interactions and the associated hydrological and biogeochemical processes occurring at different spatio-temporal scales within RZ. Mixing of different solutes, and high microbial activities are only some of the factors responsible for the high potential for contaminant attenuation and general solutes turnover within RZ. However, an adequate representation of these coupled processes, and their variations in space and time is challenging due to the multiple interactions between the hydrological and biogeochemical processes. This PhD addresses this challenge by aiming at an evaluation of the effects of flow dynamics on riparian reactive potential at different scales. The three consecutive studies comprising this thesis were carried out in a well-instrumented RZ located at the low-land portion of the Selke River catchment, a 4^{th}-order stream, central Germany. The location is well suited for this type of research since it is well instrumented and has a long history of agricultural activity within the riparian corridor with associated inputs of nitrate (NO_3^-) into the riparian aquifer. This thesis combines data-driven and numerical modelling in order to explore and disentangle the different factors and processes shaping water quality at the different scales within the RZ.

As dissolved oxygen (DO) is a key-component regulating the redox state of the system, in the data-driven analyses (Study 1), a suite of tracer-tests were carried out and combined with high-resolution hydrological and chemical data to characterize the near stream system (appx. 20m from stream bank) for aerobic respiration. For that, Damköhler numbers for DO (DA_{DO}) were employed. Results showed that seasonal and short-term variations in temperature are major controls shaping the reactive state of the system. Seasonal temperature variations in GW induce a shift on reactive state from transport-limited ($DA_{DO}>1$) in summer to reaction-limited conditions ($DA_{DO}<1$) in winter. On the other hand, short-term events had only minor impacts on the system, resulting in slightly less transport-limited conditions due to decreasing temperature and transit-times associated with the events. The study also shows that assuming a constant water temperature along a SW infiltration flowpath could lead to an over- or underestimation of reaction rates by a factor of 2-3 due to different infiltrating water temperature at the SW-GW interface. Also assuming constant water transit-times throughout the hydrological year results in an underestimation of NO_3^- removal (40%-50% difference).

The numerical modelling of Study 2 focused on the simulation of water flow and mass (DO and NO_3^-) transport using the measured data from Study 1 but extended the spatial scale. The modelling concept combined a fully-integrated 3D transient numerical flow model with a temperature-dependent reactive

transport along subsurface flow paths. Results revealed that temperature variations shift the reactive zone for NO_3^-, whereas this zone is near the stream under warmer conditions. Even under limited carbon availability (as an electron donor) and low-temperatures, NO_3^- removal fractions (R_{NO3}) were greater further from the stream than along short hyporheic flow paths (R_{NO3}=0.4 and R_{NO3}=0.1, respectively). Conversely, transit-times and DO concentrations constrained nitrate removal at the near stream region. Additionally, with increasing temperature, the effects of stream flow and solute concentrations on biogeochemical turnover and the redox zonation around the stream strongly decreased. The modelling concept of this study provides an adaptive framework to quantify reach-scale biogeochemical turnover around hydrological dynamic streams.

In Study 3, the flow model is coupled with a Hydraulic Mixing Cell method for mapping the source composition of water and tracking their spatio-temporal evolution within RZ. This allowed the identification of mixing hotspots which can be defined to have nearly equal fractions of SW and GW per aquifer volume. These mixing hotspots can facilitate mixing-dependent reactions and solute turnover. Only about 9% of the total simulated domain could be identified as mixing hot-spots (mainly at the fringe of the geochemical hyporheic zone), but this value could be 1.5x higher following large discharge events. Such events increase mixing further away from the stream, whereas near the stream the rapid increase of SW influx shifts the ratio between the water fractions to SW, reducing the potential for mixing and the associated reactions. The study also provides an easy-to-transfer approach to assess spatio-temporal patterns of mixing processes and mixing-dependent turnover reactions in riparian zones.

In summary, findings from the three studies elucidated the relationships and controls among hydrology and biogeochemistry at different scales in the RZ. By combining innovative methods and using coupled, mechanistic models, this thesis advanced the understanding of reactive potentials within the RZ, which can be useful to devise further research and actions for integrated aquatic ecosystem management and recovery.

Zusammenfassung

Die Bereiche Fließgewässer (SW) und Grundwasser (GW) sind Teile eine hydrologischen Kontinuums, das durch eine Übergangszone verbunden ist. Die Flussauen (RZ), als Übergangszone zwischen aquatischen und terrestrischen Ökosystemen, ist für ihr großes Potenzial zur Regulierung der Wasserqualität in Flusskorridoren bekannt. Dieses Potenzial hängt hauptsächlich mit den Wechselwirkungen zwischen hydrologischen und biogeochemischen Prozessen zusammen, die auf verschiedenen räumlichen und zeitlichen Skalen innerhalb der RZ stattfinden. SW-GW-Austauschprozesse, die Durchmischung verschiedener gelöster Stoffe und hohe mikrobielle Aktivität sind nur einige der Faktoren, die für das hohe Potenzial zur Schadstoffabschwächung und zum weiteren Stoffumsatz in den Flussauen verantwortlich sind. Die Darstellung solcher gekoppelter Prozesse sowie ihrer räumlichen und zeitlichen Variationen ist jedoch aufgrund der vielfältigen Wechselwirkungen zwischen den hydrologischen und biogeochemischen Prozessen, die beim Durchfluss des Wassers durch die Ufersedimente berücksichtigt werden müssen, schwierig. Daher ist die Bewertung der Auswirkungen der Abflussdynamik auf das reaktive Potenzial von RZ auf verschiedenen Ebenen ein anspruchsvolles Ziel, zu dem dieses Dissertationsprojekt beitragen soll. Die drei verschiedenen Studien, die diese Dissertation umfassen, wurden in einer RZ im unteren Einzugsgebiets der Selke, einem Fluss vierter Ordnung in Mitteldeutschland durchgeführt. Der Standort ist für die Untersuchung sehr gut geeignet, da er gut instrumentiert ist und das Gebiet durch eine langjährige landwirtschaftliche Nutzung und eine damit verbundene Verschmutzung des Grundwassers mit Nitrat (NO_3^-) geprägt ist. In dieser Arbeit werden datengestützte und numerische Modellierung kombiniert, um die verschiedenen Faktoren und Prozesse, die die Wasserqualität auf den verschiedenen Skalen innerhalb der RZ prägen, zu untersuchen und zu verstehen.

Da gelöster Sauerstoff (DO) eine Schlüsselkomponente ist, die den Redox-Zustand des Systems reguliert, wurden in den datengestützten Analysen (Studie 1) eine Reihe von Tracer-Tests durchgeführt und mit hochauflösenden hydrologischen und chemischen Daten kombiniert, um das flussnahe System (ca. 20 m vom Flussufer entfernt) hinsichtlich des DO-Umsatzpotenzials zu charakterisieren. Dazu wurden Damköhler-Zahlen für den DO-Verbrauch (DA_{DO}) verwendet. Die Ergebnisse zeigen, dass saisonale und kurzfristige Temperaturschwankungen den reaktiven Zustand des Systems maßgeblich beeinflussen. Saisonale Temperaturschwankungen im Grundwasser verschieben den reaktiven Zustand des Systems von transportlimitierten ($DA_{DO}>1$) im Sommer zu reaktionslimitierten Bedingungen ($DA_{DO}<1$) im Winter. Andererseits hatten kurzfristige Ereignisse nur geringfügige Auswirkungen auf das System. Da hydrologische Ereignisse durch verminderte Wassertemperatur und kürzere Aufenthaltszeiten charakterisiert sind, reduzierte sich die Transportlimitierung des Systems leicht, Die Studie zeigt auch, dass die Annahme einer konstanten Wassertemperatur entlang eines SW-Infiltrationspfades zu einer Über- oder Unterschätzung der Reaktionsraten um den Faktor 2-3 führen kann, wenn sich die Temperatur des infiltrierenden Wassers von der in der Flussaue unterscheidet. Auch die Annahme konstanter Verweilzeiten

des Wassers während des gesamten hydrologischen Jahres führt zu einer Unterschätzung des NO_3^- Abbaus (40-50% Unterschied).

Die numerische Modellierung in Studie 2 konzentrierte sich auf die Simulation des Wasserflusses und des Stofftransports (DO und NO_3^-) unter Verwendung der Messdaten aus Studie 1, wobei die räumliche Skala erweitert wurde. Diese Modellierung kombinierte ein vollständig integriertes instationäres, numerisches 3D-Strömungsmodell mit einem temperaturabhängigen reaktiven Transport entlang Grundwasserfließpfaden. Die Ergebnisse zeigen, dass Temperaturschwankungen die reaktive Zone für NO_3^- verschieben, während diese Zone unter wärmeren Bedingungen in der Nähe des Flusses liegt. Sogar bei begrenzter Kohlenstoffverfügbarkeit (als Elektronendonor) und niedrigen Temperaturen waren die Anteile der NO_3^- Entfernung (R_{NO3}) weiter entfernt vom Fluss größer als entlang kurzer hyporheischer Fließpfade (R_{NO3}=0,4 bzw. R_{NO3}=0,1). Umgekehrt schränkten Transitzeiten und DO-Konzentrationen den Nitratabbau in der stromnahen Region ein. Mit zunehmender Temperatur verringerten sich die Auswirkungen der Strömungmuster und der Konzentration gelöster Stoffe auf den biogeochemischen Umsatz und die Redoxzonierung in der Umgebung des Flusses stark. Darüber hinaus bietet diese Studie einen anpassungsfähigen Rahmen zur Quantifizierung des biogeochemischen Umsatzes auf Reichweitenbasis in hydrologisch dynamischen Fließgewässern.

In Studie 3 wurde das Strömungsmodell mit einer Hydraulic Mixing Cell Methode gekoppelt, um die Quellzusammensetzung der Wässer zu kartieren und ihre räumlich-zeitliche Entwicklung in der Flussaue zu verfolgen. Dies ermöglichte die Identifizierung von Zonen mit ähnlichen Anteilen von SW und GW pro Aquifervolumen (d. h. "Mischungs-Hotspots"), die mischungsabhängige Reaktionen ermöglichen. Nur etwa 9% des gesamten simulierten Bereichs wurden als Mischungs-Hotspots identifiziert (hauptsächlich am Rande der geochemischen hyporheischen Zone), aber dieser Wert konnte nach großen Abflussereignissen bis zu 1,5-mal höhere Werte erreichen. Solche Ereignisse verstärken die Durchmischung von Fluss- und Grundwasser in größerer Entfernung vom Fluss, wohingegegen in der Nähe des Flusses der rasche Anstieg des SW-Zuflusses das Verhältnis zwischen den Wasserfraktionen zu SW verschiebt, wodurch das Potenzial für die Durchmischung und die damit verbundenen Reaktionen verringert wird. Die Studie bietet einen leicht übertragbaren Ansatz zur Bewertung der räumlich-zeitlichen Muster des Durchmischungsprozesses und dessen Auswirkungen auf die Biogeochemie der Auenzone in Bezug auf mischungsabhängige Umsatzprozesse.

Zusammenfassend verdeutlichen die Ergebnisse der drei Studien die Beziehungen zwischen hydrologischen und biogeochemischen Prozessen auf verschiedenen Raumskalen in der RZ. Durch die Kombination von innovativer Methoden und gekoppelten, mechanistichen Modellen hat diese Arbeit das Verständnis des reaktiven Potenzials von Falussauen verbessert, was eine Grundlage für weitere Forschung sowie Maßnahmen für eine integrierte Bewirtschaftung zur Wiederherstellung aquatischer Ökosysteme in Flussauen bieten kann.

Chapter One

Extended Summary

1.1 Introduction

1.1.1 Riparian zones – where stream and groundwater interact

Environmental awareness is generally higher for visible things, such as endangered animals, deforestation, or the water quality of a nearby surface water body (e.g., stream, lake, and wetland). On Earth, however, about 95% of the total available (liquid) fresh-water for human usage and consumption is stored below the surface as groundwater (Fetter, 1980; Gleick et al., 1993), which is practically "invisible" to the human eye. Notwithstanding, it has been acknowledged already for some time that surface water (SW) and groundwater (GW) are hydraulically-connected parts of one hydrologic continuum, rather than two separate components (Winter et al., 1998), and that SW-GW interactions take place across a range of scales in almost every region on Earth. Processes and changes at one domain can largely affect the water quality and the quantities available in the other (Triska et al., 1989; Woessner, 2000). Thus, understanding the interactions between (visible) surface water and (invisible) groundwater within the connecting "transition zones" is essential for improving the management and further restoration of aquatic systems.

Riparian zones, the transition zones between terrestrial and aquatic environments, are typically a small area within a watershed, but they are known for a disproportionate influence on water and solute exchanges between SW and GW domains (Boano et al., 2014; Lohse et al., 2009; McClain et al., 2003; Vidon et al., 2010), and are critical "ecosystem control-points" (Bernard-Jannin et al., 2017). For example, several studies of riparian zones in the USA, New Zealand, France, and Denmark have reported that nitrate (NO_3^-) concentrations of subsurface inputs decline by >90% within riparian corridors (Hill, 1996; Vidon and Hill, 2004). Moreover, SW-GW interactions within riparian zones can cover several spatial and temporal scales: the transport of surface water through subsurface flow paths that return to surface water (i.e., hyporheic flows) span from millimetres up to thousands of meters, and can range from seconds to years depending on factors like geological structure, surface morphology, and climatic conditions (Boano et al., 2014; Buffington and Tonina, 2009; Cardenas, 2009; Harvey et al., 1996; Tóth, 1963). Also, the direction and magnitude of SW-GW exchange can vary on space and time, depending primarily on the hydraulic gradient between SW and GW according to Darcy's law (1856). Consequently, short-term single precipitation events as well as long-term seasonal variations can change stream stages and groundwater tables, and thereby temporally change the direction and magnitude of SW-GW exchange fluxes. Thus, a stream reach that is

usually a GW discharge area (i.e., gaining stream) can temporarily become a source of water and solutes (or contaminants) for the riparian aquifer (i.e., losing stream) - or vice versa.

During transition through riparian sediments, infiltrating SW can interact with aquifer material, further mix with ambient GW, and facilitate various biogeochemical processes that can impact the whole aquatic system (Brunke and Gonser, 1997; Hester et al., 2017; McMahon, 2001; Pinay et al., 1998; Zarnetske et al., 2011). The interactions between hydrology and biogeochemistry in riparian zones have been extensively investigated in recent years (Boano et al., 2008; Gu et al., 2012; Hill, 1996; Hill et al., 1998; Lohse et al., 2009; Pescimoro et al., 2019; Ranalli and Macalady, 2010; Stegen et al., 2016; Zarnetske et al., 2012). Despite that, disentangling reaction and transport processes and their importance for subsurface reactions modulated by short-term events and seasonal variations is difficult due to highly dynamic bio-geophysical characteristics of riparian environments (Kolbe et al., 2019; Krause et al., 2017; Pinay et al., 2015). Taking advantage of innovative high-resolution measurement techniques, as well as growing computational capacities, the research on SW-GW interactions would benefit of comprehensive and combined field-modelling approaches to further assess feedback mechanisms and interactions between flow dynamics and biogeochemical cycling on scales that are important to coupled SW-GW systems and human interactions (Schilling et al., 2019; Simmons et al., 2020).

1.1.2 Reactive potential of riparian zones: a dynamic and complex coupled system

The interplay between hydrology and biogeochemistry in a riparian zone can lead to different reactive potentials for turnover of solutes, that is, the degree at which a certain solute (or compound) can be transformed or reacted to another depending on local thermo-physical conditions. The reactive potential along a subsurface flow path highly depends on the time that a water parcel stays in contact with the reactive media (Gu et al., 2007; Oldham et al., 2013). The longer water travels through the riparian subsurface, the greater the exposure to potentially reactive zones. However, discharge events might reduce GW transit-times in riparian zones due to sudden increases of SW-GW hydraulic gradients, limiting the exposure time to reactive zones, whereas relatively shorter time is available for reactions to take place, thus reducing net reactions (Gu et al., 2007).

Additionally, stream stage variations can also increase SW-GW exchange magnitudes within riparian zones, and enhance solute turnover by increasing the supply and the mixing of reactants on the subsurface (Gu et al., 2012; Hester et al., 2014; Trauth et al., 2018, 2015; Trauth and Fleckenstein, 2017). For instance, Trauth et al. (2018) have shown that, particularly in riparian zones along losing stream sections, infiltrating stream water can improve the availability of dissolved organic carbon (DOC) as an electron donor in the subsurface and in turn enhance denitrification of agricultural NO_3^-. This mixing creates unique

biogeochemical conditions that can attenuate contaminants from either upstream surface water or groundwater, whereas groundwater-borne solutes may be more dependent on such mixing due to limited reactants availability in the subsurface (Hester et al., 2013). Yet, relatively little attention has been given to the relation between hydrological transience, the resulting spatio-temporal dynamics of SW-GW mixing, and the implications to riparian biogeochemistry despite its importance for mixing-dependent reaction processes (Biehler et al., 2020; Cirpka and Kitanidis, 2000; Conant et al., 2004; Gassen et al., 2017; Hester et al., 2019, 2017; Trauth et al., 2018).

Temperature is a crucial control on the activity of both, aerobic and anaerobic bacteria, significantly affecting biogeochemical reactions in riparian zones (O'Connell, 1990; Peterjohn, 1991; Pietikäinen et al., 2005; Trauth et al., 2018). Hence, seasonal and short-term temperature fluctuations driven by SW-GW exchanges may either fuel or hinder reactions depending on characteristics of infiltrating SW in contrast to GW (Greskowiak et al., 2006; Henzler et al., 2016; Sharma et al., 2012). In winter, for example, cold air temperatures result in colder SW pulses to the shallow (usually warmer than SW) riparian groundwater. Conversely, with high temperatures in the summer, groundwater (usually colder than SW) can be heated by infiltrating warmer SW (Engelhardt et al., 2013; Munz et al., 2017). Besides, water and heat propagate along subsurface flow paths at different rates, with heat signals being strongly retarded and damped due to interaction with the sediment matrix. Nevertheless, the transient effects of SW heat pulses that propagates to GW on biogeochemical processes, the scale to which they are affected, and the variability between transport and reaction processes on both short-term and long-term scales are still not widely explored at scales larger than few meters from streambanks (Song et al., 2018; Vieweg et al., 2016; Zheng et al., 2016; Zheng and Bayani Cardenas, 2018).

Finally, different solutes can react or be transformed in different locations and at different times in the subsurface given the presence (or absence) of one solute that can largely inhibit (or trigger) the transformation of another. For instance, the reactive potential for redox-sensitive solutes such as NO_3^- is largely controlled by the presence of dissolved oxygen (DO). Only after strong oxygen depletion, facultative anaerobes will progress to anaerobic heterotrophic processes, which follows a very defined sequence of electron acceptors, from most to less energetically favourable substances: DO > NO_3^- > manganese(IV) (MnO_2) > iron(III) (FeOOH) > sulphate (SO_4^{2-}) > hydrogen (H^+) (Appelo and Postma, 2005; Edmunds et al., 1982). Therefore, the bulk DO concentration in water is a key variable defining the redox-state of the system and regulating biogeochemical processes such as denitrification that might take place within riparian flow paths. However, DO concentration in water is temperature dependent, as well as it is the DO consumption via aerobic respiration (Brugger et al., 2001; O'Connell, 1990; Pietikäinen et al., 2005; Thamdrup et al., 1998; Weiss, 1970), which adds extra complexity on the biogeochemical system.

Additionally, infiltration of stream water rich in DO into the riparian aquifer can equally modify and shifts the occurrence of consecutive biogeochemical processes (e.g., nitrification/denitrification, iron and sulphate reduction, mineralization of organic material) (Boano et al., 2010; Zarnetske et al., 2012, 2011). For instance, Zarnetske et al. (2012) used the concept of Damköhler numbers (Fogler, 2005) to show how a small in-stream gravel bar can be characterized either as a sink or a source for NO_3^- depending on water DO concentrations and transit-times. Still, due to the highly dynamic environment, a portion of the riparian aquifer can exhibit a certain condition, which strongly differs from that of another nearby location, whereas a temporal change can also occur depending on the combination of hydrological and meteorological drivers (Song et al., 2018).

There is a complex interaction between hydrological variations at different time scales, the associated heat and solute transport between SW-GW, and the biogeochemical reactions controlled by these variations. To understand how nutrients (such as carbon or nitrogen) are transported and transformed within SW-GW coupled systems, a combined approach entailing hydrological and biogeochemical perspectives is essential.

1.1.3 Relating flow dynamics and reactive potential within riparian zones

The principles of subsurface water flow, SW-GW exchange, and the link to main biogeochemical processes associated to them are well understood up-to-date. Nevertheless, disentangling the reaction and transport processes and their controls on subsurface reactions, which are modulated by seasonal variations and short-term events is challenging due to highly dynamic bio-geophysical characteristics of riparian environments (Kolbe et al., 2019; Pinay et al., 2015).

Given all of these complexities, it is only recently with advancing sensor technologies and the availability of longer and high-frequency observations that it has become possible to assess the relationships between river dynamics and observed biogeochemical patterns using data-driven approaches. Thus, to date only a few data-driven analyses have attempted to explore them in field studies of SW-GW coupled systems (e.g., Biehler et al., 2020; Vieweg et al., 2016; Zarnetske et al., 2012). Still, such empirical data-driven approaches relate input variables directly to observed outputs, and thus do not explicitly consider the underlying physical processes. While these approaches alone may not uncover every underlying process, they can still provide insights on the main characteristics and relations of observed phenomenon (Sivapalan, 2006).

On the other hand, the use of spatially-explicit, physically-based numerical models, which account for spatial organization of relevant hydrologic and biogeochemical parameters and represent processes based on their actual governing physical laws has grown exponentially in the last years (Brunner et al., 2017; Moeck et al., 2015; Schilling et al., 2019; Simmons et al., 2020). They can handle different hydrological

and meteorological boundary conditions, while representing multiple hydro-biogeochemical processes that occur in different spatio-temporal scales (e.g., oxygen consumption, plant uptake, solute mobilization and transport). Even if the famous aphorism "*All models are wrong*" (Box, 1979) still valid up to date, "*some models provide remarkably useful estimates*" (Box, 1979). On the top of that, the equifinality problem of parameter sets can be reduced with multiple dataset types available for model calibration, which allows for a more robust parameterization, (Doherty, 2015; Doherty and Johnston, 2003; Doherty and Hunt, 2010; Fienen et al., 2009; Schilling et al., 2019) and the application of a model for the understanding of hydro-biogeochemical processes is reinforced. In that sense, research on their controlling mechanisms at multiple spatio-temporal scales represents a step forward on understanding the functioning of the SW-GW interface as buffer, filter and reactive area.

Because diffuse NO_3^- contamination still presents a big threat to aquatic ecosystems despite efforts to reduce inputs (Abbott et al., 2018; Ebeling et al., 2021; Steffen et al., 2015), and since global food production only tends to increase likely leading to continuously high use of N-based fertilizers (ultimately leading to NO_3^- fluxes to water systems), this research had a strong focus on NO_3^- dynamics. The only process that completely removes NO_3^- from the aquatic system is denitrification via its reduction to N_2 and N_2O gases. Denitrification rates are controlled by local factors including NO_3^- and DO concentrations, pH, temperature, and availability of electron donors (e.g., DOC, Fe^{2+}, and CH_4). In aquifers, NO_3^- reduction mainly occurs through the oxidation of organic matter (Appelo & Postman, 2005; Hill, 1998, Pescimoro et al., 2019; Rivett et al., 2008). The process is well understood, however difficult to assess in the field due to its dependency on multiple aspects. Thus, the question lies on what extent NO_3^- is transported as a conservative solute through the aquifer, and how biogeochemical processes may attenuate high concentrations. Moreover, since denitrification is a redox-sensitive process, tightly coupled to DO dynamics, the mechanisms uncovered and the framework presented here also have the potential to be applied on the assessment of other similar redox-sensitive solutes and processes, such as the attenuation of emerging micropollutants (Henzler et al., 2016; Munz et al., 2019). This is the research field to which this PhD research aims to contribute by combining available field data, their further analyses and numerical modelling techniques.

1.2 Research Objectives and Outline

1.2.1 Motivation and Objectives

The overarching objective of the research was to advance the understanding of coupled hydrologic and biogeochemical processes in RZs and to evaluate the trade-offs between short and long-term changes in water transit-times and the supplies of reactants due to flow variations, as well as the effects of temperature fluctuations on the reactivity of the system. Specifically, high-frequency field data, data-driven analysis and further numerical modelling were combined to provide a general framework and the respective tools to assess the relations between flow dynamics and the reactive potential within riparian zones. The specific objectives of this dissertation were to:

I - Evaluate the relationship between flow dynamics and short-term and long-term seasonal controls of the reactive state of the riparian system;

II - Assess the impacts of stream flow and temperature variations on patterns of DO and NO_3^- concentrations at the stream-corridor scale;

III - Map the different water sources and assess the dynamics of their mixing and their relation with biogeochemical processes within a riparian zone.

1.2.2 Organization of the thesis

The Chapter 1 presents the synopsis of the thesis, depicting the overall methods and results from the research. At the end of this chapter, the main conclusions and outlook from the work are drawn.

In Chapter 2, a data-driven analyses carried out in a near stream riparian zone of a losing stream reach is described. Specifically, a suite of natural-gradient well-to-well tracer-tests employing salt (NaCl) and DO as tracers is carried out in the riparian aquifer covering a range of hydrologic conditions in terms of stream flow and temperature, and combined with high-frequency data of water levels, temperature, electrical conductivity, and DO in the stream and in groundwater. Thus, major features controlling spatio-temporal variations of transit-times and DO consumption rates in the near riparian aquifer with a specific focus on the interplay between seasonal and event-scale variability can be addressed.

In Chapter 3, the data acquired during the first study presented in Chapter 2 is subsequently used for the setup and calibration of a fully-integrated hydrological numerical model that covers the entire floodplain

of the site. The calibrated flow and mass transport model is coupled with a reactive transport according to simulated flow paths using a streamtube reaction approach based on temperature-dependent reactions. In Chapter 3 we investigate how the biogeochemical processes occurring in the floodplain are affected by changes in both hydrological and meteorological drivers. In detail, oxygen and nitrate dynamics are further investigated since it still challenging to do this with field data alone.

In Chapter 4, a framework to identify mixing hot-spots between infiltrating SW and riparian GW at the stream-corridor scale is displayed. Here a Hydraulic Mixing-Cell (HMC) method (Partington et al., 2011) is coupled to the numerical flow model to track different water sources compositions and their contribution within the model domain to further analyse spatio-temporal patterns of mixing in the floodplain. The underlining assumption/hypothesis for this study comes from previous works showing that mixing-dependent turnover of groundwater-borne solutes in the riparian zone are higher at the fringe of the hyporheic zone, where they mix with stream water-borne solutes triggering biogeochemical processes such as denitrification of groundwater-borne NO_3^- (Hester et al., 2019, 2013; Trauth et al., 2018; Trauth and Fleckenstein, 2017). The main objectives of Chapter 4 were to assess and quantify the areas and patterns of mixing between different water sources in the floodplain under transient hydrological conditions, and present an easy-to-transfer framework to assess and locate high potential reactive areas for groundwater-borne solutes related to mix with stream water-borne solutes.

1.3 Materials and Methods

1.3.1 Study site

The field experiments and numerical modelling were carried out in the floodplain of the Selke Stream (51°43’37.79”N, 11°18’51.0”E), a fourth-order reach, around a well instrumented and studied site (Trauth et al., 2018; Vieweg et al., 2016) within the Bode Observatory of the TERENO initiative, and operated by the Helmholtz Centre for Environmental Research-UFZ (Wollschläger et al., 2017). The Selke catchment covers a total area of 456 km^2. At the studied site, which marks the transition from the mountainous upper catchment to the flatter, lower catchment, the 2 km long stream reach is lined by a band of riparian vegetation up to 50 m wide, consisting of willow and beech trees intermixed with pasture, surrounded by agricultural fields, which are mostly wheat, sugar beet, rapeseed, corn, and turnip, Figure 1.

Mean annual temperature is around 10°C (±1.7) although it can vary from -10°C to above 30°C, in winter and summer periods, respectively. Mean annual precipitation varies between 350 mm and 910 mm (median of 616.6 mm), with slightly higher average monthly values during summer periods. At the site, mean annual

stream discharge is 1.5 m^3/s. However, baseflow can be below 0.2 m^3/s during summer, while discharges up to 15 m^3/s and overbank flow can occur during spring snowmelt with associated sediment movement.

The local riparian aquifer was formed during the Plio- and Pleistocene, with deposition of alluvial sediments mainly consisting of greywacke and slate stone originating from the central-east Harz Mountains (Bachmann et al., 2008; Trauth et al., 2018). The riparian aquifer is up to 8 m thickness, ranging from medium sands to coarse gravels, underlain by clay-silt deposits forming the bottom of the alluvial aquifer. Drilling core samples from the vicinity of the stream reveals a layered system, with a continuous less-permeable unit (fine sand) at around 3-4 m below ground near the stream. The hydraulic conductivity of the aquifer material, determined by salt-tracer and slug-tests in the riparian wells, ranges from 1.7×10^{-3} to 1.2×10^{-2} m/s (geometric mean: 3.72×10^{-3} m/s). Groundwater levels are generally shallow, with mean depths to groundwater of 0.5 and 1.8 m in the winter and summer, respectively. Further away from the stream, groundwater levels increase and reach mean values of 4 m below ground. Additionally, geophysical and borelog data indicates that the aquifer thickness steadily decreases with distance from the stream (Lutz et al., 2020; Trauth et al., 2018).

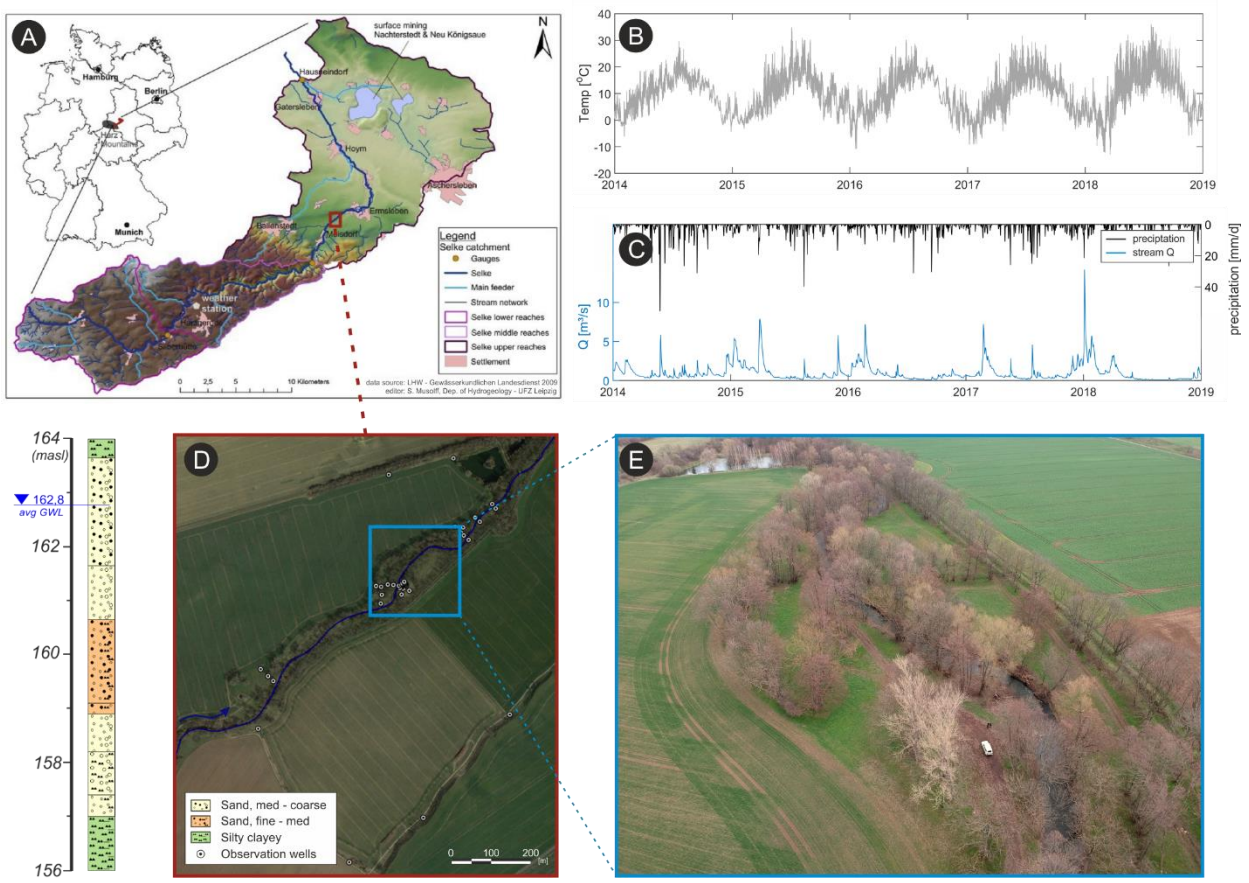

Figure 1: Location of studied field site **(a)** with aerial photographs **(d-e)**; **(b)** Daily measurements of air temperature, **(c)** stream discharge and precipitation. A borelog representative of the local geology units at the site is presented in **(d)** with indication of local average groundwater level. The stream flows from bottom-right to top-left on the drone picture in **(e)**.

1.3.2 Data Collection and Field Experiments

High-frequency data collection

Water levels, electrical conductivity (EC) and water temperature in stream (T_{SW}) and groundwater (T_{GW}) were measured by self-contained Solinst Levellogger Junior loggers installed at observation wells near the stream banks. Dissolved oxygen (DO) concentrations were monitored by self-contained DO loggers (HOBO Dissolved Oxygen Data Logger) in both stream and in groundwater. A total of 11 nested 2" PVC monitoring wells, screened at depths between 1 and 6 m below ground (mbg), were selected for groundwater monitoring. All loggers were set to a 10-min measuring interval from November 2017 until December 2018, comprising one full year of high-frequency measurements with few data gaps in between (10% of total dataset). Stream discharge (Q) was calculated from a stream stage-discharge relation, based on stage

readings and monthly manual discharge measurements using an electromagnetic flow meter (MF pro, Ott, Germany). Daily precipitation data was acquired from a federal weather station of the German Meteorological Service 15 km upstream of the site (Harzgerode, DWD-Station #2044).

1.3.3 Seasonal and short-term controls of riparian dissolved oxygen (Chapter 2)

Well-to-well tracer-tests

On the top of the high-frequency data collected, eight natural gradient well-to-well tracer-tests were carried out in the riparian aquifer adjacent to the stream between November 2017 and September 2018. The tests were performed in order to acquire a temporal variation of transit-times (τ) by tracing the EC signal of the injected salt tracer. The same wells selected for high-frequency data collection were used for the performance of the tracer-tests. A detailed description of the protocol followed for the tracer-tests is presented in the methods section of Chapter 2 and only a brief summary about the applied techniques and methods is given in this section. Conservative transport of the EC signal was assumed so that the 1D advection-dispersion equation without retardation and no sorption (Koestel et al., 2011) applies:

$$\frac{\partial C}{\partial t} = -V_{GW}\frac{\partial C}{\partial x} + D_h\frac{\partial^2 C}{\partial x^2} \quad \text{Eq.1}$$

where C is solute concentration [M^3L^{-1}], V_{GW} is the groundwater velocity [MT^{-1}], D_h is the dispersion coefficient, t is time and x is distance to injection point [L]. With the initial condition that a slug mass M is injected at x= 0 and t= 0, at any given moment τ and at x, the tracer concentration can be represented by:

$$C(x,\tau) = \frac{M}{2\sqrt{\tau\pi D_h}}\ exp\left[-\left(\frac{(x-V_{GW}\,\tau)^2}{4D_h\tau}\right)\right] \quad \text{Eq.2}$$

where M is the solute mass [M] in terms of EC, τ is the transit-time [T], and other parameters are the same as in Equation (1). Alongside the EC measured during the tracer-tests, DO concentrations were measured to derive *in-situ* DO consumption rates. Locally, groundwater DO consumption is mainly attributed to organic matter degradation via aerobic respiration, while other processes as iron-minerals oxidation and nitrification are negligible (Trauth et al., 2018; Vieweg et al., 2016). Since half-saturation constants of aerobic respiration are typically small (0.03–0.3 mg O_2/L), a first-order kinetics reaction was employed:

$$C = C_0\ exp(-k_{DO}\,\tau) \quad \text{Eq.3}$$

where C is the measured DO concentration in the monitoring well [ML^{-3}], C_0 is the initial DO concentration in the tracer [ML^{-3}], k_{DO} is the first-order rate constant for aerobic respiration (T^{-1}), and τ is the mean transit-time [T]. Empirical k_{DO} were correlated to measured T_{GW} at the time of the experiment following Arrhenius equation (Pietikäinen et al., 2005), Equation (4). Thus, high-frequency DO consumption rates could be inferred from T_{GW} values for periods not covered by the tests.

$$k_{DO-T_{GW}}(t) = \ a \exp(b\, T_{GW(t)}) \quad \text{Eq.4}$$

where $k_{DO\text{-}TGW}$ is the reaction rate, T_{GW} is the groundwater temperature, and a and b are fitting parameters.

Riparian DO simulations and associated seasonal and short-term controls

To assess effects of short-term fluctuations of temperature and stream discharge on riparian DO dynamics, which are likely not captured by tracer-tests, DO concentrations were simulated based on Equation (3) according to the high-frequency relations between transit-times and stream discharge, as well as k_{DO} and T_{GW}, and assuming stream DO concentrations prior to infiltration (t-τ) as C_0 in each time-step. To account for water temperature changes from infiltration along transit to the observation wells, an effective temperature (T_{eff}) was implemented in the simulations as an optimization parameter, constrained between T_{SW} and T_{GW}, and found through the minimization of the objective function (ε) for observed DO concentrations in each time-step:

$$\varepsilon = \sqrt{\{DO_{obs(t)} - [DO_{sw(t-\tau)} \exp(-a \exp(b\, T_{eff(t)})\, \tau_{(t)})]\}^2} \quad \text{Eq.5}$$

where a and b are fitted parameters from Equation (4). Based on T_{eff}, a temperature corrected DO consumption rate ($k_{DO\text{-}Teff}$) was derived for each time-step, and further used to compute riparian DO concentrations.

In order to evaluate whether the riparian system was limited by the reaction rate or by the supply of reactants, the dimensionless Damköhler numbers for oxygen (DA_{DO}) was employed, computed as:

$$DA_{DO}(t) = \ k_{DO(t)}\ \tau_{(t)} \quad \text{Eq.6}$$

where k_{DO} and τ represent the first-order DO consumption rates [T^{-1}] and transit-times [T], respectively. If $DA_{DO}<1$, the DO supply rate is above its biogeochemical demand and the system is reaction limited. $DA_{DO}=1$ represents a balanced system, where DO supply equals its demand. For $DA_{DO}>1$, the DO supply rate is smaller than its demand and the system tends to show anoxic conditions as it becomes transport limited. In turn, this has implications for other redox-reactions as DO concentrations control the occurrence of reactions such as denitrification, which only occurs after DO depletion (Zarnetske et al., 2012).

1.3.4 Fully-coupled Hydrological Modelling (Chapter 3 and Chapter 4)

The fully-integrated surface-subsurface flow and mass transport simulations in this thesis (Chapter 3 and Chapter 4) were carried out using the code HydroGeoSphere (HGS, Therrien *et al.*, 2010). HGS is a finite

element code that solves Richard's equation for variably saturated flow in three-dimensions. Van Genuchten parameters (Genuchten, 1980) are incorporated into the model for computation of unsaturated hydraulic conductivity and simulation of variably saturated flow (Therrien et al., 2010). Overland and stream flow are solved numerically in 2D using the diffusion-wave equation together with Manning's equation. For coupling the surface and groundwater domains, a dual node approach was used to approximate the continuity of pressure heads, assuming that the exchange fluxes among the domains depend on the hydraulic head gradient across a coupling interface, as well as the vertical saturated hydraulic conductivity, and a first-order exchange coefficient (Therrien et al., 2010).

Spatial Discretization, Boundary and Initial Conditions

The extent of the simulated domain was approximately 900 m x 770 m x 10 m (width, length, and thickness). An unstructured 2D triangular mesh of finite elements was generated for the top of the domain, representing the land and streambed topographies. The element sizes varied from a maximum of 40 m in the floodplain to about 1.0 m around the streambed and observation wells in the near-stream riparian zone. The 2D mesh was extended vertically to form a 3D mesh consisting of quadrilateral elements in 15 layers, with thicknesses varying from 0.1 m in the top layers to 2.0 m in the bottom layer of the model. The depth of the simulated domain was set according to the less permeable clay-silt deposits that form the bottom of the alluvial aquifer.

Initial conditions for hydraulic heads were assigned for the whole subsurface domain based on interpolated average field measurements. At first, to reach a quasi-steady state conditions, the model was run using constant, average values of stream discharge (1.5 m^3/s) and groundwater recharge (as 33% of daily precipitation, 0.0003 mm/d), which was computed through an external routine using HYDRUS-1D. Next, a transient run with daily updated boundary conditions (BC) from November 2016 to November 2017 (i.e., spin-up period) was done to achieve more realistic hydraulic heads throughout the domain. Following the spin-up period, the model was run with a similar time-step updating of the BCs, when model calibration and validation were carried out. In sum, prescribed hydraulic heads (Dirichlet) and a prescribed water flux (Neumann) were assigned at the downstream and upstream lateral sides of the subsurface domain, respectively. At the surface domain, prescribed water flux (Neumann) and critical depth boundary, and groundwater recharge (as a fraction of precipitation) were applied at the stream inlet and outlet, and at the model top, respectively. The other laterals and bottom of the domain presented no flow boundaries. A more detailed description of the BCs applied on the domain is provided in the methods sections of the Chapter 3 and Chapter 4.

Parameterization, Model Calibration and Validation

The subsurface domain was divided into four units with anisotropic hydraulic conductivity (preliminary $K_{xy}/K_z=10$). Initial hydraulic conductivity was set as homogeneous in X and Y directions for the different units and based on field measurements (section 3.2). Van Genuchten parameters were assigned based on literature values typical for medium sand. Surface properties (Manning's roughness coefficients, *x* and *y* friction values, and rill storage heights) for the streambed and floodplain were based on literature values. Detailed values are presented in the methods section of Chapter 3. The model was calibrated against observed groundwater heads and stream discharge (covering 130 days of high-frequency measurements, Figure A1), and measured tracer concentrations from performed well-to-well tracer-tests, comprising 8 of the 18 BTCs recorded in different aquifer depths. Hydraulic and transport parameters were calibrated simultaneously against all available observation types using a weighted multivariate objective function through PEST (Doherty, 2018, 1994). A Tikhonov regularization was introduced to reduce parameter nonuniqueness. Different observation types were weighted according to their total number of observations to feature equally in the objective function, and tracer concentrations were inversely weighted to give higher importance to the tails of breakthrough curves. The model quality was evaluated using the average water balance error, the mean absolute error (MAE) between observed and simulated heads and tracer concentrations, as well as the Nash Sutcliffe efficiency (NSE) criteria.

1.3.5 Coupling hydrology and biogeochemistry (Chapter 3)

The interactions between hydrology and biogeochemistry were investigated using a coupled hydrological-biogeochemical modelling framework. A reaction stream tube approach was used for coupling hydrology and biogeochemistry, assuming that subsurface flow and transport occurs along defined flow paths in the floodplain. Stream water infiltration flow paths were extracted from the calibrated numerical flow model through an advective particle tracking on every simulated time-step, based on the resulting transient velocity fields through the software TecPlot 360X. Each subsurface flow path was split into different interconnected sub-sections based on particles locations, where biogeochemical reactions were simulated according to computed solutes concentrations of previous sub-section, Figure 2. Using a Lagrangian approach, the integration time-step between flow path sub-sections was on average 0.1 day, guaranteeing a good spatio-temporal discretization of results. Around 1,800 particles per time-step and their progressive transit through the domain (resulting in around 200,000 subsections per flow path) were coupled with the multispecies solution reactions simulation. The respective reaction equations were implemented in MATLAB®.

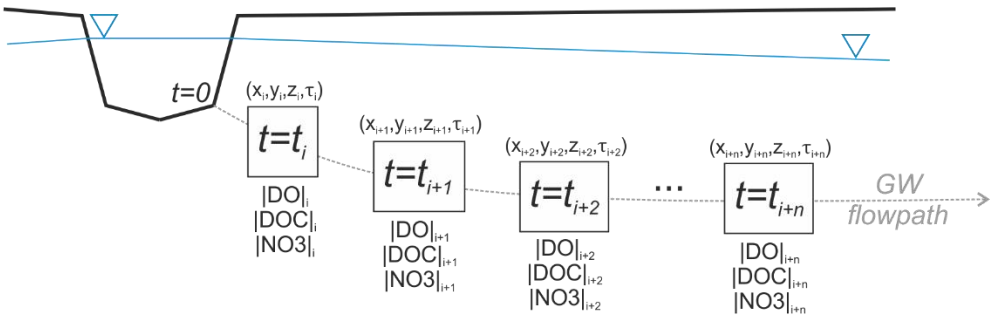

Figure 2: Conceptual stream tube reaction approach for biogeochemical processes simulation within an individual infiltrating water flow path (GW flowpath). Individual flow paths are split into sub-sections (i) representing a point in space and time within the flow path where biogeochemical processes are simulated. Apart from the first sub-section, boundary and initial conditions of each sub-section are defined from simulation of preceding sub-section. X,Y and Z are spatial coordinates from extracted particles, and τ represents the respective transit-time since infiltration t. The simulated solutes concentrations are presented at the bottom of each sub-section.

Specifically, aerobic respiration (AR) and denitrification (DN) of organic matter (DOC) represented by carbohydrate CH_2O were simulated along individual subsurface flow paths following the reaction equations:

$$\textit{Aerobic respiration: } CH_2O + O_2 \rightarrow CO_2 + H_2O \qquad \text{Eq. 7}$$

$$\textit{Denitrification: } 5CH_2O + 4NO_3^- + 4H^+ \rightarrow 5CO_2 + 2N_2 + 7H_2O \qquad \text{Eq. 8}$$

Solutes transport into the subsurface was assumed as purely driven by infiltrating stream water, and reaction rate coefficients were considered as temperature-dependent. Besides, the stream tube approach implies that there is no mixing between the individual flow paths due to hydrodynamic dispersion (mechanic dispersion + diffusion). Since oxygen availability is a key variable that either triggers or suppresses redox-sensitive processes, here biogeochemical reactions were simulated using Monod-kinetics with an inhibition factor (I_{DO}) for DN, hence, significant NO_3^- consumption occurs only if DO concentrations are below 1.0 mgL^{-1}. Moreover, DOC can be consumed for both AR and DN until their exhaustion following the reaction rate coefficients in each sub-section:

$$k_{AR(t)} = f_T \left[\mu_{max\_AR} \left(\frac{C_{DO(t)}}{K_{DO} + C_{DO(t)}} \right) \left(\frac{C_{DOC(t)}}{K_{DOC} + C_{DOC(t)}} \right) \right] \qquad \text{Eq. 9}$$

$$k_{DN(t)} = f_T \left[\mu_{max\_DN} \left(\frac{C_{NO3(t)}}{K_{NO3} + C_{NO3(t)}} \right) \left(\frac{C_{DOC(t)}}{K_{DOC} + C_{DOC(t)}} \right) I_{DO(t)} \right] \qquad \text{Eq. 10}$$

$$I_{DO(t)} = \frac{K_I}{K_I + C_{DO(t)}} \qquad \text{Eq. 11}$$

where k_{AR} and k_{DN} is the overall reaction rates of DO and NO_3^-, respectively; μmax_{AR} and μmax_{DN} represent maximum reaction rates for AR and DN, respectively; C_{DO}, C_{DOC} and C_{NO3} are the concentrations of DO, DOC and NO_3^-; and K_{DO}, K_{DOC} and K_{NO3} are the half-saturation constants for DO, DOC and NO_3^-, respectively, and K_I is the inhibition coefficient, Table 1. The maximum reaction rate of AR (μmax_{AR} = 0.478 mmol $L^{-1}d^{-1}$ = 15.3 mg $L^{-1}d^{-1}$) was based on field values, while maximum reaction rate of DN (μmax_{DN} = 0.086 mmol $L^{-1}d^{-1}$ = 5.3 mg $L^{-1}d^{-1}$), as well the solute half saturation constants were based on values from the literature (Gu et al., 2007; Trauth et al., 2014; Zarnetske et al., 2011). To account for the temperature dependency of rate coefficients, the temperature factor (f_T) was introduced in Eq. 9 and Eq. 10 according to the expression proposed by O'Connell (1990):

$$f_{T(t)} = exp\left[\alpha + \beta\, T_{GW(t)}\left(1 - 0.5\,\frac{T_{GW(t)}}{T_{opt}}\right)\right] \qquad \text{Eq. 12}$$

where α and β are fitting parameters, T_{GW} is the monthly averaged groundwater temperature, and T_{opt} is the optimal temperature for DOC consumption taken as 35°C. The f_T was parameterized using combined in-situ measurements of DO and EC from the carried out well-to-well tracer-tests, with α and β estimations (-3.5 and 0.22, respectively) within the range of literature values, and been successfully applied in other river bank filtration studies (Diem et al., 2013; Greskowiak et al., 2006; Kirschbaum, 2000; Sharma et al., 2012). Although infiltrating stream water with different temperature than that of groundwater can impact reaction rate coefficients in the vicinity of the stream (Song et al., 2018), diurnal heat pulses from the stream are strongly damped in the first few meters in the aquifer (Engelhardt et al., 2013; Munz et al., 2017; Rau et al., 2014). Thus, it is expected that flow path temperatures reach T_{GW} further away from the stream. For the spatial scale under analysis (tens to hundreds of meters) temperature variations occur predominantly at seasonal time scale. Therefore, to represent the expected water temperature at the floodplain, monthly averaged T_{GW} from near stream piezometers (that are also affected by infiltrating stream water to a certain extent) were preferred in Eq. 12. The resulting T_{GW} lies between stream water temperature (strongly varying over the year, 8.5°C±6.0) and the temperature of the end-member groundwater (far from the stream - solely influenced by seasonality, 10°C±1.5) (Figure A2). Thus, the seasonal subsurface temperature variations were well captured. With this approach, simulations of DO concentrations using transit-times derived from the HGS model yielded a NSE= 0.82 and R^2= 0.91 for a near stream well during the same observation period (Figure A2).

Initial Solute Concentrations and Biogeochemical Boundary Conditions

Apart from the first sub-section of each flow path, solute concentrations and reaction rates for a subsequent sub-section were based on results of preceding sub-sections. Solute concentrations and reaction rates for

the first sub-section of each flow path were based on initial solute concentrations (Table 1). Since stream water is saturated in DO prior to infiltration, initial dissolved oxygen concentrations were set as constant (0.031 $mmolL^{-1}$ = 10 mgL^{-1}) for all first sub-sections of flow paths. A constant DOC concentration of 0.66 mmol L^{-1} (20 mgL^{-1}) was also assumed, twice the molar mass of DO, to ensure that there was a DOC source available for denitrification after near complete DO consumption.

For initial NO_3^-, in a first scenario, concentrations were related to stream discharge (Q) following field data (Table 1), which indicates a nearly linear increase of solute concentration with discharge. Simulated NO_3^- concentrations using this relation matched well observed NO_3^- concentrations in a groundwater well (NSE= 0.53 and R^2=0.75, Figure A2). To further assess the reactive potential of denitrification in the floodplain for elevated NO_3^- concentrations (e.g., coming from soil top or from larger distance groundwater), additional scenarios considering a high constant initial value of 1.0 $mmolL^{-1}$ (62 mgL^{-1}) for NO_3^- concentrations were carried out. This also reflects the high NO_3^- concentrations at the groundwater on the site (Trauth et al., 2018). By imposing the high initial concentrations we can assess where significant NO_3^- turnover occurs regardless of the origin of the source, thus estimating the overall locations of high DN rates within the floodplain. The constant initial solute concentrations may be considered unrealistic regarding the usual relationship between solute concentrations and discharge for most streams (Dupas et al., 2017; Musolff et al., 2015; Sawyer et al., 2014), but by doing this the effects of pure changes in hydraulic and thermal conditions can be better evaluated in these scenarios.

Additionally to the simulations based on measured T_{GW}, other scenarios using a range of constant water temperatures (0.5-25°C) were considered for evaluating the interplay between transit-times and water temperature on the biogeochemical processes. Lastly, simulations with a more limited carbon source were also considered to assess the impacts of limited DOC.

Table 1 – Parameter values used in defining the reaction kinetics.

Rate constants (Eq.9 and Eq.10)	*Value*
μmax_{AR}	0.4780 mmol $L^{-1}d^{-1}$
μmax_{DN}	0.0864 mmol $L^{-1}d^{-1}$
Half saturation constants (Eq.9 and Eq.10)	
K_{DO}	0.00625 mmol L^{-1}
K_{DOC}	0.10700 mmol L^{-1}
K_{NO3}	0.03230 mmol L^{-1}

Inhibition coefficient for Denitrification (Eq.11)	
K_I	0.03130 mmol L^{-1}
Temperature factor (f_T) (Eq.12)	
α	-3.5
β	0.22
T_{opt}	35ºC

Initial solutes concentrations for each flow path

Solute	*Initial concentration in mmol L^{-1} (mg L^{-1})*
Dissolved Oxygen (DO)	0.31 (*10.0*)
Organic Matter (DOC)	0.66 (*20.0*)
Nitrate (NO_3^-)	0.08xQ+0.048 (*5xQ+3*)
Nitrate (NO_3^-) – additional scenarios	1.00 (*62.0*)
Organic Matter (DOC) – additional scenarios	0.33 (*10.0*)

Values in round brackets are concentrations in mg L^{-1}. Q is the stream discharge.

Evaluation of the subsurface aerobic zone and nitrate removal fractions

Based on simulated DO concentrations, the points where groundwater DO≤2 mgL^{-1} (i.e., anaerobic conditions) in each infiltrating flow path were delimited. In the following, the 3D convex envelope encompassing those points were generated, which closely defines the aerobic zones around the stream in each simulated time-step by using the *boundary* function in MATLAB®. By doing so, one can assess the changes in the volume of the aerobic zone given the different Q and T_{GW} scenarios.

Nitrate removal fractions (R_{NO3}) were computed by calculating the cumulative amount of NO_3^- removed through denitrification in each flow path sub-section divided by the initial NO_3^- in each flow path:

$$R_{NO3} = \frac{denitrified\ NO3}{initial\ NO3} \qquad \text{Eq. 13}$$

The fraction ranges between 0 and 1, with larger values representing higher removal fractions relative to initial NO_3^- concentrations, hence higher removal efficiency. A value of 1 represents complete removal of the initial flow path NO_3^-. With that, the changes on the time required to remove 50% of the initial NO_3^- concentration (R_{NO3}=0.5) in each scenario, for instance, were assessed for the different flow and temperature scenarios. Results were evaluated according to field measured R_{NO3}, which were previously

calculated for the site (Lutz et al., 2020; Trauth et al., 2018). Further specific details on reactive transport simulation and evaluation are presented in the methods sections of the Chapter 3.

1.3.6 Assessing different water sources compositions and mixing degrees in the floodplain (Chapter 4)

Hydrological Modelling and the Hydraulic Mixing Cell Method

On the study presented in Chapter 3, mainly stream borne solutes were considered within the stream tube reaction approach, which does not consider mixing between different water sources in the floodplain. Even if solutes could have being progressively incorporated at the different sub-sections of simulated flow paths to represent groundwater-borne solutes there, the uncertainty by doing this would be large, and results somewhat speculative. So that, on the study of Chapter 4, the Hydraulic Mixing Cell (HMC) method (Partington et al., 2011) was coupled to the numerical flow model presented in Chapter 3. This supports the computation of different water sources contribution to each numerical model cell, thus allowing for the identification of water "mixing hot-spots" in the floodplain. By doing that, the continuous and transient effects of flow variations on mixing, as well as the areas and moments in which different water sources mix and have the potential to enhance biogeochemical reactions - especially important for groundwater-borne solutes around stream corridors - could be assessed. In this study, mixing is referred as the colocation of different source waters within the subsurface, rather than necessarily true-mixing, where solutes from different source waters are present simultaneously in an overlapping area (Dentz et al., 2011; Kitanidis, 1994). The HMC method was originally developed to identify contribution of different water sources - namely surface water (e.g., surface runoff) and groundwater - to the total streamflow hydrograph (Partington et al., 2013, 2012). The method uses the "modified mixing rule", which simulates a mixing regime between perfect mixing and piston flow. Different water sources are mixed according to volumes of water flowing in and out of a model cell accordingly (Partington et al., 2011):

$$f_{i(w)}^{t} = \left(\frac{V_i^{t-1}}{V_i^{t}} - \frac{Vbc_{out}^{t} + \sum_{j=1}^{m} V_{ij}|_{t-1}^{t}}{V_i^{t}} \right) f_{j(w)}^{t-1} + \frac{Vbc_{w}^{t} + \sum_{j=1}^{n} V_{ji}|_{t-1}^{t} \; f_{j(w)}^{t-1}}{V_i^{t}} \qquad \text{Eq. 14}$$

where $f_{i(w)}^{t}$ [-] is the computed water fraction *w* at time-step *t* in cell *i*, *n* and *m* are sources and sinks for cell *i*, $f_{j(w)}^{t-1}$ denotes the water fraction *w* at time *t-1* in a neighbouring cell *j*, *V* denotes the water volume with the superscript denoting time-step and subscript denoting the cell, *ij* denoting volume into cell *j* from cell *i* over the time-step from *t-1* to *t*, *ji* denoting volume from neighbour cell *j* into cell *i*, and Vbc_{w}^{t} is the volume from the inflowing boundary condition associated with water fraction *w* and Vbc_{out}^{t} is the volume

summed from all outflowing boundary conditions at cell *i*. Inflow from adjacent cells is assigned the computed water fractions from the upstream cell. There were three pre-defined water sources here, namely stream water (f_{SW}, any water parcel flowing through streambed cells), groundwater (f_{GW}, any inflowing water from the subsurface lateral domain at the south boundary), and floodplain water (f_{FW}, any water flowing from soil surface apart from streambed cells). A more detailed description of the applied method and the required assumptions is given in the methods section of Chapter 4.

Hydrochemical Data and Validation of HMC Results

Other hydrochemical data used in part of this research was derived from collected stream water and groundwater samples from observation wells. Groundwater was sampled with a peristaltic pump placed at the middle of the fully screened wells. Groundwater samples were taken only when field parameters (e.g., DO, EC, and pH) were steady. Surface water samples were taken as grab sample. Samples were collected, stored, and analysed following standard lab protocols for water samples. Due to limited hydrochemical data for the main analysed period (2017-2019), data collected by Trauth *et al.* (2018) between April 2014 and April 2016 in a four weeks interval complemented part of this research. In order to compare their results with the numerical simulations, the previously calibrated numerical flow model for 2017-2019 was applied to the period of 2013-2016, whit only hydrological BCs being adjusted accordingly. The other calibrated parameters were kept identical. The HMC results were validated by comparing the simulated stream water fractions (f_{SW}) in riparian groundwater with computed stream water fractions (F_{RIV}) in groundwater observation wells based on a chloride (Cl^-) linear mixing model (Appelo and Postma, 2005) according to collected water samples:

$$F_{STR} = \frac{[Cl^-_{obs}]-[Cl^-_{GW}]}{[Cl^-_{SW}]-[Cl^-_{GW}]} \quad \text{Eq. 15}$$

where $[Cl^-_{obs}]$, $[Cl^-_{GW}]$, and $[Cl^-_{SW}]$ indicates the Cl^- concentrations based on water samples collected from observation wells, in the groundwater distant from the stream, and in the stream, respectively. The $[Cl^-_{GW}]$ end-member was taken from the observation well B10 water samples, farthermost groundwater well from the stream. For some groundwater samples (30%), Cl^- concentrations were temporally lower than in the stream water end-member and they were excluded from further analyses. Simulated f_{SW} values of the observation wells were extracted from the numerical model by averaging the values from all fully-saturated cells that comprises each well location in a given time-step. That was done to approximate how water samples were collected at the fully screened wells, which likely results in sampling of a mix of the whole saturated column rather than of a specific groundwater depth. In a perfect model, $F_{STR}=f_{SW}$ independent of the other simulated HMC water fractions. The quality of the results was evaluated in terms of correlation coefficient (R^2) between F_{STR} and f_{SW} values, as well as with the nonparametric Wilcoxon rank-sum test

(Ziegel et al., 2011) about the medians of F_{STR} and f_{SW} datasets. Finally, using the different HMC fractions as scalar variables, model cells were spatially aggregated to assess their different contributions to the simulated domain, as detailed in in the methods section of Chapter 4.

HMC Mixing Degrees Calculation and Mixing hot-spots

The mixing degree (d) quantified the extension to which different water sources mix within a model cell. In other words, the quantification of mixing does not refers to true-mixing, but it gives an indication on how different water sources are mixed within a numerical cell in a given time-step based on neighbouring cells water inflows and outflows. For a three end-member mixing, where each end-member is a different water source (e.g., SW, GW, and FW), any three fractions combined could be represented by a vector in a 3D coordinate space: $d=[f_{SW}, f_{GW}, f_{FW}]$, whereas a "perfect mixing" (e.g., equal fractions of different water sources) is represented by a vector $d_p=[{}^1/_3, {}^1/_3, {}^1/_3]$. Like so, d can be calculated as the Euclidean distance between the vectors d and d_p taking into account that a maximum value for a given fraction can only be 1, as well as that the fractions within a cell have to sum up to 1 (for an error-free fluid mass balance). A more general equation to quantify the mixing degree for three (or more) end-members (w) could be written as:

$$d = 1 - \left[\frac{\sqrt{\left({}^1/_w - f_1\right)^2 + \left({}^1/_w - f_2\right)^2 + \ldots + \left({}^1/_w - f_w\right)^2}}{\left(\sqrt{2} \times {}^{\sqrt{w}}/_w\right)} \right] \quad \text{Eq. 16}$$

where f_1, f_2,... f_w represent different HMC fractions. A value of $d=1$ represents the "perfect mixing" within a cell at a given time-step (e.g., equal water fractions within the model cell), and smaller d values indicate a disproportional contribution of one or another water sources to the mixture (e.g., too much of one water source and too few of other). Based on preliminary results, it was observed that actual volumes of f_{FW} were very low in comparison to f_{GW} and f_{SW} in the fully saturated portion of the domain. Therefore, a simplified version of the Equation (16) considering a two end-member mixing only was employed. To do so, the two end-members f_{GW} and f_{FW} were combined to a single one (e.g., $[f_{GW}+ f_{FW}]$), which reduces the mixing model to a 2D case as detailed in in the methods section of Chapter 4. This streamlined two end-member mixing was preferred for the mixing analyses because otherwise resulting d values would be consistently very low in the simulations, which would impair further analyses. Cells presenting different mixing degrees (e.g., $d > 0$, $d \geq 0.25$, $d \geq 0.50$, and $d \geq 0.75$) were aggregated in each time-step and compared to the total volume of the *geochemical* HZ (Triska et al., 1989), here defined as regions presenting $f_{SW} \geq 0.5$, as well as to the total volume of the simulated floodplain to assess their variation according to flow dynamics. Details on the aggregation methods are presented in the methods section of Chapter 4. Mixing hot-spots (d_h) were

defined as $d \geq 0.75$ (Berezowski et al., 2019), where mixing of different water sources are relatively high (nearly equal water fractions within a model cell) and biogeochemical reactions have higher potential to take place (Boano et al., 2010; Gomez-Velez et al., 2017; Zarnetske et al., 2011).

Finally, since time is also a relevant variable for biogeochemical processes, knowing the time that a certain water parcel resides within mixing hot-spots could be as equally important as solely identifying their occurrence in the floodplain. So that, exposure-time ($d_{h\text{-}\tau}$), defined as the time that a water parcel resides in a mixing hot-spot was also evaluated. Water transit-times were computed based on a transient particle tracking analyses according to flow model results. Flow paths sub-sections were individually analysed in terms of transit-times, HMC fractions, mixing degrees d, and consequently $d_{h\text{-}\tau}$. Thus, the changes of $d_{h\text{-}\tau}$ (and water transit-times) due to transient hydrological conditions in comparison to the changes and the simple occurrence of mixing hot-spots could be jointly assessed.

1.4 Results and Discussion

1.4.1 Seasonal and short-term controls of riparian dissolved oxygen dynamics and the implications for redox processes (*Chapter 2*)

The continuous *in-situ* measurements with high spatio-temporal discretization of stream water and groundwater physico-chemical parameters, combined with the multiple well-to-well tracer test offered an advanced approach to acquire relations between surface flow dynamics and subsurface processes. Given that conditions at the site are not-ideal to acquire reliable high-frequency groundwater transit-times by other means, such as cross-correlation analyses of electrical conductivity (EC) of infiltrating stream water (Nixdorf and Trauth, 2018), the multiple natural gradient tracer-tests proved to have captured the general changes in groundwater transit-times driven by stream stage fluctuations at the losing stream reach. Transit-times of infiltrating stream water generally decreased with increasing stream discharge (Q) (Figure 3), which is related to the slightly smaller hydraulic gradient between the stream and adjacent riparian groundwater developed under such conditions, resulting in higher groundwater velocities. The groundwater transit-times resulting from the tracer-tests were correlated with Q through a power-law ($\tau = a \times Q^b$) to derive high-frequency transit-times directly from stream discharge. The *in-situ* dissolved oxygen consumption rates (k_{DO}) calculated alongside the measured EC throughout the tracer-tests showed a strong correlation with groundwater temperature (T_{GW}). The T_{GW} explained about 90% of k_{DO} variations, indicating a strong temperature control of the reactions. There was a systematic increase of rates towards the summer when

T_{GW} was equally high. Through the Arrhenius equation, k_{DO} was correlated with T_{GW} to derive high-frequency k_{DO} values ($k_{DO\text{-}TGW}$) (Figure 3).

Simulation of riparian dissolved oxygen (DO) using the aforementioned high-frequency relations for two different aquifer depths resulted in good fits (NSE= 0.63 and NSE= 0.53, respectively). When constant transit-times (found through optimization to match observed DO) were used within the simulations, fits only slightly improved, indicating the minor control of transit-times on the DO dynamics in contrast to temperature. Still, high frequency variations in DO were not captured well by either models. DO simulations were only improved when considering an optimized effective temperature (T_{eff}), which accounts for changes in water temperature from infiltration point along transit to observation wells, and hence leads to a temperature corrected DO consumption rate coefficient ($k_{DO\text{-}Teff}$) (Figure 4).

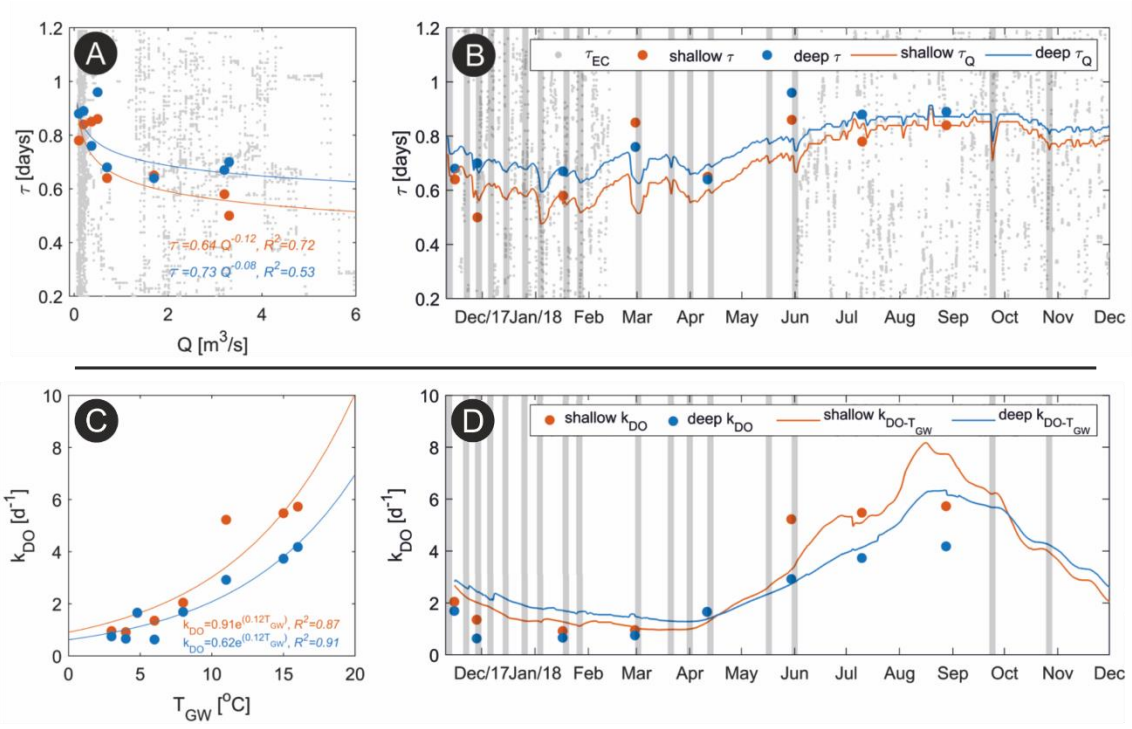

Figure 3: **(a)** Shallow and deep GW transit-times and stream discharge (Q) relation used to derive transient τ_Q; **(b)** temporal variation of GW transit-times for shallow and deep aquifer obtained from tracer-tests (shallow τ and deep τ, respectively), transient GW transit-times for shallow and deep aquifer based on stream discharge (shallow τ_Q and deep τ_Q, respectively). Grey dots in (a) and (b) represent the EC cross-correlation transit-times (τ_{EC}); **(c)** Groundwater temperature (T_{GW}) and k_{DO} relation used to derive high-frequency k_{DO}; (d) temporal variation of empirical DO consumption rates acquired from tracer-tests (k_{DO}), and the transient empirical k_{DO} based on T_{GW} relation ($k_{DO\text{-}TGW}$) for shallow and deep aquifers. Grey bars in (c-d) highlight discharge events identified for the observed period.

The $k_{DO\text{-}Teff}$ based on T_{eff} was 2-3 times higher than the empirical $k_{DO\text{-}TGW}$ in summer, indicating underestimations of DO consumption rates if only T_{GW} is considered, in line with results from the modelling study carried by Song et al. (2018) on temperature effects of high-frequency flow variations on thermal regimes and biogeochemical processes within hyporheic zones. The effects of temperature on DO consumption rate coefficients and the improvement in DO simulations for the shallow aquifer are shown in Figure 4. Since more degrees of freedom were added to the model, simulations employing $k_{DO\text{-}Teff}$ had better model fits (NSE= 0.89 and NSE= 0.95, respectively) and high-frequency DO variations were better represented. The carried out data-driven analyses and the collected field data reveals that even for short transit-times, water temperature is not constant along a flowpath from the infiltration point at the streambed to the observation well, but instead changes according to stream dynamics and water temperature differences between the stream and ambient groundwater.

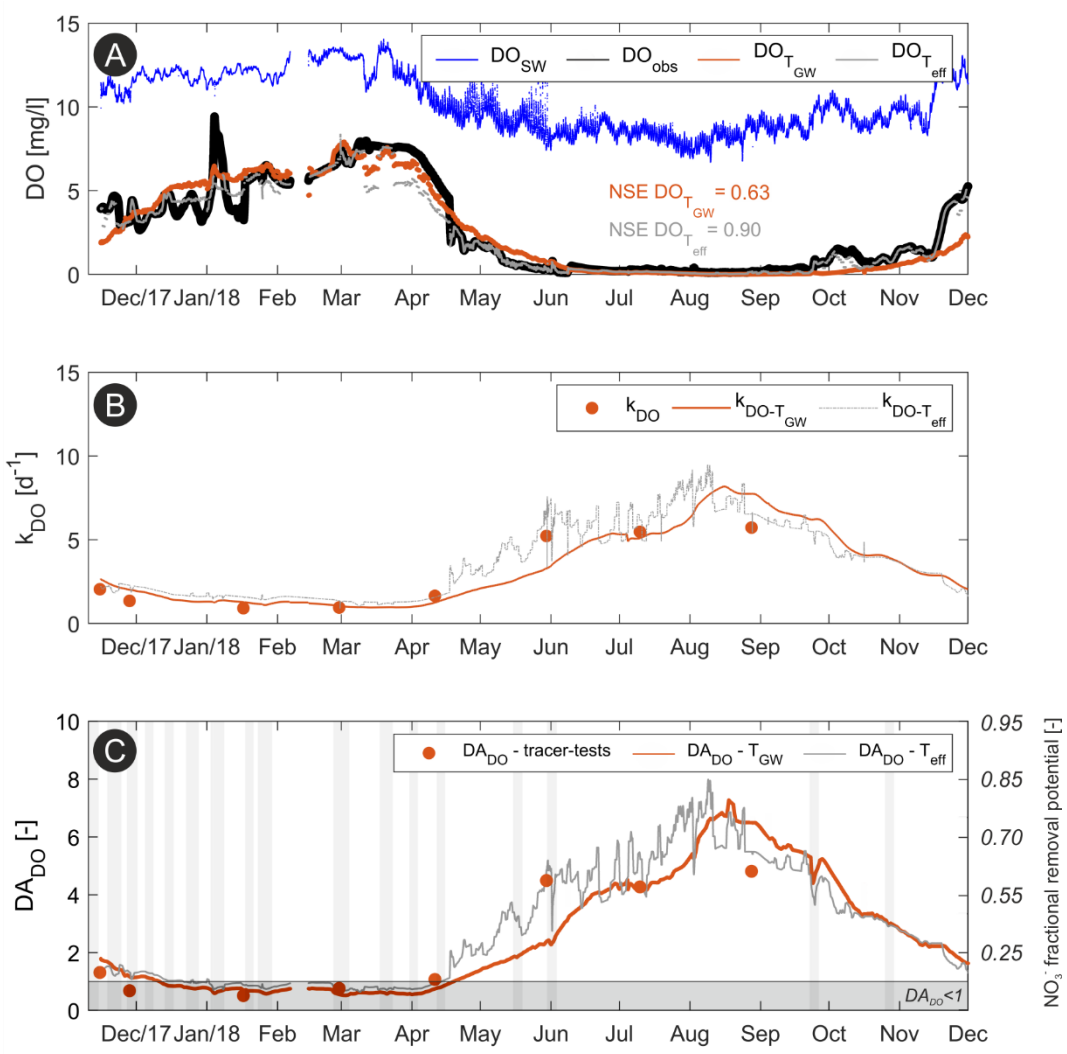

Figure 4: **(a)** Observed stream water and groundwater dissolved oxygen concentrations (DO_{SW} and DO_{obs}, respectively) together with simulated DO concentrations using two different model parameterizations (DO_{TGW} and DO_{Teff}); **(b)** DO consumption rate coefficients acquired from the tracer-tests (k_{DO}), high-frequent consumption rates based solely on groundwater temperatures ($k_{DO\text{-}TGW}$),and rates based on an effective temperature ($k_{DO\text{-}Teff}$); **(c)** Damköhler number variations computed from the tracer-tests (DA_{DO} - tracer-tests), based on $k_{DO\text{-}TGW}$ (DA_{DO} - T_{GW}), and based on $k_{DO\text{-}Teff}$ (DA_{DO} - T_{eff}). NO_3^- fractional removal potentials in (c) are based on Zarnetske et al. (2012). Grey bars in (c) highlight discharge events identified for the observed period. The shaded area in (c) represents $DA_{DO}<1$ (reaction limited system).

The changes of the reactive regime were assessed through Damköhler numbers for dissolved oxygen (DA_{DO}). In sum, the riparian DA_{DO} values indicated distinct seasonal-shifts in the reactive regime of the system, from reaction limitation ($DA_{DO}<1$) during the winter to transport limitation ($DA_{DO}>1$) in late spring/summer. In terms of short-term effects, only small drops in DA_{DO} values were observed during events in comparison to baseflow, indicating a tendency towards less transport limited conditions, which can be explained by: (1) somewhat shorter transit-times during events, resulting in less time for DO consumption, thus bringing the balance of the system towards less transport limited; (2) most of the discharge events (60%) result in a drop of T_{SW} and T_{GW} contrary to conditions immediately prior to the event, leading to smaller consumption rates, and reinforcing the decrease of DA_{DO}. The results corroborate that the regime was mainly regulated by temperature variations controlling DO consumption rates since DA_{DO} patterns were similar despite the transit-time scenario considered. Nevertheless, especially during summer computed DA_{DO} using constant transit-times were smaller in comparison to DA_{DO} computed using varying transit-times. Equally, DA_{DO} were generally smaller in the summer if a T_{eff} was not taken into account for the computation of DO consumption rate coefficients, which can have implications when assessing redox sensitive related processes, Figure 4c. These findings indicate that event-driven changes in SW-GW exchange not only affect riparian oxygen consumption via associated variations in subsurface transit-times, but predominantly via induced changes in subsurface temperatures that affect the reaction rates. Further assessments of riparian reactive potentials and solute turnover should consider not only the hydrological variability, but also the variability of temperature conditions rather than constant values along flow paths.

1.4.2 Transit-time and temperature control the spatial patterns of aerobic respiration and denitrification in the riparian zone (*Chapter 3*)

The calibrated numerical flow and mass transport model exhibited very good results for simulated stream discharge (R^2=0.92) and groundwater heads (overall R^2=0.98), Figure A1. The model also reasonably captured the general tracer transit-time patterns (R^2=0.74 for mean tracer transit-times) despite the simplification of the geological media in the numerical model, suggesting that other minor geological heterogeneities not represented in the simulations probably pose a minor effect on flow and solute transport processes. Moreover, especially in near-stream areas where anisotropy of hydraulic conductivity and flow variability are high, the transient simulations and the further incorporation of more unconventional observations (i.e., multiple tracer transit-times and concentrations) in the model calibration process can assure a more sound parameter calibration (Gianni et al., 2019; Schilling et al., 2019; Xu and Gómez-Hernández, 2016) and should be contemplated in other numerical models whenever possible.

Results from simulated redox-sensitive solutes based on particle-tracking analyses and varying groundwater temperature (T_{GW}) reveal good match with field observations for both DO and NO_3^- concentrations (R^2=0.91 and R^2=0.75, respectively), Figure A2. Simulated NO_3^- removal fractions (R_{NO3}) also matched well observed values near the stream, ranging between 0.1 and 0.8 depending on the combination of T_{GW} and Q values (Figure A2). A similar range of R_{NO3} values was estimated in the preceding chapter for the same observation wells (Figure 4c), reinforcing the controls of DO concentrations on the results. Moreover, even if a R_{NO3}=0.5 cannot be achieved in the winter at the near stream wells given the combination of low T_{GW} and high Q (hence short transit-times), the results indicate that substantial denitrification (DN) can still occur further away from the stream after DO is sufficient depleted. Under such conditions, for instance, DN is supressed in near stream regions due to the presence of high DO concentrations, which strongly diminishes DN rates and shifts the location along the groundwater flow paths where significant DN can take place, Figure 5. As the majority of simulated flow paths were long and most of the water did not immediately return to the stream within the simulate domain, DN and complete NO_3^- removal (R_{NO3}=1.0) still occurred at later times and further away from the stream (given that DOC was not completely consumed through AR). Contrary, for the hyporheic flow paths (infiltrating SW particles returning to the stream) observed in the domain, maximum R_{NO3} values were only between 0.11 to 0.15 for low Q and high Q, respectively (for T_{GW}=25ºC). Different from R_{NO3} of long flow paths within the floodplain, the hyporheic R_{NO3} were slightly higher under high stream discharge due to slightly longer (and deeper) hyporheic flow paths and transit-times in comparison to low stream discharge, which is in line with findings from Trauth & Fleckenstein (2017) for an in-stream gravel bar at the site.

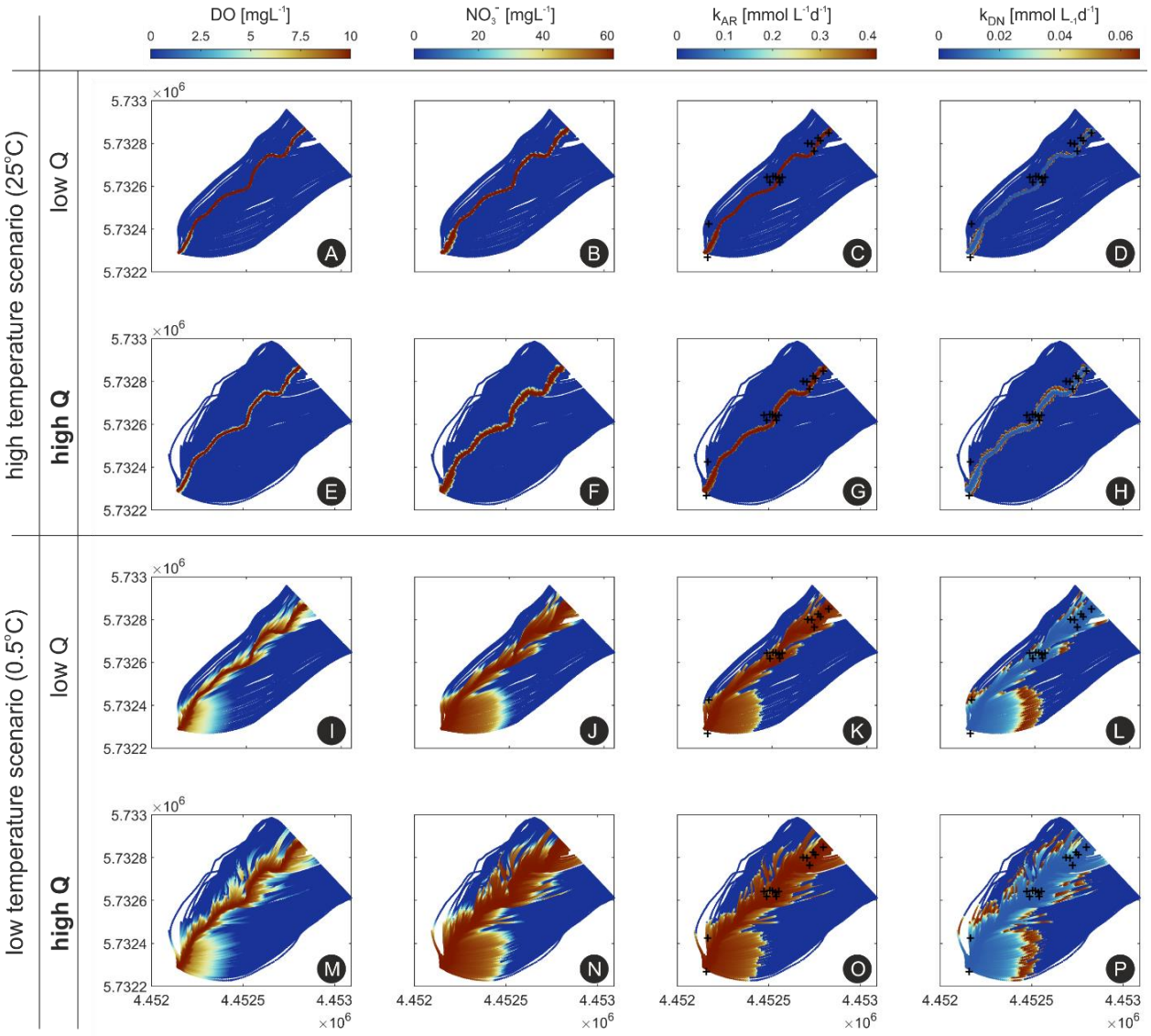

Figure 5: Distribution of dissolved oxygen (DO), Nitrate (NO_3^-), aerobic respiration (k_{AR}), and denitrification (k_{DN}) for four different scenarios of stream discharge and water temperature. The low Q and **high Q** represent 0.12 m^3s^{-1} and 12.0 m^3s^{-1}, respectively. The black crosses in the plots show the locations of the wells used for specific analyses of NO_3^- removal fractions. Note: deeper flow paths are not visible in the plots.

The combined effects of transit-times and temperature variations (alongside the effects of varying NO_3^-) on the overall NO_3^- removal efficiency in the floodplain, is illustrated by the changes on R_{NO3} at the observation wells (Figure 6a), and furthermore on the transit-times required to achieve R_{NO3}=0.5 in the floodplain, whereas shorter transit-times indicate higher removal efficiencies. Firstly, overall high R_{NO3} are attained under high T_{GW} regardless of the stream discharge values, indicating that changes in temperature pose a stronger control on the system reactivity in comparison to changes in stream discharge affecting groundwater transit-times. Yet, for the same T_{GW} scenario, R_{NO3} values were slightly smaller for increasing

discharge (Figure 6a) due to shorter time available for reactions to occur under high Q conditions. Also, for the same T_{GW} scenario, it can be noted that R_{NO3} values for low Q values were slightly larger for the scenario with varying initial NO_3^- concentrations than under the scenario with constant initial NO_3^- concentration because the initial NO_3^- concentrations for the former scenario were relatively smaller than on the second, indicating the effects of solute variation on R_{NO3}.

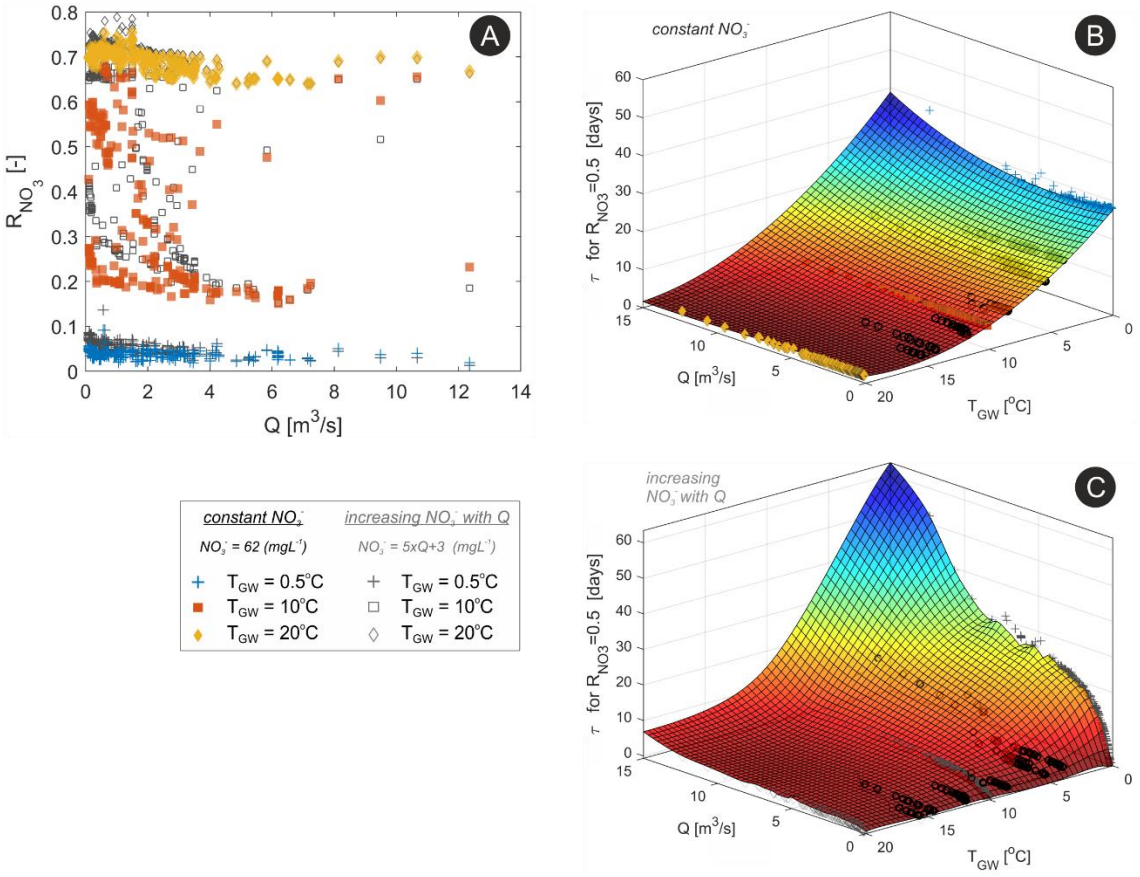

Figure 6: **(a)** NO_3^- removal fractions (R_{NO3}) on the near stream wells versus Q for various T_{GW} and NO_3^- concentration scenarios; **(b)** mean transit-time required for R_{NO3}=0.5 for various Q and T_{GW} scenarios with constant initial NO_3^- concentrations; **(c)** mean transit-time required for R_{NO3}=0.5 for various Q and T_{GW} scenarios with varying initial NO_3^- concentrations; black circles in the 3D plots show the results from the simulated period. Warmer colours on the fitted surfaces represent a higher reactive system, in which a shorter transit-time is required to reach R_{NO3}=0.5.

Secondly, the decrease in reactive efficiency (i.e., increase on the time required for R_{NO3}=0.5) is more prominent under low T_{GW} conditions indicating a more transport controlled system (Figure 6b-c). Particularly, under low T_{GW} the time required for R_{NO3}=0.5 strongly increased with Q from the nearly constant value of 35 days for the scenario with constant initial NO_3^- concentrations to slightly more than

60 days for the scenario with varying initial NO_3^- concentrations (Figure 6b-c). This also underlines the effects of increasing solute concentration on the overall removal efficiency. On the other hand, under high T_{GW}, the time required for R_{NO3}=0.5 only slightly increased with stream discharge (from 0.5 to 4 days) between the different initial NO_3^- scenarios. This absolute change under high T_{GW} is only minor because the system is less sensitive to variations in solute concentrations and transit-times under high T_{GW}; in other words, a reaction controlled system.

The high DOC availability in the simulations was imposed to reflect the general availability of electron donors from other sources in the riparian zone (e.g. particulate organic carbon in the sediments), which can be incorporate during water transit through streambed and aquifer sediments. This assumption is supported by the good agreement between simulated and measured R_{NO3} indicating that DOC is not a limiting factor for DN in the vicinity of the stream (Trauth et al., 2018). Yet, if only half of the initial DOC was considered (e.g., DOC= 10 mg L^{-1}), the new R_{NO3} at the observation wells would have been reduced (on average by 40%). This translate to mean final R_{NO3} between 0.3-0.4 at the end of flow paths (achieved when all DOC is completely depleted), for low and high T_{GW}, respectively (data not shown), which still higher than computed values along hyporheic water flow paths. This indicates that the potential for NO_3^- removal in the floodplain can be underestimated in studies targeting areas too close to the stream that might overlook longer groundwater flow paths and the related processes taking place along them.

As shown in Study 1, near the streambed and on the near stream region, reaction rate coefficients can indeed be affected by an "effective temperature", and in analyses on such scale this should be regarded. But since heat signals from the stream to groundwater are strongly damped in the riparian aquifer, simulations on such floodplain scale can be carried out much more efficiently by applying the streamtube approach and the monthly average T_{GW} values than carrying out full heat-transport simulations. The coupled flow path-reaction approach, which evaluates flow and reactive transport consecutively, adequately reproduced general spatio-temporal patterns of redox-sensitive solute concentrations and removal fractions in the river-corridor. For detailed assessments of complex local reactions and dynamics a fully coupled model might still be indispensable, but for a river-corridor-scale assessment this approach provides a viable, computationally less demanding alternative. Yet, with the flow path-reaction approach, hydrodynamic processes like dispersion and diffusion that may affect solute concentrations within and between flow paths due to solute relocation are not taken into account. They could result in more gradual and smooth anaerobic and DN fringes, for example. However, this effect would likely be large only for low discharge conditions when a less advectively dominated system is expected (e.g., low groundwater velocities), or under low T_{GW} when the system is more sensitive to changes in transport processes.

1.4.3 Spatio-temporal variations of water sources and mixing spots in a riparian zone (*Chapter 4*)

Results from the numerical flow model (previous calibrated for the 2017-2019 period) yielded to equally good results for the 2013-2016 period in terms of groundwater heads and stream discharge, with mean Kling-Gupta-Efficiency (KGE) of 0.73 and 0.84, respectively. This reinforces the application of the numerical flow model to other periods after BCs adjustments (e.g., stream inflow, groundwater heads at the boundary), as well as it lends confidence in the Hydraulic Mixing Cell (HMC) results. From the HMC results, simulated stream water fractions (f_{SW}) were comparable to observed stream water fractions (F_{RIV}) at groundwater wells. Generally, the near stream wells exhibited higher fractions of stream water (between 0.7 and 1.0, Figure 7) than other components like groundwater. The F_{RIV} and simulated f_{SW} showed reasonable correlation coefficients for most of wells (R^2 shown in Figure 7), whereas F_{RIV} presented slightly larger variations. The Wilcoxon-test performed between F_{RIV} and f_{SW} individually for each observation well also indicated that medians of the datasets in each well were not statistically different for the majority (indicated by h=0 on Figure 7). Moreover, the small differences between calculated F_{RIV} and simulated f_{SW} are acceptable given that a rigorous model calibration to hydrochemical data was not the objective of this study. Finally, the validation of the HMC results on the top of the flow results can further enhance model reliability and parameterization (Partington et al., 2020; Schilling et al., 2017, 2019) and should be considered within numerical models given its relatively small additional computational effort.

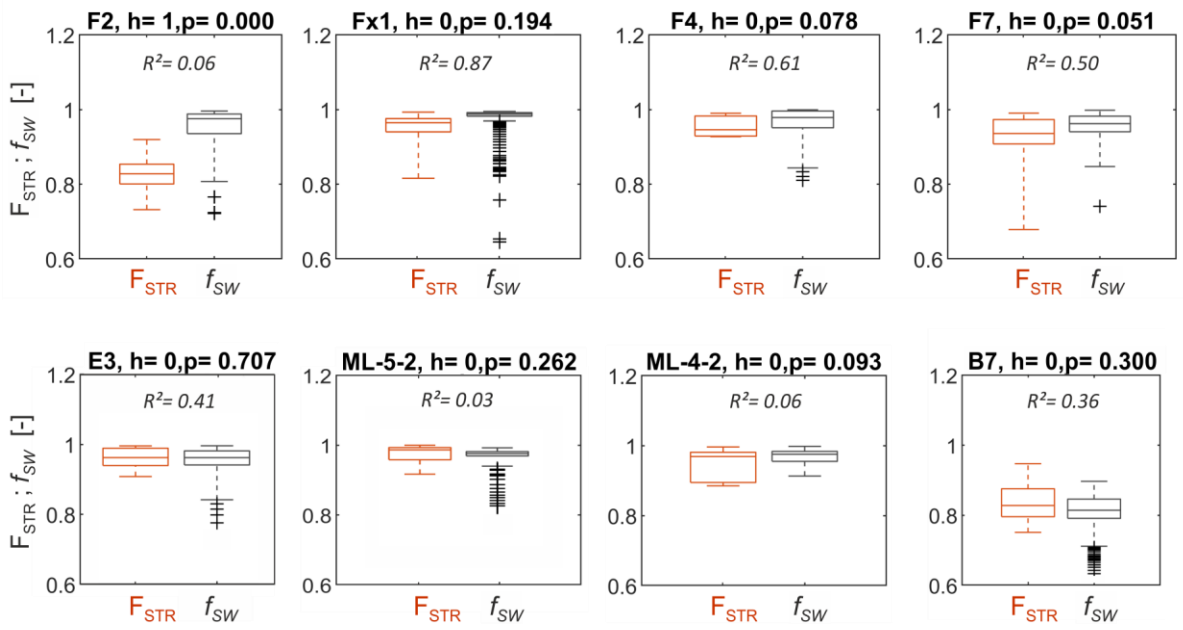

Figure 7: Observed and simulated stream water fractions (F_{RIV} and f_{SW}, respectively) for some observation wells in the study area. The *h* values represent the results of the Wilcoxon-test between F_{RIV} and f_{SW} datasets with respective *p-values* (p): h=0 indicates that the F_{RIV} and f_{SW} groups are from continuous distributions with equal medians, while h=1 indicates the difference between the medians is statistically significant; The R^2

values show the correlation coefficient between the F_{RIV} and f_{SW} datasets**.** The names of the wells are showed at the top of each plot.

As HMC results indicate the water-origin rather than the water content in each model cell, the results were further evaluated considering only the fully-saturated portion of the model domain, which can then be related to total HMC water contents. Nearly 80% of the saturated domain presented $f_{SW} \geq 0.1$ and about 20% presented $f_{SW} \geq 0.9$ (Figure A3). Spatially, there was a nearly pure occurrence of stream water around the stream (Figure 8), which is maintained over time by the strong losing condition of the stream reach. This is an important fact since stream-borne solutes (e.g., DOC) can be transported to the subsurface where bioavailable DOC is usually low, boosting biogeochemical processes like denitrification (Gassen et al., 2017; Trauth et al., 2018) as showed on the previous chapter. With distance from the stream, as infiltrating stream water mixes with local floodplain waters, the f_{SW} decreases and both f_{GW} and f_{FW} proportions increase, Figure 8. This distribution was somewhat constant over time with only minor fluctuations (Figure A3).

The large percentage of stream water in the floodplain might seem high. However, other studies performed in different alluvium floodplains, revealed an equally large percentage of stream water in the subsurface with distance from the stream (up to 250m), which is mainly controlled by the permeability of the aquifer material affecting the influx of SW to the subsurface (Schilling et al., 2017). Similarly, Poole *et al.* (2008) showed that aquifer water at the Minthorn study site (gravel-alluvial dominated floodplain) was essentially all derived from the main stream channel of the Umatilla River. They also found that the *geochemical* HZ penetrates to the entire local floodplain (about 300m wide) (Jones et al., 2008). In contrast, Sawyer *et al.* (2009) estimated the *geochemical* HZ extent to be only up to 30 m from the banks of the Colorado River near the Hornsby Bend site. In their case, however, the hydraulic conductivity of the aquifer material was nearly one order of magnitude smaller. Those previous studies and the findings presented here are in line with the propositions of Boulton *et al.* (1998) and Wondzell (2011) on the combined influence of hydrogeology and stream flow dynamics on the development of the HZ and exchanges around streams.

The *geochemical* HZ ($f_{SW} \geq 0.5$) was about 50% of the total saturated domain. Yet, nearly 80% of the HZ volume was comprised by f_{SW}, followed by f_{GW} (15%) and f_{FW} (5%), Figure A3. Differently, at the HZ fringe (where f_{SW}=0.5), there was a larger parcel of f_{GW} and f_{FW}, respectively 0.4 and 0.1, indicating a higher potential for mixing between different water sources, thus a higher potential for groundwater-borne solute turnover (Hester et al., 2019; Trauth and Fleckenstein, 2017). In fact, the fringe of the HZ presented the highest HMC mixing degrees *d* together with the smallest standard deviation (σ_d), reinforcing the steady presence of mixing hot-spots there in comparison to other places in the floodplain, Figure 8m-p.

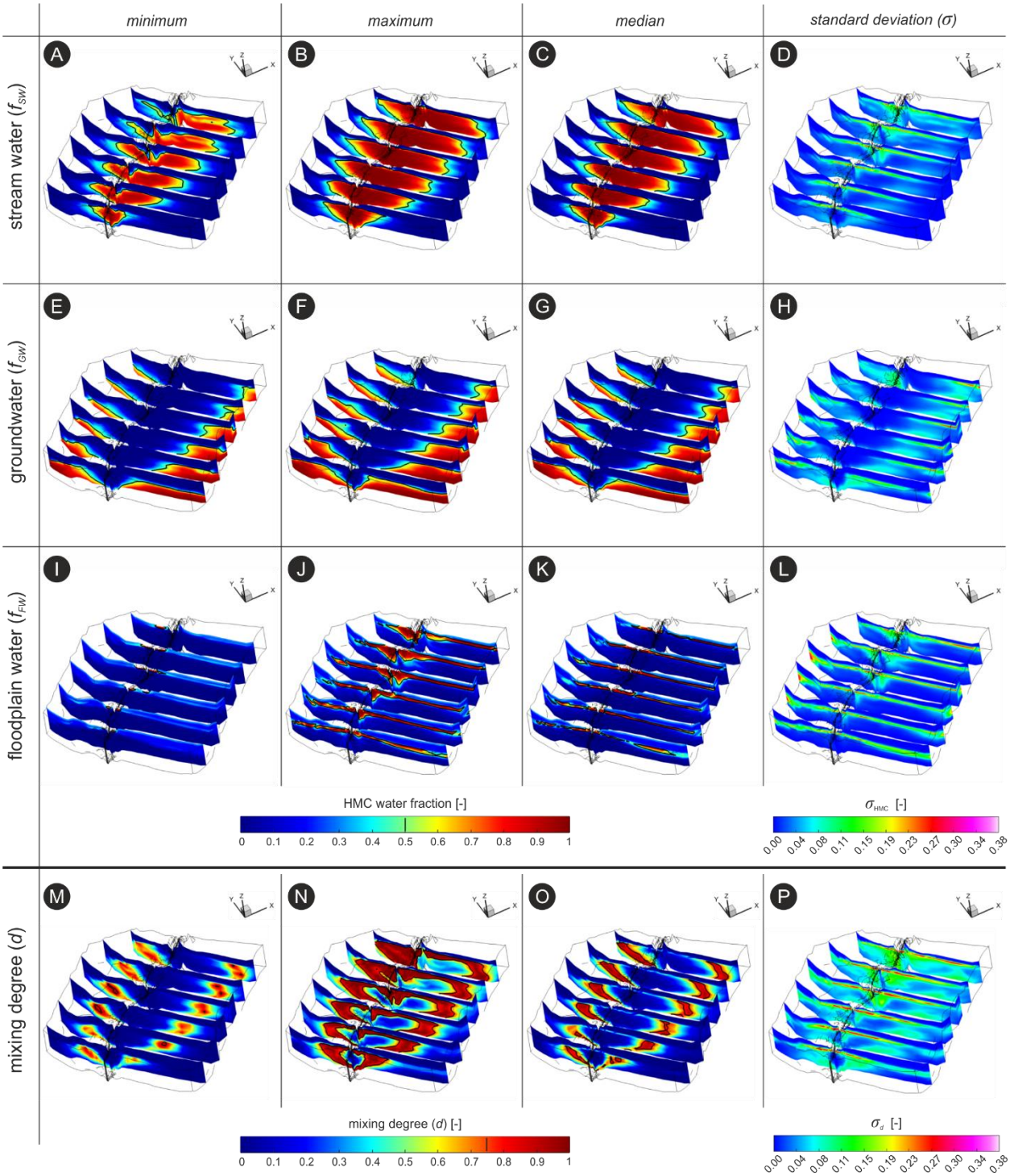

Figure 8: Minimum, maximum, median values, as well as standard deviations (σ) of **(a-d)** stream water (f_{SW}), **(e-h)** groundwater (f_{GW}), **(i-l)** floodplain water (f_{FW}) fractions, and **(m-p)** mixing degrees (d) for the entire simulation period. The HMC fractions are multiplied by the maximum saturation value that was recorded in each model cell during the entire simulation period. The black line in the HMC fraction plots indicates the location where HMC fractions equal 0.5 (i.e., the geochemical HZ fringe in a-c plots, f_{SW}=0.5). The black lines in the mixing degree plots (m-o) indicate regions where d=0.75 (mixing hot-spots, d_h). Note the vertical exaggeration of the 3D plots (20x).

Nevertheless, some high *d* values occurred also near the streambanks, especially after flooding of the near stream region. This leads to episodically large percolation of top-soil water through the vadose zone, which mixes with infiltrating SW and with local flowing groundwater. Comparing these findings with results from Gassen *et al.* (2017) (Figure 9a-b), who monitored groundwater quality at the study site, there is strong similarity between the vertical variation of HMC mixing degrees and their defined denitrification fringe (i.e., high DOC and bicarbonate concentrations). It is argued that, despite the seasonal temperature controls on denitrification rates (Figure 9c), mixing with stream-borne DOC is most likely the processes responsible for the high denitrification rates at the groundwater-table interface, leading to much smaller NO_3^- concentrations below the interface than ones observed in the vadose zone (< 3 mg L^{-1} and up to 70 mg L^{-1}, respectively).

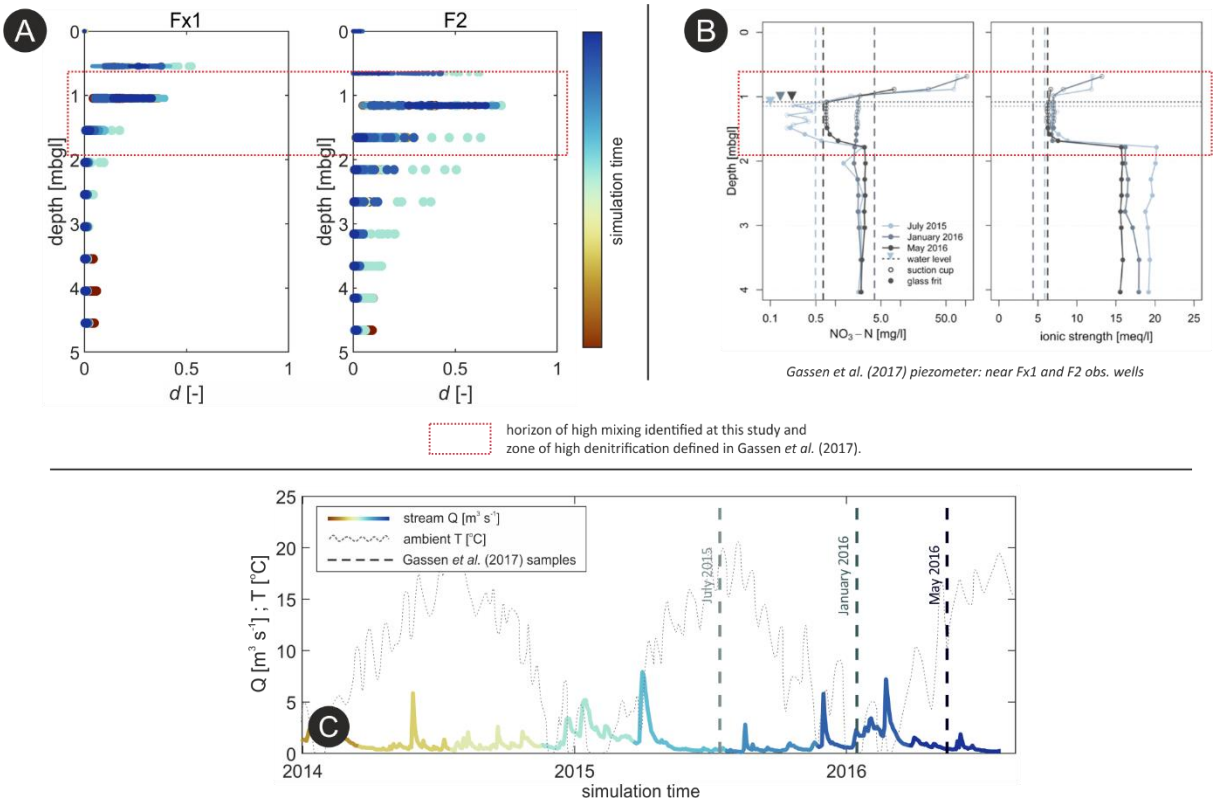

Figure 9: **(a)** Mixing degrees with depth for two observation wells. Colours indicate simulation time; **(b)** measurements of NO_3–N concentrations and ionic strength in a multilevel piezometer for three different sampling dates. Vertical dashed lines represent NO_3–N concentrations/ionic strength of the stream water, horizontal dotted lines represent the groundwater-table at the corresponding sampling date (reprinted (adapted) with permission from Gassen *et al.* (2017); and **(c)** ambient temperature alongside stream discharge coloured according to simulation time. Vertical dashed lines indicate the sampling dates of Gassen *et al.* (2017).

Around 80% of the domain presented some mixing ($d > 0$), which strongly varied over time and indicates the activation of areas that do not present mixing throughout the simulation, Figure A4. Areas presenting $d \geq 0.25$ were on average 40% of the total domain. Yet, d_h represented 7-12% of the total domain volume (or 15-30% of the HZ, Figure A4), being highly correlated to the peak prominence of discharge events (R^2=0.96). These findings are qualitatively consistent with previous smaller-scale studies showing that mixing hot-spots between SW-GW tend to occur in thin zones at the fringe of the HZ (Hester et al., 2013; Sawyer and Cardenas, 2009; Trauth and Fleckenstein, 2017).

Finally, exposure-times ($d_{h\text{-}\tau}$) of hyporheic flow paths were shorter in comparison to the $d_{h\text{-}\tau}$ of floodplain flow paths. With increasing stream discharge, SW influx into the riparian aquifer increases due to increase SW depth (Buffington and Tonina, 2009), which shifts the SW-GW mixing front to regions farther from the stream (Hester et al., 2019) and hyporheic $d_{h\text{-}\tau}$ decreases. Thus, mixing far from the stream is mainly enhanced by increasing stream discharge, which brings SW to farther distances within the aquifer where it can mix with ambient groundwater. Contrary, under low stream discharge, hyporheic $d_{h\text{-}\tau}$ were the highest due to increasing GW upwelling (and subsequent SW-GW mixing). Nevertheless, in strongly gaining stream reaches with a dominance of GW-seepage to the stream (e.g., limited or absent hyporheic flow paths), hyporheic transit-times (Cardenas, 2009; Trauth et al., 2014, 2013), as well as SW-GW mixing (e.g., in terms of flux magnitude) (Hester et al., 2013; Sawyer et al., 2009) would be smaller, and consequently the potential for turnover of groundwater-borne solutes would be smaller too (Hester et al., 2019). These findings highlight the important role of losing streams on water sources mixing and the increasing potential of mixing-triggered solute turnover in riparian zones.

The HMC method can be complementary to field sampling and remote sensing techniques for mapping water clusters and their dynamics in the floodplain and watershed scales (Berezowski et al., 2019; Schilling et al., 2017). These latter, conventional methods are more elaborate and limited by spatial coverage, as well as labour intensive, which can be reduced with the complementary use of the HMC method. An upcoming use of this approach (in combination with more advanced chemical data) could be to locate regions within the floodplain with high potentials for such mixed-triggered biogeochemical reactions. For instance, areas with high denitrification rates found in Study 2 with distance from the stream (i.e., following DO depletion in winter) coincide with the mixing hot-spots identified here (at the fringe of the hyporheic zone), which reinforces the potential for groundwater-borne NO_3^- turnover at such locations (Trauth et al., 2018). These identified areas could be further assessed for the quantification of solute turnover in relation to different water fractions and other flow and field characteristics. Understanding the patterns and dynamics of macroscopic mixing between SW and GW in riparian zones can help to better understand patterns of reactive turnover or the redistribution of other, non-reactive solutes or small particulate substances (e.g., micro plastic particles) in the riparian zone.

1.5 Conclusions and Outlook

A key objective of this research was to assess the relationship between variations in subsurface flow and the associated reactive potentials for the turnover of redox sensitive solutes such as NO_3^- within the riparian zone. The thesis focused on advancing the understanding of coupled hydrological and biogeochemical processes, which take place under variable temperature conditions throughout the hydrological year within river-corridors. This advance was achieved by combining field data analyses and numerical simulations of flow and reactive mass transport covering different spatio-temporal scales.

Results from the data-driven analyses revealed that within the first meters from the streambed towards the riparian aquifer, infiltrating stream water with temperature different than that of ambient groundwater can alter reaction rate coefficients. For instance, when stream water is warmer than ambient groundwater during summer, reaction rates can be 2-3 times higher than values calculated solely based on groundwater temperature measurements; whereas the opposite can occur during winter. This should be considered when assessing solute turnover processes in the active exchange zone between surface water (SW) and groundwater (GW), since neglecting short-term temperature changes related to hydrologic events could lead to a significant underestimation of reactive potentials (up to 40% for NO_3^-). Even though discharge events did not significantly alter subsurface transit-times locally, disregarding variations in water transit-times due to stream stage fluctuations could similarly lead to an underestimation of solute turnover potentials. It is emphasized that over longer time scales and at larger spatial scales, seasonal temperature variations control the general reactive regime of the system (i.e. reaction versus transport limitation) to a larger degree than short-lived temperature fluctuations induced by stream water, which are strongly damped over distances of decimeters to meters into the riparian aquifer.

Furthermore the numerical simulations revealed that even under a reaction limited regime (i.e., low temperatures), denitrification can take place providing the availability of an electron donor and a sufficiently long subsurface flow path, which compensates for the reduced reaction rates. Under the predominantly losing conditions (streamflow losses to the aquifer) at the site, this implies that the reactive zone for NO_3^- turnover in the winter is located further away from the stream than under warmer summer conditions. This shift in the reactive zone highlights the key effect of temperature on spatial patterns of reactions. The simulations showed that even under low temperature and limited carbon availability, NO_3^- removal can be 3x higher further away from the stream than along the rather short, near-stream hyporheic flow paths. On the top of the aforementioned results, the approach of Study 2, which considers both hydrological and temperature variations, provides a viable, computationally less demanding alternative for assessments of riparian biogeochemical processes at stream-corridor scale.

Finally, results from the coupling of the HMC method to the previously calibrated flow model revealed that the spatial extent of mixing hot-spots, locations characterized by nearly equal fractions of the different water sources (mainly stream water and groundwater) in the water mixture, is rather small in comparison to the total volume of the riparian aquifer. A large portion of the near stream aquifer consisted of infiltrated stream water, whereas a large degree of mixing with other water sources only occurred at the fringes of the geochemical hyporheic zone (>50% stream water). Ultimately, this suggests that steam-borne solutes could reach locations in the aquifer far from the stream, where they can react with groundwater borne reactants. The framework of Study 3 can support the explicit quantification of such mixing rates and areas within the riparian zone with a large degree of reliability. Also, it can aid decisions towards integrated water resources management, for example, on defining suitable locations to install water supply wells, while respecting a defined mixing threshold between different water sources.

The methods and findings presented in this thesis may support the development of novel *in-situ* experiments and targeted monitoring programs in riparian zones. Furthermore the results can point to potential future research. The framework of Study 1 could be tested in more dynamic stream reaches, whereas results could be used to further explore riparian turnover processes and solute export in stream reaches alternating between gaining and losing conditions. Concerning the modelling experiments from Studies 2 and 3, in a future approach, the use of (less-invasive) indirect methods for mapping and characterizing subsurface processes, such as geophysical and other indirect methods (e.g., airborne) could complement conventional survey methods. Also, the use of other tracers (environmental or artificial, both conservative and reactive) and unconventional data could further improve the calibration/validation of numerical models at the stream-corridor and larger scales. The incorporation of supplementary, less conventional field data, such as the results from tracer-tests for the validation and calibration of numerical models might increase the reliability of results and reduce uncertainties in parameter values, which underlines the added value of using multiple data-sets in model calibration. A relative data-worth analyses indicated that the predictive uncertainty of groundwater levels, for instance, could be further decreased by up to 30% with the incorporation of the tracer-test data in the model calibration (Study 2). Alongside a more extensive data-worth analyses, similar to the one carried out by Partington et al. 2020, for instance, results could assist to define "what to measure and where " given a specific research goal or hypothesis.

Other aspects such as the influence of geological heterogeneity at different scales (A.H. Sawyer, 2015), the sporadic occurrence of organic matter as an electron donor in the aquifer material (Pescimoro et al., 2019), and other ecological constituents (e.g., solute plant-uptake and other root-zone and microbial processes – Lupon et al., 2018) were not systematically assessed in this research, but they could affect riparian processes to a certain extent. Accordingly, future projects should take advantage of multiple datasets and tools

available in order to disentangle the factors controlling hydrological and biogeochemical processes at various spatio-temporal scales.

In view of such findings, measures for improving water quality within stream corridors should be integrated (not only focusing on either stream or groundwater alone) and cover wider spatio-temporal scales in the assessment. It is important to keep the big picture in mind when decisions for measures to improve the state of aquatic systems are taken. Foremost, decreasing the input of substances that can deteriorate water quality or ecosystem health should be a priority. Additionally, the minimal distances from stream banks to where activities involving considerable land use changes may take place (e.g., agricultural activities, constructions, general subsurface alterations) should reflect the natural dynamics of stream and groundwater (e.g., oscillation of hyporheic zone, shift of reactive zones) in order to safeguard the healthy functioning of riparian environments.

1.6 References

Abbott, B.W., Moatar, F., Gauthier, O., Fovet, O., Antoine, V., Ragueneau, O., 2018. Trends and seasonality of river nutrients in agricultural catchments: 18 years of weekly citizen science in France. Sci. Total Environ. 624, 845–858. https://doi.org/10.1016/j.scitotenv.2017.12.176

Appelo, C.A.J., Postma, D., 2005. Geochemistry, Groundwater and Pollution - 2nd Edition. A.A. BALKEMA PUBLISHERS, Amsterdam.

Bachmann, G.H., Ehling, B.C., Eichner, R., Schwab, M., 2008. Geologie von Sachsen- Anhalt, 1ed ed. Schweizerbart Science Publishers, Stuttgart, Germany.

Berezowski, T., Partington, D., Chormański, J., Batelaan, O., 2019. Spatiotemporal Dynamics of the Active Perirheic Zone in a Natural Wetland Floodplain. Water Resour. Res. 55, 9544–9562. https://doi.org/10.1029/2019WR024777

Bernard-Jannin, L., Sun, X., Teissier, S., Sauvage, S., Sánchez-Pérez, J.M., 2017. Spatio-temporal analysis of factors controlling nitrate dynamics and potential denitrification hot spots and hot moments in groundwater of an alluvial floodplain. Ecol. Eng. 103, 372–384. https://doi.org/10.1016/j.ecoleng.2015.12.031

Biehler, A., Chaillou, G., Buffin-Bélanger, T., Baudron, P., 2020. Hydrological connectivity in the aquifer–river continuum: Impact of river stages on the geochemistry of groundwater floodplains. J. Hydrol. 590, 125379. https://doi.org/10.1016/j.jhydrol.2020.125379

Boano, F., Demaria, A., Revelli, R., Ridolfi, L., 2010. Biogeochemical zonation due to intrameander hyporheic flow. Water Resour. Res. 46, 1–13. https://doi.org/10.1029/2008WR007583

Boano, F., Harvey, J.W., Marion, A., Packman, A.I., Revelli, R., Ridolfi, L., Wörman, A., 2014. Hyporheic flow and transport processes: Mechanisms, models, and biogeochemical implications. Rev. Geophys. 52, 603–679. https://doi.org/10.1002/2012RG000417

Boano, F., Revelli, R., Ridolfi, L., 2008. Reduction of the hyporheic zone volume due to the stream-aquifer interaction. Geophys. Res. Lett. 35, 1–5. https://doi.org/10.1029/2008GL033554

Boulton, A.J., Findlay, S., Marmonier, P., Stanley, E.H., Valett, H.M., 1998. The Functional Significance of the Hyporheic Zone in Streams and Rivers. Annu. Rev. Ecol. Syst. 29, 59–81. https://doi.org/10.1146/annurev.ecolsys.29.1.59

Box, G.E.P., 1979. Robustness in the Strategy of Scientific Model Building, in: Robustness in Statistics. Elsevier, pp. 201–236. https://doi.org/10.1016/B978-0-12-438150-6.50018-2

Brugger, A., Wett, B., Kolar, I., Reitner, B., Herndl, G.J., 2001. Immobilization and bacterial utilization of dissolved organic carbon entering the riparian zone of the alpine Enns River, Austria. Aquat. Microb. Ecol. 24, 129–142. https://doi.org/10.3354/ame024129

Brunke, M., Gonser, T., 1997. The ecological significance of exchange processes between rivers and groundwater. Freshw. Biol. 37, 1–33. https://doi.org/10.1046/j.1365-2427.1997.00143.x

Brunner, P., Therrien, R., Renard, P., Simmons, C.T., Franssen, H.J.H., 2017. Advances in understanding river-groundwater interactions. Rev. Geophys. 55, 818–854. https://doi.org/10.1002/2017RG000556

Buffington, J.M., Tonina, D., 2009. Hyporheic exchange in mountain rivers II: Effects of channel morphology on mechanics, scales, and rates of exchange. Geogr. Compass 3, 1038–1062. https://doi.org/10.1111/j.1749-8198.2009.00225.x

Cardenas, M.B., 2009. Stream-aquifer interactions and hyporheic exchange in gaining and losing sinuous streams. Water Resour. Res. 45, 1–13. https://doi.org/10.1029/2008WR007651

Cirpka, O.A., Kitanidis, P.K., 2000. Characterization of mixing and dilution in heterogeneous aquifers by means of local temporal moments. Water Resour. Res. 36, 1221–1236. https://doi.org/10.1029/1999WR900354

Conant, B., Cherry, J.A., Gillham, R.W., 2004. A PCE groundwater plume discharging to a river: Influence of the streambed and near-river zone on contaminant distributions. J. Contam. Hydrol. 73, 249–279. https://doi.org/10.1016/j.jconhyd.2004.04.001

Dentz, M., Le Borgne, T., Englert, A., Bijeljic, B., 2011. Mixing, spreading and reaction in heterogeneous media: A brief review. J. Contam. Hydrol. 120–121, 1–17. https://doi.org/10.1016/j.jconhyd.2010.05.002

Diem, S., Cirpka, O.A., Schirmer, M., 2013. Modeling the dynamics of oxygen consumption upon riverbank filtration by a stochastic–convective approach. J. Hydrol. 505, 352–363. https://doi.org/10.1016/j.jhydrol.2013.10.015

Doherty, J., 2018. PEST: Model-independent parameter estimation. User Manual.

Doherty, J., 2015. Calibration and Uncertainty Analysis for Complex Environmental Models, Groundwater. https://doi.org/10.1111/gwat.12360

Doherty, J., 1994. PEST: A Unique Computer Program for Model-independent Parameter Optimisation. Water Down Under 94, 551–554.

Doherty, J., Johnston, J.M., 2003. Methodologies for calibration and predective analysis of a watershed model. J. of Am. Water Resour. Assoc. 39, 251–265. https://doi.org/10.1111/j.1752-1688.2003.tb04381.x

Doherty, J.E., Hunt, R.J., 2010. Approaches to Highly Parameterized Inversion : A Guide to Using PEST for Groundwater-Model Calibration. U.S. Geological Survey Scientific Investigations Report.

Dupas, R., Musolff, A., Jawitz, J.W., Rao, P.S.C., Jäger, C.G., Fleckenstein, J.H., Rode, M., Borchardt, D., 2017. Carbon and nutrient export regimes from headwater catchments to downstream reaches. Biogeosciences 14, 4391–4407. https://doi.org/10.5194/bg-14-4391-2017

Ebeling, P., Dupas, R., Abbott, B., Kumar, R., Ehrhardt, S., Fleckenstein, J.H., Musolff, A., 2021. Long-Term Nitrate Trajectories Vary by Season in Western European Catchments. Global Biogeochem. Cycles 35, 1–19. https://doi.org/10.1029/2021GB007050

Edmunds, W.M., Bath, A.H., Miles, D.L., 1982. Hydrochemical evolution of the East Midlands Triassic sandstone aquifer, England. Geochim. Cosmochim. Acta 46, 2069–2081. https://doi.org/10.1016/0016-7037(82)90186-7

Engelhardt, I., Prommer, H., Moore, C., Schulz, M., Schüth, C., Ternes, T.A., 2013. Suitability of temperature, hydraulic heads, and acesulfame to quantify wastewater-related fluxes in the hyporheic and riparian zone. Water Resour. Res. 49, 426–440. https://doi.org/10.1029/2012WR012604

Fetter, C.W., 1980. Applied Hydrogeology, 4th ed, Applied Hydrogeology. Prentice Hall, New Jersey, USA. https://doi.org/0-13-088239-9

Fienen, M.N., Muffels, C.T., Hunt, R.J., 2009. On constraining pilot point calibration with regularization in PEST. Ground Water 47, 835–844. https://doi.org/10.1111/j.1745-6584.2009.00579.x

Fogler, H.S., 2005. Elements of Chemical Reaction Engineering, 4th ed. ed. Prentice Hall, Boston, Mass.

Gassen, N., Griebler, C., Werban, U., Trauth, N., Stumpp, C., 2017. High Resolution Monitoring Above and Below the Groundwater Table Uncovers Small-Scale Hydrochemical Gradients. Environ. Sci. Technol. 51, 9. https://doi.org/10.1021/acs.est.7b03087

Genuchten, V. M., 1980. A closed-form equation for predicting the hydraulic conductivity of unsaturated soils. Soil Sci. Soc. Am. J. 44, 892–898.

Gianni, G., Doherty, J., Brunner, P., 2019. Conceptualization and Calibration of Anisotropic Alluvial Systems: Pitfalls and Biases. Groundwater 57, 409–419. https://doi.org/10.1111/gwat.12802

Gleick, H.P., Shiklomanov, I.A., Nash, L., Covich, A.P., Postel, S., Falkenmark, M., Lindh, G., McCaffrey, S.C., 1993. Water in crisis : a guide to the world's fresh water resources. Oxford University Press, New Yorkk.

Gomez-Velez, J.D., Wilson, J.L., Cardenas, M.B., Harvey, J.W., 2017. Flow and Residence Times of Dynamic River Bank Storage and Sinuosity-Driven Hyporheic Exchange. Water Resour. Res. 53, 8572–8595. https://doi.org/10.1002/2017WR021362

Greskowiak, J., Prommer, H., Massmann, G., Nützmann, G., 2006. Modeling seasonal redox dynamics and the corresponding fate of the pharmaceutical residue phenazone during artificial recharge of groundwater. Environ. Sci. Technol. 40, 6615–6621. https://doi.org/10.1021/es052506t

Gu, C., Anderson, W., Maggi, F., 2012. Riparian biogeochemical hot moments induced by stream fluctuations. Water Resour. Res. 48, 1–17. https://doi.org/10.1029/2011WR011720

Gu, C., Hornberger, G.M., Mills, A.L., Herman, J.S., Flewelling, S.A., 2007. Nitrate reduction in streambed sediments: Effects of flow and biogeochemical kinetics. Water Resour. Res. 43. https://doi.org/10.1029/2007WR006027

Harvey, J.W., Wagner, B.J., Bencala, K.E., 1996. By Was S); Hyporheic Exchange Persisted When Base Flow Was Decreasing By. Water Resour. 32, 2441–2451.

Henzler, A.F., Greskowiak, J., Massmann, G., 2016. Seasonality of temperatures and redox zonations during bank filtration - A modeling approach. J. Hydrol. 535, 282–292. https://doi.org/10.1016/j.jhydrol.2016.01.044

Hester, E.T., Cardenas, M.B., Haggerty, R., Apte, S. V., 2017. The importance and challenge of hyporheic mixing. Water Resour. Res. 53, 3565–3575. https://doi.org/10.1002/2016WR020005

Hester, E.T., Eastes, L.A., Widdowson, M.A., 2019. Effect of Surface Water Stage Fluctuation on Mixing-Dependent Hyporheic Denitrification in Riverbed Dunes. Water Resour. Res. 55, 4668–4687. https://doi.org/10.1029/2018WR024198

Hester, E.T., Young, K.I., Widdowson, M.A., 2014. Controls on mixing-dependent denitrification in hyporheic zones induced by riverbed dunes: A steady state modeling study. Water Resour. Res. 50, 9048–9066. https://doi.org/10.1002/2014WR015424

Hester, E.T., Young, K.I., Widdowson, M.A., 2013. Mixing of surface and groundwater induced by riverbed dunes: Implications for hyporheic zone definitions and pollutant reactions. Water Resour. Res. 49, 5221–5237. https://doi.org/10.1002/wrcr.20399

Hill, A.R., 1996. Nitrate Removal in Stream Riparian Zones. J. Environ. Qual. 25, 743–755. https://doi.org/10.2134/jeq1996.00472425002500040014x

Hill, A.R., Labadia, C.F., Sanmugadas, K., 1998. Hyporheic zone hydrology and nitrogen dynamics in relation to the streambed topography of a N-rich stream. Biogeochemistry 42, 285–310. https://doi.org/10.1023/A:1005932528748

Jones, K.L., Poole, G.C., Woessner, W.W., Vitale, M. V., Boer, B.R., O'Daniel, S.J., Thomas, S.A., Geffen, B.A., 2008. Geomorphology, hydrology, and aquatic vegetation drive seasonal hyporheic flow patterns across a gravel-dominated floodplain. Hydrol. Process. 22, 2105–2113. https://doi.org/10.1002/hyp.6810

Kirschbaum, M.U.F., 2000. Will changes in soil organic carbon act as a positive or negative feedback on global warming? Biogeochemistry 48, 21–51. https://doi.org/10.1023/A:1006238902976

Kitanidis, K., 1994. The concept of the dilution index 30, 2011–2026. https://doi.org/https://doi.org/10.1029/94WR00762

Koestel, J.K., Moeys, J., Jarvis, N.J., 2011. Evaluation of nonparametric shape measures for solute breakthrough curves. Vadose Zo. 10, 1261–1275.

Kolbe, T., de Dreuzy, J.-R., Abbott, B.W., Aquilina, L., Babey, T., Green, C.T., Fleckenstein, J.H., Labasque, T., Laverman, A.M., Marçais, J., Peiffer, S., Thomas, Z., Pinay, G., 2019. Stratification of reactivity determines nitrate removal in groundwater. Proc. Natl. Acad. Sci. 116, 2494–2499. https://doi.org/10.1073/pnas.1816892116

Krause, S., Lewandowski, J., Grimm, N.B., Hannah, D.M., Pinay, G., McDonald, K., Martí, E., Argerich, A., Pfister, L., Klaus, J., Battin, T., Larned, S.T., Schelker, J., Fleckenstein, J., Schmidt, C., Rivett, M.O., Watts, G., Sabater, F., Sorolla, A., Turk, V., 2017. Ecohydrological interfaces as hot spots of ecosystem processes. Water Resour. Res. 53, 6359–6376. https://doi.org/10.1002/2016WR019516

Lohse, K.A., Brooks, P.D., McIntosh, J.C., Meixner, T., Huxman, T.E., 2009. Interactions Between Biogeochemistry and Hydrologic Systems. Annu. Rev. Environ. Resour. 34, 65–96. https://doi.org/10.1146/annurev.environ.33.031207.111141

Lupon, A., Ledesma, J.L.J., Bernal, S., 2018. Riparian evapotranspiration is essential to simulate streamflow dynamics and water budgets in a Mediterranean catchment. Hydrol. Earth Syst. Sci. 22, 4033–4045. https://doi.org/10.5194/hess-22-4033-2018

Lutz, S.R., Trauth, N., Musolff, A., Van Breukelen, B.M., Knöller, K., Fleckenstein, J.H., 2020. How Important is Denitrification in Riparian Zones? Combining End-Member Mixing and Isotope Modeling to Quantify Nitrate Removal from Riparian Groundwater. Water Resour. Res. 56. https://doi.org/10.1029/2019WR025528

McClain, M.E., Boyer, E.W., Dent, C.L., Gergel, S.E., Grimm, N.B., Groffman, P.M., Hart, S.C., Harvey, J.W., Johnston, C.A., Mayorga, E., McDowell, W.H., Pinay, G., 2003. Biogeochemical Hot Spots and Hot Moments at the Interface of Terrestrial and Aquatic Ecosystems. Ecosystems 6, 301–312. https://doi.org/10.1007/s10021-003-0161-9

McMahon, P.B., 2001. Aquifer/aquitard interfaces: Mixing zones that enhance biogeochemical reactions. Hydrogeol. J. 9, 34–43. https://doi.org/10.1007/s100400000109

Moeck, C., Hunkeler, D., Brunner, P., 2015. Tutorials as a flexible alternative to GUIs: An example for advanced model calibration using Pilot Points. Environ. Model. Softw. 66, 78–86. https://doi.org/10.1016/j.envsoft.2014.12.018

Munz, M., Oswald, S.E., Schäfferling, R., Lensing, H.-J., 2019. Temperature-dependent redox zonation, nitrate removal and attenuation of organic micropollutants during bank filtration. Water Res. 162, 225–235. https://doi.org/10.1016/j.watres.2019.06.041

Munz, M., Oswald, S.E., Schmidt, C., 2017. Coupled Long-Term Simulation of Reach-Scale Water and Heat Fluxes Across the River-Groundwater Interface for Retrieving Hyporheic Residence Times and Temperature Dynamics. Water Resour. Res. 53, 8900–8924. https://doi.org/10.1002/2017WR020667

Musolff, A., Schmidt, C., Selle, B., Fleckenstein, J.H., 2015. Catchment controls on solute export. Adv. Water Resour. 86, 133–146. https://doi.org/10.1016/j.advwatres.2015.09.026

Nixdorf, E., Trauth, N., 2018. Evaluating the reliability of time series analysis to estimate variable riparian travel times by numerical groundwater modelling. Hydrol. Process. 32, 408–420. https://doi.org/10.1002/hyp.11428

O'Connell, A.M., 1990. Microbial decomposition (respiration) of litter in eucalypt forests of South-Western Australia: An empirical model based on laboratory incubations. Soil Biol. Biochem. 22, 153–160. https://doi.org/10.1016/0038-0717(90)90080-J

Oldham, C.E., Farrow, D.E., Peiffer, S., 2013. A generalized Damköhler number for classifying material processing in hydrological systems. Hydrol. Earth Syst. Sci. 17, 1133–1148. https://doi.org/10.5194/hess-17-1133-2013

Partington, D., Brunner, P., Frei, S., Simmons, C.T., Werner, A.D., Therrien, R., Maier, H.R., Dandy, G.C., Fleckenstein, J.H., 2013. Interpreting streamflow generation mechanisms from integrated surface-subsurface flow models of a riparian wetland and catchment. Water Resour. Res. 49, 5501–5519. https://doi.org/10.1002/wrcr.20405

Partington, D., Brunner, P., Simmons, C.T., Therrien, R., Werner, A.D., Dandy, G.C., Maier, H.R., 2011. A hydraulic mixing-cell method to quantify the groundwater component of streamflow within spatially distributed fully integrated surface water-groundwater flow models. Environ. Model. Softw. 26, 886–898. https://doi.org/10.1016/j.envsoft.2011.02.007

Partington, D., Brunner, P., Simmons, C.T., Werner, A.D., Therrien, R., Maier, H.R., Dandy, G.C., 2012. Evaluation of outputs from automated baseflow separation methods against simulated baseflow from a physically based, surface water-groundwater flow model. J. Hydrol. 458–459, 28–39. https://doi.org/10.1016/j.jhydrol.2012.06.029

Partington, D., Knowling, M.J., Simmons, C.T., Cook, P.G., Xie, Y., Iwanaga, T., Bouchez, C., 2020. Worth of hydraulic and water chemistry observation data in terms of the reliability of surface water-

groundwater exchange flux predictions under varied flow conditions. J. Hydrol. 590, 125441. https://doi.org/10.1016/j.jhydrol.2020.125441

Pescimoro, E., Boano, F., Sawyer, A.H., Soltanian, M.R., 2019. Modeling Influence of Sediment Heterogeneity on Nutrient Cycling in Streambeds. Water Resour. Res. 55, 4082–4095. https://doi.org/10.1029/2018WR024221

Peterjohn, W.T., 1991. Denitrification: Enzyme content and activity in desert soils. Soil Biol. Biochem. 23, 845–855. https://doi.org/10.1016/0038-0717(91)90096-3

Pietikäinen, J., Pettersson, M., Bååth, E., 2005. Comparison of temperature effects on soil respiration and bacterial and fungal growth rates. FEMS Microbiol. Ecol. 52, 49–58. https://doi.org/10.1016/j.femsec.2004.10.002

Pinay, G., Peiffer, S., Dreuzy, J. De, Krause, S., Hannah, D.M., Fleckenstein, J.H., Sebilo, M., Bishop, K., Hubert-moy, L., 2015. Upscaling Nitrogen Removal Capacity from Local Hotspots to Low Stream Orders ' Drainage Basins. Ecosystems 18, 1101–1120. https://doi.org/10.1007/s10021-015-9878-5

Pinay, G., Ruffinoni, C., Wondzell, S., Gazelle, F., 1998. Change in groundwater nitrate concentration in a large river floodplain: Denitrification, uptake, or mixing? J. North Am. Benthol. Soc. 17, 179–189. https://doi.org/10.2307/1467961

Poole, G.C., O'Daniel, S.J., Jones, K.L., Woessner, W.W., Bernhardt, E.S., Helton, A.M., Stanford, J.A., Boer, B.R., Beechie, T.J., 2008. Hydrologic spiralling: the role of multiple interactive flow paths in stream ecosystems. River Res. Appl. 24, 1018–1031. https://doi.org/10.1002/rra.1099

Ranalli, A.J., Macalady, D.L., 2010. The importance of the riparian zone and in-stream processes in nitrate attenuation in undisturbed and agricultural watersheds - A review of the scientific literature. J. Hydrol. 389, 406–415. https://doi.org/10.1016/j.jhydrol.2010.05.045

Rau, G.C., Andersen, M.S., McCallum, A.M., Roshan, H., Acworth, R.I., 2014. Heat as a tracer to quantify water flow in near-surface sediments. Earth-Science Rev. 129, 40–58. https://doi.org/10.1016/j.earscirev.2013.10.015

Sawyer, A.H., 2015. Enhanced removal of groundwater-borne nitrate in heterogeneous aquatic sediments. Geophys. Res. Lett. 42, 403–410. https://doi.org/10.1002/2014GL062234

Sawyer, A.H., Cardenas, M.B., 2009. Hyporheic flow and residence time distributions in heterogeneous cross-bedded sediment. Water Resour. Res. 45, 1–12. https://doi.org/10.1029/2008WR007632

Sawyer, A.H., Cardenas, M.B., Bomar, A., Mackey, M., 2009. Impact of dam operations on hyporheic exchange in the riparian zone of a regulated river. Hydrol. Process. 23, 2129–2137. https://doi.org/10.1002/hyp.7324

Sawyer, A.H., Kaplan, L.A., Lazareva, O., Michael, H.A., 2014. Hydrologic dynamics and geochemical responses within a floodplain aquifer and hyporheic zone during Hurricane Sandy. Water Resour. Res. 50, 4877–4892. https://doi.org/10.1002/2013WR015101

Schilling, O.S., Cook, P.G., Brunner, P., 2019. Beyond Classical Observations in Hydrogeology: The Advantages of Including Exchange Flux, Temperature, Tracer Concentration, Residence Time, and Soil Moisture Observations in Groundwater Model Calibration. Rev. Geophys. 57, 146–182. https://doi.org/10.1029/2018RG000619

Schilling, O.S., Gerber, C., Partington, D.J., Purtschert, R., Brennwald, M.S., Kipfer, R., Hunkeler, D., Brunner, P., 2017. Advancing Physically-Based Flow Simulations of Alluvial Systems Through Atmospheric Noble Gases and the Novel37Ar Tracer Method. Water Resour. Res. 53, 10465–10490. https://doi.org/10.1002/2017WR020754

Sharma, L., Greskowiak, J., Ray, C., Eckert, P., Prommer, H., 2012. Elucidating temperature effects on seasonal variations of biogeochemical turnover rates during riverbank filtration. J. Hydrol. 428–429, 104–115. https://doi.org/10.1016/j.jhydrol.2012.01.028

Simmons, C.T., Brunner, P., Therrien, R., Sudicky, E.A., 2020. Commemorating the 50th anniversary of the Freeze and Harlan (1969) Blueprint for a physically-based, digitally-simulated hydrologic response model. J. Hydrol. 584, 124309. https://doi.org/10.1016/j.jhydrol.2019.124309

Sivapalan, M., 2006. Pattern, Process and Function: Elements of a Unified Theory of Hydrology at the Catchment Scale. Encycl. Hydrol. Sci. https://doi.org/10.1002/0470848944.hsa012

Song, X., Chen, X., Stegen, J., Hammond, G., Song, H., Dai, H., Graham, E., Zachara, J.M., 2018. Drought Conditions Maximize the Impact of High-Frequency Flow Variations on Thermal Regimes and Biogeochemical Function in the Hyporheic Zone. Water Resour. Res. 54, 7361–7382. https://doi.org/10.1029/2018WR022586

Steffen, W., Richardson, K., Rockström, J., Cornell, S.E., Fetzer, I., Bennett, E.M., Biggs, R., Carpenter, S.R., De Vries, W., De Wit, C.A., Folke, C., Gerten, D., Heinke, J., Mace, G.M., Persson, L.M., Ramanathan, V., Reyers, B., Sörlin, S., 2015. Planetary boundaries: Guiding human development on a changing planet. Science (80-.). 347. https://doi.org/10.1126/science.1259855

Stegen, J.C., Fredrickson, J.K., Wilkins, M.J., Konopka, A.E., Nelson, W.C., Arntzen, E. V., Chrisler, W.B., Chu, R.K., Danczak, R.E., Fansler, S.J., Kennedy, D.W., Resch, C.T., Tfaily, M., 2016. Groundwater-surface water mixing shifts ecological assembly processes and stimulates organic carbon turnover. Nat. Commun. 7. https://doi.org/10.1038/ncomms11237

Thamdrup, B., Hansen, J.W., Jørgensen, B.B., 1998. Temperature dependence of aerobic respiration in a coastal sediment. FEMS Microbiol. Ecol. 25, 189–200. https://doi.org/10.1016/S0168-6496(97)00095-0

Therrien, R., McLaren, R.G., Sudicky, E.A., Panday, S.M., 2010. HydroGeoSphere. A three-dimensional numerical model describing fully-integrated subsurface and surface flow and solute transport. Groundw. Simulations Gr. 457. https://doi.org/10.5123/S1679-49742014000300002

Tóth, J., 1963. A theoretical analysis of groundwater flow in small drainage basins. J. Geophys. Res. 68, 4795–4812. https://doi.org/10.1029/JZ068i016p04795

Trauth, N., Fleckenstein, J.H., 2017. Single discharge events increase reactive efficiency of the hyporheic zone. Water Resour. Res. 53, 779–798. https://doi.org/10.1111/j.1752-1688.1969.tb04897.x

Trauth, N., Musolff, A., Knöller, K., Kaden, U.S., Keller, T., Werban, U., Fleckenstein, J.H., 2018. River water infiltration enhances denitrification efficiency in riparian groundwater. Water Res. 130, 185–199. https://doi.org/10.1016/j.watres.2017.11.058

Trauth, N., Schmidt, C., Maier, U., Vieweg, M., Fleckenstein, J.H., 2013. Coupled 3-D stream flow and hyporheic flow model under varying stream and ambient groundwater flow conditions in a pool-riffle system. Water Resour. Res. 49, 5834–5850. https://doi.org/10.1002/wrcr.20442

Trauth, N., Schmidt, C., Vieweg, M., Maier, U., Fleckenstein, J.H., 2014. Hyporheic transport and biogeochemical reactions in pool-riffle systems under varying ambient groundwater flow conditions. J. Geophys. Res. Biogeosciences 119, 910–928. https://doi.org/10.1002/2013JG002586

Trauth, N., Schmidt, C., Vieweg, M., Oswald, S.E., Fleckenstein, J.H., 2015. Hydraulic controls of in-stream gravel bar hyporheic exchange and reactions. Water Resour. Res. 51, 2243–2263. https://doi.org/10.1002/2014WR015857

Triska, F.J., Kennedy, V.C., Avanzino, R.J., Zellweger, G.W., Bencala, K.E., 1989. Retention and transport of nutrients in a third-order stream: channel processes. Ecology 70, 1877–1892. https://doi.org/10.2307/1938119

Vidon, P., Allan, C., Burns, D., Duval, T.P., Gurwick, N., Inamdar, S., Lowrance, R., Okay, J., Scott, D., Sebestyen, S., 2010. Hot spots and hot moments in riparian zones: Potential for improved water quality management. J. Am. Water Resour. Assoc. 46, 278–298. https://doi.org/10.1111/j.1752-1688.2010.00420.x

Vidon, P.G.F., Hill, A.R., 2004. Landscape controls on nitrate removal in stream riparian zones. Water Resour. Res. 40, 1–14. https://doi.org/10.1029/2003WR002473

Vieweg, M., Kurz, M.J., Trauth, N., Fleckenstein, J.H., Musolff, A., Schmidt, C., 2016. Estimating time-variable aerobic respiration in the streambed by combining electrical conductivity and dissolved oxygen time series. J. Geophys. Res. Biogeosciences 121, 2199–2215. https://doi.org/10.1002/2016JG003345

Weiss, R.F., 1970. The solubility of nitrogen, oxygen and argon in water and seawater. Deep. Res. Oceanogr. Abstr. 17, 721–735. https://doi.org/10.1016/0011-7471(70)90037-9

Winter, T.C., Harvey, J.W., Lehn Franke, O., Alley, W.M., 1998. Ground Water and Surface Water: A Single Resource. U.S. Geological Survey, Denver, Colorado.

Woessner, W.W., 2000. Stream and Fluvial Plain Ground Water Interactions: Rescaling Hydrogeologic Thought. Ground Water 38, 423–429. https://doi.org/10.1111/j.1745-6584.2000.tb00228.x

Wollschläger, U., Attinger, S., Borchardt, D., Brauns, M., Cuntz, M., Dietrich, P., Fleckenstein, J.H., Friese, K., Friesen, J., Harpke, A., Hildebrandt, A., Jäckel, G., Kamjunke, N., Knöller, K., Kögler, S., Kolditz, O., Krieg, R., Kumar, R., Lausch, A., Liess, M., Marx, A., Merz, R., Mueller, C., Musolff, A., Norf, H., Oswald, S.E., Rebmann, C., Reinstorf, F., Rode, M., Rink, K., Rinke, K., Samaniego, L., Vieweg, M., Vogel, H.-J., Weitere, M., Werban, U., Zink, M., Zacharias, S., 2017. The Bode hydrological observatory: a platform for integrated, interdisciplinary hydro-ecological research within the TERENO Harz/Central German Lowland Observatory. Environ. Earth Sci. 76, 29. https://doi.org/10.1007/s12665-016-6327-5

Wondzell, S.M., 2011. The role of the hyporheic zone across stream networks. Hydrol. Process. 25, 3525–3532. https://doi.org/10.1002/hyp.8119

Xu, T., Gómez-Hernández, J.J., 2016. Characterization of non-Gaussian conductivities and porosities with hydraulic heads, solute concentrations, and water temperatures. Water Resour. Res. 52, 6111–6136. https://doi.org/10.1002/2016WR019011

Zarnetske, J.P., Haggerty, R., Wondzell, S.M., Baker, M.A., 2011. Dynamics of nitrate production and removal as a function of residence time in the hyporheic zone. J. Geophys. Res. 116, G01025. https://doi.org/10.1029/2010JG001356

Zarnetske, J.P., Haggerty, R., Wondzell, S.M., Bokil, V.A., González-Pinzón, R., 2012. Coupled transport and reaction kinetics control the nitrate source-sink function of hyporheic zones. Water Resour. Res. 48, 1–15. https://doi.org/10.1029/2012WR011894

Zheng, L., Bayani Cardenas, M., 2018. Diel Stream Temperature Effects on Nitrogen Cycling in Hyporheic Zones. J. Geophys. Res. Biogeosciences 123, 2743–2760. https://doi.org/10.1029/2018JG004412

Zheng, L., Cardenas, M.B., Wang, L., 2016. Temperature effects on nitrogen cycling and nitrate removal-production efficiency in bed form-induced hyporheic zones. J. Geophys. Res. G Biogeosciences 121, 1086–1103. https://doi.org/10.1002/2015JG003162

Ziegel, E.R., Gibbons, J., Chakraborti, S., 2011. Nonparametric Statistical Inference, 5th ed, Technometrics. CRC Press, Boca Raton. https://doi.org/10.2307/1269693

1.7 Appendix

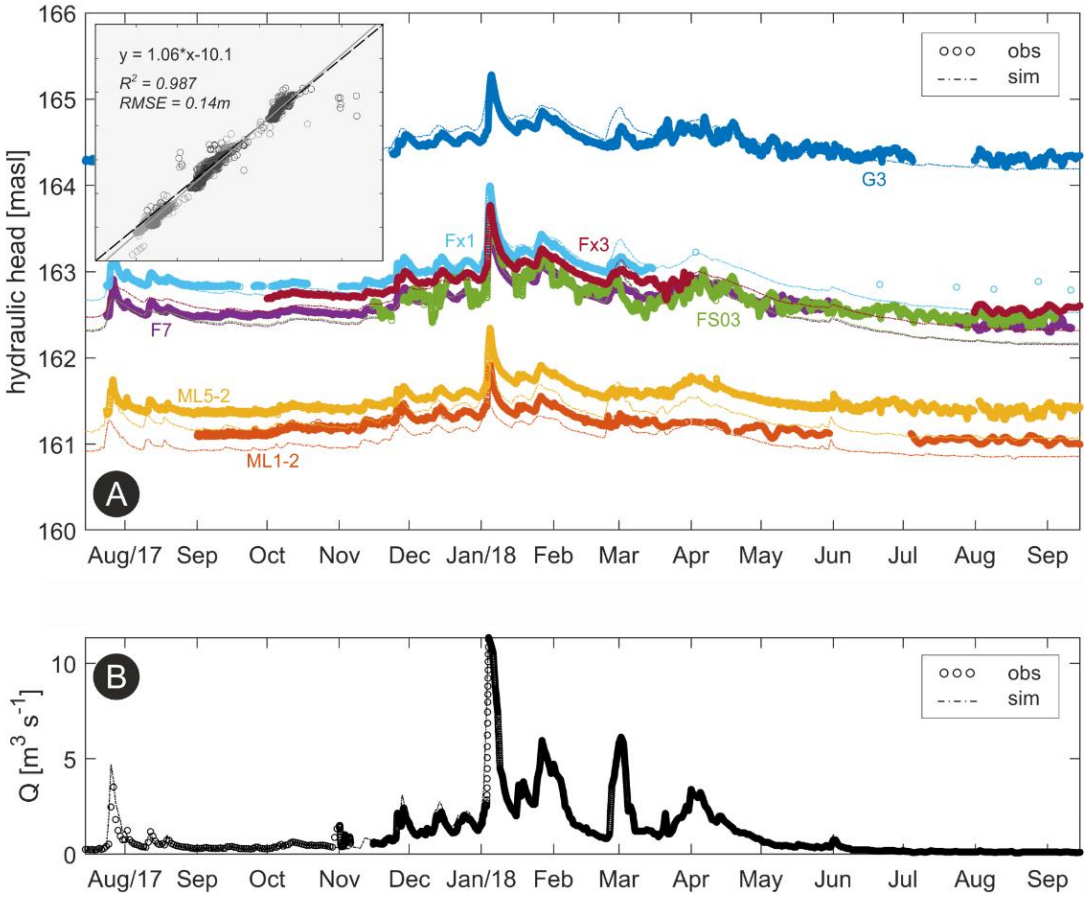

Figure A1: Observed (circles) and simulated (dots) groundwater hydraulic heads (a) and stream discharge (Q) (b) for the simulated period. Different colours in (a) represent different observation wells. The inset plot in (a) shows the overall correlation coefficient (R^2) and root mean square error (RMSE) between simulated and observed values.

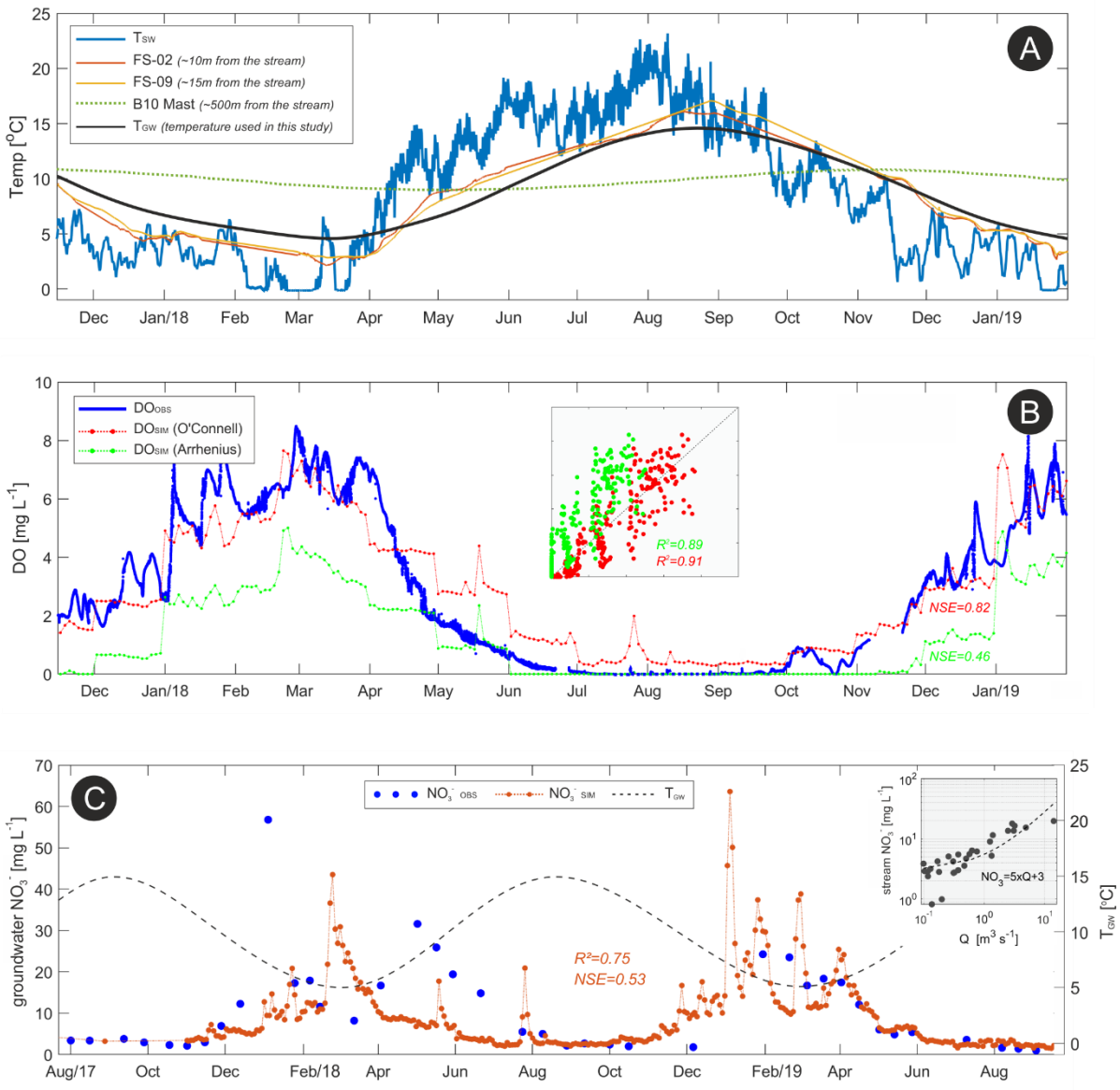

Figure A2: **(a)** water temperature time-series: stream water temperature (T_{SW}), groundwater temperature from different observation wells with increasing distance from the stream (FS-02, FS-09, and B10, respectively), and the groundwater temperature used in this study (T_{GW}) for the calculation of varying reaction rate coefficients. It can be depicted that heat propagation and short-term fluctuations from the stream are damped already few meters from the stream, whereas only the general seasonal patterns are preserved on the near stream groundwater; **(b)** example of observed and simulated riparian dissolved oxygen (DO) for the observation well F7 based on transit-times extracted from the numerical flow model and the application of the flow path-reaction model. Two DO simulations and their Nash Sutcliffe Efficiency (NSE) are shown to compare the two different expression accounting for the temperature correction of reaction rate coefficients (see details on Chapter 4). The inset plot in (b) shows the correlation coefficient (R^2) between simulated and observed DO values; and **(c)** observed and simulated nitrate (NO_3^-) in the groundwater observation well F7 alongside T_{GW}. Simulations are based on field-data scenarios considering increasing initial NO_3^- concentrations with stream discharge (NO_3^- = 5xQ+3, inset plot), the transit-times extracted from the numerical flow model, and the application of the flow path-reaction model. The NSE and R^2 between simulated and observed groundwater NO_3^- concentrations are shown in the plot. Note that as only biweekly measurements of NO_3^- were available for the simulation period, a different time-period from plots (a) and (b) are exhibited in order to better picture the relation between observed and simulated NO_3^- concentrations.

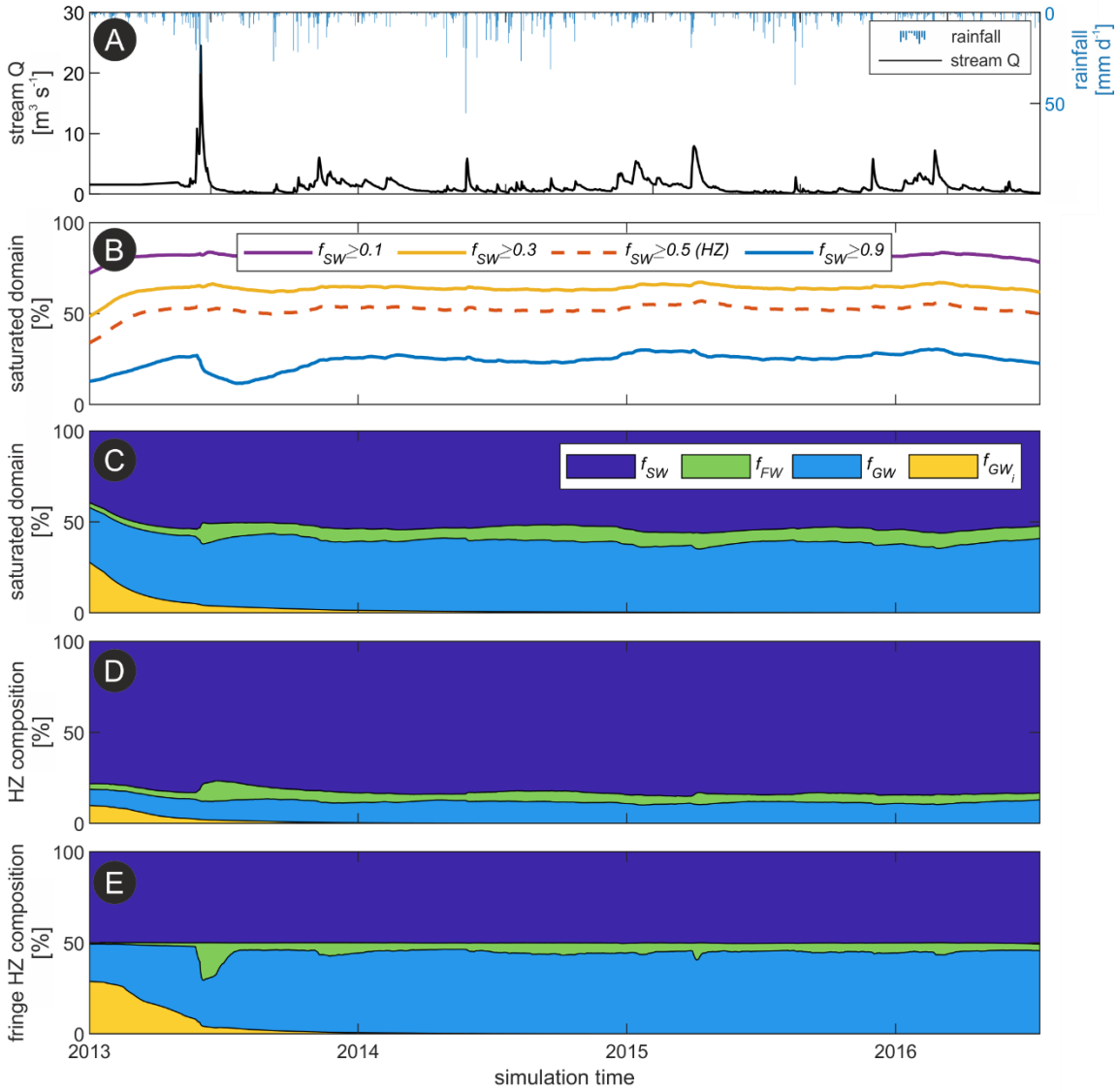

Figure A3: **(a)** Stream discharge (Q) and rainfall time-series; **(b)** temporal variation of the saturated domain comprised by at least a certain amount of stream water fraction (f_{SW}); **(c)** contribution of different fractions to the saturated domain (stream water (f_{SW}), floodplain (f_{FW}), groundwater (f_{GW}), and initial groundwater (f_{GWi})); **(d)** composition of different fractions to the hyporheic zone (HZ, f_{SW}≥0.5); **(e)** composition of different fractions at the fringe of the HZ (f_{SW}=0.5). Note that the start of the simulation (when f_{GWi}=100%) is not shown in the plot.

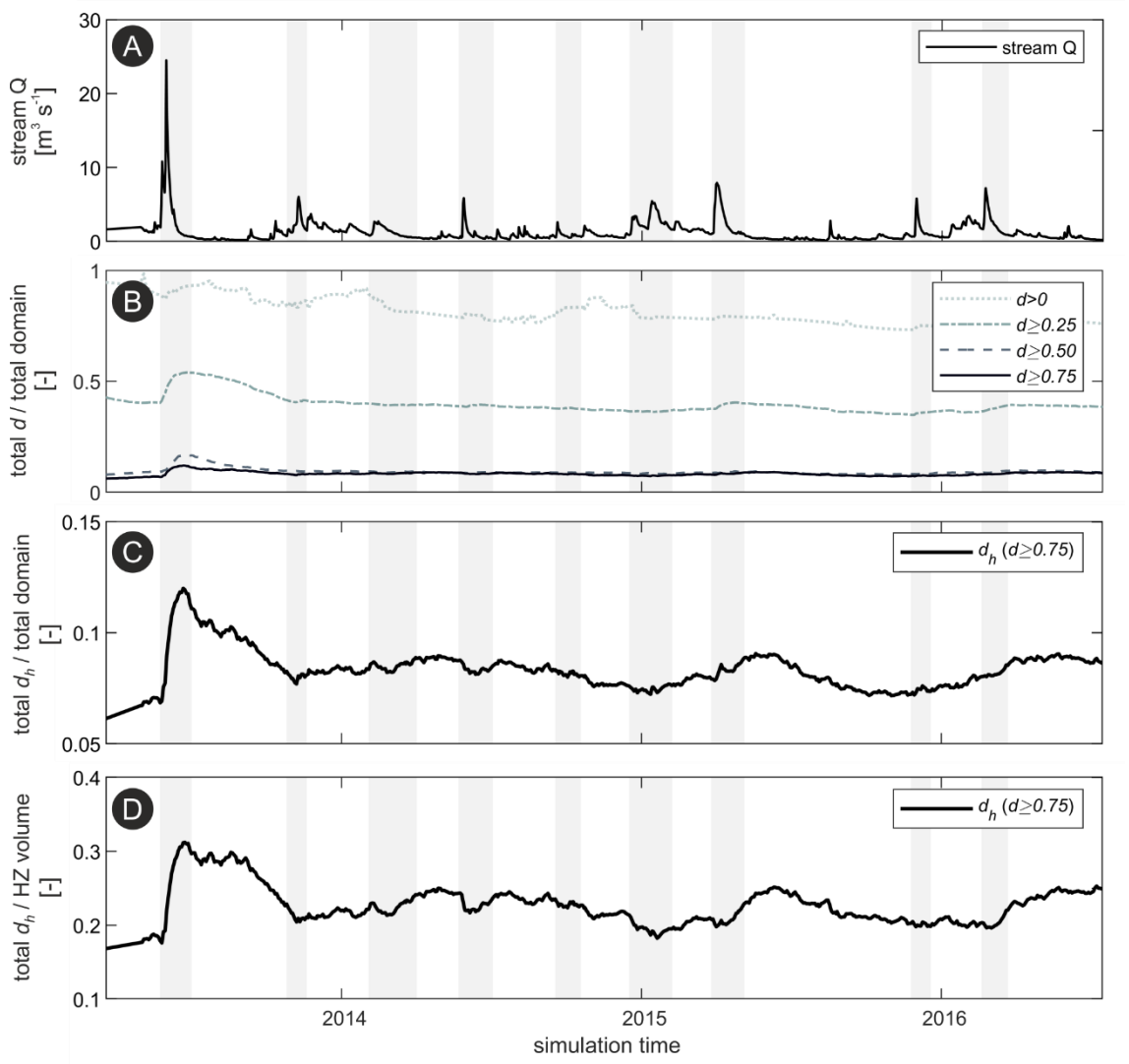

Figure A4: **(a)** Time-series of stream discharge for the period of 2013-2016; **(b)** total volume of cells presenting a certain degree of mixing (d>0, d≥0.25, d≥0.50, and d≥0.75) in relation to total domain volume; **(c)** total volume of mixing hot-spots (d_h, d≥0.75) in relation to total domain volume; and **(d)** total volume of d_h in relation to total hyporheic zone (HZ) volume. Grey vertical bars indicate discharge events periods.

1.8 Contributions to included Manuscripts

Chapter two: "*Seasonal and short-term controls of riparian oxygen dynamics and the implications for redox processes*"

Status: Published in Hydrological Processes 35(2), 2021, DOI: 10.1002/hyp.14055
Authors: Guilherme E. H. Nogueira, Christian Schmidt, Nico Trauth, Jan H. Fleckenstein

GN, NC and CS designed the study; GN carried out the analysis; all the authors discussed and interpreted the results; GN wrote the original draft of the paper; all the authors helped finalizing the manuscript. NT, CS and JF were responsible for supervision; JF was responsible for funding acquisition, resources and project administration.

Own contribution:

- Concept and study design: 80%
- Data acquisition and analyses: 100%
- Interpretation of the results: 80%
- Preparation of the manuscript: 90%

Chapter three: "*Transit-time and temperature control the spatial patterns of aerobic respiration and denitrification in the riparian zone*"

Status: Published in Water Resources Research 57, 2021, DOI: 10.1029/2021WR030117
Authors: Guilherme E. H. Nogueira, Christian Schmidt, Philip Brunner, Daniel Graeber, Jan H. Fleckenstein

GN performed the formal analysis, the investigation and wrote the original draft of the manuscript; all the authors contributed to review, final writing and editing; GN, CS, JF conceptualized the study; GN, CS, PB, DG and JF conceived the methodology; GN, CS, JF and DG worked on the validation of the study; CS and JF were responsible for supervision; JF was responsible for funding acquisition, resources and project administration.

Own contribution:

- Concept and study design: 70%
- Data acquisition and analyses: 100%
- Interpretation of the results: 90%
- Preparation of the manuscript: 90%

Chapter four: "*Spatio-temporal variations of water sources and mixing spots in a riparian zone*"

Status: Under review in Hydrological Earth Soil Sciences, DOI: 10.5194/hess-2021-573
Authors: Guilherme E. H. Nogueira, Christian Schmidt, Daniel Partington, Philip Brunner, Jan H. Fleckenstein

GN performed the formal analysis, the investigation and wrote the original draft of the manuscript; all the authors contributed to review, final writing and editing; GN, CS, and JF conceptualized the study; GN, DP, PB, and JF conceived the methodology; GN, CS, DP, and JF worked on the validation of the study; CS and JF were responsible for supervision; JF was responsible for funding acquisition, resources and project administration

Own contribution:

- Concept and study design: 80%
- Data acquisition and analyses: 90%
- Interpretation of the results: 90%
- Preparation of the manuscript: 90%

Chapter two

Seasonal and short-term controls of riparian oxygen dynamics and the implications for redox processes

G. E. H. Nogueira[(1)], C. Schmidt[(1,2)], N. Trauth[(1,3)], J. H. Fleckenstein[(1,4)]

(1) Department of Hydrogeology, Helmholtz Centre for Environmental Research-UFZ, Leipzig, Germany.

(2) Department of Aquatic Ecosystem Analysis, Helmholtz Centre for Environmental Research-UFZ, Magdeburg, Germany

(3) Björnsen Beratende Ingenieure Erfurt GmbH, NL Leipzig.

(4) Bayreuth Center of Ecology and Environmental Research, University of Bayreuth, Bayreuth, Germany

Published in Hydrological Processes 35(2), 2021, DOI: 10.1002/hyp.14055

Abstract

Riparian zones are highly-dynamic transition zones between surface water (SW) and groundwater (GW) and function as key biogeochemical-reactors for solutes transitioning between both compartments. Infiltration of SW rich in dissolved oxygen (DO) into the riparian aquifer can supress removal processes of redox sensitive compounds like NO_3^-, a nutrient harmful for the aquatic ecosystem at high concentrations. Seasonal and short-term variations of temperature and hydrologic conditions can influence biogeochemical reaction rates and thus the prevailing redox conditions in the riparian zone. We combined GW tracer-tests and a one-year high-frequency dataset of DO with data-driven simulations of DO consumption to assess the effects of seasonal and event-scale variations in temperature and transit-times on the reactive transport of DO. Damköhler numbers for DO consumption (DA_{DO}) were used to characterize the system in terms of DO turnover potential. Our results suggest that seasonal and short-term variations in temperature are major controls for DO turnover and the resulting concentrations at our field site, while transit-times are of minor importance. Seasonal variations of temperature in GW lead to shifts from transport-limited ($DA_{DO}>1$) to reaction-limited conditions ($DA_{DO}<1$), while short-term events were found to have minor impacts on the state of the system, only resulting in slightly less transport-limited conditions due to decreasing temperature and transit-times. The data-driven analyses show that assuming constant water temperature along a flowpath can lead to an over- or underestimation of reaction rates by a factor of 2-3 due to different infiltrating water temperature at the SW-GW interface, whereas the assumption of constant transit-times results in incorrect estimates of NO_3^- removal potential based on DA_{DO} approach (40%-50% difference).

Keywords: *Damköhler number, discharge events, dissolved oxygen, losing stream, reactive potential, Selke River, tracer-tests, transit-times*

2.1 Introduction

The notion that surface water (SW) and groundwater (GW) should be perceived as one entity rather than two separate components has been established over the last 20 years (Fleckenstein et al., 2010; Winter et al., 1998). Water and solute fluxes between SW and GW can significantly impact water quantity and quality of both compartments (Boano et al., 2010; Brunner et al., 2017). These fluxes vary seasonally due to periodic fluctuations of stream stage and GW elevations (Bernard-Jannin et al., 2017; Ranalli & Macalady, 2010), but also at shorter, event-driven temporal scales (Shuai et al., 2017). Disentangling reaction and transport processes and their importance for subsurface reactions modulated by seasonal variations and

short-term events is challenging due to highly dynamic bio-geophysical characteristics of riparian environments (Kolbe et al., 2019; Pinay et al., 2015; Song et al., 2018).

Stream stage variations can increase exchange magnitudes within hyporheic and riparian zones, and enhance subsurface solute-turnover (Kirchner, 2009; Trauth et al., 2016). Trauth et al. (2018) showed that, particularly in riparian zones along losing stream sections, infiltrating stream water can improve the availability of dissolved organic carbon (DOC) as an electron donor in the subsurface and in turn enhance denitrification of agricultural nitrate (NO_3^-). However, as denitrification requires low DO concentrations it also hinges on prior DO consumption in the infiltrating, oxygen-rich stream water, typically via aerobic respiration (Boano et al., 2010). Understanding the key controls and the spatio-temporal variations of these redox reactions is essential for defining appropriate measures to improve the natural attenuation of potentially harmful substances such as nitrate in river corridors (Abbott et al., 2016; Oldham et al., 2019).

The reactive potential along a subsurface flowpath depends on the time that a water parcel stays in contact with the reactive media (Oldham et al., 2013). The greater water travels through the riparian subsurface, the greater the exposure to potentially reactive zones. However, discharge events can reduce GW transit-times in riparian zones due to sudden increase of SW-GW hydraulic gradients, limiting the exposure time to reactive zones and reducing net reactions (Sharma et al., 2012). In the riparian zone, subsurface transit-times have been quantified applying natural tracers like: heat, electrical conductivity (EC), stable water isotopes, and noble gases (e.g., ^{222}Rn, ^{37}Ar) (Schilling et al., 2017). Among them, cross-correlation analyses of natural EC variations is a simple, robust approach to derive transit-times in losing stream reaches by estimating time lags between the input (stream) and the output EC-signals measured in a monitoring well (Diem et al., 2013; Vieweg et al., 2016). However, Nixdorf and Trauth (2018) reported that the observed EC-signals in some riparian wells at losing stream sections could not only be attributed to direct surface water infiltration, but were instead also affected by stream water that had previously been stored in the banks. They found the estimated transit-times to be as much as two orders of magnitude lower compared to “true” transit-times derived from introduced (e.g., natural gradient) tracer-tests. This indicates that transit-time estimates based on natural tracers such as EC may be uncertain under non-ideal conditions and that artificial tracers or a combination of both might be a more realiable alternative.

In addition to transit-times and DO concentrations, the biogeochemical reactions are temperature regulated (Pietikäinen et al., 2005; Sharma et al., 2012). Thus, seasonal and short-term temperature fluctuations driven by SW-GW exchanges may either fuel or hinder reactions depending on characteristics of infiltrating water in contrast to GW (Greskowiak et al., 2006; Zarnetske et al., 2011). Besides, water and heat propagate along subsurface flowpaths at different rates, with heat being strongly retarded due to interaction with the sediment matrix. There is a complex interaction between hydrological variations at different time scales,

the associated heat and solute transport between SW-GW, and the biogeochemical reactions controlled by these variations. However, these complex interactions are difficult to characterize in the field and hence it is not surprising that to date only a few studies have attempted to explore them in field studies of GW-SW systems (Vieweg et al., 2016; Zarnetske et al., 2012).

This study extends these previous studies and aims to address major features controlling spatio-temporal variations of transit-times and DO consumption rates in riparian aquifers with a specific focus on the interplay between seasonal and event-scale variability. A fourth-order reach of the Selke Stream, a well instrumented and studied site (Nixdorf and Trauth, 2018; Vieweg et al., 2016) within the Bode Observatory of the TERENO initiative (Wollschläger et al., 2017) is used as a test case. At the site, we combined GW tracer-tests with high-frequency data of water levels, EC, and DO in the stream and in groundwater. We carried out a suite of well-to-well groundwater tracer-tests, employing salt (NaCl) and DO as tracers, in the riparian zone under a range of hydrologic conditions in terms of stream flow to: i) derive GW transit-times; and ii) acquire *in-situ* DO consumption rates (k_{DO}). A simple DO consumption model was parameterized based on the acquired data and subsequently applied to high-frequency observation data. We show how temporal variations of temperature and transit-times affect riparian DO reactions and transport processes. Finally, the relationship between DO consumption rates and transit-times was evaluated using the concept of Damköhler numbers in order to characterize the reactive state of the system.

2.2 Methods

2.2.1 Study area

Our field site is located at the Selke River, central Germany (51°43’37.79”N, 11°18’51.0”E), Fig.1. Previous studies at the site covered different aspects of flow, transport and reactions at the SW-GW interface with focus on in-stream and near-stream hyporheic processes (Munz et al., 2017; Trauth et al., 2014; Vieweg et al., 2016), however the interplay between transit-time and temperature variations in regulating redox state and processes within the riparian zone has been faintly explored. Measurements of hydraulic heads in the streambed and in riparian wells reveal that the stream reach is characterized by predominantly losing conditions (Munz et al., 2016). Mean annual discharge at the site is 1.5 m^3/s. During summer, baseflow can be below 0.2m^3/s, while bankfull discharge (about 15 m^3/s) can occur during spring snowmelt.

The riparian aquifer consists of fluvial sediments of up to 8 m thickness, ranging from medium sands to coarse gravels, underlain by clay-silt deposits forming the bottom of the alluvial aquifer. Groundwater

levels are generally shallow, with mean depths to groundwater of 0.5 and 1.8 m in the winter and summer, respectively. Drilling core samples from the vicinity of the stream showed a layered system (Fig.1), with a continuous less-permeable unit (fine sand) at around 3-4 meters below ground separating the system into two connected aquifer compartments, referred to as shallow and deep groundwater. The hydraulic conductivity of the aquifer material, determined by salt-tracer and slug-tests in the riparian wells, ranges from $1.7x10^{-3}$ to $1.2x10^{-2}$ m/s (geometric mean: $3.72x10^{-3}$ m/s).

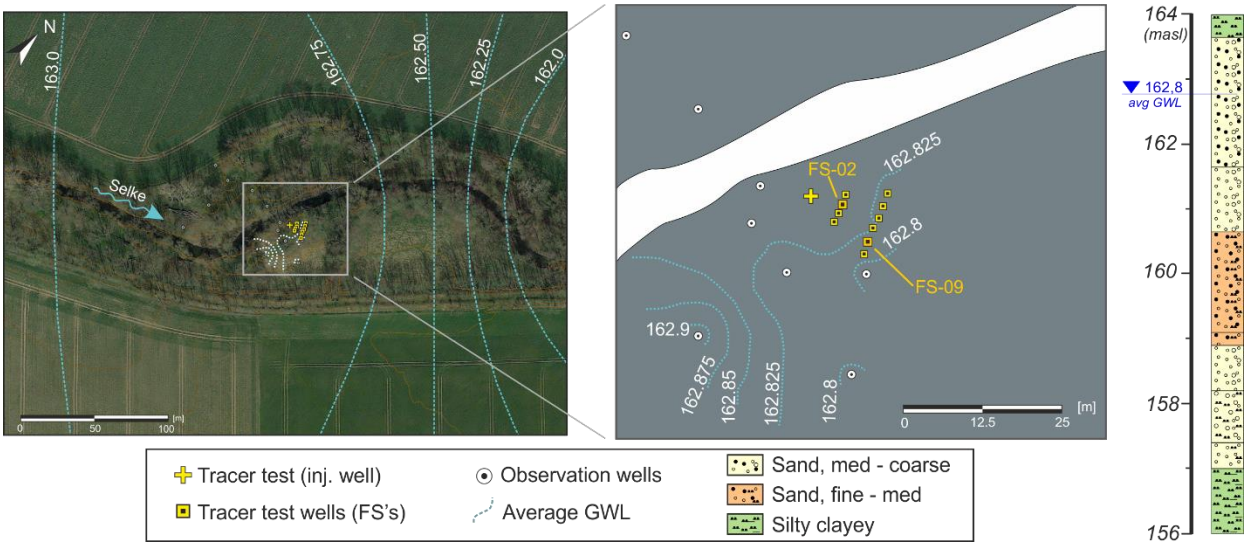

Fig.1: *Aerial view of the field site with average groundwater level contours (GWL) and detailed view of nested wells where groundwater tracer-tests were conducted; A driller's log (right) with observed lithology giving an indication of local heterogeneity and aquifer layering.*

2.2.2 High-frequency data collection

Water levels, electrical conductivity (EC) and water temperature in stream (T_{SW}) and groundwater (T_{GW}) were measured by self-contained Solinst Levellogger Junior loggers (LTC). DO concentrations were monitored by self-contained DO loggers (HOBO Dissolved Oxygen Data Logger) in both stream and in groundwater. For capturing short temporal fluctuations, all loggers were set to a 10-minute measuring interval from November 2017 until December 2018, comprising one full year of high-frequency measurements with few data gaps in between (10% of total dataset) due to probe malfunctioning and probe removal during maintenance. Stream discharge was calculated from a stream stage-discharge relation (Fig.S1, supplementary material), based on stage readings and monthly manual discharge measurements using an electromagnetic flow meter (MF pro, Ott, Germany).

Discharge time-series decomposition

Discharge time-series were divided into baseflow and discharge events components to assess their different effects on subsurface processes. Baseflow separation was based on a rolling five days local minima (Gustard & Demuth, 2009); discharge events were defined according to the first derivatives of the discharge time-series using the functions *findpeaks* and *localminima* in MATLAB®. Significant events were defined as having a minimum peak prominence of at least 15% above the preceding baseflow value, with a minimum peak separation of 5 days imposed to avoid diminutive discharge variations and overlapping/double peak events that were counted as one large event.

2.2.3 GW transit-times from tracer-tests in the riparian aquifer

We carried out eight natural gradient tracer-tests in the riparian aquifer adjacent to the stream between Nov 2017 – Sep 2018 (Table 1). The tracer-tests captured changes in main flow directions and transit-times of the infiltrating stream water. A total of 11 nested 2" PVC monitoring wells (including an 'injection-well'), screened at depths between 1 and 6 m below ground (mbg), were equipped with LTC-loggers to monitor tracer breakthrough curves in different depths, at a one minute interval and over a minimum period of seven days after injection. The monitored locations were the same as for the long-term high-frequency data collection. Tracer (NaCl diluted in stream water) was injected below the groundwater table in the injection-well using a peristaltic pump. A packer isolated the well at 2.5 mbg to optimize tracer insertion by releasing it where maximum transport is expected. The tracer-test protocol was kept identical between different experiments with only the injection volumes and NaCl concentrations varying according to the hydrologic conditions. Injection durations varied, but were no longer than 20 min. Groundwater level variations in the injection-well were minimal during tracer-tests and considered to be negligible. In three of the experiments, a packer system was inserted in one of the monitoring wells to evaluate inner well mixing as the wells are fully screened. However, no significant differences between the wells with and without packer system were found. The specification of tracer-tests are summarized in Table 1.

Table 1: Tracer-tests parameters and related field conditions during the experiments. "Q" represents mean stream discharge during the tracer-test.EC is the electrical conductivity, DO is the dissolved oxygen.

Tracer-test		Date	Stream				Groundwater (average)			Tracer		Injection	
			Q (m^3/s)	EC (mS/cm)	DO (mg/l)	Temp (°C)	EC (mS/cm)	DO (mg/l)	Temp (°C)	NaCl (g/l)	EC (mS/cm)	Vol. (l)	Rate (l/min)
1	▽	15/11/2017	0. 7	0.39	11.3	12	0.39	3.5	8	83.3	118.5	30	2.0
2	▽	28/11/2017	3.3	0.31	12.4	5	0.40	5.0	6	100.0	140.7	30	2.0
3	▽	17/01/2018†	3.2	0.31	12.2	4	0.44	6.5	4	100	146.0	30	2.0

4	▼	28/02/2018†	0.3	0.60	13.3	1	0.55	7.5	3	92.3	133.0	130	7.2
5	▼	11/04/2018†	1.7	0.35	10.7	10	0.50	6.0	5	100	145.0	32	4.0
6	▼	30/05/2018	0.4	0.51	9.2	23	0.51	4.0	11	100	135.9	40	4.0
7	▼	10/07/2018	0.1	0.59	11.6	16	0.57	<2.0	15	95	132.0	105	7.0
8	▼	28/08/2018	0.2	0.65	8.5	23	0.60	<2.0	16	100	121.0	40	2.8

† *with packer system*

Tracer concentration was measured in terms of EC values. Conservative transport of the EC signal was assumed so that the 1-D advection-dispersion equation without retardation and no sorption (Koestel et al., 2011) applies:

$$\frac{\partial C}{\partial t} = -V_{GW}\frac{\partial C}{\partial x} + D_h\frac{\partial^2 C}{\partial x^2} \quad \text{Eq.1}$$

where C is solute concentration [M³/L], V_{GW} is the groundwater velocity [M/T], D_h is the dispersion coefficient, t is time and x is distance to injection point [L]. With the initial condition that a slug mass M is injected at $x = 0$ and $t = 0$, at any given moment t and at x, the tracer concentration can be represented by:

$$C(x,\tau) = \frac{M}{2\sqrt{\tau\pi D_h}}\ exp\left[-\left(\frac{(x-V_{GW}\,\tau)^2}{4D_h\tau}\right)\right] \quad \text{Eq.2}$$

where M is the solute mass [M] in terms of EC, τ is the transit-time [T], and other parameters are the same as in Eq.1. We fitted Eq.2 to each observed tracer breakthrough curve (BTC) for M, D_h and V_{GW} through the least squares method. Before fitting, BTCs were corrected for background EC, and BTCs with changes smaller than 1.0% to background EC were not considered for further analyses. Based on fitted V_{GW} and D_h, Peclet numbers ($Pe = V_{GW}\,x/D_h$) were computed to assess whether transport was advection or diffusion dominated. By fitting the parameter M for each observation point, we were able to derive the centre of mass of the plume, i.e. the main GW flow direction for each test. The large number of BTCs (51 in total) was essential for identifying flowpaths where tracer passage was persistently observed within the nested observation wells during the different tests (i.e., a clear EC signal above background values, nearly complete BTC across the entire season). Thus, the large number of wells and BTCs were needed to select the best subset of points allowing for a precise quantification of τ, which were further analysed. For a same tracer-test, transit-times differences among wells equidistant to the injection-well were similar, whereas differences were larger between the shallow and deep observation points within a same well. Based on the acquired data, the subset of BTC from the monitoring well FS-02 were selected for further analyses.

Mean transit-times were derived according to V_{GW} and distance to injection point ($\tau = x/V_{GW}$) for the 16 BTC of well FS-02, eight from shallow (Fs) and eight from deep groundwater (Fd). We hypothesize that τ can

be correlated to stream discharge values since the stream reach is predominantly losing and GW heads are directly influenced by stream stage variations. This conceptually implies that GW transit-times are driven by stream stage variations and no stream water infiltrates to the subsurface when Q=0. Thus, high-frequency GW transit-times (τ_Q) can be computed from an independent hydrological variable for periods not covered by the tests.

2.2.4 DO consumption rates

Although DO water solubility decreases with temperature (Weiss, 1970), groundwater DO variations at the site cannot be explained solely by temperature variations. Locally, groundwater DO consumption can mainly be attributed to organic matter degradation via aerobic respiration, while other processes such as iron-minerals oxidation and nitrification can be neglected (Trauth et al., 2018; Vieweg et al., 2016). We derived DO consumption rates from DO concentration measurements in the observation wells during tracer-tests. Since half-saturation constants of aerobic respiration are typically small (0.03–0.3 mg O2/l) the reaction can be simplified to 1st-order kinetics instead of Michaelis–Menten kinetics (Diem et al., 2013; Greskowiak et al., 2006):

$$C = C_0 \, exp(-k_{DO} \, \tau) \qquad \text{Eq.3}$$

where C is the measured DO concentration in the monitoring well [M/L³], C_0 is the initial DO concentration in the tracer [M/L³], k_{DO} is the 1st-order rate constant for respiration (1/T), and τ is the mean transit-time. We considered transit-times from the EC-BTC because first arrival times, peak times, and mean transit-times derived from DO breakthrough curves were similar (and not statistically different). The k_{DO} for each measurement point was determined by plotting the natural logarithm of relative DO concentrations versus transit-times. Best-fit slopes (e.g., mean reaction rates) for each tracer-test were found by linear regression. A stronger correlation between 1st-order rates and T_{GW} further supported our use of 1st-order kinetics instead of 0th-order rates (R^2*=078*, R^2*=0.32*, respectively).

Empirical k_{DO} derived from tracer-tests were correlated to measured T_{GW} at the time of the experiment following Arrhenius equation (Pietikäinen et al., 2005), Eq.4. Thus, high-frequency DO consumption rates could be inferred from T_{GW} values.

$$k_{DO-T_{GW}}(t) = \; a \exp(b \, T_{GW(t)}) \qquad \text{Eq.4}$$

where $k_{DO\text{-}TGW}$ is the reaction rate, T_{GW} is the GW temperature, and a and b are fitting parameters. We graphically derived activation energy (E_A) values for each point characterizing the temperature sensitivity of respiration based on the negative slope from the Arrhenius plot ($\ln(k_{DO})$ *vs.* T^{-1}) (Atkins and de Paula, 2011).

2.2.5 Simulation of riparian DO concentrations

In order to assess effects of short-term fluctuations of temperature and stream discharge on riparian DO dynamics, which are likely not captured by tracer-tests, we extended the analyses of GW transit-times and DO consumption rates to a high-frequency dataset. We simulated DO concentrations based on Eq.3, assuming stream DO concentrations prior to infiltration (t-τ) as C_0 in each time-step with negligible input of other DO source. In a first step, we used results acquired from tracer-tests and the relation between stream stage and transit-time to simulate riparian DO concentrations. We compared results with a range of constant transit-time scenarios based on tracer-tests results, and with transit-times based on EC-cross correlation following the procedure of Vieweg et al. (2016).

Effective temperature between stream and groundwater

As stream water infiltrates into the subsurface, water temperature is altered along transit from the stream to the observation wells. Thus, the temperature associated with the reaction is likely neither the stream (T_{SW}) nor the groundwater temperature (T_{GW}) but an effective temperature (T_{eff}) between the two. We implemented T_{eff} as an optimization parameter in the simulations constrained between T_{SW} and T_{GW}. Best computed T_{eff} resulted from minimizing the objective function (ε) for observed DO concentrations (DO_{obs}) in each time-step:

$$\varepsilon = \sqrt{\{DO_{obs(t)} - [DO_{sw(t-\tau)} \exp(-a \exp(b\, T_{eff(t)})\, \tau_{(t)})]\}^2} \qquad \text{Eq.5}$$

where *a* and *b* are fitted parameters from Eq.4. Based on T_{eff}, a temperature corrected consumption rate ($k_{DO\text{-}Teff}$) was derived for each time-step, and further used to compute riparian DO concentrations using Eq.3.

Theoretical transit-times

To evaluate our transit-time and discharge relation we also computed the theoretical transit-times (τ*) that would be required to perfectly match observed DO concentrations based on $k_{DO\text{-}Teff}$. τ* were calculated with $k_{DO\text{-}Teff}$ while allowing transit-time in Eq.3 to vary boundless in each time-step to match observed DO concentrations. Thus, we can analyse the patterns and values of independently computed τ*and whether differences from empirical τ_Q were physically plausible changes (i.e., realistic ranges for the field site) not captured by our streamlined model, or if other variables and processes influence the biogeochemical system.

2.2.6 Damköhler numbers for dissolved oxygen

To compare the roles of reaction and transport processes and to evaluate whether the system was limited by the reaction rate or by the supply of reactants, we used dimensionless Damköhler numbers. They have

been extensively applied in chemical engineering and hydrological studies to assess the balance between reactive and transport processes (Fogler, 2005; Oldham et al., 2013; Vieweg et al., 2016). The Damköhler number for oxygen (DA_{DO}) is computed as:

$$DA_{DO}(t) = k_{DO(t)}\ \tau_{(t)} \quad \text{Eq.6}$$

where $k_{DO(t)}$ and τ_t represent the 1st-order DO consumption rates [T^{-1}] and transit-times [T], respectively. If DA_{DO} <1, the DO supply rate is above its biogeochemical demand and the system is reaction limited. DA_{DO}=1 indicates a balanced system, where DO supply equals its demand. For DA_{DO}>1, the DO supply rate is smaller than its demand and anoxic conditions tend to emerge as the system is transport limited. This in turn has implications for denitrification. For instance, Zarnetske et al. (2012) used the DA_{DO} concept to evaluate whether a system is characterized by net-nitrifying (DA_{DO}<1) or net-denitrifying (DA_{DO}>1) conditions. From 10,000 reactive transport simulations, they found that net-denitrification outcompeted net-nitrification in 20% of the cases when DA_{DO}>1 and in 95% of the cases with DA_{DO}=10, above which nitrification was negligible.

2.3 Results

2.3.1 Hydraulic conditions and high-frequency measurements

Time-series of stream discharge, precipitation, SW and GW temperatures, and DO for the hydrological year of 2018 are presented in Fig.2. Stream discharge was highest between January and March (up to 14 m^3/s), whereas from July until December, extremely low baseflow discharges of 0.1 m^3/s occurred as a result of the dry summer of 2018. A total of 16 discharge events (most in winter) were identified for the year 2018 (grey shaded areas in Fig.2a). We also observed that most of the discharge events (around 60%) resulted in reduced stream water temperatures (T_{SW}) and consequently under the prevailing losing conditions also in lower GW temperatures (T_{GW}) (up to 4.5ºC lower in January) relative to the temperature prior to the event (Fig.S2, supplementary material).

The T_{SW} and T_{GW} followed a seasonal pattern as imposed by ambient air temperature, with higher values in summer and lower values during winter. The variation of T_{GW} is increasingly lagging behind variations in T_{SW} with increasing distance from the stream (Fig.2b). Highest and lowest temperatures were slightly different for T_{SW} and T_{GW}, maximum and minimum water temperatures were 23ºC and 0ºC for T_{SW} (μ=8.7ºC), and 20ºC and 2.7ºC for T_{GW} (μ=13.5ºC), respectively. T_{GW} and DO concentrations in Fig.2 are vertically averaged values over the entire saturated thickness of the aquifer since temperature differences

between shallow and deep GW were generally below 2ºC and DO concentrations differences were smaller than 2 mg/l at different depths.

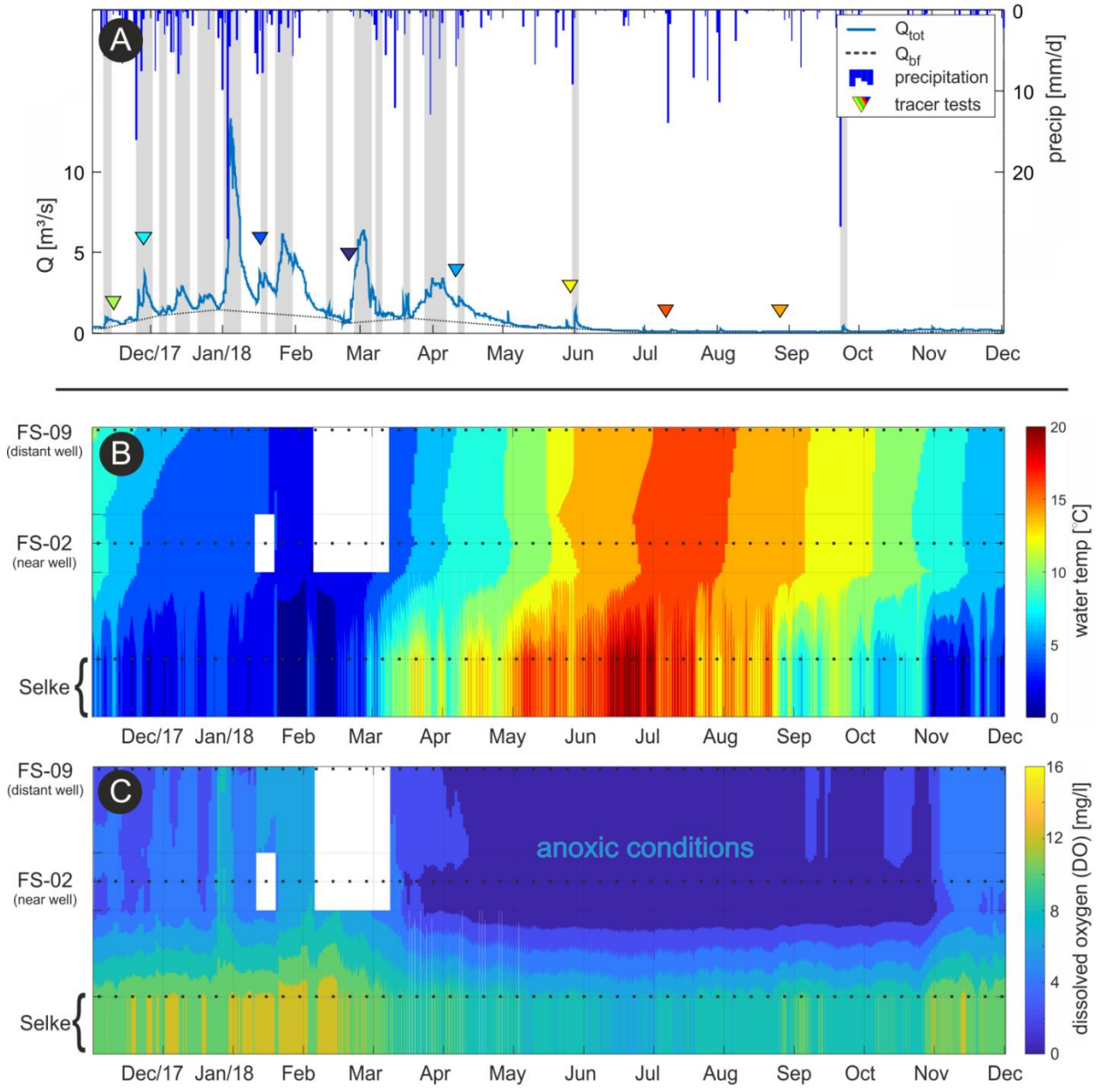

Fig.2: a) *time-series of precipitation, total stream discharge (Q_{tot}) and baseflow component (Q_{bf}), and carried out groundwater tracer-tests (triangles);* ***b)*** *temperature in the Selke stream and in two different riparian wells, and* ***c)*** *spatio-temporal series of dissolved oxygen (DO). Values between stream and measure points (dotted lines) were linearly interpolated for visualization purposes only. Grey bars in* ***(a)*** *highlight discharge events identified in the observed period. White polygons in* ***(b)*** *and* ***(c)*** *denote periods with no data; "anoxic conditions" indicates period and location with DO<2 mg/l.*

Stream DO remained close to saturation (corrected for temperature) with only minor diurnal fluctuations linked to stream metabolism. In groundwater, DO concentrations exhibited a high spatio-temporal variation, generally decreasing with increasing distance from the stream (Fig.2c). During summer, prolonged periods of anoxia (DO< 2mg/l) occurred in all observation wells. DO concentrations in the stream and in groundwater increased during discharge events, especially during winter (Fig.2c, and Fig.S2, supplementary material).

2.3.2 Groundwater transit-times

GW tracer-test transit-times

Transit-times (τ) were derived based on performed groundwater tracer-tests. The resulting τ from fitting Eq.2 to the 16 EC BTC from Fs and Fd of well FS-02 are presented in Fig.3a in relation to stream discharge at the time of tracer injection.

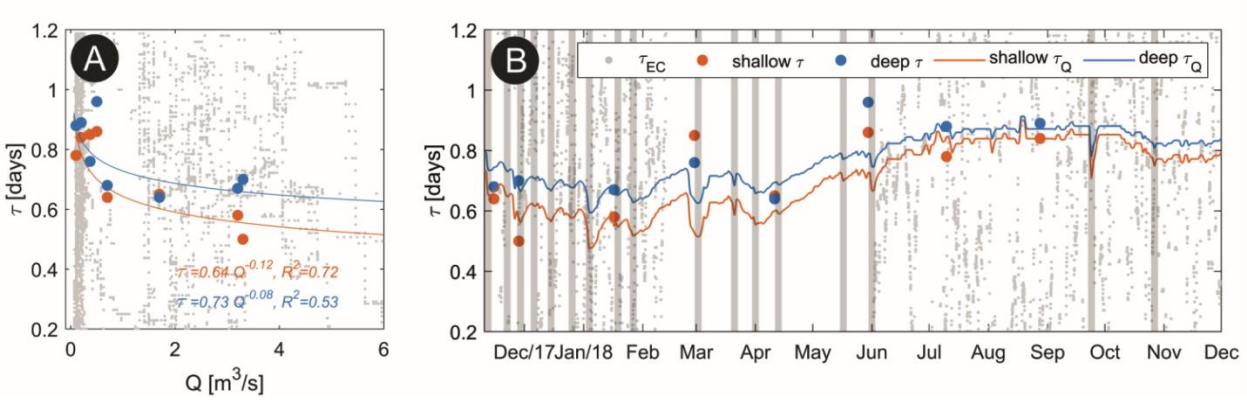

Fig.3: a) *shallow and deep GW transit-times and stream discharge (Q) relation used to derive transient τ_Q;* ***b)*** *temporal variation of GW transit-times for shallow and deep aquifer obtained from tracer-tests (shallow τ and deep τ, respectively), transient GW transit-times for shallow and deep aquifer based on stream discharge (shallow τ_Q and deep τ_Q, respectively). Grey dots in* ***(a)*** *and* ***(b)*** *represent the EC cross-correlation transit-times (τ_{EC}). Grey bars in* ***(b)*** *highlight discharge events identified in the observed period.*

The range of GW transit-times for Fs was between 0.6-0.8 day (μ=0.7 day), whereas for Fd the range and values were slightly longer, between 0.6-1.0 day (μ=0.8 day). Even though temporal changes of τ were small, GW transit-times were statistically different between the experiments (Kruskal-Wallis-Test, p-value=0.03), and decreased with increased stream discharge. Based on the results, we observed that GW transit-times were correlated with stream discharge through a power law ($\tau=aQ^b$, Fig.3a). For Fs, the fitting parameters *a* and *b* were 0.64 and -0.12 (R^2=0.72), and for Fd, 0.73 and -0.06 (R^2=0.53) respectively. We use this power law relationship for deriving high-frequency transit-times directly from stream discharge. High-frequency GW transit-times based on stream discharge (τ_Q) are presented for Fs and Fd in Fig.3b. For

both locations, τ_Q increased from winter to summer (lower Q), whereas a decrease in values during discharge events could also be observed, however not to a large extent.

Groundwater velocities (V_{GW}) derived from Eq.2 were on average 8 m/d and 11 m/d for Fs and Fd, respectively, with values up to 16 m/d for Fd under high stream discharges. Peclet numbers computed between 2 and 10 for the Fs, and between 2.5 and 19.5 for the Fd, also increasing with Q, indicated an advection-dominated transport for the range of stream discharges covered by the tests.

EC cross-correlation transit-times (τ_{EC})

The EC time-series between the Fs and Fd were not significantly different and, therefore, EC cross-correlation transit-times (τ_{EC}) were only calculated based on Fs EC time-series. The resulting τ_{EC} was highly variable in time, but with similar mean values to transit-times from tracer-tests for the same depth (μ=0.7), Fig.3b. However, despite the pre-processing applied, such as detrending and optimized smoothing of stream EC-values to increase signal correlations (Fig.S3, supplementary material), and testing of different cross-correlation window sizes (e.g., Vieweg et al, 2016), the resulting τ_{EC} were very noisy and mostly unreliable (PCC<0.75), indicating that transit-times based on EC cross-correlation do not perform well at our site.

2.3.3 DO consumption rates (k_{DO})

Computed k_{DO} was higher for Fs, with averages values of 2.9 d^{-1} and 2.0 d^{-1} for Fs and Fd, respectively. Rates increased with T_{GW}, Fig.4a, and were significantly different among tests (Kruskal-Wallis-Test, p-value<0.001). The k_{DO} values showed strong negative correlation with stream discharge (R_{spear}= -0.71, p-value<0.01), because high Q is typically associated with lower temperatures at our site, which seems true also for short-term discharge events (Figs.3a and 3b). Coefficients of variation of k_{DO} were 0.51 and 0.65 for Fs and Fd respectively. The activation energies fitted from tracer-tests according to the Arrhenius equations were 1.03 eV for Fs and 0.93 eV for Fd.

T_{GW} explained 87% of k_{DO} variations for Fs and 91% for Fd, indicating a strong temperature control of the reactions. There was a systematic increase of rates towards the summer, however differences between the shallow and the deep groundwater can be seen, Fig.4b. In the winter, T_{GW} in the deep groundwater was slightly warmer than in the shallow groundwater. Therefore the resulting k_{DO} values were slightly higher in the deep groundwater. In the summer the opposite was observed.

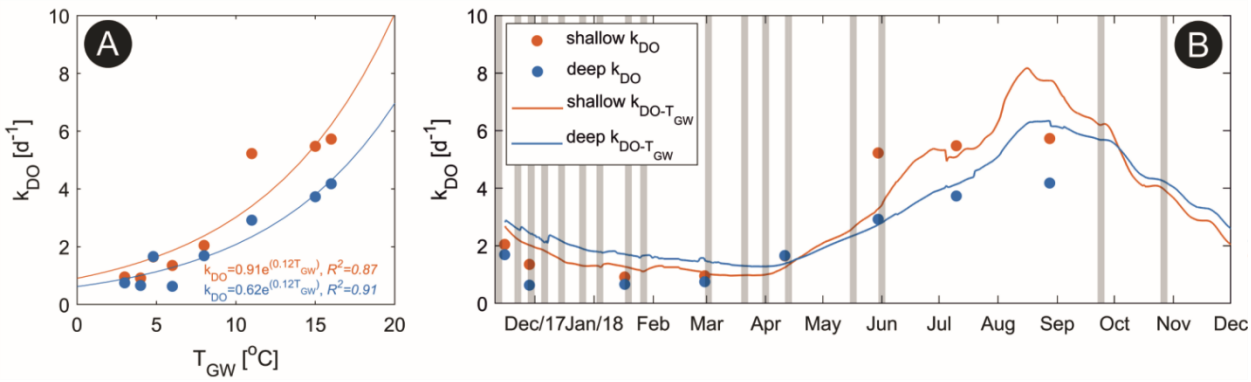

Fig.4: a) *groundwater temperature (T_{GW}) and k_{DO} relation used to derive high-frequency k_{DO};* ***b)*** *temporal variation of empirical DO consumption rates acquired from tracer-tests (k_{DO}), and the transient empirical k_{DO} based on T_{GW} relation ($k_{DO\text{-}TGW}$) for shallow and deep aquifers. Grey bars in* ***(b)*** *highlight discharge events identified in the observed period.*

2.3.4 Controls of riparian DO

In order to further constrain the interplay and major short/long-term controlling factors of riparian DO concentrations, we used different parameterizations of Eq.3 to simulate riparian DO concentrations. As k_{DO} can only be estimated based on observed DO concentrations and given transit-times, uncertainties in transit-time are directly reflected in the value of k_{DO}.

Explicit simulations of DO concentrations

Firstly, we simulated DO concentrations applying the stream discharge tau relationship (τ_Q) for transit-times and consumption rates based on T_{GW} ($k_{DO\text{-}TGW}$). To assess effects of different transit-times on riparian DO concentrations, simulation results are presented alongside simulations employing τ_{EC} (for the shallow groundwater) and with optimized constant transit-times (opt-τ). Optimal constant transit-times were obtained from different simulations using values between the upper and lower limits of transit-times from tracer-tests (in a 0.025 day interval) and taking into account $k_{DO\text{-}TGW}$. Only the best fitting constant transit-time models for each depth are presented.

For Fs the simulations using constant and varying transit-times based on stream discharge captured low-frequency/seasonal fluctuations of DO concentrations well, suggesting that transit-time variations have a minor influence on DO at seasonal timescale, Fig.5a. The opt-τ found for Fs was 0.48 d (below the average τ of 0.7 from tracer-tests), and resulted in a NSE=0.881 and R^2=0.946. The model with τ_Q had a poorer fit in comparison to the former, NSE=0.633 and R^2=0.935, however main DO variations were captured equally well.High frequency variations in DO were not captured well by either model.

Simulated DO concentrations based on τ_{EC} had the poorest fit (NSE=0.433 and R^2=0.694). Similarly to EC-transit-times, resulting DO values were very noisy and highly variable. Satisfactory results were only achieved after strongly smoothing τ_{EC}, leading to smoothed DO values and a NSE=0.826 and R^2=0.909. Since posterior smoothing of τ_{EC} is not meaningful, results are discarded from further analyses.

Simulation of DO concentrations for Fd yielded different results than those for Fs. The model with opt-τ=0.73 day (near average value of 0.8 day from tracer-tests) performed much better than the model using τ_Q, Fig.5b. The former had NSE= 0.813 and R^2=0.932, while the latter had NSE= 0.531 and R^2= 0.926, even though main DO dynamics were captured. However, both models systematically overestimated DO concentrations during summer.

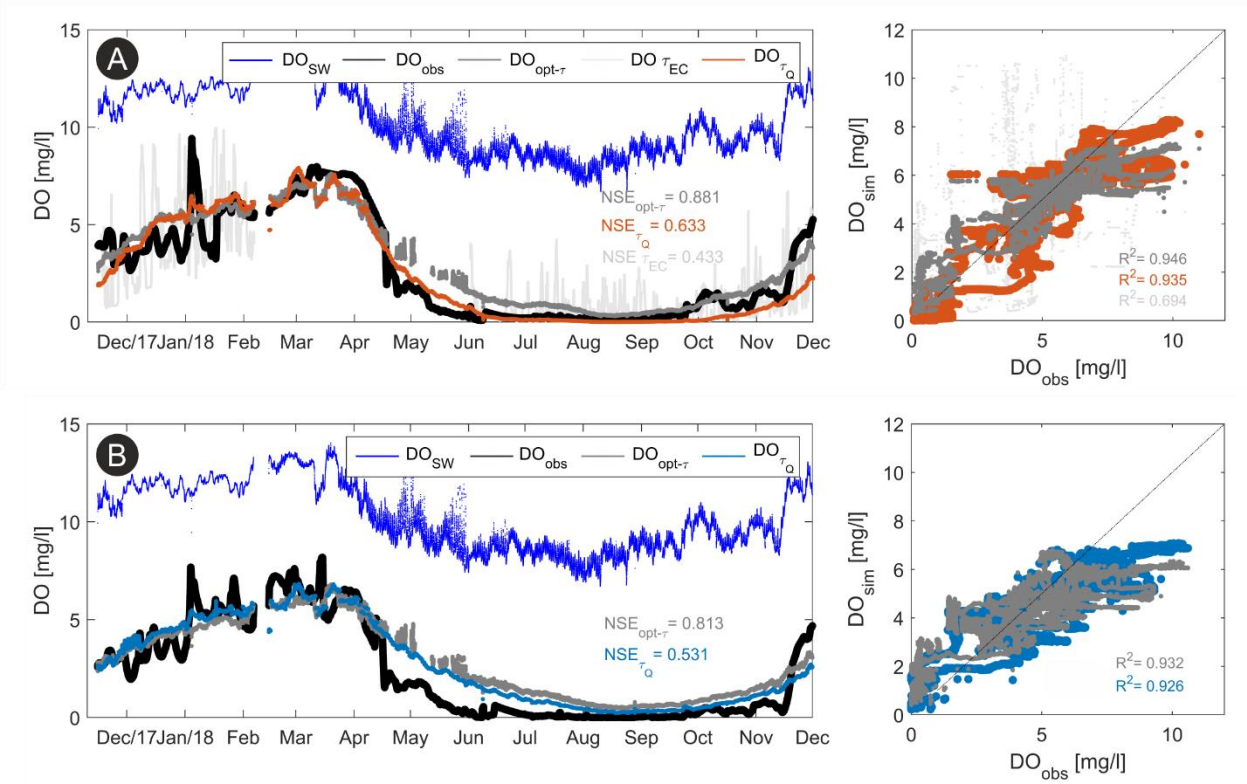

Fig.5: *observed DO concentrations in stream (DO_{SW}) and groundwater (DO_{obs}), and simulated results considering optimized constant transit-times ($DO_{opt\text{-}\tau}$), transient transit-times ($DO_{\tau Q}$), and EC-based transit-times ($DO_{\tau EC}$) for shallow **(a)** and deep **(b)** aquifer.*

DO simulations with effective temperatures

Although model fits of section 3.4.1 were acceptable, subsurface temperatures in the riparian zone are affected by both the temperature of the freshly infiltrating stream water as well as the local groundwater temperature, Fig.2b. To better represent the true, yet unknown temperature that best represents the

temperature dependent consumption rate ($k_{DO\text{-}T_{eff}}$), we computed an effective temperature (T_{eff}) for the different transit-time scenarios of section 3.4.1. Hence, we can jointly assess the sensitivity of DO concentrations to $k_{DO\text{-}T_{eff}}$ and to different transit-times.

Since more degrees of freedom were added to the model, simulations employing $k_{DO\text{-}T_{eff}}$ had better model fits in comparison to simulations relying on T_{GW}. By employing $k_{DO\text{-}T_{eff}}$, the scenario with opt-τ was better than the simulation using τ_Q for Fs (NSE= 0.926 and NSE= 0.897, respectively). However, the opposite was observed for Fd, where the model using τ_Q had a slightly higher NSE than the model considering opt-τ (NSE=0.953 and NSE=0.938, respectively). Comparing to $k_{DO\text{-}T_{GW}}$, the $k_{DO\text{-}T_{eff}}$ exhibited earlier summer peak times, Fig.6b and 6d. There, the resulting $k_{DO\text{-}T_{eff}}$ was 2-3 times higher than $k_{DO\text{-}T_{GW}}$, which can be attributed to a higher T_{eff} caused by infiltrating warmer stream water. If this is not taken into account and k_{DO} is purely based on T_{GW}, consumption rates could be underestimated in summer, whereas they could be overestimated in the winter.

T_{eff} showed a shift from being close or at T_{GW} towards T_{SW} especially in the summer when transit-times were generally longer and $T_{SW}>T_{GW}$ (Fig.S4, supplementary material). We noted that T_{eff} reached the warmer temperature boundary in winter when $T_{GW}>T_{SW}$ and on average 47% and 35% of the simulated time for Fs and Fd respectively, which implies that the simulated DO concentrations were still not perfectly matching observed values. This suggests, for instance, longer transit-times than the previously computed values may be required to match the measured concentrations at those specific times. One way to test whether the residuals between simulated and observed values have the structure of random noise or reflect a systematic error of the models is to analyse their distribution and evaluate the theoretical transit-times needed to match the observed concentrations.

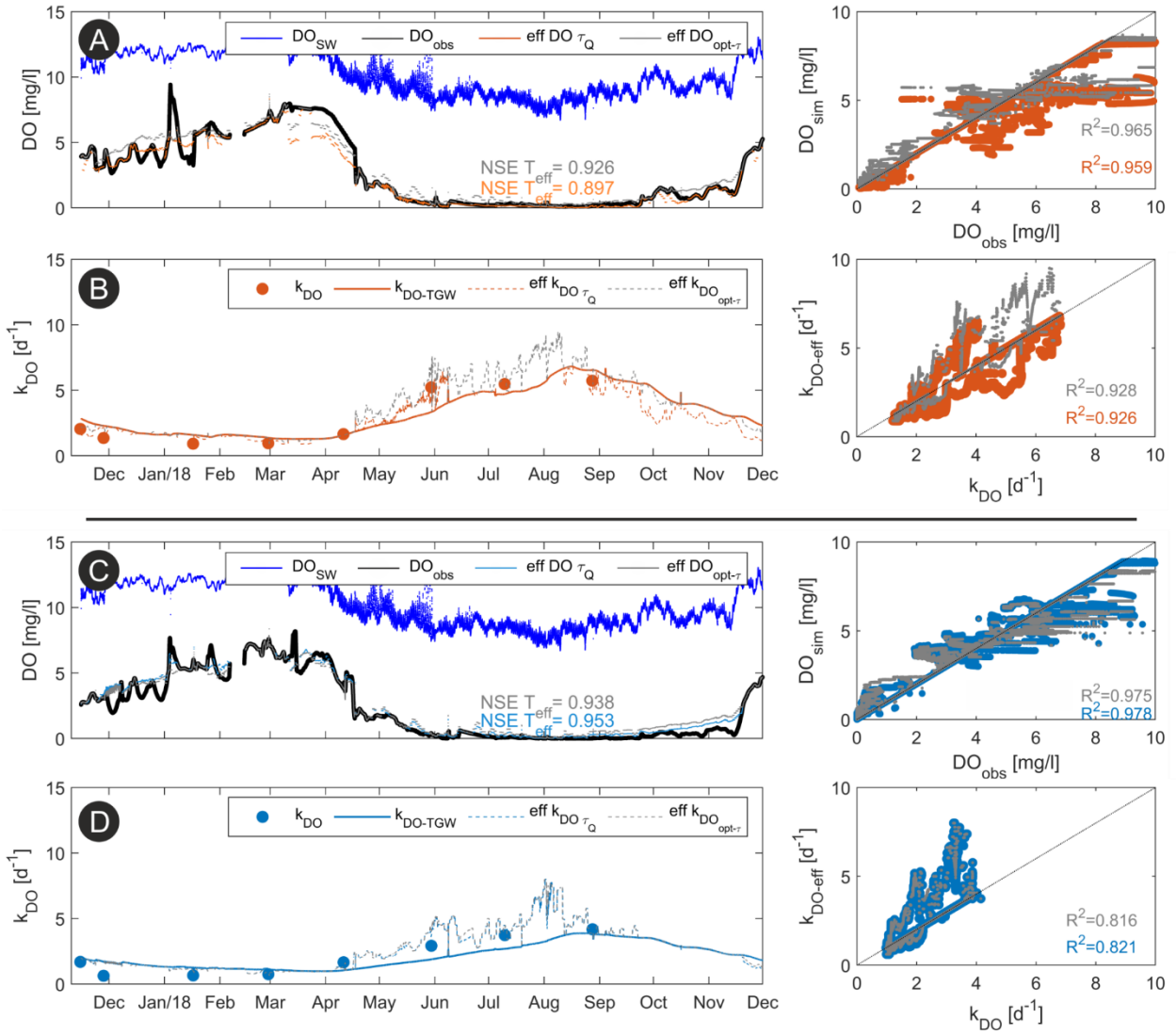

Fig.6: *observed DO concentrations in stream (DO_{SW}) and groundwater (DO_{obs}), and simulated values with optimized consumption rates under varying and constant transit-times (eff DO τ_Q and eff DO $_{opt}$-τ, respectively) for the shallow* ***(a)*** *and the deep* ***(c)*** *aquifer; temporal variation of k_{DO} and $k_{DO\text{-}TGW}$ together with optimized effective rates for varying and constant transit-times (eff $k_{DO}\tau_Q$ and eff k_{DOopt}-τ, respectively) for shallow* ***(b)*** *and deep* ***(d)*** *aquifer.*

DO residuals and theoretical transit-times

Simulations employing $k_{DO\text{-}Teff}$ had good NSE (≥0.9) but did not match all of observed DO variations. DO residuals were approximately normally distributed for both depths, which indicates that there is no substantial systematic error in the models. Thus, we calculated the required theoretical transit-times (τ*) to perfectly match observed DO concentrations based on $k_{DO\text{-}Teff}$ (section 2.5.2) in each time-step. Theoretical transit-times were calculated based on $k_{DO\text{-}eff}$ since we consider the rates as the best estimates employing all local knowledge.

Equally to τ_Q, computed τ*resulted in shorter transit-times under high stream discharge, Fig.7b. For instance, during the high discharge event of Jan/2018 (Q>10 m³/s), τ*resulted in 0.2/0.5 day and τ_Q were 0.47/0.59 day for Fs/Fd respectively. V_{GW} computed on the basis of τ*would be 25 and 11 m/d during this event for Fs and Fd, respectively. These high V_{GW} would still be close to the range of measured velocities based on tracer-tests and thus plausible at the site.

During summer, residuals between observed and simulated DO concentrations were very small in absolute values. But since DO concentrations were equally low and consumption rates were the highest, big changes in τ*are needed to match even small deviations in DO concentrations. Nevertheless, stream discharge was nearly constant at the same period and it is not likely that we can attribute variations of τ* to true variations since changes in transit-time during baseflow conditions are not expected. Thus, theoretical transit-times during baseflow should be considered implausible. Overall, the back-calculation of τ*from best estimates of k_{DO} corroborate the applicability of the relation between stream stage and transit-times.

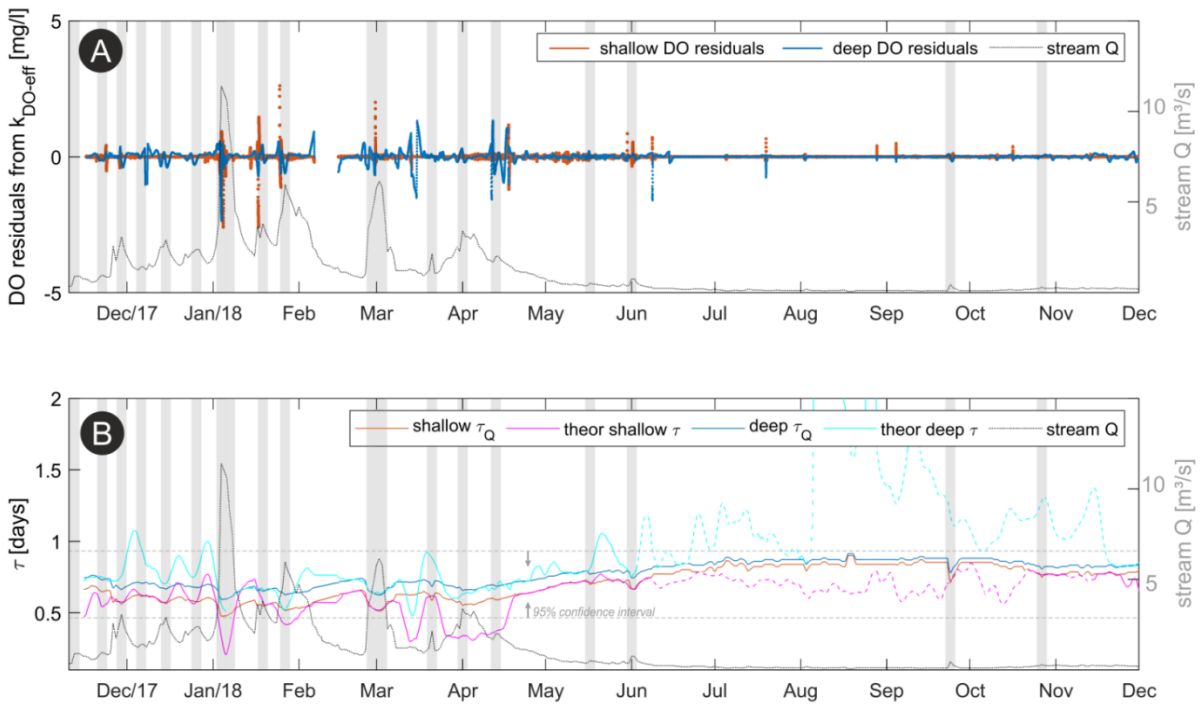

Fig.7: a) *temporal distribution of DO concentrations residuals from simulations using $k_{DO\text{-}eff}$: positive residuals indicate overestimations of DO concentrations, negative residuals indicate underestimations;* ***b)*** *τ_Q for shallow and deep aquifer together with computed theoretical transit-times. Black dotted lines in (a) and (b) represent stream discharge (stream Q), dashed horizontal lines in (b) represent the 95% confidence interval based on mean τ_Q.*

2.3.5 Damköhler numbers for DO (DA_{DO})

To assess changes of the reactive regime, we derived Damköhler numbers for Oxygen (DA_{DO}) applying computed GW transit-times and DO consumption rates according to Eq.6.

Low-frequency DA_{DO}

Low-frequency DA_{DO} values (shallow DA_{DO} and deep DA_{DO}) were computed directly from the results of the tracer-tests. They captured main seasonal changes in the system. For both Fs and Fd, the conditions changed from reaction limitation ($DA_{DO}<1$) during the winter to transport limitation ($DA_{DO}>1$) in late spring, Fig.8a. For Fs, resulting DA_{DO} ranged from 0.5 to 4.5 ($\mu=2.2$), whereas for Fd DA_{DO} ranged between 0.5 and 3.3 ($\mu=1.7$). From the tracer-tests is was apparent that DA_{DO} for shallow groundwater was generally higher than DA_{DO} for the deeper system. Even if transit-times were somewhat longer for Fd, consumption rates were slightly lower, resulting in similar DA_{DO}.

High-frequency and theoretical DA_{DO}

High-frequency DA_{DO} were based on $k_{DO\text{-}eff}$ to assess short temporal variations of stream water temperature on the reactive regime of the subsurface system. On average, low-frequency and high-frequency mean DA_{DO} values look similar, however, a much greater variability can be observed in the high-frequency data, Fig.8b. Especially for Fd, high-frequency DA_{DO} can be 2-3 times higher than low-frequency DA_{DO} based on $k_{DO\text{-}T_{GW}}$. Still, general regime patterns are very similar since its main control is the seasonal water temperature variation and the effect of discharge events was minimal.

Independent of whether DA_{DO} is computed considering constant or varying/theoretical transit-times, results corroborate that the regime is mainly regulated by temperature variations controlling DO consumption rates since DA_{DO} patterns were similar despite the transit-time scenario. Nevertheless, especially during summer constant transit-times DA_{DO} were smaller in comparison to DA_{DO} computed using varying transit-times, which can have implications when assessing redox sensitive related processes.

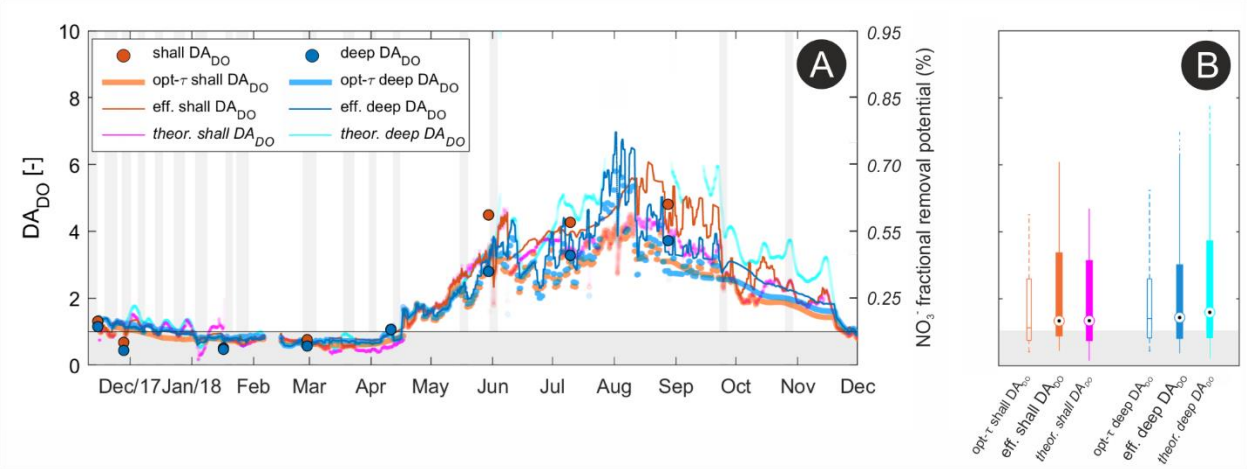

Fig.8: a) *Damköhler numbers for dissolved oxygen (DA_{DO}) along a hydrological year for shallow and deep aquifer considering different DO consumption rates and different GW travel-time calculations; shallow DA_{DO} and deep DA_{DO} represent low-frequency DA_{DO} (from tracer-tests); opt-τ shallow DA_{DO} and opt-τ deep DA_{DO} were based on constant transit-times; eff. shallow DA_{DO} and eff. deep DA_{DO} were computed with variant transit-times (τ_Q); theor. shallow DA_{DO} and theor. deep DA_{DO} were computed according to theoretical transit-times; b) boxplot of high-frequency DA_{DO} values presented in **(a)** following their same notation.*

2.4 Discussion

2.4.1 GW transit-times

Transient groundwater transit-times have often been computed based on signal analysis methods such as deconvolution (e.g., Cirpka et al., 2007; Liao et al., 2014) or cross-correlation (e.g., Vieweg et al., 2016; Vogt et al., 2010) of natural tracer data. Here, we obtained transient GW transit-times directly from stream discharge values (Q) through a power-law relationship developed from salt tracer-test results. This approach yielded better results, mainly because of the fact that at the site natural EC stream signals were strongly dampened in the observation wells, limiting the use of signal analysis methods for the EC data. Additionally, Nixdorf and Trauth (2018) had argued that for using EC time-series to calculate riparian transit-times, EC variations and their propagation into the subsurface are a necessary but not sufficient condition to constrain travel times. Additionally, it is also required EC variations to be higher relative to stream discharge variations for successful application of EC-based transit-times analysis. At our site relative EC variations are smaller than relative Q variations and the transmission of EC signals to the observation wells may be affected by other processes that we could not account for.

Conceptually, the τ_Q relationship is based on the dependency of infiltrating stream water transit-time on stream discharge, and the assumption that at Q≈0 no water infiltrates into the subsurface, and therefore, infiltration time goes to infinity. The method is straight-forward and conceptually simple, with the

advantage of providing transient riparian transit-times for infiltrating water from a losing stream section directly from an independent and usually continuously measured hydrologic variable, while requiring only small field calibrations on the fitted function from tracer-tests. Computed theoretical transit-times based on $k_{DO\text{-}eff}$ allowed us to evaluate that the power-law seemed a good approximation of transit-times. We compared our relation with median transit-times from Munz et al. (2017), who simulated flow and heat transport at a losing reach a few meters downstream from our site. The relationship between their modelled median transit-times and stream discharge could also be well represented by a power-law of the same type ($\tau_Q=0.268Q^{-4.6}$, $R^2=0.87$). The greater exponent in their study compared to ours seems to indicate that transit-times to their observations wells were more sensitive to stream discharge than at our observation well, in agreement with the greater distance of our well to the stream in comparison to their observation wells.

At our site, GW transit-times decreased with increasing stream discharge as it has also been reported based on modelling of a larger losing stream by Sharma et al. (2012). In their work, simulated V_{GW} around 10 m/d were observed during discharge events, whereas at our site V_{GW} was higher, but in the range of values acquired from tracer-tests. High values could be related to high conductive layers at the site leading to shorter transit-times, or along tree roots in the riparian zone (Bargués Tobella et al., 2014). Nevertheless, very short theoretical transit-times and thus very high V_{GW} during or just after flood events ($Q>10$ m³/s) are likely related to a shortening of the dominant flowpaths (e.g. by infiltration from the upper soil due to inundation of the riparian zone caused by flooding) rather than really meaningful V_{GW}.

DO simulations using constant transit-times also yielded high NSE values, but we believe this is an oversimplification of the system since we observed differences in transit-times during tracer-tests. Nevertheless, time-invariant transit-time has been used to simulate losing stream systems as demonstrated in Diem et al. (2013) through EC-signal deconvolution.

2.4.2 DO consumption rates

Temperature dependency of DO consumption rates

Temperature was found to be the main driver of k_{DO} variations in our system, explaining about 90% of its variations. Our $k_{DO\text{-}T_{GW}}$ relation was close to the one derived by Vieweg et al. (2016) (*Vieweg et al., 2016*: $k=0.34\exp^{(0.2Temp)}$). Our rather higher intercept values may be explained by the consumption of organic matter that is either stored in the aquifer or imported from other sources than stream water (Diem et al., 2013). This could be related to additional autochthonous DOC mobilized during high flow events (Kirchner,

2009; Sawyer et al., 2014), or DOC produced within the unsaturated and root zones (Adeleke et al., 2017; Baker and Vervier, 2004). Since respiration sensitivity to temperature can differ in time and space, it is usually described by the activation energy (Ea) from the Arrhenius equation. Ea values of 1.03 and 0.9 eV respectively for Fs and Fd were lower than values found by Vieweg et al. (2016) for an instream gravel bar few meters upstream of our site (1.47 eV in average). However, also our values confirm that aerobic respiration at the site is more sensitive to temperature than reported for other sites (in average, 0.62eV, Yvon-Durocher et al., 2012).

Due to high temporal dynamics of T_{GW} near losing stream sections, a constant ambient groundwater temperature at some distance from the stream is not a good estimate of the effective temperature relevant for DO consumption, which can lead to incorrect estimations of solute turnover due to erroneous temperature-dependent rates (Munz et al., 2017). The $k_{DO\text{-}T_{eff}}$ based on T_{eff} was 2-3 higher than the empirical $k_{DO\text{-}T_{GW}}$ in summer (Fig.6), leading to underestimations of DO consumption rates if only T_{GW} is considered. Our results are in line with results from an analysis by Song *et al.* (2018) on temperature effects of high-frequency flow variations on thermal regimes and biogeochemical processes within hyporheic zones. Using a numerical model, they showed that temperature contribution to DOC consumption was greater within the fluctuation zone, where infiltrating cold water and its long-term storage led to locally reduced reaction rates (0.1C decrease resulted on about 1% decrease in reaction rates).

Hydrologic and temperature controls on DO consumption rates

Our findings elucidate strong effects of temperature on reactions in the biogeochemical system of the near-stream riparian zone, which seem to be more pronounced than the effects of variable groundwater transit-times. In contrast to Sharma et al. (2012), who attributed short temporal changes in reaction patterns mainly to changes in transit-times, we found that discharge events did not significantly alter subsurface transit-times, but instead changed groundwater temperatures in the near-stream aquifer with effects on DO consumption rates. Furthermore our field data suggest that even for short transit-times, water temperature is not constant along a flowpath from the infiltration point at the streambed to the observation well, but instead changes according to stream dynamics and water temperature differences between the stream and ambient groundwater. This is different from Diem et al. (2013) who assumed constant water temperature along stream-groundwater flowpaths for all hydrologic conditions ranging from discharge events to baseflow conditions. In contrast, Vieweg et al. (2016) used T_{eff} for computing temperature dependent DO respiration rates by shifting T_{SW} time-series based on EC-derived transit-times. However, one expects that heat presents different transit-times from other solutes due to different transport mechanisms.

Accounting for temperature effects on reactive turnover in riparian groundwater requires a thorough characterization of temperature patterns. Methods as the use of heat as a tracer and direct temperature measurements in the streambed (Munz et al., 2011; Schmidt et al., 2007) alongside measurements in GW can assist in obtaining an improved understanding of local heat exchange patterns and drivers.

2.4.3 DA_{DO} controls and variations

DA_{DO} variations and biogeochemical implications

Computed DA_{DO} exhibited small ranges ($0.5 \leq DA_{DO} \leq 6$), mainly regulated by temperature fluctuations and the resulting variations of k_{DO}. The DA_{DO} values varied within a hydrological year, indicating shifts in the limiting factors of the reactive system (Fig.8). During 61% of the observation period $DA_{DO}>1$ prevailed. The limitation in DO supply ($DA_{DO}>1$) can mainly be attributed to high effective temperatures and rapid DO depletion. In the winter, however, DA_{DO} was slightly below one for both points, the system becomes reaction limited, and although transit-times do not dramatically changed compared to summer low flow conditions smaller DO mass is consumed and longer periods of oxic conditions tend to prevail.

Zarnetske et al. (2012) showed how a riparian system can be classified as either net-nitrifying ($DA_{DO}<1$) or net-denitrifying ($DA_{DO}>1$). In the winter the site shows potential for net-nitrification, whereas in summer favourable conditions for denitrification dominate ($DA_{DO}\approx4$). As denitrification is known to occur at the site (Trauth et al., 2018), we can estimate the NO_3^- fractions remaining after a water parcel has travelled through the riparian zone directly from DA_{DO} values taking into account that sufficient DOC is available for the process after DO depletion (see section 4.2.1). This was done using an S-shaped curve (Fig.S5, supplementary material), which approximates the relation between DA_{DO} values and NO_3^- fractional changes according to model results presented by Zarnetske et al. (2012), established in a site with similar conditions to ours. Using this relation to derive denitrification rates from DA_{DO} values yields to values between 0.2-0.6 mg-N/L/day for DA_{DO} of 3-6 respectively, within the range previously assessed by Trauth et al. (2018) using NO_3^- isotopic data for the site (0.2-1.0 mg-N/L/day, 15%-75% NO_3^- removal fractions, respectively).

However, depending on how DA_{DO} was computed (e.g., constant or varying transit-times), an underestimation of net-potentials might arise. For instance, the NO_3^- fraction removal potential is only 40% if constant transit-time are considered ($DA_{DO}\approx3$) in contrast to 70% under varying transit-times ($DA_{DO}\approx6$). Although temperature is the main control of the system, assumptions of constant GW transit-times could lead to a misrepresentation of actual net-potentials. Even larger removal fraction underestimations would occur if DO consumption rates were solely based on T_{GW} instead of T_{eff} (reduction from 70% to 30% of

NO_3^- fraction removal potential). This is not surprising given that other studies observed the importance of temperature and transit-times on NO_3^- removal potential (Boano et al., 2010; Shuai et al., 2017; Zarnetske et al., 2011), but our findings highlight the dominant control of temperature variations in regulating riparian net-turnover potentials for redox sensitive species compared to effects of changes in transit-times. Nevertheless, it is important to highlight that, even if the bulk conditions indicate aerobic conditions (DO>2 mg/l), anoxic microsites (DA_{DO}<1) may develop at pore scale within the sediments, and denitrification may occur at substantial rates (Briggs et al., 2015; Song et al., 2018).

Baseflow and discharge events DA_{DO}

For both Fs and Fd, we observed only small drops of DA_{DO} during events in comparison to baseflow, indicating a tendency towards less transport limited conditions, Fig.9. As suggested by Vieweg et al. (2016), extra influx of DO during events might lower DA_{DO}. However, two other mechanisms could also be responsible for this decline during events. Firstly, transit-times are somewhat shorter during events, resulting in less time for DO consumption, thus bringing the balance of the system towards less transport limited. Secondly, most of the discharge events (~60%) result in a drop of T_{SW} and T_{GW} contrary to conditions immediately prior to the event, leading to smaller consumption rates, and reinforcing the decrease of DA_{DO}. This minor impact of events on the system regime goes alongside findings of Trauth et al. (2018) who argued that discharge events at the site had a subordinate effect for the riparian reactive potential for DO and consequently NO_3^-. However, their findings were still not fully conclusive in terms of short temporal effects of events, which becomes more apparent from our high-frequency DA_{DO}.

Discharge events do not have the potential to completely shift the biogeochemical regime of the system, mainly because of the superimposed seasonal temperature controls and the observed weak effect of discharge events on transit-times. Nevertheless, discharge events especially during summer might carry greater DOC to be stored in the streambed that affect DO consumption rates at a later point and stimulate other biogeochemical processes, such as denitrification. Further high spatio-temporal analyses of DOC concentrations in the streambed and in different points of the aquifer alongside temperature, as well as numerical modelling of reactive transport in the riparian zone can help to better depict associated time-lags and transport/reaction processes influenced by stream dynamics at different time scales.

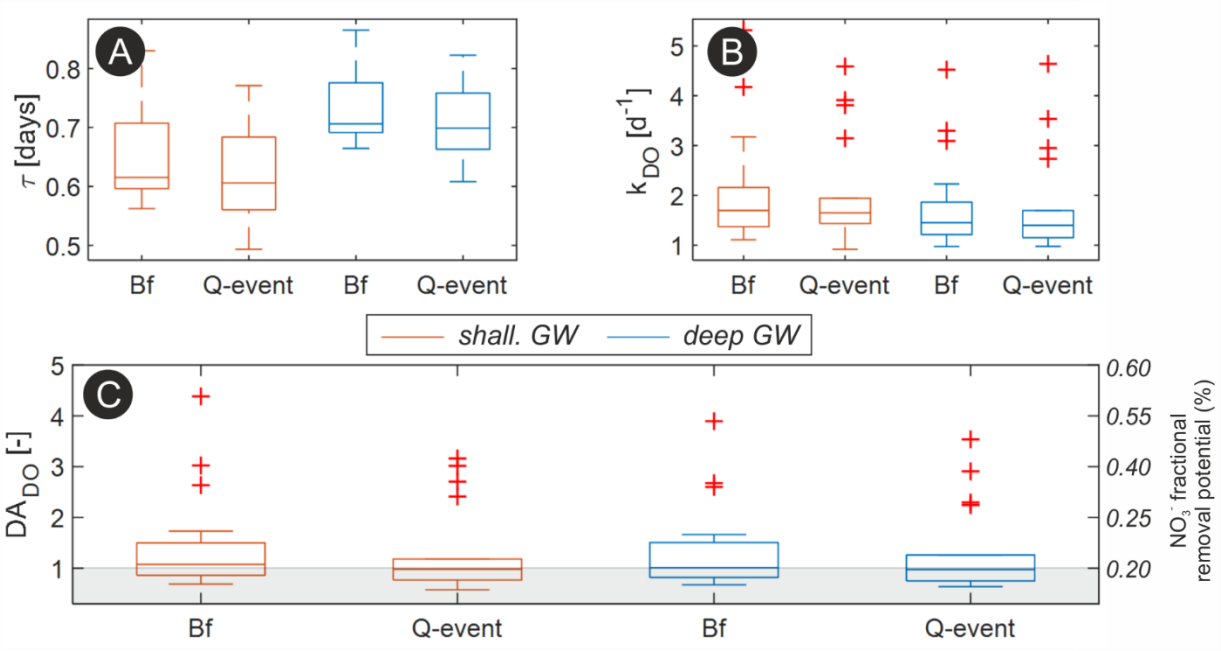

Fig.9: a) *mean GW transit-times;* ***b)*** *mean temperature corrected DO consumption rates;* ***c)*** *resulting mean* DA_{DO} *considering* τ_Q *and* $k_{DO\text{-}eff}$*, and computed* NO_3^- *fraction removal potential for shallow (orange) and deep (blue) groundwater distinctly for baseflow (Bf) and discharge events (Q). Shaded area in* (**c**) *represents* $DA_{DO}<1$ *(oxic conditions, net-nitrifying potential).* NO_3^- *fractional removal potentials in* (**c**) *are based on Zarnetske et al. (2012).*

2.5 Conclusions

In this study we combined GW tracer-tests with high-frequency data to assess spatio-temporal variations of GW transit-times (τ) and DO consumption rates (k_{DO}) of a riparian aquifer under different hydrological conditions. To evaluate the effect of different transit-times on k_{DO}, we simulated riparian DO concentrations under different transit-times scenarios based on acquired field data. Results demonstrate that τ and k_{DO} at our near stream GW system are influenced by seasonal and short-term stream stage and temperature fluctuations. Our data showed that transit-times decreased with increased stream stage, whereas k_{DO} was strongly temperature dependent. The variability of k_{DO} was higher than variability of τ, with coefficient of variations equal to 0.51/0.65 and 0.18/0.14, respectively for shallow/deep riparian aquifer.

At our losing stream reach, estimates of τ directly from stream discharge and of k_{DO} from an effective temperature appropriately captured spatio-temporal variations in DO concentrations. We observe that seasonal temperature fluctuations and short-term stream water temperature oscillations conveyed to GW pose stronger controls on the reactive regime of the near stream riparian aquifer and DO variabilities than transport processes (transit-times). Neglecting temperature influences of infiltrating SW can result in an underestimation of riparian DO consumption rates by factor 2-3. Due to strong temperature control, the DO

simulations were equally sound regardless of whether variant or constant transit-times were assumed. Nevertheless, computed removal potentials of redox sensitive compounds like NO_3^- based on DA_{DO} were significantly different for variant and constant transit-times, 70% and 40%, respectively, highlighting the importance of considering variant transit-times rather than oversimplified constant values.

Finally, the estimated riparian DA_{DO} values indicated distinct seasonal-shifts in the reactive regime of the system (from transport to reaction limited conditions in summer and winter, respectively), that superimpose effects of short-term event fluctuations, which can move the system to slightly less transport limited conditions (shorter transit-times and smaller consumption rates). During short-term events the variations of transit-times led by discharge fluctuations on DO consumption were smaller than changes in consumption rates caused by changes in water temperature, which were generally lower than before the event. Under climate-change scenarios (e.g., greater/longer discharge events, higher temperatures), these effects might increase, and impact the reactive state of the system (oxic-anoxic conditions) ultimately leading to short-term transitions of the redox-state of the near stream aquifer.

2.6 Acknowledgments

This research is part of the ENIGMA-ITN project that has received funding from the European Union's Horizon 2020 research and innovation programme under the Marie Sklodowska-Curie Grant Agreement No 722028.

2.7 Data availability statement

The data that support the findings of this study are openly available in HydroShare at https://doi.org/10.4211/hs.51b3933c4987427e94e51e3339237755.

2.8 References

Abbott BW, Baranov V, Mendoza-Lera C, Nikolakopoulou M, Harjung A, Kolbe T, Balasubramanian MN, Vaessen TN, Ciocca F, Campeau A, et al. 2016. Using multi-tracer inference to move beyond single-catchment ecohydrology. Earth-Science Reviews 160: 19–42 DOI: 10.1016/J.EARSCIREV.2016.06.014

Atkins P, de Paula J. 2011. Physical Chemistry for the Life Sciences. Oxford University Press: Oxford.

Bernard-Jannin L, Sun X, Teissier S, Sauvage S. 2017. Spatio-temporal analysis of factors controlling nitrate dynamics and potential denitrification hot spots and hot moments in groundwater of an alluvial floodplain. Ecological Engineering 103: 372–384 DOI: 10.1016/j.ecoleng.2015.12.031

Boano F, Demaria A, Revelli R, Ridolfi L. 2010. Biogeochemical zonation due to intrameander hyporheic flow. Water Resources Research 46 (2): 1–13 DOI: 10.1029/2008WR007583

Brunner P, Therrien R, Renard P, Simmons CT, Franssen HJH. 2017. Advances in understanding river-groundwater interactions. Reviews of Geophysics 55 (3): 818–854 DOI: 10.1002/2017RG000556

Cirpka OA, Fienen MN, Hofer M, Hoehn E, Tessarini A, Kipfer R, Kitanidis PK. 2007. Analyzing bank filtration by deconvoluting time series of electric conductivity. Ground Water 45 (3): 318–328 DOI: 10.1111/j.1745-6584.2006.00293.x

Diem S, Cirpka OA, Schirmer M. 2013. Modeling the dynamics of oxygen consumption upon riverbank filtration by a stochastic-convective approach. Journal of Hydrology 505: 352–363 DOI: 10.1016/j.jhydrol.2013.10.015

Fleckenstein JH, Krause S, Hannah DM, Boano F. 2010. Groundwater-surface water interactions: New methods and models to improve understanding of processes and dynamics. Advances in Water Resources 33 (11): 1291–1295 DOI: 10.1016/j.advwatres.2010.09.011

Fogler HS. 2005. Elements of Chemical Reaction Engineering. Prentice Hall: Boston, Mass.

Greskowiak J, Prommer H, Massmann G, Nützmann G. 2006. Modeling seasonal redox dynamics and the corresponding fate of the pharmaceutical residue phenazone during artificial recharge of groundwater. Environmental Science and Technology 40 (21): 6615–6621 DOI: 10.1021/es052506t

Gustard A, Demuth S. 2009. Manual on Low-flow Estimation and Prediction.

Koestel JK, Moeys J, Jarvis NJ. 2011. Evaluation of nonparametric shape measures for solute breakthrough curves. Vadose Zone 10: 1261–1275

Kolbe T, Dreuzy J De, Abbott BW, Aquilina L, Babey T. 2019. Stratification of reactivity determines nitrate removal in groundwater. 116 (7): 1–6 DOI: 10.1073/pnas.1816892116

Liao Z, Osenbrück K, Cirpka OA. 2014. Non-stationary nonparametric inference of river-to-groundwater travel-time distributions. Journal of Hydrology 519 (PD): 3386–3399 DOI: 10.1016/j.jhydrol.2014.09.084

Mader M, Roberts AM, Porst D, Schmidt C, Trauth N, van Geldern R, Barth JAC. 2018. River recharge versus O2 supply from the unsaturated zone in shallow riparian groundwater: A case study from the Selke River (Germany). Science of the Total Environment 634: 374–381 DOI: 10.1016/j.scitotenv.2018.03.230

Munz M, Oswald SE, Schmidt C. 2011. Sand box experiments to evaluate the influence of subsurface temperature probe design on temperature based water flux calculation. Hydrology and Earth System Sciences 15 (11): 3495–3510 DOI: 10.5194/hess-15-3495-2011

Munz M, Oswald SE, Schmidt C. 2016. Analysis of riverbed temperatures to determine the geometry of subsurface water flow around in-stream geomorphological structures. Journal of Hydrology 539: 74–87 DOI: 10.1016/j.jhydrol.2016.05.012

Munz M, Oswald SE, Schmidt C. 2017. Coupled Long-Term Simulation of Reach-Scale Water and Heat Fluxes Across the River-Groundwater Interface for Retrieving Hyporheic Residence Times and Temperature Dynamics. Water Resources Research 53 (11): 8900–8924 DOI: 10.1002/2017WR020667

Nixdorf E, Trauth N. 2018. Evaluating the reliability of time series analysis to estimate variable riparian travel times by numerical groundwater modelling. Hydrological Processes (August 2016): 408–420 DOI: 10.1002/hyp.11428

Nogueira, G. (2020). Low land Selke Stream and adjacent riparian aquifer high-frequency dataset, central Germany, HydroShare, https://doi.org/10.4211/hs.51b3933c4987427e94e51e3339237755.

Oldham C, Beer J, Blodau C, Fleckenstein J, Jones L, Neumann C, Peiffer S. 2019. Controls on iron(II) fluxes into waterways impacted by acid mine drainage: A DamkÖhler analysis of groundwater seepage and iron kinetics. Water Research 153: 11–20 DOI: 10.1016/j.watres.2018.12.024

Oldham CE, Farrow DE, Peiffer S. 2013. A generalized Damköhler number for classifying material processing in hydrological systems. Hydrology and Earth System Sciences 17 (3): 1133–1148 DOI: 10.5194/hess-17-1133-2013

Pietikäinen J, Pettersson M, Bååth E. 2005. Comparison of temperature effects on soil respiration and bacterial and fungal growth rates. FEMS Microbiology Ecology 52 (1): 49–58 DOI: 10.1016/j.femsec.2004.10.002

Pinay G, Peiffer S, Dreuzy J De, Krause S, Hannah DM, Fleckenstein JH, Sebilo M, Bishop K, Hubert-moy L. 2015. Upscaling Nitrogen Removal Capacity from Local Hotspots to Low Stream Orders ' Drainage Basins. Ecosystems 18 (6): 1101–1120 DOI: 10.1007/s10021-015-9878-5

Ranalli AJ, Macalady DL. 2010. The importance of the riparian zone and in-stream processes in nitrate attenuation in undisturbed and agricultural watersheds - A review of the scientific literature. Journal of Hydrology 389 (3–4): 406–415 DOI: 10.1016/j.jhydrol.2010.05.045

Schilling OS, Gerber C, Partington DJ, Purtschert R, Brennwald MS, Kipfer R, Hunkeler D, Brunner P. 2017. Advancing Physically-Based Flow Simulations of Alluvial Systems Through Atmospheric Noble Gases and the Novel37Ar Tracer Method. Water Resources Research 53 (12): 10465–10490 DOI: 10.1002/2017WR020754

Schmidt C, Conant B, Bayer-Raich M, Schirmer M. 2007. Evaluation and field-scale application of an analytical method to quantify groundwater discharge using mapped streambed temperatures. Journal of Hydrology 347 (3–4): 292–307 DOI: 10.1016/j.jhydrol.2007.08.022

Sharma L, Greskowiak J, Ray C, Eckert P, Prommer H. 2012. Elucidating temperature effects on seasonal variations of biogeochemical turnover rates during riverbank filtration. Journal of Hydrology 428–429: 104–115 DOI: 10.1016/j.jhydrol.2012.01.028

Shuai P, Cardenas MB, Knappett PSK, Bennett PC, Neilson BT. 2017. Denitrification in the banks of fluctuating rivers: The effects of river stage amplitude, sediment hydraulic conductivity and dispersivity, and ambient groundwater flow. Water Resources Research 53 (9): 7951–7967 DOI: 10.1002/2017WR020610

Song X, Chen X, Stegen J, Hammond G, Song HS, Dai H, Graham E, Zachara JM. 2018. Drought Conditions Maximize the Impact of High-Frequency Flow Variations on Thermal Regimes and Biogeochemical Function in the Hyporheic Zone. Water Resources Research 54 (10): 7361–7382 DOI: 10.1029/2018WR022586

Tobella AB, Reese H, Almaw A, Bayala J, Malmer A, Laudon H, Ilstedt U. 2014. The effect of trees on preferential flow and soil infiltrability in an agroforestry parkland in semiarid Burkina Faso. Water Resources Research: 1–17 DOI: 10.1002/2013WR014333.Received

Trauth N, Fleckenstein JH. 2017. Single discharge events increase reactive efficiency of the hyporheic zone. Water Resources Research: 613–615 DOI: 10.1029/2008WR006912.M

Trauth N, Schmidt C, Fleckenstein JH. 2016. Stream discharge events increase the reactive efficiency of the hyporheic zone of an in-stream gravel bar. 18: 18304

Trauth N, Schmidt C, Vieweg M, Maier U, Fleckenstein JH. 2014. Hyporheic transport and biogeochemical reactions in pool-riffle systems under varying ambient groundwater flow conditions. Journal of Geophysical Research: Biogeosciences 119 (5): 910–928 DOI: 10.1002/2013JG002586

Vieweg M, Kurz MJ, Trauth N, Fleckenstein JH, Musolff A, Schmidt C. 2016. Estimatingtime-variable aerobic respiration in the streambed by combining electrical conductivity and dissolved oxygen time series. Journal of Geophysical Research: Biogeosciences 121: 2199–2215 DOI: 10.1002/2016JG003345

Vogt T, Hoehn E, Schneider P, Freund A, Schirmer M, Cirpka OA. 2010. Fluctuations of electrical conductivity as a natural tracer for bank filtration in a losing stream. Advances in Water Resources 33 (11): 1296–1308 DOI: 10.1016/j.advwatres.2010.02.007

Weiss RF. 1970. The solubility of nitrogen, oxygen and argon in water and seawater. Deep-Sea Research and Oceanographic Abstracts 17 (4): 721–735 DOI: 10.1016/0011-7471(70)90037-9

Winter TC, Harvey JW, Lehn Franke O, Alley WM. 1998. Ground Water and Surface Water: A Single Resource. U.S. Geological Survey: Denver, Colorado.

Wollschläger U, Attinger S, Borchardt D, Brauns M, Cuntz M, Dietrich P, Fleckenstein JH, Friese K, Friesen J, Harpke A, et al. 2017. The Bode hydrological observatory: a platform for integrated, interdisciplinary hydro-ecological research within the TERENO Harz/Central German Lowland Observatory. Environmental Earth Sciences 76 (1) DOI: 10.1007/s12665-016-6327-5

Yvon-Durocher G, Caffrey JM, Cescatti A, Dossena M, Giorgio P Del, Gasol JM, Montoya JM, Pumpanen J, Staehr PA, Trimmer M, et al. 2012. Reconciling the temperature dependence of respiration across timescales and ecosystem types. Nature 487 (7408): 472–476 DOI: 10.1038/nature11205

Zarnetske JP, Haggerty R, Wondzell SM, Baker MA. 2011. Dynamics of nitrate production and removal as a function of residence time in the hyporheic zone. Journal of Geophysical Research: Biogeosciences 116 (1): 1–12 DOI: 10.1029/2010JG001356

Zarnetske JP, Haggerty R, Wondzell SM, Bokil VA, González-Pinzón R. 2012. Coupled transport and reaction kinetics control the nitrate source-sink function of hyporheic zones. Water Resources Research 48 (11): 1–15 DOI: 10.1029/2012WR011894

Supplementary Material

Seasonal and short-term controls of riparian oxygen dynamics and the implications for redox processes

G. E. H. Nogueira, C.Schmidt, N. Trauth, J. H Fleckenstein*

Fig. S1: *stream stage-discharge relation obtained from monthly discharge measurements, and used for acquiring high-frequency stream discharge values directly from stream stage readings. The fitted polynomial equation and its correlation coefficient are presented in the plot.*

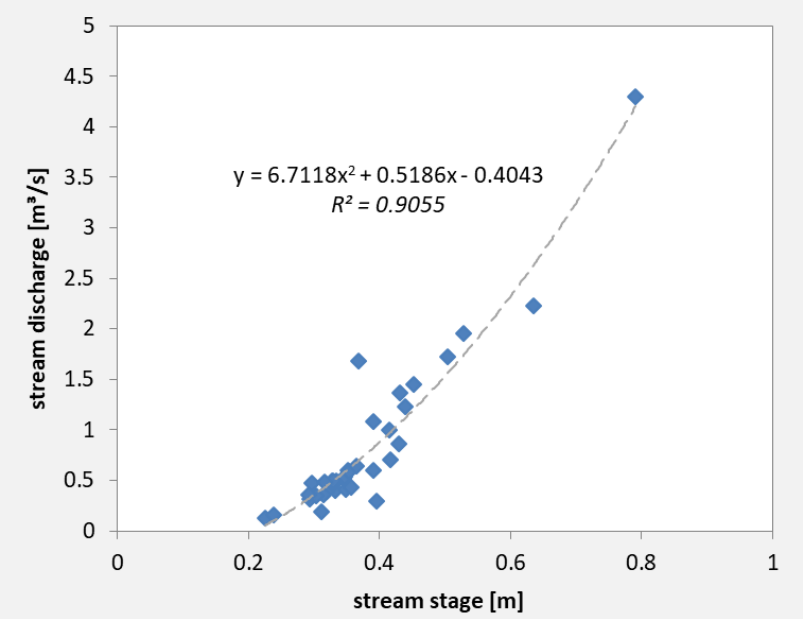

Fig. S2a: *detail of increase of DO concentrations in SW and GW under different discharge events at the end of 2018.* ***S1b:*** *detail of water temperature changes under different discharge events at the end of 2018.* ***S1c:*** *detail of hydraulic heads in the stream and in the well FS-02, alongside their water level differences (Δh), and the transit-times based on stream discharge values (τ_Q). Even though simple, the relation of transit-times and stream discharge translate small variations of water level between SW and GW to shorter transit-times due to resulting higher gradients at these moments.*

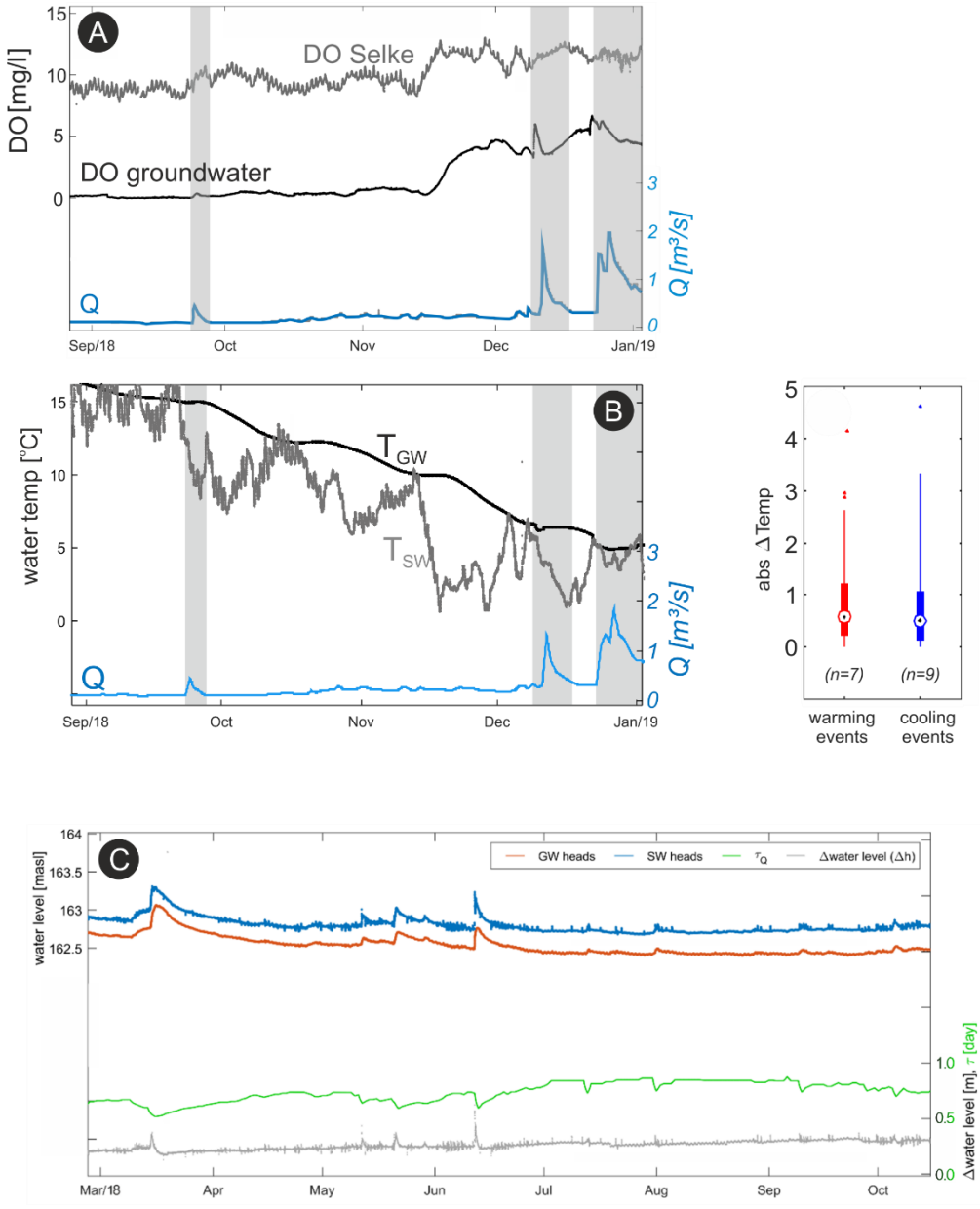

Fig. S3: *detail of normalized and detrended-normalized EC time-series from stream and from groundwater (GW) used for EC cross-correlation transit-times calculation (τ_{EC}). The period highlighted in grey indicates time when a GW tracer-test was carried out disturbing the GW EC values. The weak correlation between stream and GW EC can be depicted from the plot.*

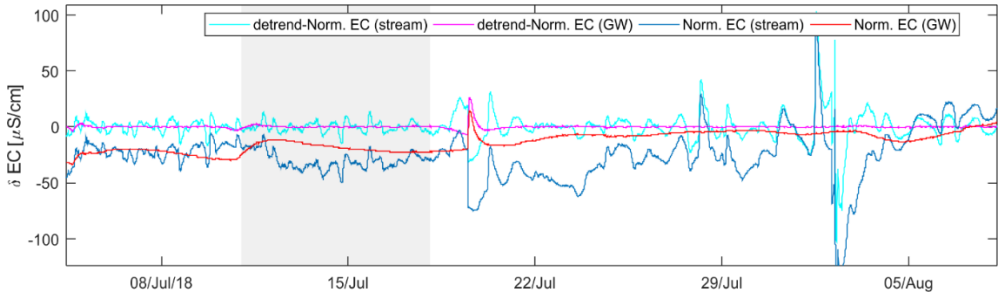

Fig. S4: *temporal distribution of optimized effective temperatures (T_{eff}) for shallow **(a)** and deep **(b)** groundwater considering varying and constant transit-times alongside stream Q. Grey areas indicate times when T_{eff} was equal to T_{GW} under constant transit-times simulation (opt-τ).*

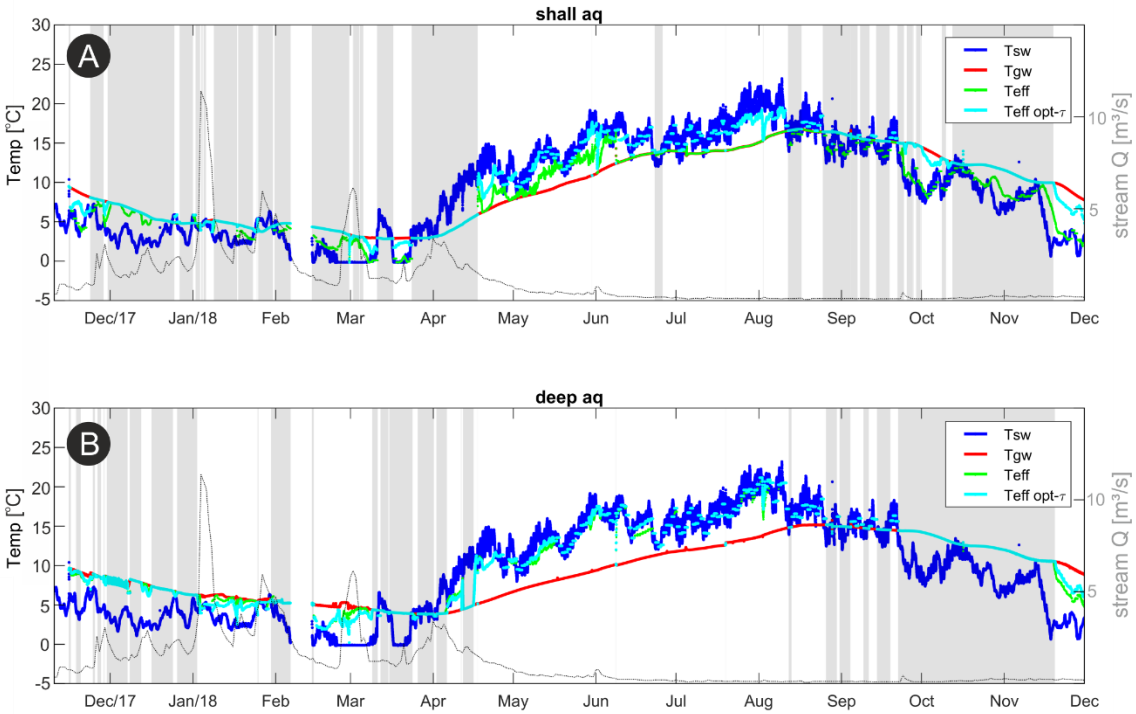

Fig. S5: *Relation between DA_{DO} and fractional NO_3^- removal (F_{NO_3}). The plotted values are from modelling work of Zarnetske et al. (2012). The fitted S-shaped equation and its correlation with their data are presented in the plot. The grey shaded area represents $DA_{DO}<1$, aerobic conditions (net-nitrifying potential). The equation is used to compute potential NO_3^- removal fractions through denitrification, given that sufficient DOC is present at the system.*

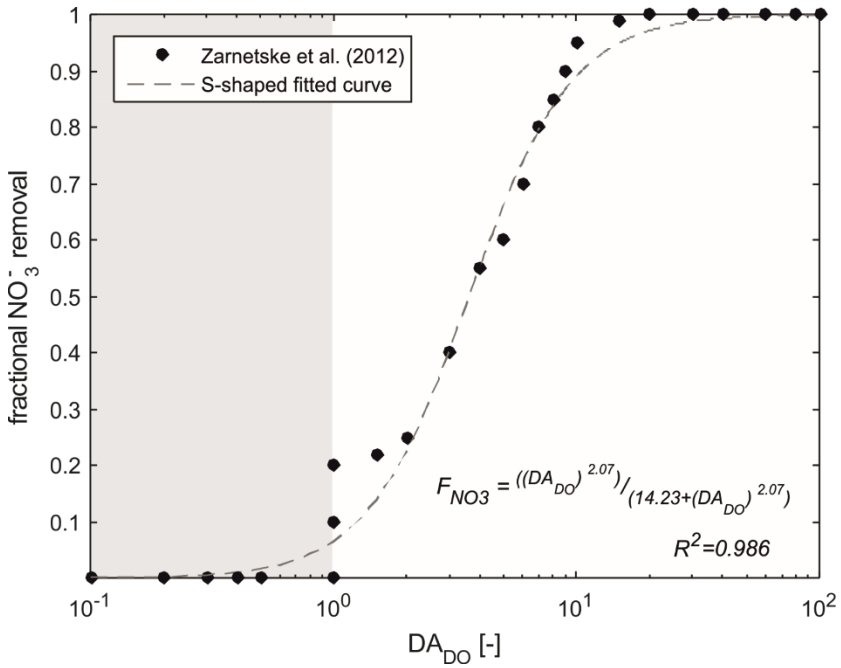

Chapter three

Transit-time and temperature control the spatial patterns of aerobic respiration and denitrification in the riparian zone

G. E. H. Nogueira[(1)], C. Schmidt[(1,2)], P. Brunner[(3)], D. Graeber[(2)], J. H. Fleckenstein[(1,4)]

(1) Department of Hydrogeology, Helmholtz Centre for Environmental Research-UFZ, Leipzig, Germany.

(2) Department of Aquatic Ecosystem Analysis, Helmholtz Centre for Environmental Research-UFZ, Magdeburg, Germany

(3) Centre of Hydrogeology and Geothermics (CHYN), Neuchâtel, Switzerland

(5) Bayreuth Centre of Ecology and Environmental Research, University of Bayreuth, Bayreuth, Germany

Published in Water Resources Research 57, 2021, DOI: 10.1029/2021WR030117

Abstract

During the flow of stream water from losing reaches through aquifer sediments, aerobic and anaerobic respiration (denitrification) can deplete dissolved oxygen and nitrate (NO_3^-), impacting water quality in the floodplain and downstream gaining reaches. Such processes, which vary in time with short and long-term changes in stream flow and temperature, need to be assessed at the stream corridor scale to fully capture their effects on net turnover, but this has rarely been done. To address this gap, we combine a fully-integrated 3D transient numerical flow model with temperature-dependent reactive transport along advective subsurface flow paths to assess aerobic and anaerobic respiration dynamics at the stream corridor scale in a predominantly losing stream. Our results suggest that given carbon availability (as an electron donor), complete NO_3^- removal occurred further away from the stream after complete oxygen depletion and was relatively insensitive to variations in temperature and transit-times. Conversely, transit-times and oxygen concentrations constrained nitrate removal along short hyporheic flow paths. Even under limited carbon availability and low-temperatures, NO_3^- removal fractions (R_{NO3}) will be greater at locations further from the stream than along shorter hyporheic flow paths (R_{NO3}=0.4 and R_{NO3}=0.1, respectively). With increasing temperature, the relative effects of stream flow and solute concentrations on biogeochemical turnover and the redox zonation around the stream decreased. The study highlights the importance of seasonal variations of stream flow and temperature for water quality at the stream-corridor scale. It also provides an adaptive framework to assess and quantify reach-scale biogeochemical turnover around dynamic streams.

Plain Language Summary

Nitrate pollution is a widespread problem in many catchments with intense agricultural activities. Denitrification is a redox process that removes nitrate from the aquatic system via its transformation to nitrogen gas. Denitrification is difficult to assess at larger scales since it depends on multiple factors, such as solute concentrations, temperature variations, and also the time that water resides in the subsurface, where reactions can take place. To evaluate how these factors can influence denitrification, we employed a coupled modeling approach representing the riparian zone of a 4th order stream in central Germany. We found that temperature variations strongly regulate the process and that during the winter the aerobic (oxygen rich) zone around the stream expands, which further inhibits denitrification in the near stream groundwater. However, even in the winter denitrification occurs, but at larger distance from the stream where oxygen has been depleted sufficiently. With increasing temperature, the influence of other factors on denitrification and on the redox zonation around the stream decreases. Coupled numerical models can provide further insights into the occurrence and interrelations of the multiple processes controlling water quality patterns in river corridors.

Key Points

- Fully-integrated 3D transient flow model coupled to a temperature-dependent flow path-reaction model to assess riparian solutes turnover
- Turnover mainly controlled by high temperature in summer; in winter solute concentrations and transit-times variations become more important
- Assessments of riparian turnover restricted to near stream areas might overlook processes affecting overall downstream water quality

Keywords: biogeochemical turnover, temperature, denitrification, floodplain, hydrogeosphere, transient simulation

3.1 Introduction

The exchange zone between streams and their surrounding riparian groundwater is essential for solute turnover and the ecological regulation of stream ecosystems (Bernhardt et al., 2017; Mayer et al., 2006; Vidon and Hill, 2006). In this zone, water and solute exchange strongly vary in time and space, being influenced by different factors, such as stream stage, aquifer properties, and hydraulic connectivity (Kurz et al., 2017; Munz et al., 2017; Ocampo et al., 2006; Oldham et al., 2013), leading to significant changes in water quality. Both short-term and seasonal stream stage fluctuations modify water and solute exchange fluxes and affect short- and long term biogeochemical responses in the riparian zone (Boutt and Fleming, 2009; Chen et al., 2020; Diem et al., 2013; Jensen et al., 2017; Liang et al., 2018; Liao et al., 2014; Liu et al., 2019; Sawyer et al., 2014).

Several studies have illustrated the importance of aerobic respiration (AR) and the resulting dissolved oxygen (DO) depletion in regulating the redox conditions of near stream environments, affecting the turnover of redox-sensitive compounds like nitrate (NO_3^-) via denitrification (DN) (Boano et al., 2010; Briggs et al., 2015; Frei et al., 2012; Rivett et al., 2008; Sharma et al., 2012; Shuai et al., 2017; Trauth et al., 2014; Zarnetske et al., 2011). DO consumption and the subsequent redox reactions are jointly governed by hydrologic dynamics (e.g., changes in water transit-times) and the reaction rates that are temperature dependent, both of which are subject to short-term (event scale) and long-term (seasonal scale) fluctuations. A rising stream stage will increase the hydraulic gradients between the stream and local groundwater (GW),

increasing stream water (SW) infiltration fluxes and reducing the transit-times of infiltrating water parcels. Additionally, short-term and seasonal temperature variations affect biogeochemical reaction rates, leading to different chemical patterns depending on the combination of transport and reaction processes at a given time and location (Nogueira et al., 2021; Song et al., 2018; Vieweg et al., 2016), which are often not explicitly considered in studies on SW-GW interactions.

In predominantly losing stream reaches, which are becoming increasingly common as a result of global change (Jasechko et al., 2021), and not just in semi-arid and arid regions, the exchange zone expands beyond the streambed and hyporheic zone into the floodplain (Brunner et al., 2009; Irvine et al., 2012; Treese et al., 2009). For these conditions, it is not sufficient to only look at the streambed and banks, and instead, an evaluation of the entire stream corridor and its complex 3D geometry is needed for an adequate assessment of DO dynamics and the resulting turnover potentials, e.g. for NO_3^-, at the system-scale. As high-resolution monitoring campaigns are hard to implement at the scale of entire stream corridors, numerical models are good tools to achieve such understanding (Brunner et al., 2017).

Most modelling studies to date, however, have either looked at idealised 2D systems primarily focusing on the streambed and stream banks or have focused on individual aspects, such as temperature effects on turnover or effects of short-term dynamics (e.g., discharge events) and not jointly at event- and seasonal times scales. For instance, Zheng et al. (2016) used an idealised 2D model to illustrate the effects of temperature variations on DN below a bed form-induced hyporheic zone using steady-state flow fields. Trauth and Fleckenstein (2017) used a 3D coupled flow and reactive transport numerical model to assess impacts of discharge events on hyporheic turnover assuming constant water temperature, revealing how short-term events increased the hyporheic reactive efficiency (solute consumption as a fraction of influx) of an in-stream gravel bar. While Song et al. (2018) jointly assessed the impacts of high-frequency stream stage and thermal variations on biogeochemical reactions in the hyporheic zone, their 2D model was spatially limited to the stream banks, disregarding turnover processes in the floodplain. These and other recent studies (Shuai et al., 2017; Singh et al., 2020) have illustrated the effects of hydrologic conditions and landscape controls on water flux and reactive solute transport in streambeds and banks. To our knowledge, the combined effects of flow (transit-times) and temperature on riparian DO concentrations and subsequent DN across event and seasonal time scales have not yet been fully addressed in an integrated modelling study of an entire stream corridor.

This study aims to overcome some of these deficiencies by jointly assessing the hydraulic (flow variations, transit times) and thermal controls (temperature) of the biogeochemical reactions of DO and DN in a riparian aquifer that receives DO-rich SW infiltration from a predominantly losing stream reach. We employ an adaptive method to couple biogeochemical processes to a fully-coupled and spatially-distributed

numerical flow model based on a particle tracking analysis using a Lagrangian flow path-reaction approach to evaluate DO and nitrate turnover at the stream corridor scale, using a simplified representation of key reactions along subsurface flow paths. With that, we address the following three major research questions: (1) How do variable hydrological and biogeochemical conditions affect the biogeochemical turnover of stream borne DO and NO_3^- in the riparian aquifer? (2) How do stream flow and water temperature variations shape the aerobic zone (DO_z) around the stream? and (3) How do riparian DO dynamics affect DN patterns of NO_3^- in the riparian corridor for different transient streamflow and temperature scenarios? We conducted an explorative modelling informed by data from the well-instrumented Selke site as a test-case to address these questions. Combining advective particle tracking with the simulation of biogeochemical reactions along the identified flow paths using field temperature and solute concentration data to constrain the model, we assess the impacts of stream flow and temperature variations on patterns of DO and NO_3^- concentrations in the riparian aquifer.

3.2 Materials and Methods

In this section, following the study site presentation, we describe how we developed and calibrated the numerical flow model. We then present how we implemented the reactive transport of specific solutes (coupling hydrology and biogeochemistry). We also describe how we evaluated the results and which scenarios we considered for analyses.

3.2.1 Field Site and data collection

The study site is located within the Selke River catchment, a 4th-order perennial stream (low discharge=0.23 m^3s^{-1}, mean discharge=1.51 m^3s^{-1}, and high discharge=15.6 m^3s^{-1}), central Germany, around the high-intensity test-site of a TERENO observatory (Wollschläger et al., 2017). The studied stream reach (appx. 900 m) is characterised by net losing conditions, with downstream discharge generally 25% smaller than discharge upstream (Schmadel et al., 2016). The local aquifer consists of up to 8 m-thick fluvial sediments, with grain sizes ranging from medium sands to coarse gravels, underlain by less permeable clay-silt deposits forming the bottom of the alluvial aquifer.

Hydraulic heads and stream stage were continuously measured for a period of one year (2017-2018) with a temporal resolution of 10 min. The hydraulic heads were measured in 20 piezometers distributed in the area. Head measurements in nested piezometers varied equally for shallow and deep wells (Nixdorf and Trauth, 2018). Stream stage values were converted to stream discharge (Q), available through a stream stage-discharge relationship based on biweekly manual discharge measurements. Also, a total of seven high-resolution well-to-well tracer-tests were carried out near the stream covering a whole hydrological

year (2017-2018) and providing extra information about flow dynamics and main groundwater flow directions. Detailed descriptions of these experiments can be found in Nogueira et al. (2021). DO concentrations were monitored by self-contained loggers (HOBO Dissolved Oxygen Data Logger) in both stream and in groundwater with a 10-min interval. Further hydrochemical data (such as DOC and NO_3^- concentrations) was assessed through manual sampling in a biweekly interval, which were analysed in the laboratory following standard procedures for stream water and groundwater sampling and analyses as described in Trauth et al. (2018).

3.2.2 Integrated surface-subsurface flow and mass transport

The fully integrated surface-subsurface flow and transport model HydroGeoSphere (*https://www.aquanty.com/hydrogeosphere*) was used to simulate water and solute exchange across the SW-GW continuum. HydroGeoSphere (HGS) is a finite element code that solves Richards' equation for variably saturated flow in three-dimensions (Brunner and Simmons, 2012; Simmons et al., 2020). Overland flow is solved numerically using the diffusion-wave equation together with Manning's equation. For coupling the surface and groundwater environments, we selected the dual node approach to approximate the continuity of pressure heads. The approach assumes that exchange fluxes among the domains depend on the hydraulic head gradient across a coupling interface, the vertical saturated hydraulic conductivity, and a coupling length value (Therrien et al., 2010). The coupling length represents the thickness of the interface between the two domains, which enforces near-continuity between the surface and subsurface, minimising the influence of the first-order coupling coefficient while preserving the underlying physics-based nature of the model (Ebel et al., 2009). Details on the governing flow and transport equations for HGS can be found in Therrien et al. (2010).

Flow and mass transport model setup

The extent of the model domain is approximately 900 m x 770 m x 10 m (width, length, and thickness, Figure 1). An unstructured 2D triangular mesh of finite elements was generated with the Algomesh software (2018 HydroAlgorithmics Pty Ltd) for the top of the domain, representing the land and streambed surfaces. The topography of the domain was interpolated from an aerial survey covering the floodplain and the streambed, with a horizontal resolution of 1 m and a vertical accuracy of 0.1 m. The triangular element sizes varied from a maximum of up to 40 m in the floodplain to about 2.0 m in the streambed and were further refined to about 1.0 m around observation wells in the near-stream riparian zone (FS wells, Figure 1). The 2D mesh is replicated in the vertical direction to form a 3D mesh consisting of quadrilateral elements in 15 layers, with thicknesses varying from 0.1 m in the top layers to 2.0 m in the bottom layer of the model (~152 masl). The depth of the lower boundary of the domain was set according to the less permeable clay-

silt deposits that form the bottom of the alluvial aquifer (around 7-8 m below the surface). A total of 136,682 elements and 74,955 nodes comprise the model domain.

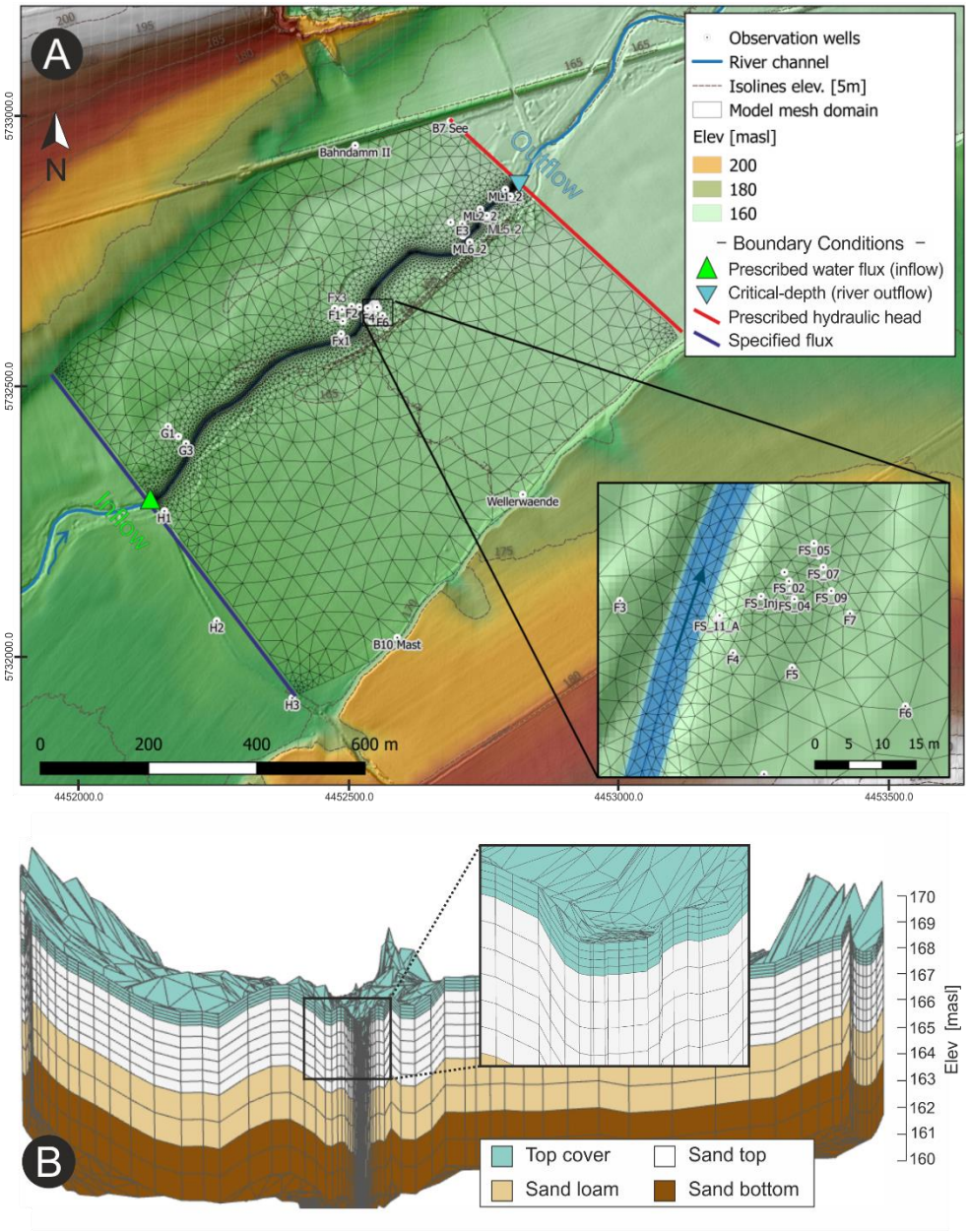

Figure 1: a) Mesh of the model domain and applied BC's; the inset plot shows the region where well-to-well tracer-tests were performed; **b)** lateral view of model domain coloured with hydrogeological units, and detail to layer thickness on the top cells near the stream.

We divided the aquifer into four units with anisotropic hydraulic conductivity (initial Kx=Ky and Kxy/Kz=10, Table 1) based on field data and previously conducted geological surveys of the area (Figure S1, supplementary material). Van Genuchten parameters (Genuchten, 1980) were assigned based on literature values typical for medium sand. For the two bottom units, these values are merely a characteristic of the material as they remain fully-saturated throughout the year. We defined two different set of surface properties (Manning's roughness coefficients, *x* and *y* friction values, and rill storage heights) for the streambed and floodplain. In contrast, different coupling lengths were assigned for individual reaches of the streambed, and another for the floodplain areas. This guarantees a more flexible parameterisation in terms of exchange fluxes between SW-GW for the different stream reaches and the floodplain during model calibration.

Table 1 – *Flow and transport parameters for HGS model*

Parameter	**Symbol**	**Initial values**	**Final values (calibrated)**
Surface (streambed / floodplain)			
Friction streambed (roughness, x=y) (m $s^{-1/3}$)[a]	F_r	0.04	--
Friction floodplain (roughness, x=y) (m $s^{-1/3}$)[a]	F_f	0.30	--
Coupling length stream (range) (m)	l_s	0.1-10	0.1-15
Coupling length floodplain (m)	l_e	0.1	8
Rill storage height (both areas) (m)[a]	r	$1.0x10^{-4}$	--
Porous media (for each zone/material)			
Top cover – Porosity ([-])	n	0.2	0.29
Hydraulic conductivity (m s^{-1})	K_x; K_y; K_z	$1.0x10^{-3}$; $1.0x10^{-3}$; $1.0x10^{-4}$	$7.9x10^{-4}$; $1.5x10^{-3}$; $4.3x10^{-4}$
Long; Trans; Vert. Dispersivity (m)	α_L; α_T; α_V	1.0; 1.0; 1.0	8.3; 1.2; 0.08
Residual saturation; α; β ([-]; m^{-1};[-])[a]	θ_s; α; β	0.1; 8.0; 2.0	--
Sand top – Porosity ([-])	n	0.2	0.28
Hydraulic conductivity (m s^{-1})	K_x; K_y; K_z	$1.0x\ 10^{-3}$; $1.0x10^{-3}$; $1.0x10^{-4}$	$7.5x10^{-3}$; $6.5x10^{-3}$; $2.2x10^{-4}$
Long; Trans; Vert. Dispersivity (m)	α_L; α_T; α_V	1.0; 1.0; 1.0	0.6; 0.26; 0.15
Residual saturation; α; β ([-]; m^{-1};[-])[a]	θ_s; α; β	0.045;14.0; 2.0	--
Sandy loam – Porosity ([-])	n	0.2	0.26
Hydraulic conductivity (m s^{-1})	K_x; K_y; K_z	$7.0x10^{-4}$; $7.0x10^{-4}$; $7.0x10^{-5}$	$7.2x10^{-3}$; $6.0x10^{-4}$; $4.9x10^{-5}$
Long; Trans; Vert. Dispersivity (m)	α_L; α_T; α_V	1.0; 1.0; 1.0	1.2; 1.5; 0.18

Residual saturation; α; β ([-]; m^{-1};[-])[a]	θ_s; α; β	0.06; 14.0; 2.0	--
Sand bottom – Porosity ([-])	n	0.2	0.31
Hydraulic conductivity (m s^{-1})	K_x; K_y; K_z	$1.0x10^{-3}$; $1.0x10^{-3}$; $1.0x10^{-4}$	$1.1x10^{-2}$; $3.5x10^{-3}$; $3.3\ x10^{-4}$
Long; Trans; Vert. Dispersivity (m)	α_L; α_T; α_V	1.0; 1.0; 1.0	1.0; 0.98; 0.07
Residual saturation; α; β ([-]; m^{-1};[-])[a]	θ_s; α; β	0.045; 14.0; 2.0	--

a = not included in the calibration

Initial conditions for the hydraulic heads for the whole domain were achieved by a first model run (appx. one year in simulation time) using constant, average values for hydraulic heads, precipitation and stream discharge (i.e., *quasi-steady state* conditions). Next, a transient run with daily updated boundary conditions (BCs) from Nov 2016 to Nov 2017 (i.e., *spin-up period*) was performed to achieve realistic hydraulic heads throughout the domain. Following the *spin-up period*, the model was run with a similar time-step updating of the BCs, when automated calibration and model validation were carried out based on observed GW heads, stream discharge, and tracer breakthrough curves (BTCs) as described in the model calibration section below (see also Figure S2, supplementary material). For this last period, two other BCs were implemented to represent the performed tracer-tests. The following BCs were applied in the model:

- Prescribed hydraulic head (Dirichlet) applied at the northern side of the model domain representing hydraulic heads at the downstream side of the study area. Based on measured hydraulic heads in the wider area of the floodplain (observation wells outside the study site), the heads were linearly interpolated and extended to the entire domain lateral. The heads were updated according to observed field values, representing the GW seasonal fluctuations.
- Prescribed water flux (Neumann) applied at the Southside (upstream) of the model domain representing GW inflow. A constant GW flow boundary was selected instead of prescribed hydraulic heads because early model runs showed that this option resulted in a better representation of water table fluctuations near the boundary. An initial value of 2.5 m^3d^{-1} was chosen based on the outflow from the *quasi-steady state* model run. A constant optimised value of 2.6 m^3d^{-1} was found through automated calibration.
- No flow boundary applied at the East and West sides, as well as on the bottom of the model domain.
- Prescribed water flux (Neumann) applied at the stream inlet (at a daily time resolution), according to discharge measurements at the nearby gauging station at Meisdorf (51°41’29.1’’N, 11°17’02.2’’E).
- Critical-depth boundary applied at the stream outlet, forcing the water depth at the boundary to be equal to the critical depth, which is calculated by the model together with stream discharge.

- Groundwater recharge applied at the surface of the domain. Daily precipitation was measured at the nearby climate station Aschersleben (51°43’33.6’’N, 11°30’39.6’’E) of the German weather service. Evapotranspiration (ET) rates were computed through HYDRUS-1D and used to calculate the percentage from rainfall applied in the model surface as GW recharge. No further internal calculations of ET were done in the model. For the simulation period, recharge values varied over time, ranging from 28% to 36% of total precipitation (mean= 33%, std.d= 4.8%). However, since deviations from the mean value were not large, a constant value of 33% of observed daily precipitation value was applied as GW recharge in each time-step.
- For the tracer tests, the additional BC were implemented accordingly: 1) Prescribed water flux (Neumann) describing the injected water volume for the injection periods. 2) Specified mass flux representing the total added tracer mass. This guarantees correct representation of both flow and mass changes in the system (Table S1, supplementary material). Both BCs were applied to a single subsurface node 2.5 m below the surface at FS-inj (Figure 1) representing the nearest depth in which tracer was injected.

Flow and mass transport calibration and evaluation

The model was calibrated against the observed GW heads and stream discharge (covering 130 days of high-frequency measurements), as well as measured tracer concentrations from 8 of the 18 BTCs recorded in different aquifer depths during tracer-tests (Nogueira et al., 2021). Hydraulic and transport parameters were calibrated simultaneously against all available observation types using a weighted multivariate objective function through PEST (Doherty, 2018, 1994). A simultaneous calibration of all model parameters against all observation types has the potential to provide a better model parametrisation as discussed in detail in Doherty (2003), Moore et al. (2010), and Schilling et al. (2019). We utilised a Tikhonov regularisation to address parameter nonuniqueness, introducing a penalty to the objective function if parameters under calibration diverge excessively from preferred values (prior knowledge of field parameters). Different observation types were weighted to feature equally in the objective function by using the PEST software suite PWTADJ1 (Doherty and Hunt, 2010), and tracer concentrations were inversely weighted to give higher importance to the tails of BTCs.

We evaluated the model quality using the average water balance error, the mean absolute error (MAE) between observed and simulated heads and tracer concentrations, as well as the Nash Sutcliffe efficiency (NSE) criteria. Model results were visualised with ParaView, Version 5.8.1 (Ahrens et al., 2005), and with TecPlot 360 EX, Version 2019 R1 (Constellation Software, Inc.).

Flow paths and particle tracking analysis

To evaluate the effects of stream stage changes on groundwater transit-times, and subsurface biogeochemical processes in infiltrating SW, we used the transient velocity fields from HGS for an advective particle tracking analysis. Particle transport is based on a second-order Runge-Kutta integration of simulated subsurface velocity fields using the software TecPlot 360 EX. Massless particles were released from each mesh cell at the wetted streambed in every time-step (around 1,800 particles per time-step), being subjected to subsequent changes of the velocity fields until the end of the simulation or until they have left the model domain (either back to the stream or via the subsurface boundary). A continuous release of particles in each time-step assures that they are subjected to transitions in GW velocity fields that are influenced by stream stage variations. The locations, transit-times and velocities of each particle were then extracted in each time-step for the following flow path-reaction simulations.

3.2.3 Flow path reactive transport: coupling hydrology and biogeochemistry

Coupled reactions and reaction rate calculations

Since in HGS it is not yet possible to simulate temperature-dependent reactions, we employed a Lagrangian flow path-reaction model based on the particle tracking results. A similar biogeochemical simulation along individual subsurface flow paths was employed by Frei et al. (2012). Reactions occur in individual sub-sections (i) of each flow path, based on the extracted particle transit-times and locations. The integration time-step between flow path sub-sections was on average 0.1 day (±0.9 day) with larger intervals only towards the end of each flow path, guaranteeing a good spatio-temporal discretisation of the transport problem. We implemented the respective reaction equations in MATLAB® (Figure S3, supplementary material). We focused on the simulation of redox-sensitive biogeochemical processes in the riparian zone, specifically aerobic respiration (AR) and denitrification (DN) of organic matter (DOC) represented by carbohydrate CH_2O, according to the following reaction equations:

$$\text{Aerobic respiration: } CH_2O + O_2 \rightarrow CO_2 + H_2O \quad (1)$$

$$\text{Denitrification: } 5CH_2O + 4NO_3^- + 4H^+ \rightarrow 5CO_2 + 2N_2 + 7H_2O \quad (2)$$

We did not incorporate nitrification into our simulations, specifically the production of nitrate (NO_3^-) from oxidation of Ammonium (NH_4^+), since observed NH_4^+ concentrations are very low at the site (<0.1 mg L^{-1} in stream water and in groundwater) in comparison to NO_3^- concentrations (Trauth et al., 2018). As shown by Zheng et al. (2016), high values of $\log_{10}([NO_3^-]/[NH_4^+])$ ratios (such as 1.3 in stream water at the studied site) would lead to a NO_3^- net removal higher than production; thus we consider nitrification to be negligible

in the simulations. Based on Eq.(1) and Eq.(2), a DOC source can react with dissolved oxygen (DO) and NO_3^-. We assumed that solute transport into the subsurface was purely driven by infiltrating stream water, and that reaction rate coefficients are temperature-dependent. Apart from the first sub-section of each flow path, solute concentrations and reaction rates for a subsequent sub-section are based on results of the preceding sub-section (Figure S3, supplementary material). Reactions were simulated using Monod-kinetics with an inhibition factor (I_{DO}) for DN, hence, significant NO_3^- consumption occurs only if DO concentrations are below 1.0 mgL^{-1} (Widdowson et al., 1988; Zarnetske et al., 2011). With this formulation, denitrification can still occur (however at much lower rates) even if bulk DO concentrations indicate aerobic conditions. Completely disregarding denitrification under aerobic conditions would be an oversimplified assumption, since it can still take place within redox microzones of oxic-saturated sediments (e.g., Briggs et al., 2015; Song et al., 2018). Furthermore, we only analysed fully-saturated flow paths. In this way, we do not have to account for re-oxygenation that could affect the biogeochemical processes (Frei et al., 2012). Moreover, all DOC is assumed to be bioavailable and can be consumed for both AR and DN until its exhaustion following the reaction rate coefficients in each sub-section:

$$k_{AR(t)} = f_T \left[\mu_{max\_AR} \left(\frac{C_{DO(t)}}{K_{DO}+C_{DO(t)}} \right) \left(\frac{C_{DOC(t)}}{K_{DOC}+C_{DOC(t)}} \right) \right] \quad (3)$$

$$k_{DN(t)} = f_T \left[\mu_{max\_DN} \left(\frac{C_{NO3(t)}}{K_{NO3}+C_{NO3(t)}} \right) \left(\frac{C_{DOC(t)}}{K_{DOC}+C_{DOC(t)}} \right) I_{DO(t)} \right] \quad (4)$$

$$I_{DO(t)} = \frac{K_I}{K_I+C_{DO(t)}} \quad (5)$$

where k_{AR} and k_{DN} are the actual reaction rates of DO and NO_3^-, respectively; μmax_{AR} and μmax_{DN} represent maximum reaction rates for AR and DN, respectively; C_{DO}, C_{DOC} and C_{NO3} are the concentrations of DO, DOC and NO_3^-; and K_{DO}, K_{DOC} and K_{NO3} are the half-saturation constants for DO, DOC and NO_3^-, respectively, and K_I is the inhibition coefficient, Table 2. The maximum reaction rate of AR (μmax_{AR} = 0.478 mmol $L^{-1}d^{-1}$ = 15.3 mg $L^{-1}d^{-1}$) was based on field values (Trauth et al., 2014), while maximum reaction rate of DN (μmax_{DN} = 0.086 mmol $L^{-1}d^{-1}$ = 5.3 mg $L^{-1}d^{-1}$), as well the solute half-saturation constants were based on values from the literature (Gu et al., 2007; Trauth et al., 2014; Zarnetske et al., 2011). To account for the temperature dependency of rate coefficients, the temperature factor (f_T) is introduced in Eq.(3) and Eq.(4) according to the expression proposed by O'Connell (1990):

$$f_{T(t)} = exp\left[a + b\, T_{GW(t)} \left(1 - 0.5\, \frac{T_{GW(t)}}{T_{opt}} \right) \right] \quad (6)$$

where a and b are fitting parameters, T_{GW} is the groundwater temperature, and T_{opt} is the optimal temperature for DOC consumption taken as 35°C (Diem et al., 2013; Greskowiak et al., 2006; Kirschbaum, 1995; Sharma et al., 2012). Different from the commonly used Arrhenius equation, we selected this form of rate dependency because it better follows the concept that bulk microbial biomass, and the availability of substrates decrease with increasing temperature and thus, reaction rates tend to decline when temperatures are above an optimal value for microbial activities(Čapek et al., 2019; Carey et al., 2016; PeterJohn, 1991; Pietikäinen et al., 2005; Schipper et al., 2014). We parameterised f_T using combined in-situ measurements of DO and electrical conductivity (EC) from carried out tracer-tests. In-situ apparent AR rate coefficients were computed based on EC transit-times and related to T_{GW} at the time of the experiment (Figure S4, Supplementary material). The same temperature factor was used to compute the actual DN rates (k_{DN}) since it is expected that denitrification follows the same pattern of increasing rates with temperature up to 35-40°C (Boulêtreau et al., 2012; Veraart et al., 2011), whereas rates tend to rapidly decline when temperatures are above this threshold and approach zero when temperature is above 60 °C (PeterJohn, 1991). The a and b estimations (-3.5 and 0.22, respectively) were within the range of literature values, and have been successfully applied in other river bank filtration studies that simulate DO and NO_3^- reactions (Diem et al., 2013; Greskowiak et al., 2006; Henzler et al., 2016; Kirschbaum, 2000; Sharma et al., 2012). Final computed actual AR and DN rates were within the range of literature values (Maag et al., 1997; Matsunaga et al., 1993; Precht et al., 2004) (Figure S4 and Table S2, supplementary material).

Infiltrating SW with a different temperature than that of GW impacts the reaction rate coefficients in the vicinity of the stream (Nogueira et al., 2021; Song et al., 2018). However, short-term temperature variations induced by infiltrating stream water are strongly damped within a few decimetres (e.g. Engelhardt et al., 2013) and we expect that flow path temperatures (i.e., temperature of water along infiltrating flow path) reach T_{GW} after relatively short transit-times (Munz et al., 2017; Rau et al., 2014; Vieweg et al., 2016), especially further away from the stream (Trauth et al., 2018). For the spatial scale of our analysis (tens to hundreds of meters) temperature variations occur predominantly at seasonal time scale. Therefore, to represent the expected water temperature at the floodplain, monthly averaged T_{GW} from piezometers that are also affected by infiltrating stream water to a certain extent were used in Eq.(6), which lies between stream water temperature (strongly varying over the year, 8.5°C±6.0) and the temperature of the end-member groundwater far from the stream (solely influenced by seasonality, 10°C±1.5) (Figure S5, supplementary material). By using monthly averaged groundwater temperatures, the seasonal subsurface temperature variations were well captured. With this approach, simulations of DO concentrations using transit-times derived from the HGS model yielded a NSE=0.82 and R^2=0.91 for a near stream well during the same observation period (Figure S5, supplementary material).

Initial solute concentrations for flow path reactions

Solute concentrations and reaction rates for the first sub-section (i) of each flow path were based on initial solute concentrations (Table 2). There was no other groundwater-borne solute contribution within flow paths; solute transport into the subsurface was purely driven by infiltrating stream water. Locally, SW is saturated in DO prior to infiltration, therefore we assigned a constant initial DO concentration of 0.31 $mmolL^{-1}$ (10 mgL^{-1}) for the first sub-sections of the flow paths. Time series of DOC at a stream gauging station 5 km upstream of the site showed varying concentrations between 10 and 30 mgL^{-1} (Trauth et al., 2014). In the simulations, however, we assumed a constant DOC concentration of 0.66 mmol L^{-1} (20 mgL^{-1}), almost twice the molar mass of DO, to ensure that there is a DOC source available for denitrification after near-complete DO depletion.

For initial NO_3^-, in a first scenario, concentrations were related to stream discharge to represent the patterns of increase in solute concentrations with rising discharge (Dupas et al., 2017; Musolff et al., 2015; Sawyer et al., 2014; Trauth & Fleckenstein, 2017). At our site, field data indicates a nearly linear increase of NO_3^- concentration with discharge (Figure S6, supplementary material). Simulated NO_3^- concentrations using this relation matched well observed NO_3^- concentrations in a groundwater well (NSE=0.53 and R^2=0.75, Figure S6, supplementary material). To further assess the reactive potential of denitrification of the floodplain for elevated NO_3^- concentrations (e.g., coming from soil top or from larger distance groundwater), we ran additional scenarios considering a high constant initial value of 1.0 $mmolL^{-1}$ (62 mgL^{-1}) for NO_3^- concentrations, which also reflects the high NO_3^- concentrations at the groundwater on the site (Trauth et al., 2018). Although mean stream-borne NO_3^- is much lower than groundwater-borne NO_3^-, by imposing the high initial concentrations we can assess where significant NO_3^- turnover occurs regardless of the origin of the source, thus estimating the overall locations of high DN rates within the floodplain. The constant initial solute concentrations may be considered unrealistic regarding the usual relationship between solute concentrations and discharge for most streams, but by doing this the effects of pure changes in hydraulic and thermal conditions can be better evaluated in these scenarios.

Table 2 – *Parameter values used in defining the reaction kinetics.* †

Rate constants (Eq.3 and Eq.4)	*Value*
μmax_{AR}	0.4780 mmol $L^{-1}d^{-1}$
μmax_{DN}	0.0864 mmol $L^{-1}d^{-1}$
Half saturation constants (Eq.3 and Eq.4)	

K_{DO}	0.00625 mmol L^{-1}
K_{DOC}	0.10700 mmol L^{-1}
K_{NO3}	0.03230 mmol L^{-1}
Inhibition coefficient for Denitrification (Eq.5)	
K_I	0.03130 mmol L^{-1}
Temperature factor (f_T) (Eq.3 and Eq.4)	
a	-3.5
b	0.22
T_{opt}	35°C

Initial solutes concentrations for each flow path

Solute	*Initial concentration in mmol L^{-1} (mg L^{-1})*
Dissolved Oxygen (DO)	0.31 (*10.0*)
Organic Matter (DOC)	0.66 (*20.0*)
Nitrate (NO_3^-)	0.08xQ+0.048 (*5xQ+3*)
Nitrate (NO_3^-) – additional scenarios	1.00 (*62.0*)

†*The values in round brackets are the concentrations in mg L^{-1}; Q is the stream discharge.*

To assess the interplay between transit-times and water temperature on the biogeochemical processes, we performed additional simulations with a range of constant temperatures (0.5-25°C) to cover a wider range of climate conditions. So that the results could be evaluated separately for different combination of T_{GW} and Q scenarios.

3.2.4 Aerobic zone delineation and NO_3^- removal fractions

Based on simulated DO concentrations, we delimited the locations in each infiltrating flow path where groundwater DO≤2 mgL^{-1} (i.e., anaerobic conditions). In the following, we computed the convex envelope encompassing those points, which closely defines the aerobic zones (DO_z) around the stream for each simulated time-step by using the *boundary* function in MATLAB®. By doing so, we can assess the changes in the volume of the aerobic zone given the different Q and T_{GW} scenarios.

We quantified nitrate removal fractions (R_{NO3}) by calculating the cumulative amount of NO_3^- removed through denitrification in each flow path sub-section divided by the initial NO_3^- in each flow path:

$$R_{NO3} = \frac{denitrified\ NO3}{initial\ NO3} \quad (7)$$

The fraction ranges between 0 and 1, with larger values representing higher removal fractions, hence higher removal efficiency. A value of 1 represents complete removal of the initial flow path NO_3^-. This allowed us, for instance, to locate the time required to remove 50% of the initial NO_3^- concentration (R_{NO3}=0.5) in each scenario. We further computed the NO_3^- removal fractions on observation wells in the vicinity of the stream to assess how they change in the different scenarios. The results were compared to values calculated

from field data as recently presented by Lutz *et al.* (2020). They computed NO_3^- removal fractions by combining end-member mixing and dual-isotope (analysis of N and O isotopes of NO_3^-) modelling to account for mixing of stream water and groundwater at the riparian wells of the study site.

3.3 Results

3.3.1 Hydrological modelling and validation

Autocalibrated parameter values were within the range of values reported in the literature, Table 1. Horizontal hydraulic conductivity anisotropies (between K_x and K_y) were obtained from the calibration, and ranged between 0.5 and 3.3, decreasing towards the top of the domain. The vertical hydraulic conductivity anisotropy (between K_{xy} and K_z) varied from 2.7 to 31 for the different model hydrogeological units (Figure 1b), and was the highest for the sandy units. Simulated groundwater hydraulic heads had an overall R^2=0.987 and RMSE=0.14 m, with an underestimation of heads towards the end of the simulation period (about 0.2 m on average, Figure 2a), which could affect v_{GW} to a certain extent. Individual R^2 for different wells ranged from 0.36 (near boundaries) to 0.96 (near the stream). NSE values for individual wells ranged from 0.2 to 0.81. Low values predominantly occurred in the downstream part of the domain (wells ML1-2 and ML5-2). Some gaps in groundwater data collection existed, which resulted in periods without high-frequency data due to probes malfunctioning. Simulated stream discharge matched the observed values and their seasonal dynamics (R^2=0.92 and NSE=0.85), Figure 2b.

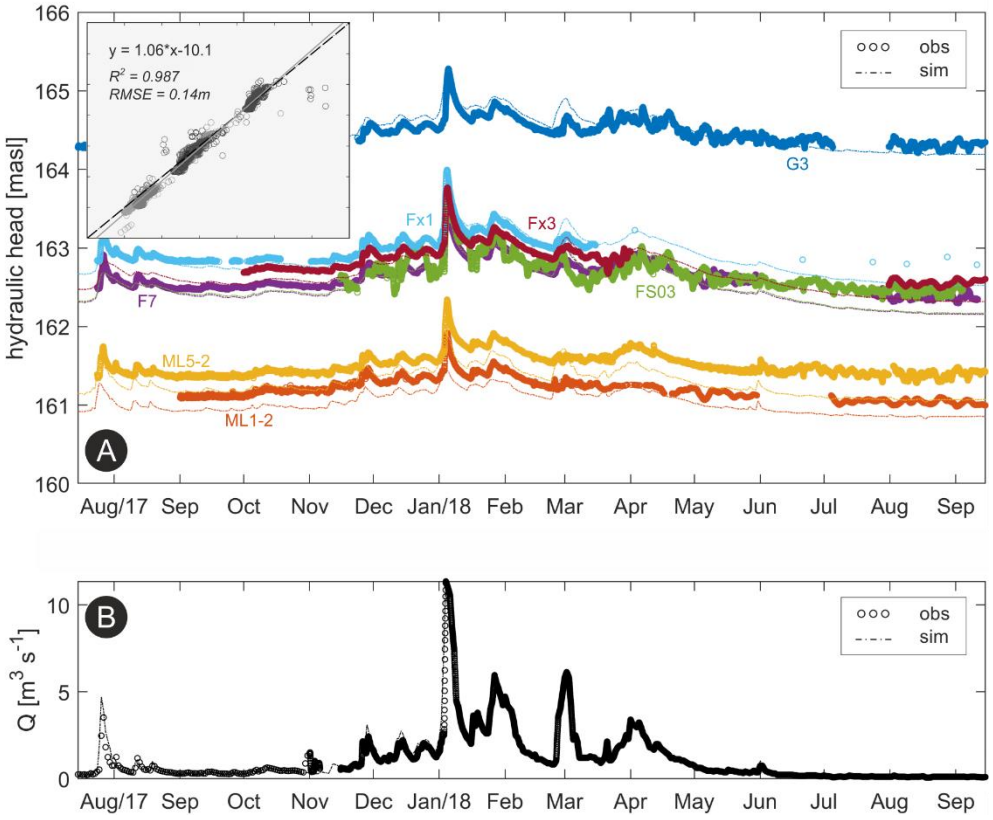

Figure 2: observed (circles) and simulated (dots) groundwater hydraulic heads **(a)** and stream discharge (Q) **(b)** for the simulated period. Different colours in (a) represent different observation wells. The inset plot in (a) shows the overall R^2 and RMSE between simulated and observed values.

Figure 3 presents the simulated tracer peak and mean transit-times from the tracer breakthrough curves. Simulations resulted in an overall R^2=0.51 between observed and simulated tracer peak-times, and R^2=0.74 between observed and simulated tracer mean transit-times. The simulations reasonably captured the general transit-time patterns despite the simplification of the geological media in the numerical model (Figure S7, supplementary material).

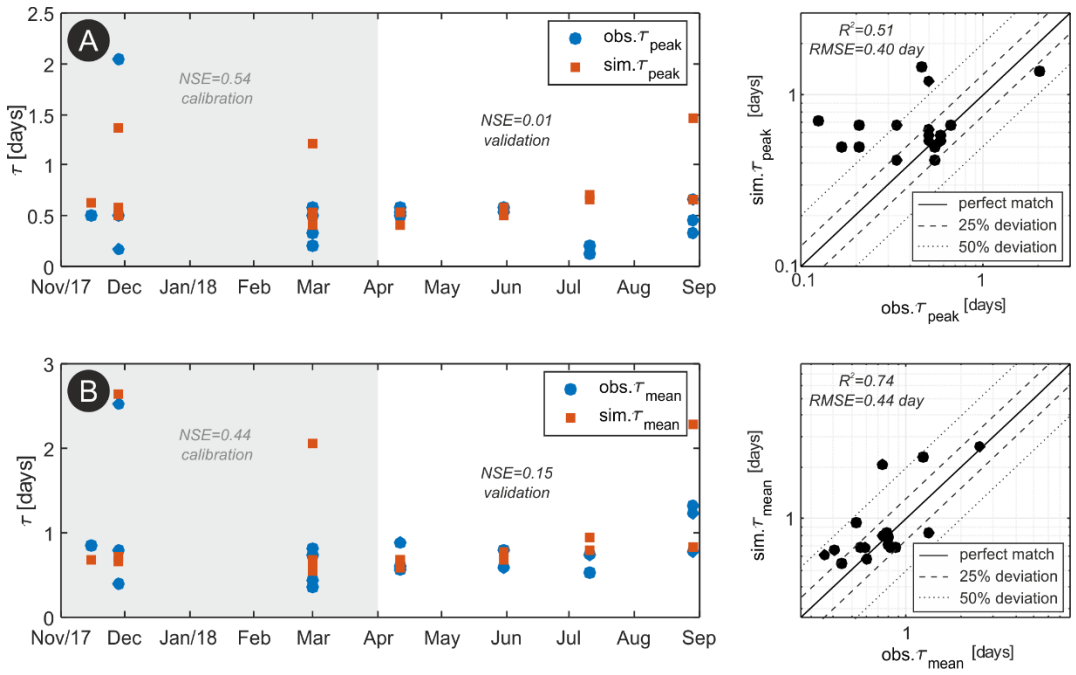

Figure 3: observed (blue circles) and simulated (orange squares) peak times **(a)** and mean transit-times **(b)** from tracer breakthrough curves. The grey shaded areas highlight the model calibration period. The *log-log* scatter plots on the right show the overall R^2 and RMSE between respective observed and simulated values.

3.3.2 Riparian particle tracking, surface water and groundwater exchange fluxes

Overall, groundwater velocity (v_{GW}) increased with increasing stream discharge (due to the increased hydraulic gradient between stream and riparian groundwater), and the calculated age of infiltrating SW particles decreased accordingly. The maximum age calculated for a particle before leaving the domain was 350 days, whereas average particles ages were 77 days and 20 days for low and high Q, respectively, see Figure 4. During high Q the SW infiltration flow paths diverge more from the stream in contrast to low Q, whereas particles reached deeper and further locations in the floodplain in comparison to low Q. Although most of the particles exited the domain through the subsurface downstream boundary, a few of them (around 1%) exfiltrated back into the stream (hyporheic flow paths). These hyporheic particles had transit-times around 2–4 days, and flow path lengths up to 50 m from infiltration to exfiltration point (Figure 5g-i and Figure S8, supplementary material).

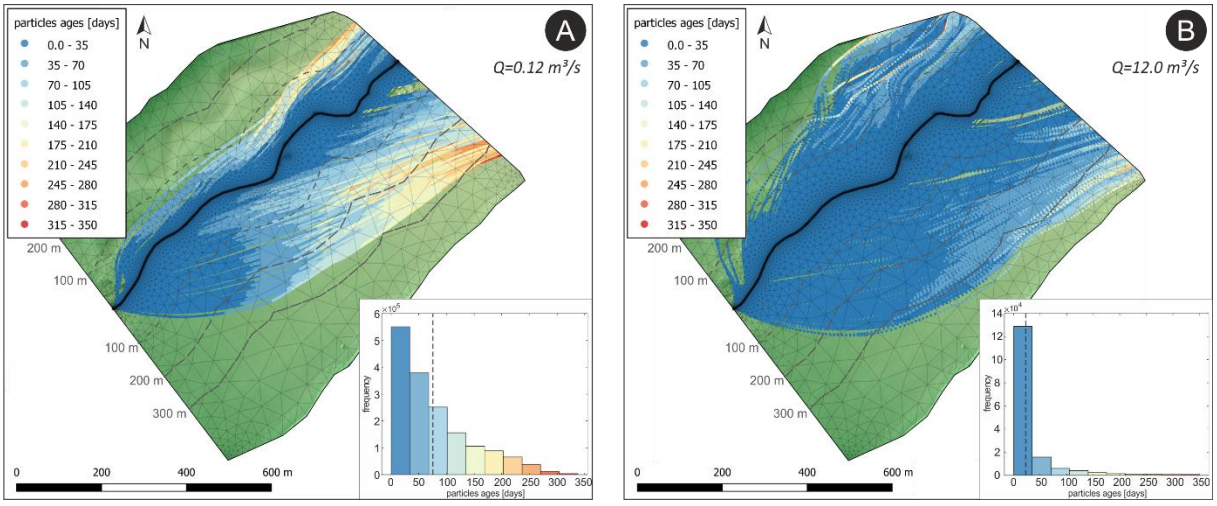

Figure 4: distribution of particles for low Q **(a)** and high Q **(b)** scenarios according to their age since infiltration. Dashed lines on maps highlight equal distances lines from the stream (100 m, 200 m, and 300 m). Dashed vertical lines in the inset histogram indicate the mean values of particle ages in each scenario (77 days and 20 days, respectively). Note: deeper flow paths are not visible in the plots.

Stream discharge variations that alter the hydraulic gradients between the stream and adjacent groundwater also regulated patterns and fluxes of SW-GW exchange. Three scenarios representing very low (Q=0.12 m^3s^{-1}), average (Q=1.44 m^3s^{-1}) and very high (Q=12.0 m^3s^{-1}) stream discharge are shown in Figure 5 and depict the changes in SW-GW exchange fluxes and subsurface flow due to Q variations. The SW-GW exchange flux patterns revealed predominantly losing conditions for the overall reach. Small gaining regions developed only around a deep pool localised downstream of the simulated reach, Figure 5a-c. For the high Q scenario, the lengths of hyporheic flow paths and transit-times were the longest in comparison to lower Q scenarios (Figure 5g-i), which is opposite to what we observed for the losing flow paths leaving the domain at the downstream boundary (histograms in Figure 4). The spatial pattern of SW-GW exchange-flux (i.e., stream gaining and losing sections) and the simulated exchange volumes were consistent with field measurements (Schmadel et al., 2016), and within the range calculated from previous numerical models of subsections of the studied reach (Munz et al., 2017).

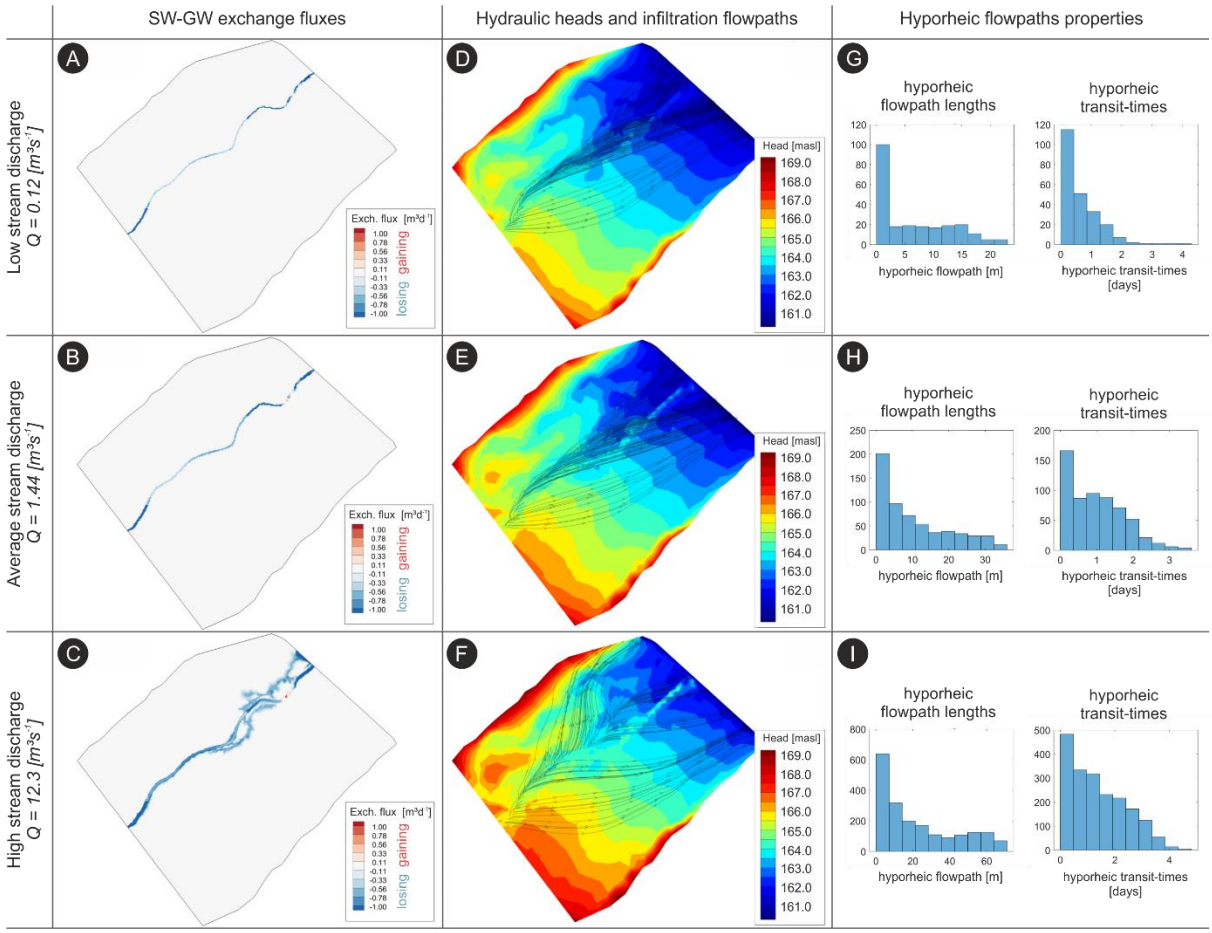

Figure 5: a-c) surface-water/groundwater exchange fluxes; **d-f)** hydraulic heads and subsurface flow paths of streambed particles; **g-i)** total lengths and transit-times of hyporheic flow paths.

3.3.3 Coupled reaction simulations

In this section we focus on the main results of DO and NO_3^- simulations with the flow path-reaction model based on the extracted particles from each time-step of the HGS model. Around 1,800 particles per time-step and their progressive transit through the domain (resulting in around 200,000 sub-sections per flow path) were coupled with the multispecies reaction simulation.

Riparian dissolved oxygen patterns

The simulated extent of the aerobic zone (DO_z), the volume with DO≥2.0 mgL^{-1} around the stream, is a function of the rate of advection of DO from the stream into the subsurface, the geometry of 3D flow field, and the rate of DO consumption (k_{DO}) in the riparian zone. Since infiltrating SW is DO-saturated (constant initial concentration throughout the simulations), DO_z volumes were mainly regulated by variations of k_{DO}

which in turn was a function of temperature (Eq.(6)). Thus, warmer temperatures led to smaller DO_z, Figure 6. The DO_z volumes ranged between $5.0x10^4$–$3.1x10^5$ m^3 in summer and winter (winter DO_z up to 6 times greater than summer DO_z), respectively. High T_{GW} during summer associated with relatively longer infiltration transit-times (low Q), favour DO depletion within a small DO_z around the stream. Contrary, low T_{GW} in winter (which results in low k_{DO}) that is typically associated with shorter transit-times (high Q) led to an increasing extent of the DO_z, Figure 6b.

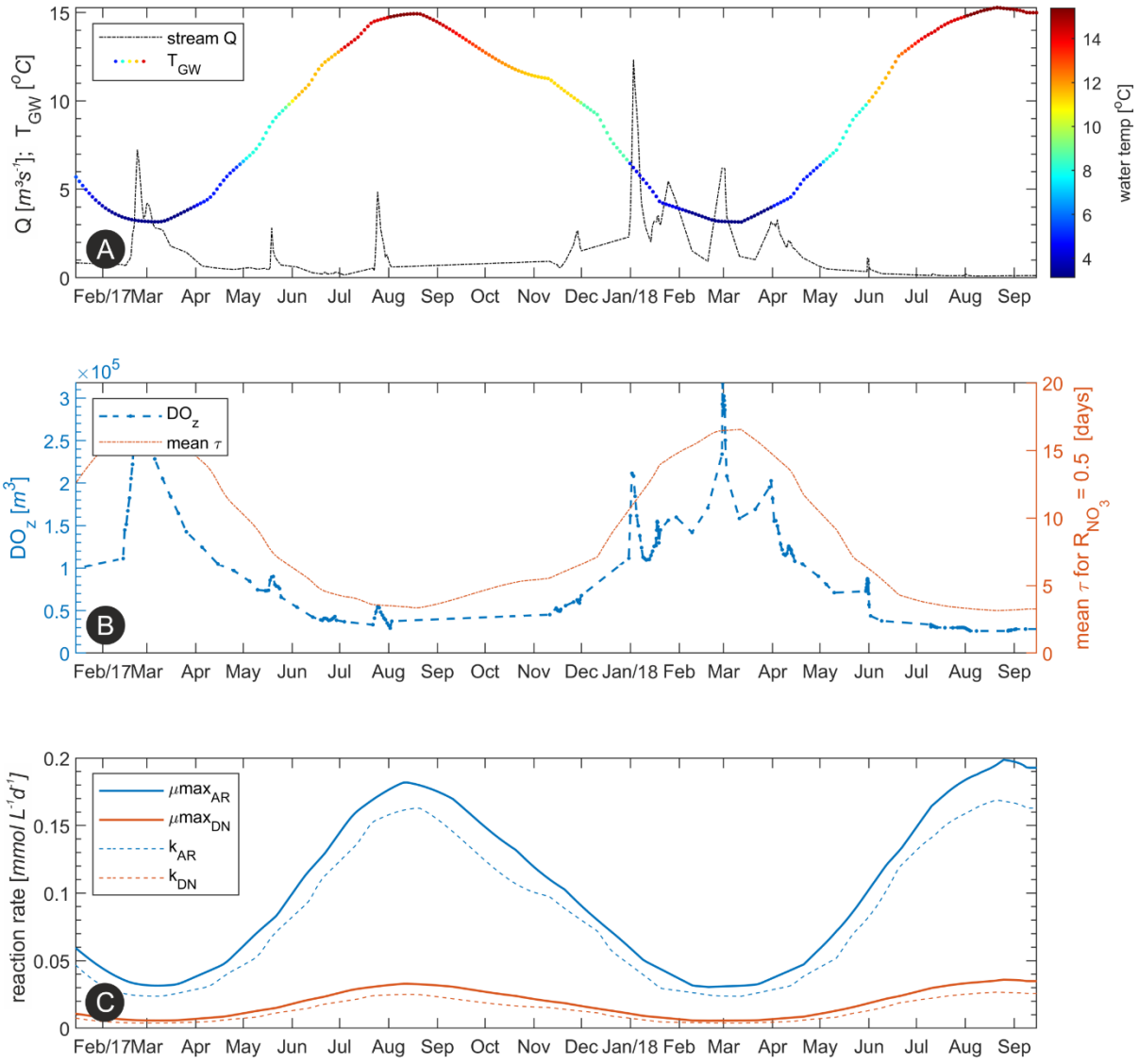

Figure 6: a) stream discharge (Q) and monthly groundwater temperature at the floodplain (T_{GW}); **(b)** computed aerobic zone volume (DO_Z) around the stream alongside mean transit-times for 50% removal of initial flow path nitrate (R_{NO3}=0.5); **(c)** maximum reaction rate coefficients for AR (μmax_{AR}) and DN (μmax_{DN}), and respective resulting rate coefficients (k_{AR}, k_{DN}) for the simulated period.

The effects of stream discharge only (and hence transit-time variations) on DO_z can be illustrated in the constant temperature simulations, Figure 7. For instance, under a constant low T_{GW} condition (T_{GW}=0.5 ºC) the DO_z ranged between 5–15% (2.5x10^5–7.0x10^5 m³) of the total simulated domain for low (Q=0.12 m³ s^{-1}) and high stream discharge (Q=12.0 m³ s^{-1}), respectively, resulting in up to 200% increase in DO_z under high Q. On the other hand, under a constant high T_{GW} scenario (T_{GW}=25.0 ºC) these values were fairly similar for both low and high Q, representing merely 0.2–0.4% (0.7x10^4–2.0x10^4 m³) of the floodplain, respectively, indicating the minor effect of transit-times variations with increasing T_{GW}.

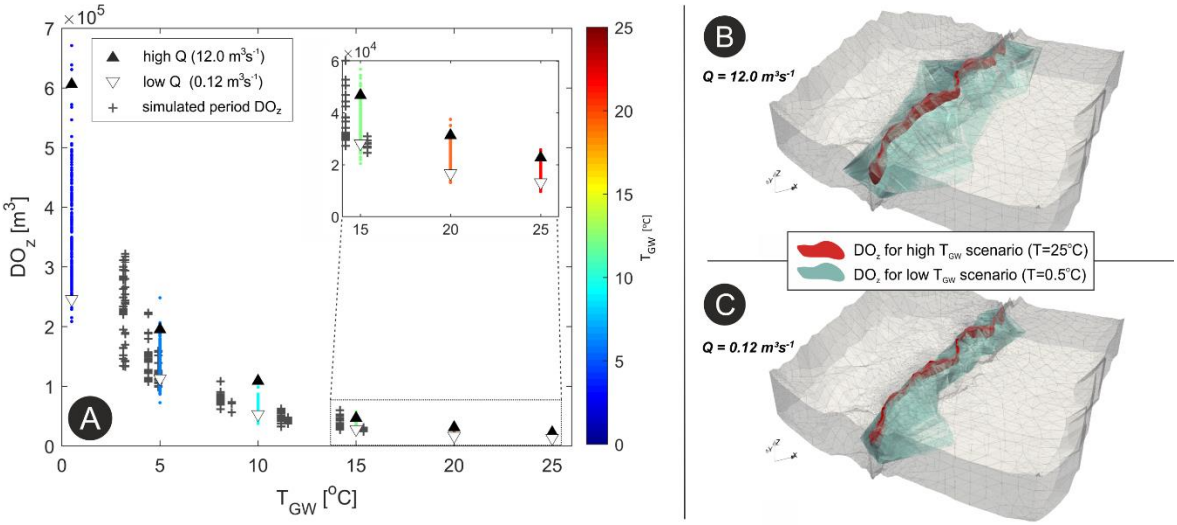

Figure 7: a) DO_z for different constant T_{GW} and varying Q scenarios. The black crosses denote the resulting DO_z volumes for the simulated period; **b-c)** 3D views of DO_z volumes for high **(b)** and for low **(c)** Q scenarios and two different T_{GW} values. Note the vertical exaggeration of the 3D plots (20x).

Denitrification and NO_3^- removal at the near stream riparian wells

Here we compare simulated and observed NO_3^- in terms of NO_3^- removal fractions (R_{NO3}) to simplify the interpretation of the two simulated scenarios (with varying and constant initial NO_3^- concentrations). By doing so, we can also disentangle the effects of varying initial NO_3^- concentrations from the effects of temperature and transit-time variations, and better evaluate the implications of overall elevated NO_3^- concentrations for floodplain reactivity. Results show that simulated R_{NO3} were similar regardless of the initial NO_3^- scenario, and were close to estimated R_{NO3} from observations in wells near the stream (Lutz et al., 2020), Figure 8a. The locations of wells are shown as black-crosses in Figure 9. The R_{NO3} are plotted

against observed T_{GW} to enable a direct comparison to field-observed R_{NO3} values. Our R_{NO3} values were slightly larger for high temperature (R_{NO3}=0.7 vs. R_{NO3}=0.5), but the values show very similar ranges and relations with T_{GW}. R_{NO3} for the scenario with varying NO_3^- were slightly larger since the initial NO_3^- concentrations were generally lower than on the scenario with constant initial NO_3^-. For low T_{GW} conditions, denitrification (DN) is still supressed at these wells due to the presence of DO (DO_z expansion), shifting the location along the flow path where significant DN can take place further downstream. This also explains why resulting R_{NO3} were relatively similar regardless of the initial NO_3^- concentration scenario.

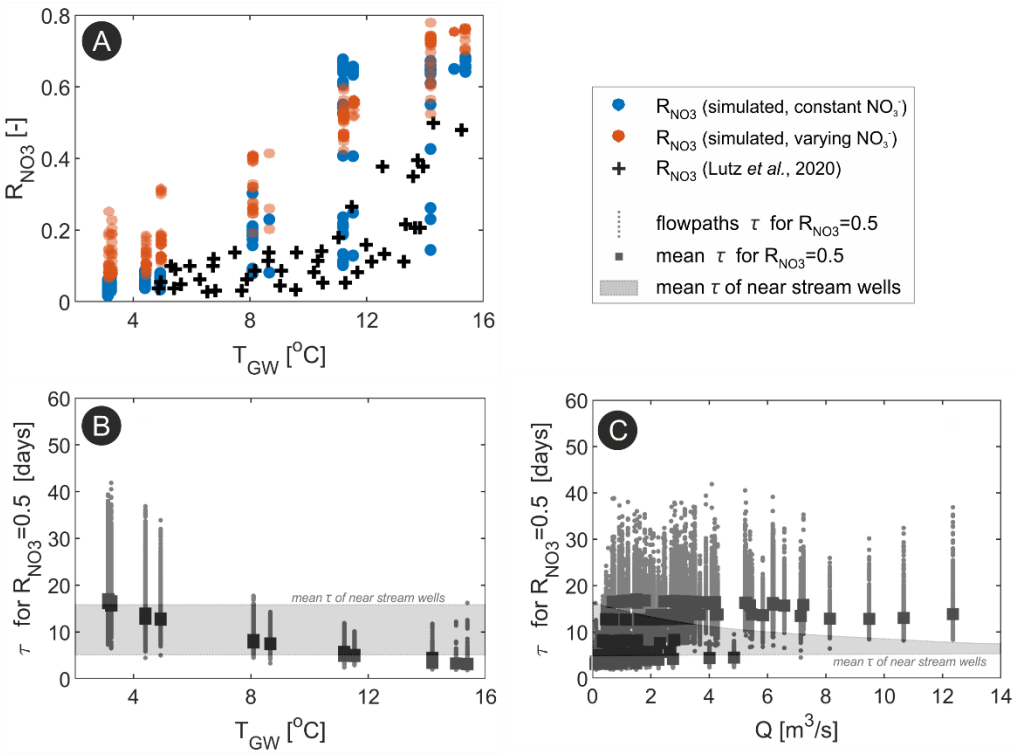

Figure 8: a) simulated NO_3^- removal fractions (R_{NO3}) on observation wells according to T_{GW} alongside R_{NO3} calculated by Lutz et al. (2020) (black crosses); time required for removing 50% of initial NO_3^- in each flow path and their mean values according to **(b)** T_{GW} and **(c)** Q for the simulation period.

Figure 8b-c shows the simulated transit-times required to achieve a removal fraction R_{NO3}=0.5 plotted versus T_{GW} and stream discharge (Q), alongside the mean τ for all wells over the simulation period. The time required for R_{NO3}=0.5 decreased from around 20 days (min=5 days, max=40 days) to about 5 days (min=2 days, max=15 days) with increasing T_{GW} (Figure 8b). In relation to Q, the time required for R_{NO3}=0.5 sharply increased from baseflow conditions up to Q=6 m³/s, and kept nearly constant for higher discharge

values, Figure 8c. Results suggest that, based on computed mean τ for the observation wells, removal fractions of R_{NO3}=0.5 may or may not be realized depending on the hydrological and thermal conditions. For low Q values, R_{NO3} in this zone is at or slightly above 0.5, while for high Q a removal fraction of R_{NO3}=0.5 cannot be realised. This suggests that, the relatively low observed R_{NO3} in these wells for low T_{GW} conditions (and high stream discharge) does not indicate that generally no significant DN takes place along this infiltrating flow path, but rather that it will take place further downstream along this flow path.

3.3.4 Nitrate concentrations and denitrification patterns at the floodplain

The extent of the aerobic zone determines where other redox-sensitive reactions such as DN occur. Since high DN rates only occur after DO has been sufficiently depleted (i.e., near anaerobic conditions), as imposed by the inhibition factor in Eq.4, we observed that the computed mean τ required for R_{NO3}=0.5 increased with the volume of the DO_z (Figure 6b). Under a large DO_z, initial NO_3^- concentrations remain practically constant until considerable DN occurs at locations further away from the stream (after longer transit-times, Figure 8). As exemplified in Figure 9 for the simulations using constant T_{GW} values, significant DN only takes place at the fringes of the DO_z. As differences in the estimated removal fractions (R_{NO3}) between the two scenarios were minimal, we only show the results for simulations with constant initial NO_3^-. For the high T_{GW} scenario (25ºC, Figure 9a-h), complete NO_3^- removal was reached closer to the stream (Figure 9b and 9f) mainly because of the high k_{DN} under warm conditions (up to 0.066 mmol $L^{-1}d^{-1}$ = 4 mg $L^{-1}d^{-1}$). At this condition, the DN fringe, the location where significant DN can take place is generally small, and only slightly larger under high Q conditions (Figure 9d and 9h), due to relatively small effects of transit-times variations under high temperature scenario (i.e., a more reaction controlled system).

Contrary, under very low-temperature conditions (0.5ºC,Figure 9i-p) significant DN only occurred further away from the stream for both Q scenarios, given that aerobic conditions prevailed for most of the flow paths and DN was strongly inhibited, Figure 9i and 9m. In comparison to high T_{GW} scenarios, the DN fringe was larger since k_{DN} was generally smaller (only up to 1.9×10^{-3} mmol $L^{-1}d^{-1}$ = 0.12 mg $L^{-1}d^{-1}$) and longer times are required for removing the same amount of NO_3^-. The DN fringe was the largest for the combined high Q and low T_{GW} scenario, Figure 9p, however it was only slightly larger than the scenario of low Q and low T_{GW}, Figure 9L.

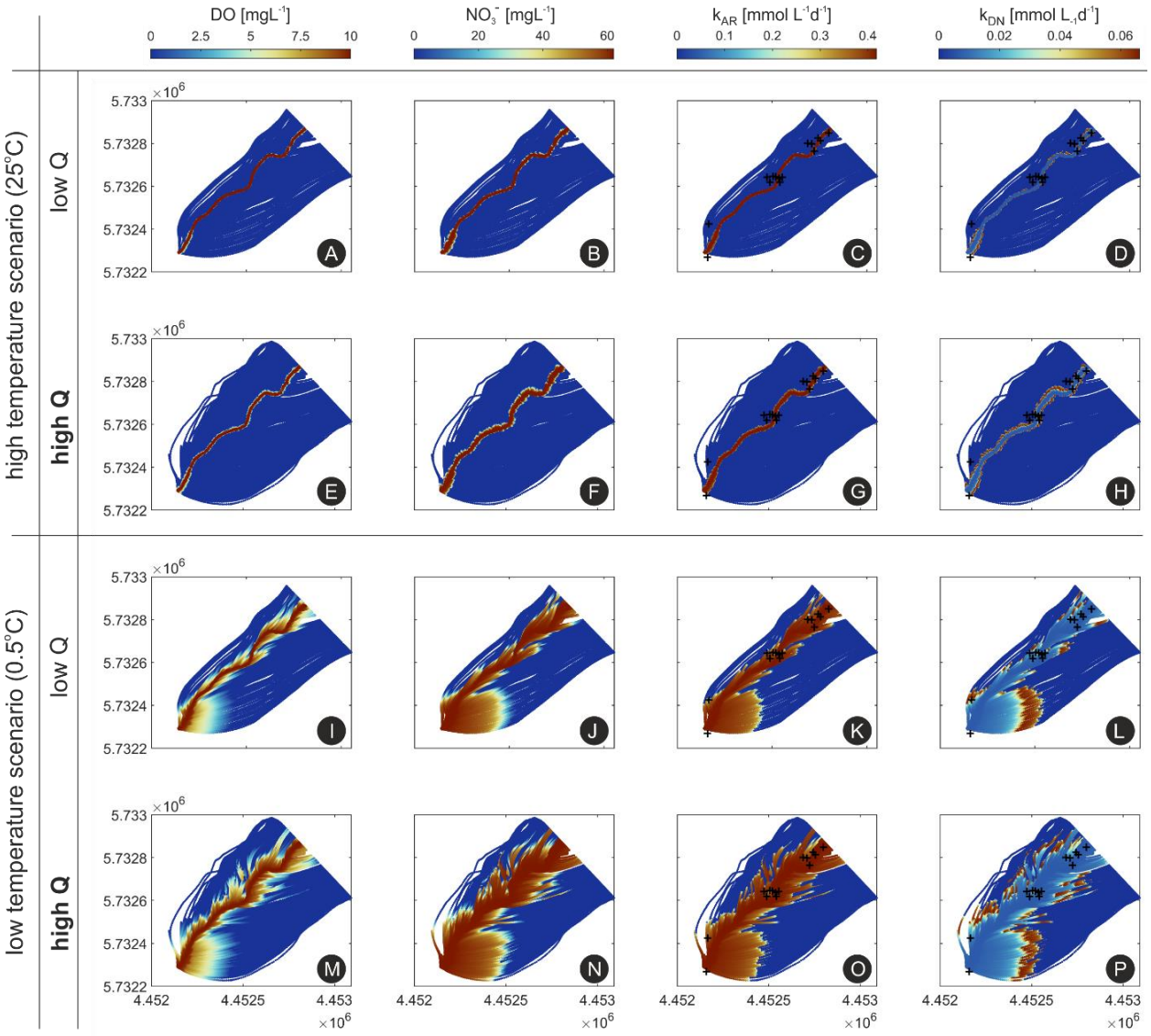

Figure 9: Distribution of dissolved oxygen (DO), Nitrate (NO_3^-), aerobic respiration (k_{AR}), and denitrification (k_{DN}) for four different scenarios of stream discharges and water temperature. The *low Q* and ***high Q*** represent 0.12 m^3s^{-1} and 12.0 m^3s^{-1}, respectively. The black crosses in the plots show the locations of the wells used for specific analyses of NO_3^- removal fractions. Note: deeper flow paths are not visible in the plots.

As the majority of simulated flow paths were long and most of the water did not immediately return to the stream via smaller hyporheic flow cells, DN and complete NO_3^- removal (R_{NO3}=1.0) still occurred at later times and further away from the stream (given that DOC was not completely consumed through AR). However, for the few hyporheic flow paths (infiltrating SW particles returning to the stream) observed in our model, maximum R_{NO3} values were only between 0.11 to 0.15 for low Q and high Q, respectively (for

T_{GW}=25ºC). The hyporheic R_{NO3} were slightly higher under high stream discharge due to somewhat longer hyporheic flow paths and transit-times in comparison to low discharge conditions (Figure S8, supplementary material).

3.3.5 Resulting effects on nitrate removal efficiency

Finally, to compare the combined effects of transit-times and temperature variations alongside the effects of varying NO_3^- on overall NO_3^- removal efficiency within the floodplain, we look on the resulting R_{NO3} of the different scenarios on the near stream observation wells. We also look specifically to the time required to achieve R_{NO3}=0.5, whereas shorter transit-times could be translated to higher removal efficiencies.

Generally, R_{NO3} at the near stream wells decreased with increasing discharge regardless of the considered T_{GW} scenario and the initial NO_3^- concentration (Figure 10a). Under high T_{GW}, overall high R_{NO3} are attained. It is important to note that, for the same T_{GW}, R_{NO3} values were slightly larger for low Q under the scenario with varying initial NO_3^- concentrations since for very low Q the initial NO_3^- at the beginning of the flow path was relatively smaller than the initial NO_3^- on the scenario with constant initial NO_3^- concentration.

From the scenario with constant initial NO_3^- concentrations (Figure 10b), we can depict the effects of transit-time and temperature variations on NO_3^- removal. First, the time required for R_{NO3}=0.5 strongly decreases with increasing T_{GW}, whereas only minor changes occur with stream discharge. Overall, the decrease in reactive efficiency (i.e., increase on the time required for R_{NO3}=0.5) is more prominent under low T_{GW} conditions indicating a more transport controlled system under such conditions. Under high T_{GW}, the time required for R_{NO3}=0.5 are generally shorter, whereas the effects due to stream discharge (hence transit-time variations) are minimal.

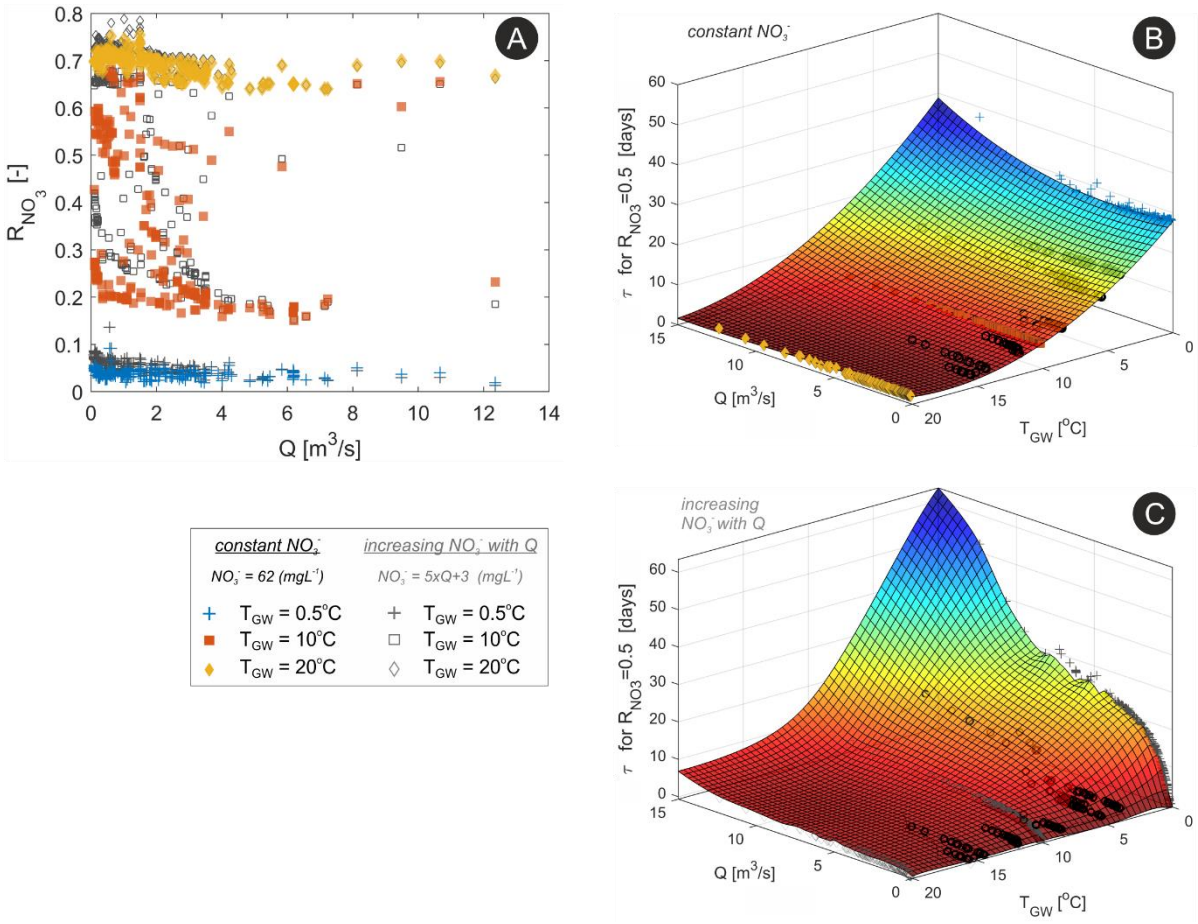

Figure 10: a) NO_3^- removal fractions (R_{NO3}) on the near stream wells versus Q for various T_{GW} and NO_3^- concentration scenarios; **(b)** mean transit-time required for R_{NO3}=0.5 for various Q and T_{GW} scenarios with constant initial NO_3^- concentrations; **(c)** mean transit-time required for R_{NO3}=0.5 for various Q and T_{GW} scenarios with varying initial NO_3^- concentrations; black circles in (a) and (b) show the results from the simulated period.

Results from the scenario of increasing initial NO_3^- concentration with Q show that, particularly under low T_{GW}, the time required for R_{NO3}=0.5 strongly increased with Q, from the nearly constant value of 35 days for the scenario with constant initial NO_3^- concentration to slightly more than 60 days. This emphasizes the effects of increasing solute concentration on the overall removal efficiency. In contrast, under high T_{GW}, the time required for R_{NO3}=0.5 only slightly increased with stream discharge (from 0.5 to 4 days). Compared to the constant initial NO_3^- concentration scenario, this minor absolute change under high T_{GW} indicates that the system is less sensitive to variations in solute concentrations and transit-times under high T_{GW}; in other words, a reaction controlled system. Again, for very low Q, the time required for R_{NO3}=0.5 under the scenario with varying initial NO_3^- concentrations were merely 0.5 day since the initial NO_3^- concentrations were relatively smaller than the initial NO_3^- on the scenario with constant initial NO_3^- concentration.

3.4 Discussion

In this study, we integrated fluid flow and reactive solute transport considering temperature-dependent reaction rates, transient flow fields and stream discharge, as well as variations in instream solute concentrations at the scale of an entire stream corridor. To avoid the excessive computational costs of a fully coupled flow, heat transport and reactive solute transport model with temperature-dependent reaction rates at this scale, we intentionally employed a simpler flow path-reaction approach. This approach, which evaluates flow and reactive transport consecutively, was able to adequately reproduce general spatio-temporal patterns of redox-sensitive solute concentrations and removal fractions in the stream corridor, which were in line with previous estimates from field measurements (Lutz et al., 2020; Nogueira et al., 2021; Trauth et al., 2018). In our approach, once an integrated surface-subsurface flow model is calibrated, the extraction of flow paths, and the setup of the routine for temperature-dependent coupled reactions is straight forward, robust and fast. As such, the approach provides a convenient tool to evaluate observed biogeochemical patterns in groundwater in entire stream corridors and to explore the underlying dominant processes and reactions. For detailed assessments of complex local reactions and dynamics a fully coupled model might still be indispensable, but for a stream-corridor-scale assessment our approach provides a viable, computationally less demanding alternative. Limitations of our approach and recommendations for future improvements will be discussed further below.

3.4.1 Fully coupled 3D hydrological model

In this study, a transient 3D surface-subsurface flow model representing a 4^{th}-order stream and its adjacent riparian aquifer was set up, aiming to avoid some of the limitations and possible pitfalls of common 2D steady-state simulations. Especially in near-stream areas where anisotropy of hydraulic conductivity and flow variability are high, transient simulations and an incorporation of multiple tracer-tests in the model calibration can yield more unbiased results and a more sound parameter calibration (Gianni et al., 2019; Schilling et al., 2019; Xu and Gómez-Hernández, 2016). Hence, the incorporation of additional, less conventional field data, such as the results from field tracer-tests, in model calibration could be a viable alternative to more conventional calibration strategies in future studies of highly dynamic, coupled SW-GW systems.

The flow and transport parameters were in the range of expected values after calibration. Still, alluvial systems are typically characterised by a high degree of heterogeneity, and any numerical model can only include a simplified representation of the real subsurface structures. Despite that, the reasonable match between observed and simulated hydraulic heads and solute transport even in the highly dynamic near-stream zone suggests that fine-scale heterogeneities may only exert minor controls on general flow patterns

and may have bearing mainly locally (Bardini et al., 2013). However, larger-scale patterns of exchange fluxes and hence also solute transport and reactions will be affected by larger-scale geologic heterogeneities (e.g. hydrofacies scale) at the scale of larger stream-corridors (Fleckenstein et al., 2006; Irvine et al., 2012; Pryshlak et al., 2015; Tang et al., 2017, 2015). Heterogeneities at this scale should generally be considered in future studies. A further assessment along those lines could be implemented by using transition probability-based geostatistical approaches to generate stochastic realizations of hydrofacies distributions (Fleckenstein et al., 2006; Labolle & Fogg, 2001), e.g. with software such as T-PROGS (Carle, 1999) and further calibrate hydrofacies properties using parameter estimation tools like PEST. On the other end, one could use pilot-points within the calibration process combined with Tikhonov regularisation, which allows a more constrained model parameterisation, while adding extra spatial flexibility for parameterising complex hydrogeological systems (Doherty, 2015, 2003; Fienen et al., 2009; Moeck et al., 2015).

The calibrated model revealed predominantly losing conditions along almost the entire stream reach (on average 25% loss over a 1km reach, or 6000 m^3d^{-1} over a 1 km reach), which is comparable to previous field assessments at this site (Munz et al., 2017; Schmadel et al., 2016). The simulated flow paths, their extent, and associated transit-times are similar to those reported from other riparian zones and river-bank-filtration sites with similar systematically losing conditions (Liao et al., 2014; Munz et al., 2019; Poole et al., 2008; Su et al., 2007; Vogt et al., 2010a, 2010b). In our domain, most of the infiltrating SW does not return to the stream immediately within the modelled area, but based on flow continuity we expect its return at some point further downstream. Therefore turnover that takes place within the riparian aquifer even at larger distance from the stream, may eventually affect stream water quality further downstream.

3.4.2 Coupled reaction simulations and reactivity controls

One objective of this study was to simultaneously evaluate hydraulic and thermal effects on riparian solute turnover potentials. Our simulations revealed that the effect of transit-times on DO_z volumes diminishes with increasing T_{GW}, indicating that hydraulic and temperature effects should be evaluated jointly in stream corridors. Our simulations further indicated that in terms of denitrification, changes in stream discharge (and in turn subsurface transit-times) - under the assumption that concentrations do not change with stream discharge (e.g., pure hydraulic effects) - are of minor importance for NO_3^- removal fractions compared to changes in T_{GW}. Yet, the removal efficiency in the near stream wells was inversely related to stream discharge regardless of initial NO_3^- concentrations. Within the riparian zone, high v_{GW} under high discharge conditions and the resulting shorter transit-times from the point of infiltration to the observation wells led to smaller R_{NO3} values (Figure 10), even though extra solute influx increases reaction rate coefficients overall in the scenario of increasing NO_3^- concentrations with discharge. This is consistent with Sawyer

(2015) and Shuai et al. (2017) who found that higher NO_3^- loads often resulted in lower removal efficiencies. For the scenario of increasing NO_3^- concentrations with discharge, the changes in overall R_{NO3} were especially large for low T_{GW} conditions indicating that the system becomes less sensitive to solute and transit-time variations with increasing T_{GW} and becomes increasingly reaction controlled. In terms of overall solute turnover, the effects of increasing temperature on reaction rates (i.e. the reaction-process) are faster and more prominent than the effects of increasing solute influx (i.e. solute-transport) in the simulations. This is supported by other studies, which demonstrated that solute removal fractions increase with the ratio between the time scale of solute-transport and the time-scale of the reaction-process expressed by the Damköhler number (Gu et al., 2007; Ocampo et al., 2006; Zarnetske et al., 2012). However, these studies did not account for the effects of variable temperatures.

In most of the hyporheic and in-stream studies assessing flow and biogeochemical processes, water temperature is usually set to a constant high value (e.g., 20°C) for simplicity, which in turn results in high reaction rate coefficients, with reaction processes being most constrained by the transit-time of water parcels through the subsurface. In contrast, Zheng et al. (2016) have shown the implications of different water temperature for biogeochemical processes occurring below the streambed. On top of their steady state simulations, our results revealed that the role of losing streams for denitrification at reach- and stream-corridor-scale might be overlooked, and nitrate removal efficiency might be underestimated (especially under low-temperature conditions) by investigations that are restricted to near-stream areas only. In other words, our results highlight that the longer infiltrating flow paths that deliver stream water into the more distant parts of the riparian aquifer in comparison to the rather short hyporheic flow paths allow for larger turnover rates and significant removal of nitrate even under low T_{GW} conditions.

The high DOC concentration of 20 mg L^{-1} in our simulations was intentionally chosen to avoid complete DOC exhaustion through AR, which would limit DN. This assumption, even though it could be considered unrealistic, reflects the general availability of electron donors also from other sources (e.g. particulate organic carbon in the sediments) and is supported by the good agreement between simulated and measured removal fractions (R_{NO3}) indicating that DOC is likely not a limiting factor for DN in the vicinity of the stream. The same assumption was already made by Trauth et al. (2018), who found R_{NO3} values between 0.15 and 0.75 similar to our simulated values (0.10-0.75). If we had considered only half of the initial 20 mg L^{-1} of DOC in SW (DOC= 10 mg L^{-1}), the new R_{NO3} at the observation wells would have been reduced by 40% (from 0.19 to 0.11 in average), whereas values were similar for low T_{GW} and differences were only observable for high T_{GW} (data not shown). Clearly, under such DOC limited conditions a complete NO_3^- removal is not expected to occur, however DN could still take place further away from the stream until bioavailable DOC (or any other electron donor) is fully depleted, leading to mean final R_{NO3} values between

0.3 and 0.4, for low and high T_{GW}, respectively (data not shown). Our results suggest that despite the low R_{NO3} in the vicinity of the stream during winter, significant NO_3^- removal is likely to take place at locations further into the floodplain aquifer. Unfortunately, no observations were available at those locations, which could have been used to directly validate our simulation results. Later NO_3^- removal would be solely limited by the flow path length (or total transit-time of the infiltrated water before returning to the stream), which could not be long enough for the system to reach anaerobic conditions for substantial denitrification to occur (as observed for the in-stream hyporheic flow paths). Alternatively, additional NO_3^- inputs would equally exhaust electron donors (such as DOC) and eventually inhibit heterotrophic denitrification (Rivett et al., 2008).

3.4.3 Limitations of this study and future work

The loose coupling of hydrology and biogeochemistry used in this work is an approach that can be easily transferred or adapted to other applications and, according to our evaluation based on field measurements, was able to capture main features and controlling factors of the hydro-biogeochemical system well. Nevertheless, with the flow path-reaction approach, hydrodynamic processes such as dispersion and diffusion that will affect solute concentrations within and between flow paths due to solute relocation are not taken into account. These processes would lead to more gradual and smooth anaerobic and DN fringes. However, we expect this effect to be greater only for low discharge conditions when a less advectively dominated system is expected, or under low T_{GW} when the system is generally more sensitive to changes in transport processes (i.e., transport limitation).

Moreover, infiltrating SW with different temperature from GW can affect subsurface reaction rate coefficients, which can be especially important within the first few meters around the streambed (Engelhardt et al., 2013; Munz et al., 2017; Nogueira et al., 2021; Song et al., 2018). But we claim that, due to strongly damped higher frequency heat signals from the stream, the reaction rate coefficients and the overall DO_z around the stream would not change to a great extent as they are mainly driven by the seasonal temperature variations (Figure S5, supplementary material). The HGS code can simulate heat fluxes, and the resulting transient temperature fields could be coupled with the reactions along flow paths in future work to assess the effects of event-driven heat fluxes for a more refined assessment of solute turnover in the SW-GW transition zone over different short-term and seasonal scales.

We did not carry out a detailed parameter sensitivity analysis on flow parameters and on solute simulations, as it was outside the scope of this study. Other hydrological and biogeochemical factors such as availability and ratio of nutrients, small scale sediment heterogeneity, and the actual relationship between DN rates and temperature, for instance, were not considered here but could impact NO_3^- removal fractions. Furthermore,

there are no additional solute sources from the groundwater in our flow path reaction approach. This could be implemented to represent groundwater-borne solutes being gradually incorporated into the different flow path subsections according to other indicators such as particle locations in terms of distance from the stream and transit-times (e.g., mixing with groundwater, increasing NO_3^-). For instance, the presence of different carbon sources (e.g., decreasing DOC bioavailability) within alluvial aquifers is known to influence AR and DN rates differently than stream borne DOC (Shuai et al., 2017; Yvon-Durocher et al., 2012), and could be assessed in future studies. Equally, the presence of organic matter (OM) or other compounds within floodplain sediments could be considered to evaluate the contribution of different electron donors on denitrification as demonstrated by Pescimoro et al. (2019) for OM, and by Dwivedi et al. (2018) for reduced minerals at the aquifer material.

Finally, the presence of Ammonium (NH_4^+) in the infiltrating SW could also impact NO_3^- concentrations and denitrification. NH_4^+ would increase DO consumption through nitrification, and concomitant earlier NO_3^- production, leading to increased NO_3^- concentrations and ultimately increased k_{DN} depending on the $[NO_3^-]/[NH_4^+]$ ratios (Shuai et al., 2017; Zarnetske et al., 2011; Zheng et al., 2016). In our model, however, we neglected nitrification since locally NH_4^+ concentrations are very low (<0.1 mg L^{-1}) compared to stream and groundwater NO_3^- concentrations (Trauth et al., 2018) and therefore nitrate removal would prevail over production. Test simulations considering initial NH_4^+ concentrations of 0.2 mg L^{-1}, for instance, showed that the additional NO_3^- produced through nitrification would only amount to 1.0 mg L^{-1} in the observation wells near the stream (data not shown). If initial NH_4^+ concentrations were 10x higher (i.e., 2.0 mg L^{-1}), the additional NO_3^- would be between 0.6-6.0 mg L^{-1}. This and other relevant biogeochemical processes could be easily incorporated into the presented mechanistic modelling framework for future studies and at other sites where they might be more relevant.

3.5 Conclusions

Biogeochemical reactions in stream corridors are inherently complex due to the magnitude of factors affecting their occurrence and rates. Changes in flow dynamics controlling both water transit-time and the supply of reactants, seasonal water temperature changes, as well as the hydrogeological and streambed characteristics (like stream morphology, hydraulic properties) are some of the main factors contributing to the complex configuration of controls governing flow, transport and turnover. In this study, we presented a transient 3D fully-integrated surface-subsurface flow model of a riparian stream corridor, loosely coupled to a Lagrangian and temperature-dependent reactive transport model. We derived groundwater flow paths based on transient velocity fields and assessed how the interplay of the enumerated factors controls spatio-temporal patterns of riparian reactivity. The model was calibrated according to conventional and additional

more unconventional observations (e.g., stream discharge and groundwater heads, and tracer-tests, respectively), which further reduced model uncertainties and could increase overall confidence in the robustness of the model for future applications. The presented modelling framework allowed flow and reactive transport simulations to be carried out in a highly efficient manner at the stream-corridor scale, lending results consistent to field observations, and can easily be employed in or adapted to other regions and conditions.

We found that while changes in transit-times driven by stream flow fluctuations affect DO and NO_3^- consumption rates, the effects are much smaller under high-temperature conditions than for low temperatures. The size of the aerobic zone around the stream controlled the occurrence of denitrification in the floodplain, inhibiting the process near the stream during low-temperature conditions due to persistently high DO concentrations. Furthermore, our results indicated that denitrification might still take place further away from the stream given sufficient availability of the reactants and that even under low-temperature conditions (and under limited DOC availability), up to 40% removal of initial NO_3^- can occur at later stages of transport along long infiltrating flow paths after DO has been sufficiently depleted. Despite the general decrease in NO_3^- removal fractions with increasing solute influx, removal efficiencies were more sensitive to changes in NO_3^- influx under low temperature than at high-temperature conditions.

There are multiple factors and feedbacks that control the complex removal efficiencies of NO_3^- in stream corridors. This work provides a tractable, practical approach to simulate relevant hydrological and biogeochemical process at a scale (stream corridor) relevant for management, while emphasizing the importance of considering the effects of both flow and temperature variations on solute turnover. Moreover, it highlights that studies restricted to the near stream area only (and rather short hyporheic flow paths) might disregard relevant processes that will ultimately affect overall system-scale turnover and water quality at downstream reaches, such as along infiltrating flow paths that travel long distances through the riparian aquifer before they may return to the stream. Our findings and the presented framework are generic and can be readily transferred to other sites for the assessment of reactive potential and flow dynamics in stream corridors.

3.6 Acknowledgments

GN performed the formal analysis, the investigation and wrote the original draft of the manuscript; all the authors contributed to review, final writing and editing; GN, CS, JF conceptualized the study; GN, CS, PB, DG and JF conceived the methodology; GN, CS, JF and DG worked on the validation of the study; CS and JF were responsible for supervision; JF was responsible for funding acquisition, resources and project

administration. This research is part of the ENIGMA-ITN project that has received funding from the European Union's Horizon 2020 research and innovation programme under the Marie Sklodowska-Curie Grant Agreement No 722028. The field observational data, the numerical model files, as well as the flow path-reaction model script are publically available and can be assessed through: https://doi.org/10.4211/hs.476a188d9f894a77a3ed404949680cab.

3.7 References

Ahrens, J., Geveci, B., & Law, C. (2005). ParaView : An End-User Tool for Large-Data Visualization. In Visualization Handbook (pp. 717–731). Butterworh Beinemann. https://doi.org/https://doi.org/10.1016/B978-012387582-2/50038-1

Bardini, L., Boano, F., Cardenas, M. B., Sawyer, A. H., Revelli, R., & Ridolfi, L. (2013). Small-scale permeability heterogeneity has negligible effects on nutrient cycling in streambeds. Geophysical Research Letters, 40(6), 1118–1122. https://doi.org/10.1002/grl.50224

Bernhardt, E. S., Blaszczak, J. R., Ficken, C. D., Fork, M. L., Kaiser, K. E., & Seybold, E. C. (2017). Control Points in Ecosystems: Moving Beyond the Hot Spot Hot Moment Concept. Ecosystems, 20(4), 665–682. https://doi.org/10.1007/s10021-016-0103-y

Boano, F., Demaria, A., Revelli, R., & Ridolfi, L. (2010). Biogeochemical zonation due to intrameander hyporheic flow. Water Resources Research, 46(2), 1–13. https://doi.org/10.1029/2008WR007583

Boulêtreau, S., Salvo, E., Lyautey, E., Mastrorillo, S., & Garabetian, F. (2012). Temperature dependence of denitrification in phototrophic river biofilms. Science of the Total Environment, 416, 323–328. https://doi.org/10.1016/j.scitotenv.2011.11.066

Boutt, D. F., & Fleming, B. J. (2009). Implications of anthropogenic river stage fluctuations on mass transport in a valley fill aquifer. Water Resources Research, 45(4), 1–14. https://doi.org/10.1029/2007WR006526

Briggs, M. A., Day-Lewis, F. D., Zarnetske, J. P., & Harvey, J. W. (2015). A physical explanation for the development of redox microzones in hyporheic flow. Geophysical Research Letters, 42(11), 4402–4410. https://doi.org/10.1002/2015GL064200

Brunner, P., & Simmons, C. T. (2012). HydroGeoSphere: A Fully Integrated, Physically Based Hydrological Model. Ground Water, 50(2), 170–176. https://doi.org/10.1111/j.1745-6584.2011.00882.x

Brunner, P., Simmons, C. T., & Cook, P. G. (2009). Spatial and temporal aspects of the transition from connection to disconnection between rivers, lakes and groundwater. Journal of Hydrology, 376(1–2), 159–169. https://doi.org/10.1016/j.jhydrol.2009.07.023

Brunner, P., Therrien, R., Renard, P., Simmons, C. T., & Franssen, H. J. H. (2017). Advances in understanding river-groundwater interactions. Reviews of Geophysics, 55(3), 818–854. https://doi.org/10.1002/2017RG000556

Čapek, P., Starke, R., Hofmockel, K. S., Bond-Lamberty, B., & Hess, N. (2019). Apparent temperature sensitivity of soil respiration can result from temperature driven changes in microbial biomass. Soil Biology and Biochemistry, 135(February), 286–293. https://doi.org/10.1016/j.soilbio.2019.05.016

Carey, J. C., Tang, J., Templer, P. H., Kroeger, K. D., Crowther, T. W., Burton, A. J., et al. (2016). Temperature response of soil respiration largely unaltered with experimental warming. Proceedings of the National Academy of Sciences of the United States of America, 113(48), 13797–13802. https://doi.org/10.1073/pnas.1605365113

Carle, S. F. (1999). T-PROGS: Transition Probability Geostatistical Software, version 2.1. University of California, Davis.

Chen, X., Chen, L., Stone, M. C., & Acharya, K. (2020). Assessing connectivity between the river channel and floodplains during high flows using hydrodynamic modeling and particle tracking analysis. Journal of Hydrology, 583(July 2019), 124609. https://doi.org/10.1016/j.jhydrol.2020.124609

Diem, S., Cirpka, O. A., & Schirmer, M. (2013). Modeling the dynamics of oxygen consumption upon riverbank filtration by a stochastic–convective approach. Journal of Hydrology, 505(November), 352–363. https://doi.org/10.1016/j.jhydrol.2013.10.015

Doherty, J. E., & Hunt, R. J. (2010). Approaches to Highly Parameterized Inversion : A Guide to Using PEST for Groundwater-Model Calibration (5169th ed.). U.S. Geological Survey Scientific Investigations Report.

Doherty, J. (1994). PEST: A Unique Computer Program for Model-independent Parameter Optimisation. Water Down Under, 94, 551–554.

Doherty, J. (2018). PEST: Model-independent parameter estimation. User Manual. Australia: Watermark Numerical Computing.

Doherty, John. (2003). Ground water model calibration using pilot points and regularization. Ground Water. https://doi.org/10.1111/j.1745-6584.2003.tb02580.x

Doherty, John. (2015). Calibration and Uncertainty Analysis for Complex Environmental Models. Groundwater. https://doi.org/10.1111/gwat.12360

Dupas, R., Musolff, A., Jawitz, J. W., Rao, P. S. C., Jäger, C. G., Fleckenstein, J. H., et al. (2017). Carbon and nutrient export regimes from headwater catchments to downstream reaches. Biogeosciences, 14(18), 4391–4407. https://doi.org/10.5194/bg-14-4391-2017

Dwivedi, D., Arora, B., Steefel, C. I., Dafflon, B., & Versteeg, R. (2018). Hot Spots and Hot Moments of Nitrogen in a Riparian Corridor. Water Resources Research, 54(1), 205–222. https://doi.org/10.1002/2017WR022346

Ebel, B. A., Mirus, B. B., Heppner, C. S., VanderKwaak, J. E., & Loague, K. (2009). First-order exchange coefficient coupling for simulating surface water-groundwater interactions: parameter sensitivity and consistency with a physics-based approach. Hydrological Processes, 23(13), 1949–1959. https://doi.org/10.1002/hyp.7279

Engelhardt, I., Prommer, H., Moore, C., Schulz, M., Schüth, C., & Ternes, T. A. (2013). Suitability of temperature, hydraulic heads, and acesulfame to quantify wastewater-related fluxes in the hyporheic and riparian zone. Water Resources Research, 49(1), 426–440. https://doi.org/10.1029/2012WR012604

Fienen, M. N., Muffels, C. T., & Hunt, R. J. (2009). On constraining pilot point calibration with regularization in PEST. Ground Water, 47(6), 835–844. https://doi.org/10.1111/j.1745-6584.2009.00579.x

Fleckenstein, J. H., Niswonger, R. G., & Fogg, G. E. (2006). River-aquifer interactions, geologic heterogeneity, and low-flow management. Ground Water, 44(6), 837–852. https://doi.org/10.1111/j.1745-6584.2006.00190.x

Frei, S., Knorr, K. H., Peiffer, S., & Fleckenstein, J. H. (2012). Surface micro-topography causes hot spots of biogeochemical activity in wetland systems: A virtual modeling experiment. Journal of Geophysical Research: Biogeosciences, 117(4), 1–18. https://doi.org/10.1029/2012JG002012

Genuchten, V. . M. (1980). A closed-form equation for predicting the hydraulic conductivity of unsaturated soils. Soil Science Society of America Journal, 44(5), 892–898.

Gianni, G., Doherty, J., & Brunner, P. (2019). Conceptualization and Calibration of Anisotropic Alluvial Systems: Pitfalls and Biases. Groundwater, 57(3), 409–419. https://doi.org/10.1111/gwat.12802

Greskowiak, J., Prommer, H., Massmann, G., & Nützmann, G. (2006). Modeling seasonal redox dynamics and the corresponding fate of the pharmaceutical residue phenazone during artificial recharge of groundwater. Environmental Science and Technology, 40(21), 6615–6621. https://doi.org/10.1021/es052506t

Gu, C., Hornberger, G. M., Mills, A. L., Herman, J. S., & Flewelling, S. A. (2007). Nitrate reduction in streambed sediments: Effects of flow and biogeochemical kinetics. Water Resources Research, 43(12). https://doi.org/10.1029/2007WR006027

Henzler, A. F., Greskowiak, J., & Massmann, G. (2016). Seasonality of temperatures and redox zonations during bank filtration - A modeling approach. Journal of Hydrology, 535, 282–292. https://doi.org/10.1016/j.jhydrol.2016.01.044

Irvine, D. J., Brunner, P., Franssen, H.-J. H., & Simmons, C. T. (2012). Heterogeneous or homogeneous? Implications of simplifying heterogeneous streambeds in models of losing streams. Journal of Hydrology, 424–425, 16–23. https://doi.org/10.1016/j.jhydrol.2011.11.051

Jasechko, S., Seybold, H., Perrone, D., Fan, Y., & Kirchner, J. W. (2021). Widespread potential loss of streamflow into underlying aquifers across the USA, 591(July 2020). https://doi.org/10.1038/s41586-021-03311-x

Jensen, K. J., Engesgaard, P., Johnsen, A. R., Marti, V., & Nilsson, B. (2017). Hydrological mediated denitrification in groundwater below a seasonal flooded restored riparian zone. Water Resources Research, 53(3), 2074–2094. https://doi.org/10.1002/2016WR019581

Kirschbaum, M. U. F. (1995). The temperature dependence of soil organic matter decomposition, and the effect of global warming on soil organic C storage. Soil Biology and Biochemistry, 27(6), 753–760. https://doi.org/10.1016/0038-0717(94)00242-S

Kirschbaum, M. U. F. (2000). Will changes in soil organic carbon act as a positive or negative feedback on global warming? Biogeochemistry, 48(1), 21–51. https://doi.org/10.1023/A:1006238902976

Kurz, M. J., Drummond, J. D., Martí, E., Zarnetske, J. P., Lee-Cullin, J., Klaar, M. J., et al. (2017). Impacts of water level on metabolism and transient storage in vegetated lowland rivers: Insights from a

mesocosm study. Journal of Geophysical Research: Biogeosciences, 122(3), 628–644. https://doi.org/10.1002/2016JG003695

Labolle, E. M., & Fogg, G. E. (2001). Role of Molecular Diffusion in Contaminant Migration and Recovery in an Alluvial Aquifer System. Transport in Porous Media, 42(1), 155–179. https://doi.org/10.1007/978-94-017-1278-1_8

Liang, X., Zhan, H., & Schilling, K. (2018). Spatiotemporal Responses of Groundwater Flow and Aquifer-River Exchanges to Flood Events. Water Resources Research, 54(3), 1513–1532. https://doi.org/10.1002/2017WR022046

Liao, Z., Osenbrück, K., & Cirpka, O. A. (2014). Non-stationary nonparametric inference of river-to-groundwater travel-time distributions. Journal of Hydrology, 519(PD), 3386–3399. https://doi.org/10.1016/j.jhydrol.2014.09.084

Liu, D., Zhao, J., Jeon, W. H., & Lee, J. Y. (2019). Solute dynamics across the stream-to-riparian continuum under different flood waves. Hydrological Processes, 33(20), 2627–2641. https://doi.org/10.1002/hyp.13515

Lutz, S. R., Trauth, N., Musolff, A., Van Breukelen, B. M., Knöller, K., & Fleckenstein, J. H. (2020). How Important is Denitrification in Riparian Zones? Combining End-Member Mixing and Isotope Modeling to Quantify Nitrate Removal from Riparian Groundwater. Water Resources Research, 56(1). https://doi.org/10.1029/2019WR025528

Maag, M., M. Malinovsky, and S. M. Nielsen (1997), Kinetics and temperature dependence of potential denitrification in riparian soils, J. Environ. Qual., 26, 215–223

Matsunaga, T., Karametaxas, G., von Gunten, H. R., & Lichtner, P. C. (1993). Redox chemistry of iron and manganese minerals in river-recharged aquifers: A model interpretation of a column experiment. Geochimica et Cosmochimica Acta, 57(8), 1691–1704. https://doi.org/10.1016/0016-7037(93)90107-8

Mayer, P. M., Reynolds, S. K., & Canfield, T. J. (2006). Riparian buffer width, vegetative cover, and nitrogen removal effectiveness: a review of current science and regulations. Epa/600/R-05/118, 1–40. Retrieved from http://nepis.epa.gov/Exe/ZyPDF.cgi/2000O182.PDF?Dockey=2000O182.PDF

Moeck, C., Hunkeler, D., & Brunner, P. (2015). Tutorials as a flexible alternative to GUIs: An example for advanced model calibration using Pilot Points. Environmental Modelling & Software, 66(4), 78–86. https://doi.org/10.1016/j.envsoft.2014.12.018

Moore, C., Wöhling, T., & Doherty, J. (2010). Efficient regularization and uncertainty analysis using a global optimization methodology. Water Resources Research, 46(8), 1–17. https://doi.org/10.1029/2009WR008627

Munz, M., Oswald, S. E., & Schmidt, C. (2017). Coupled Long-Term Simulation of Reach-Scale Water and Heat Fluxes Across the River-Groundwater Interface for Retrieving Hyporheic Residence Times and Temperature Dynamics. Water Resources Research, 53(11), 8900–8924. https://doi.org/10.1002/2017WR020667

Munz, M., Oswald, S. E., Schäfferling, R., & Lensing, H.-J. (2019). Temperature-dependent redox zonation, nitrate removal and attenuation of organic micropollutants during bank filtration. Water Research, 162(10), 225–235. https://doi.org/10.1016/j.watres.2019.06.041

Musolff, A., Schmidt, C., Selle, B., & Fleckenstein, J. H. (2015). Catchment controls on solute export. Advances in Water Resources, 86(PA), 133–146. https://doi.org/10.1016/j.advwatres.2015.09.026

Nixdorf, E., & Trauth, N. (2018). Evaluating the reliability of time series analysis to estimate variable riparian travel times by numerical groundwater modelling. Hydrological Processes, 32(3), 408–420. https://doi.org/10.1002/hyp.11428

Nogueira, G. E. H., Schmidt, C., Trauth, N., & Fleckenstein, J. H. (2021). Seasonal and short-term controls of riparian oxygen dynamics and the implications for redox processes. Hydrological Processes, 35(2), 16. https://doi.org/10.1002/hyp.14055

O'Connell, A. M. (1990). Microbial decomposition (respiration) of litter in eucalypt forests of South-Western Australia: An empirical model based on laboratory incubations. Soil Biology and Biochemistry, 22(2), 153–160. https://doi.org/10.1016/0038-0717(90)90080-J

Ocampo, C. J., Oldham, C. E., & Sivapalan, M. (2006). Nitrate attenuation in agricultural catchments: Shifting balances between transport and reaction. Water Resources Research, 42(1), 1–16. https://doi.org/10.1029/2004WR003773

Oldham, C. E., Farrow, D. E., & Peiffer, S. (2013). A generalized Damköhler number for classifying material processing in hydrological systems. Hydrology and Earth System Sciences, 17(3), 1133–1148. https://doi.org/10.5194/hess-17-1133-2013

Pescimoro, E., Boano, F., Sawyer, A. H., & Soltanian, M. R. (2019). Modeling Influence of Sediment Heterogeneity on Nutrient Cycling in Streambeds. Water Resources Research, 55(5), 4082–4095. https://doi.org/10.1029/2018WR024221

Peterjohn, W. T. (1991). Denitrification: Enzyme content and activity in desert soils. Soil Biology and Biochemistry, 23(9), 845–855. https://doi.org/10.1016/0038-0717(91)90096-3

Pietikäinen, J., Pettersson, M., Bååth, E. (2005). Comparison of temperature effects on soil respiration and bacterial and fungal growth rates. FEMS Microbiol. Ecol. 52, 49–58. https://doi.org/10.1016/j.femsec.2004.10.002

Poole, G. C., O'Daniel, S. J., Jones, K. L., Woessner, W. W., Bernhardt, E. S., Helton, A. M., et al. (2008). Hydrologic spiralling: the role of multiple interactive flow paths in stream ecosystems. River Research and Applications, 24(7), 1018–1031. https://doi.org/10.1002/rra.1099

Precht, E., Franke, U., Polerecky, L., & Huettel, M. (2004). Oxygen dynamics in permeable sediments with wave-driven pore water exchange. Limnology and Oceanography, 49(3), 693–705. https://doi.org/10.4319/lo.2004.49.3.0693

Pryshlak, T. T., Sawyer, A. H., Stonedahl, S. H., & Soltanian, M. R. (2015). Multiscale hyporheic exchange through strongly heterogeneous sediments. Water Resources Research, 51(11), 9127–9140. https://doi.org/10.1002/2015WR017293

Rau, G. C., Andersen, M. S., McCallum, A. M., Roshan, H., & Acworth, R. I. (2014). Heat as a tracer to quantify water flow in near-surface sediments. Earth-Science Reviews, 129, 40–58. https://doi.org/10.1016/j.earscirev.2013.10.015

Rivett, M. O., Buss, S. R., Morgan, P., Smith, J. W. N., & Bemment, C. D. (2008). Nitrate attenuation in groundwater: A review of biogeochemical controlling processes. Water Research, 42(16), 4215–4232. https://doi.org/10.1016/j.watres.2008.07.020

Sawyer, A. H. (2015). Enhanced removal of groundwater-borne nitrate in heterogeneous aquatic sediments. Geophysical Research Letters, 42(2), 403–410. https://doi.org/10.1002/2014GL062234

Sawyer, A. H., Kaplan, L. A., Lazareva, O., & Michael, H. A. (2014). Hydrologic dynamics and geochemical responses within a floodplain aquifer and hyporheic zone during Hurricane Sandy. Water Resources Research, 50(6), 4877–4892. https://doi.org/10.1002/2013WR015101

Schilling, O. S., Cook, P. G., & Brunner, P. (2019). Beyond Classical Observations in Hydrogeology: The Advantages of Including Exchange Flux, Temperature, Tracer Concentration, Residence Time, and Soil Moisture Observations in Groundwater Model Calibration. Reviews of Geophysics, 57(1), 146–182. https://doi.org/10.1029/2018RG000619

Schipper, L. A., Hobbs, J. K., Rutledge, S., & Arcus, V. L. (2014). Thermodynamic theory explains the temperature optima of soil microbial processes and high Q10 values at low temperatures. Global Change Biology, 20(11), 3578–3586. https://doi.org/10.1111/gcb.12596

Schmadel, N. M., Ward, A. S., Kurz, M. J., Fleckenstein, J. H., Zarnetske, J. P., Hannah, D. M., et al. (2016). Stream solute tracer timescales changing with discharge and reach length confound process interpretation. Water Resources Research, 52(4), 3227–3245. https://doi.org/10.1002/2015WR018062

Sharma, L., Greskowiak, J., Ray, C., Eckert, P., & Prommer, H. (2012). Elucidating temperature effects on seasonal variations of biogeochemical turnover rates during riverbank filtration. Journal of Hydrology, 428–429, 104–115. https://doi.org/10.1016/j.jhydrol.2012.01.028

Shuai, P., Cardenas, M. B., Knappett, P. S. K., Bennett, P. C., & Neilson, B. T. (2017). Denitrification in the banks of fluctuating rivers: The effects of river stage amplitude, sediment hydraulic conductivity and dispersivity, and ambient groundwater flow. Water Resources Research, 53(9), 7951–7967. https://doi.org/10.1002/2017WR020610

Simmons, C. T., Brunner, P., Therrien, R., & Sudicky, E. A. (2020). Commemorating the 50th anniversary of the Freeze and Harlan (1969) Blueprint for a physically-based, digitally-simulated hydrologic response model. Journal of Hydrology, 584(1969), 124309. https://doi.org/10.1016/j.jhydrol.2019.124309

Singh, T., Gomez-Velez, J. D., Wu, L., Wörman, A., Hannah, D. M., & Krause, S. (2020). Effects of Successive Peak Flow Events on Hyporheic Exchange and Residence Times. Water Resources Research, 56(8). https://doi.org/10.1029/2020WR027113

Song, X., Chen, X., Stegen, J., Hammond, G., Song, H. S., Dai, H., et al. (2018). Drought Conditions Maximize the Impact of High-Frequency Flow Variations on Thermal Regimes and Biogeochemical Function in the Hyporheic Zone. Water Resources Research, 54(10), 7361–7382. https://doi.org/10.1029/2018WR022586

Su, G. W., Jasperse, J., Seymour, D., Constantz, J., & Zhou, Q. (2007). Analysis of pumping-induced unsaturated regions beneath a perennial river. Water Resources Research, 43(8), 1–14. https://doi.org/10.1029/2006WR005389

Tang, Q., Kurtz, W., Brunner, P., Vereecken, H., & Hendricks Franssen, H. J. (2015). Characterisation of river-aquifer exchange fluxes: The role of spatial patterns of riverbed hydraulic conductivities. Journal of Hydrology, 531, 111–123. https://doi.org/10.1016/j.jhydrol.2015.08.019

Tang, Q., Kurtz, W., Schilling, O. S., Brunner, P., Vereecken, H., & Hendricks Franssen, H. J. (2017). The influence of riverbed heterogeneity patterns on river-aquifer exchange fluxes under different connection regimes. Journal of Hydrology, 554, 383–396. https://doi.org/10.1016/j.jhydrol.2017.09.031

Therrien, R., McLaren, R. G., Sudicky, E. A., & Panday, S. M. (2010). HydroGeoSphere. A three-dimensional numerical model describing fully-integrated subsurface and surface flow and solute transport. Groundwater Simulations Group, 457. https://doi.org/10.5123/S1679-49742014000300002

Trauth, N., & Fleckenstein, J. H. (2017). Single discharge events increase reactive efficiency of the hyporheic zone. Water Resources Research, 53(Jan), 779–798. https://doi.org/10.1111/j.1752-1688.1969.tb04897.x

Trauth, N., Musolff, A., Knöller, K., Kaden, U. S., Keller, T., Werban, U., & Fleckenstein, J. H. (2018). River water infiltration enhances denitrification efficiency in riparian groundwater. Water Research, 130, 185–199. https://doi.org/10.1016/j.watres.2017.11.058

Trauth, N., Schmidt, C., Vieweg, M., Maier, U., & Fleckenstein, J. H. (2014). Hyporheic transport and biogeochemical reactions in pool-riffle systems under varying ambient groundwater flow conditions. Journal of Geophysical Research: Biogeosciences, 119(5), 910–928. https://doi.org/10.1002/2013JG002586

Treese, S., Meixner, T., & Hogan, J. F. (2009). Clogging of an Effluent Dominated Semiarid River: A Conceptual Model of Stream-Aquifer Interactions. JAWRA Journal of the American Water Resources Association, 45(4), 1047–1062. https://doi.org/10.1111/j.1752-1688.2009.00346.x

Veraart, A. J., de Klein, J. J. M., & Scheffer, M. (2011). Warming can boost denitrification disproportionately due to altered oxygen dynamics. PLoS ONE, 6(3), 2–7. https://doi.org/10.1371/journal.pone.0018508

Vidon, P. G., & Hill, A. R. (2006). A landscape-based approach to estimate riparian hydrological and nitrate removal functions. Journal of the American Water Resources Association, 42(4), 1099–1112. https://doi.org/10.1111/j.1752-1688.2006.tb04516.x

Vieweg, M., Kurz, M. J., Trauth, N., Fleckenstein, J. H., Musolff, A., & Schmidt, C. (2016). Estimating time-variable aerobic respiration in the streambed by combining electrical conductivity and dissolved oxygen time series. Journal of Geophysical Research: Biogeosciences, 121(8), 2199–2215. https://doi.org/10.1002/2016JG003345

Vogt, T., Schneider, P., Hahn-Woernle, L., & Cirpka, O. A. (2010). Estimation of seepage rates in a losing stream by means of fiber-optic high-resolution vertical temperature profiling. Journal of Hydrology, 380(1–2), 154–164. https://doi.org/10.1016/j.jhydrol.2009.10.033

Vogt, T., Hoehn, E., Schneider, P., Freund, A., Schirmer, M., & Cirpka, O. A. (2010). Fluctuations of electrical conductivity as a natural tracer for bank filtration in a losing stream. Advances in Water Resources, 33(11), 1296–1308. https://doi.org/10.1016/j.advwatres.2010.02.007

Widdowson, M. A., Molz, F. J., & Benefield, L. D. (1988). A numerical transport model for oxygen- and nitrate-based respiration linked to substrate and nutrient availability in porous media. Water Resources Research, 24(9), 1553–1565. https://doi.org/10.1029/WR024i009p01553

Wollschläger, U., Attinger, S., Borchardt, D., Brauns, M., Cuntz, M., Dietrich, P., et al. (2017). The Bode hydrological observatory: a platform for integrated, interdisciplinary hydro-ecological research within the TERENO Harz/Central German Lowland Observatory. Environmental Earth Sciences, 76(1), 29. https://doi.org/10.1007/s12665-016-6327-5

Xu, T., & Gómez-Hernández, J. J. (2016). Characterization of non-Gaussian conductivities and porosities with hydraulic heads, solute concentrations, and water temperatures. Water Resources Research, 52(8), 6111–6136. https://doi.org/10.1002/2016WR019011

Yvon-Durocher, G., Caffrey, J. M., Cescatti, A., Dossena, M., Giorgio, P. Del, Gasol, J. M., et al. (2012). Reconciling the temperature dependence of respiration across timescales and ecosystem types. Nature, 487(7408), 472–476. https://doi.org/10.1038/nature11205

Zarnetske, J. P., Haggerty, R., Wondzell, S. M., & Baker, M. A. (2011). Dynamics of nitrate production and removal as a function of residence time in the hyporheic zone. Journal of Geophysical Research: Biogeosciences, 116(1), 1–12. https://doi.org/10.1029/2010JG001356

Zarnetske, J. P., Haggerty, R., Wondzell, S. M., Bokil, V. A., & González-Pinzón, R. (2012). Coupled transport and reaction kinetics control the nitrate source-sink function of hyporheic zones. Water Resources Research, 48(11), 1–15. https://doi.org/10.1029/2012WR011894

Zheng, L., Cardenas, M. B., & Wang, L. (2016). Temperature effects on nitrogen cycling and nitrate removal-production efficiency in bed form-induced hyporheic zones. Journal of Geophysical Research G: Biogeosciences, 121(4), 1086–1103. https://doi.org/10.1002/2015JG003162

Supplementary Material

Transit-time and temperature control the spatial patterns of aerobic respiration and denitrification in the riparian zone

G. E. H. Nogueira[1], C. Schmidt[1,2], P. Brunner[3], D. Graeber[2], J. H. Fleckenstein[1,4]*

[1] Department of Hydrogeology, Helmholtz-Centre for Environmental Research - UFZ, Leipzig, Germany.

[2] Department of Aquatic Ecosystem Analysis, Helmholtz-Centre for Environmental Research - UFZ, Magdeburg, Germany.

[3] Centre for Hydrogeology and Geothermics, University of Neuchâtel, Neuchâtel, Switzerland.

[4] Bayreuth Centre of Ecology and Environmental Research, University of Bayreuth, Bayreuth, Germany

* *corresponding author*: Guilherme E. H. Nogueira (*guilherme.nogueira@ufz.de*)

Contents of this file

Introduction

The data presented here supports the findings reported in the carried out study. It provides additional information concerning the materials and methods used for the coupled flow and reaction modelling work, as well as supporting information to the main results found during the study. Additional information and other specific data can be assessed through:
https://doi.org/10.4211/hs.476a188d9f894a77a3ed404949680cab

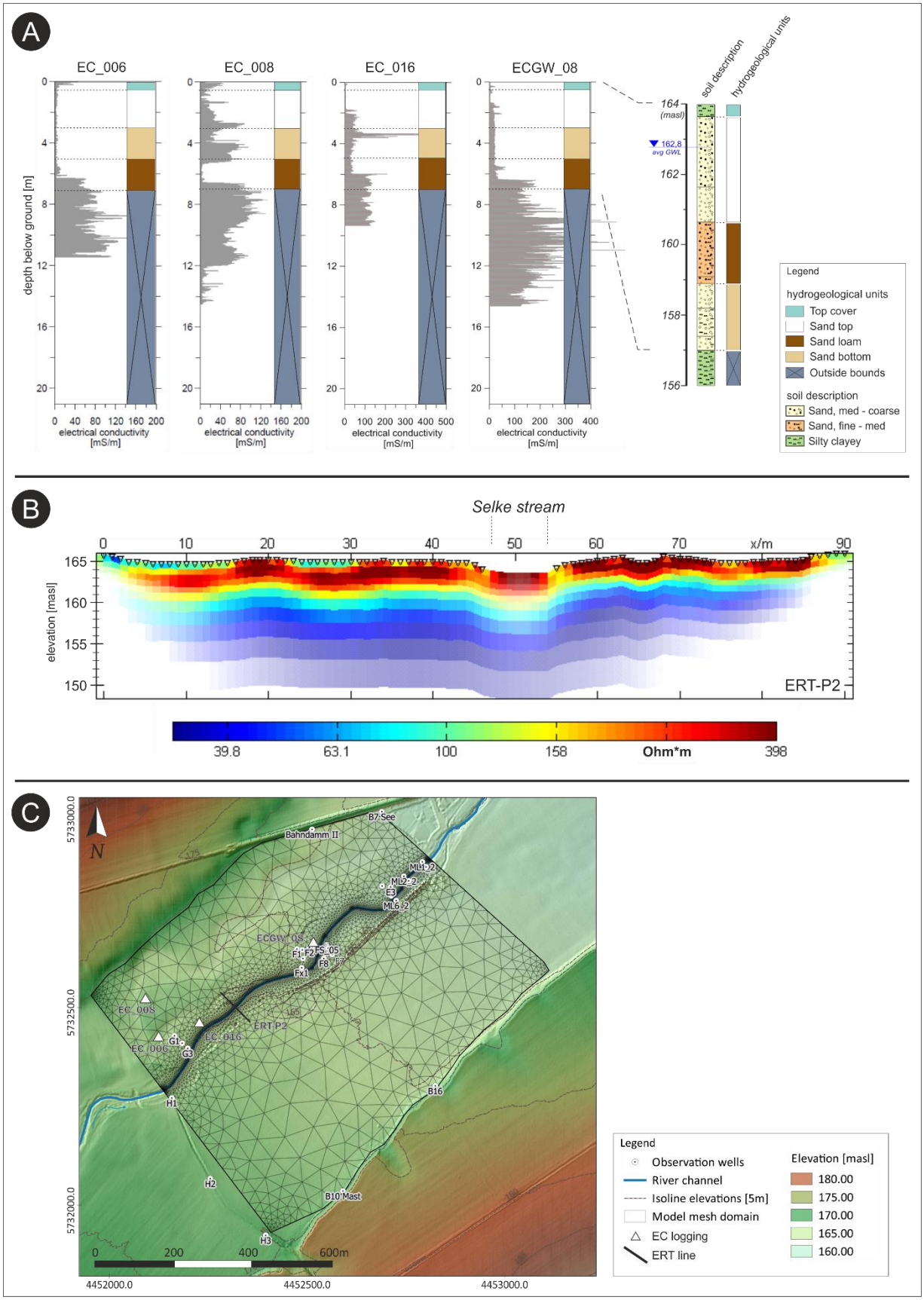
A
EC_006
EC_008
EC_016
ECGW_08
depth below ground [m]
electrical conductivity [mS/m]
soil description
hydrogeological units
164 (masl)
162.8 avg GWL
Legend
hydrogeological units
Top cover
Sand top
Sand loam
Sand bottom
Outside bounds
soil description
Sand, med - coarse
Sand, fine - med
Silty clayey
B
Selke stream
x/m
elevation [masl]
ERT-P2
39.8
63.1
100
158
Ohm*m
398
C
N
Bahndamm II
B7 See
ML1-2
ML2-2
E3
ML6-2
ECGW_08
FS_05
F1
F2
F8
F7
FX1
EC_008
ERT P2
EC_016
G1
G3
H1
H2
H3
B16
B10 Mast
0
200
400
600m
5733000.0
5732500.0
5732000.0
4452000.0
4452500.0
4453000.0
Legend
Observation wells
River channel
Isoline elevations [5m]
Model mesh domain
EC logging
ERT line
Elevation [masl]
180.00
175.00
170.00
165.00
160.00

Figure S1: a) electrical conductivity (EC) logging (higher EC values indicate a higher clay content) and soil description from borelog (Fx3) from the study area. Their locations are showed in (c).They were used for the construction of the conceptual and hydrogeological models. The hydrogeological units presented on their right are coloured according to units defined on the numerical flow model. The purple crossed area were not included in the numerical flow model (below the alluvial aquifer bottom); **b)** Electrical Resistivity Tomography (ERT) performed in the vicinity of the stream. Location showed in (c); **c)** Map of the study area showing the locations of the EC loggings and ERT line alongside the observation wells.

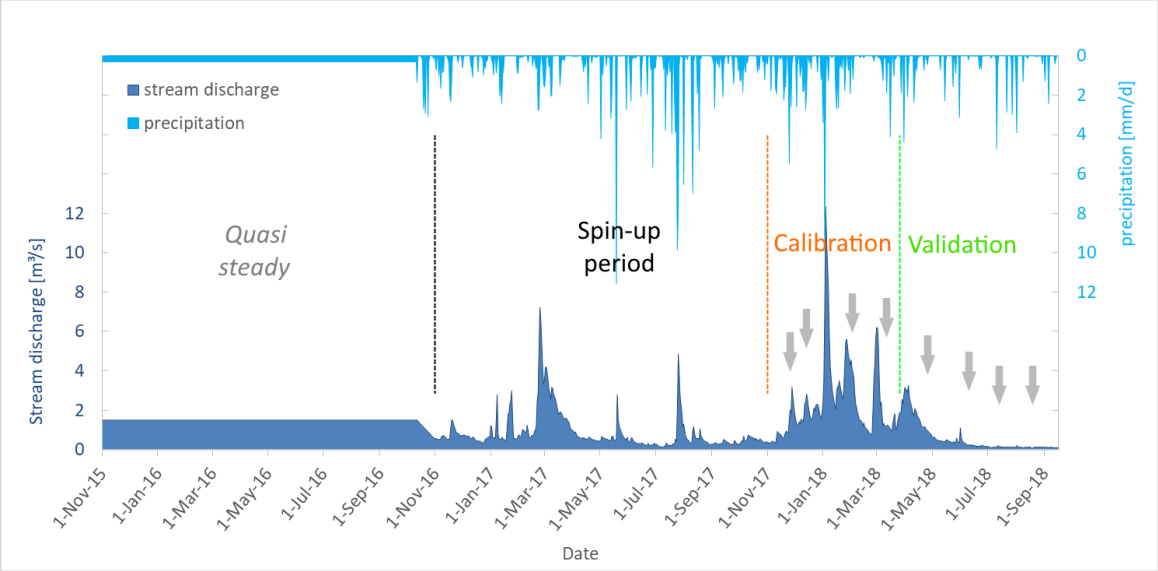

Figure S2: daily discharge and precipitation values for the simulated period. Vertical dashed lines mark, respectively, the *quasi-steady*, *spin-up*, *calibration* and *validation* periods. Grey arrows point the approximate days of carried out groundwater tracer-tests. Each calibration run comprised the sequence of *quasi-steady* and subsequent *spin-up* period to guarantee equilibrium between new parameters set by PEST and model outputs, and to assure realistic head distributions throughout the domain at the start of the calibration period.

Table S1: boundary conditions for tracer-tests and their periods in the HGS simulation. Salt concentration was converted to EC values according to a local calibration curve (and vice-versa). Tracer breakthrough curves were monitored for at least one week after tracer injection at different riparian observation wells and depths. Additional information on the experiments can be found on the provided repository link.

Tracer test	Time ON	Time OFF	Time interval (min)	Injection rate (L min^{-1} – [m^3d^{-1}])	Injected mass (Kg)
1	745.531	745.540	15	2.00 [2.80]	2.5
2	758.484	758.494	15	2.00 [2.80]	3.0
3	850.574	850.592	26	7.20 [10.36]	12.0
4	892.568	892.576	11	4.19 [6.03]	3.2
5	941.471	941.480	13	4.40 [6.34]	4.0
6	982.500	982.513	20	7.70 [11.19]	10.0
7	1031.517	1031.531	20	2.88 [4.15]	4.0

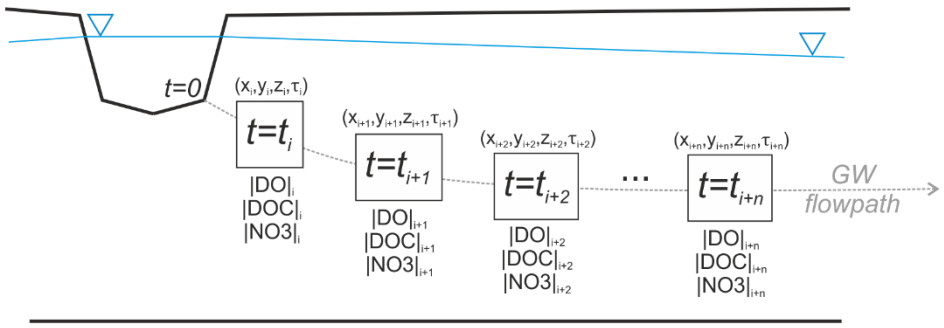

time	*reaction rate coefficients*	*solute concentrations*
$t=t_i$		$\lvert DO\rvert_{(i)}$; $\lvert DOC\rvert_{(i)}$; $\lvert NO_3^-\rvert_{(i)}$
$t=t_{i+1}$	$k_{AR(t)} = f_T\left[umax_{\_AR}\left(\frac{\lvert DO\rvert_{(i)}}{K_{DO}+\lvert DO\rvert_{(i)}}\right)\left(\frac{\lvert DOC\rvert_{(i)}}{K_{DOC}+\lvert DOC\rvert_{(i)}}\right)\right]$ $k_{DN(t)} = f_T\left[umax_{\_DN}\left(\frac{\lvert NO_3^-\rvert_{(i)}}{K_{NO3}+\lvert NO_3^-\rvert_{(i)}}\right)\left(\frac{\lvert DOC\rvert_{(i)}}{K_{DOC}+\lvert DOC\rvert_{(i)}}\right)K_I\right]$	$\lvert DO\rvert_{(i+1)} = \lvert DO\rvert_{(i)} - (k_{AR(i+1)}*(t_{(i+1)}-t_{(i)}))$ $\lvert DOC\rvert_{(i+1)} = \lvert DOC\rvert_{(i)} - ((k_{AR(i+1)}+k_{DN(i+1)})*(t_{(i+1)}-t_{(i)}))$ $\lvert NO_3^-\rvert_{(i+1)} = \lvert NO_3^-\rvert_{(i)} - (k_{DN(i+1)}*(t_{(i+1)}-t_{(i)}))$
$t=t_{i+2}$	$k_{AR(t)} = f_T\left[umax_{\_AR}\left(\frac{\lvert DO\rvert_{(i+1)}}{K_{DO}+\lvert DO\rvert_{(i+1)}}\right)\left(\frac{\lvert DOC\rvert_{(i+1)}}{K_{DOC}+\lvert DOC\rvert_{(i+1)}}\right)\right]$ $k_{DN(t)} = f_T\left[umax_{\_DN}\left(\frac{\lvert NO_3^-\rvert_{(i+1)}}{K_{NO3}+\lvert NO_3^-\rvert_{(i+1)}}\right)\left(\frac{\lvert DOC\rvert_{(i+1)}}{K_{DOC}+\lvert DOC\rvert_{(i+1)}}\right)K_I\right]$	$\lvert DO\rvert_{(i+2)} = \lvert DO\rvert_{(i-1)} - (k_{AR(i+2)}*(t_{(i+2)}-t_{(i+1)}))$ $\lvert DOC\rvert_{(i+2)} = \lvert DOC\rvert_{(i-1)} - ((k_{AR(i+2)}+k_{DN(i+2)})*(t_{(i+2)}-t_{(i+1)}))$ $\lvert NO_3^-\rvert_{(i+2)} = \lvert NO_3^-\rvert_{(i-1)} - (k_{DN(i+2)}*(t_{(i+2)}-t_{(i+1)}))$
⋮		⋮

Figure S3: schematic system of reactions taking place in each sub-section (i) of individual flow paths at every simulation time-step. The reactions were implemented in MatLab; the original script is openly available through the provided repository link.

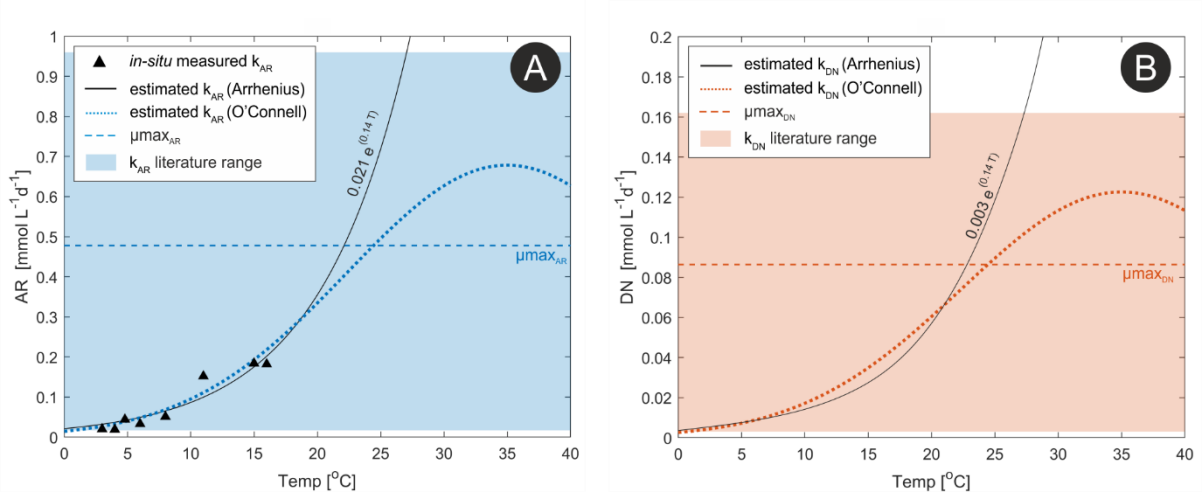

Figure S4: aerobic respiration (AR) rates **(a)** and denitrification rates (DN) **(b)** versus temperature. **a)** *in-situ* measured aerobic respiration rates (black triangles) are from Nogueira et al, 2021; estimated AR rates according to the Arrhenius equation (black line, fitted coefficients showed within the plot); estimated AR rates according to the Monod reaction rate coefficient using the O'Connell expression for the temperature correction (blue dotted line) – fitted coefficients presented in the main text; theoretical maximum AR rates (μmax_{AR}, blue dashed line); literature range of AR rates for comparison (blue shaded area); **b)** estimated DN rates according to the Arrhenius equation after Veraart et al. (2011) (black line, fitted coefficients showed within the plot); estimated DN rates using the same AR O'Connell expression for temperature correction (orange dotted line) – explanation in the main text; theoretical maximum DN rates (μmax_{DN}, orange dashed line); literature range of DN rates for comparison (orange shaded area). See table S2 for detailed information of literature range of AR and DN rates.

Table S2: Literature range of aerobic respiration (AR) and denitrification (DN) rates presented in Figure S4.

Parameter	Values (mmol L^{-1} d^{-1})	Reference
k_{AR}	0.0017 – 1.7280 [a]	*Matsunaga et al., 1993* (and references therein)
	0.0200 – 0.1840	*Nogueira et al., 2021* [b]
	0.2250 – 1.8000 [a]	*Vieweg et al., 2016*
	0.2180 – 2.6562 [a]	*Diem et al., 2013*
	0.4752 – 0.9648	*Precht et al., 2004*
μmax_{AR}	0.0173	*Henzler et al., 2016*
	0.1380	*Greskowiak et al., 2006*
	0.4780	*Trauth et al., 2014* (used in this study)
	0.1123	*Sharma et al., 2012*
	0.1382	*Frei et al., 2012*
k_{DN} [c]	0.0081	*Shuai et al., 2017*
	0.0497	*Schipper et al., 1993*
	0.1188	*Gu et al., 1997*
	0.1620	*Maag et al., 1997*
μmax_{DN}	0.0030	*Greskowiak et al., 2006*
	0.0090	*Henzler et al., 2016*
	0.0691	*Sharma et al., 2012*
	0.0860	*Trauth et al., 2014* (used in this study)
	0.0920	*Frei et al., 2012*

[a] the highest k_{AR} values (>1.0 mmol L^{-1} d^{-1}) are considered outliers and are not shown in Figure S4; [b] data used to fit the coefficients of the O'Connell temperature relation in this study; [c] presented values of k_{DN} are only the maximum DN rates present on the respective referred studies.

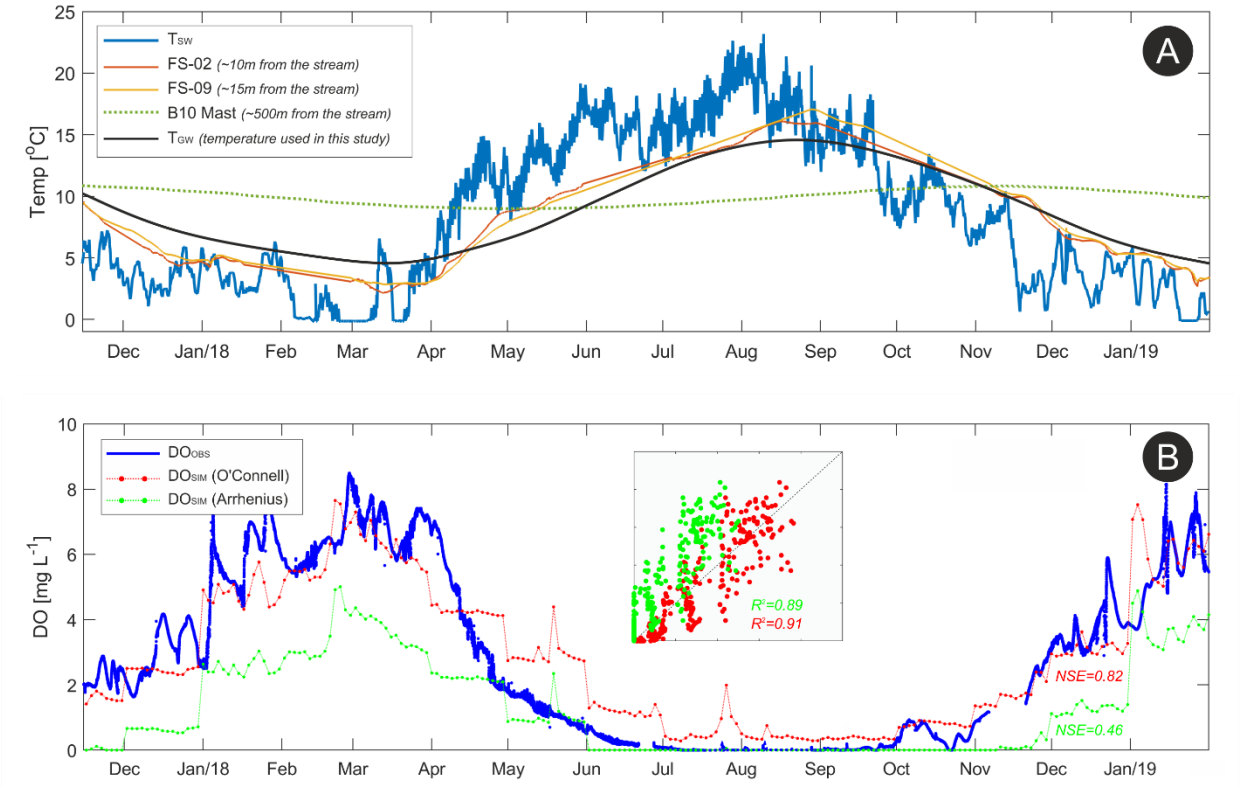

Figure S5: a) water temperature time-series: stream water temperature (T_{SW}), groundwater temperature from different observation wells with increasing distance from the stream (FS-02, FS-09, and B10, respectively), and the groundwater temperature used in this study (T_{GW}) for the calculation of varying reaction rate coefficients. It can be depicted that heat propagation and short-term fluctuations from the stream are damped already few meters from the stream, whereas only the general seasonal patterns are preserved on the near stream groundwater; **b)** example of observed and simulated riparian dissolved oxygen (DO) for the observation well F7 based on transit-times extracted from the numerical flow model and the application of the flow path-reaction model. Two DO simulations and their Nash Sutcliffe Efficiency (NSE) are shown to compare the two different expression accounting for the temperature correction of reaction rate coefficients (O'Connell and Arrhenius, Figure S4). The inset plot in (b) shows the correlation coefficient (R^2) between simulated and observed DO values.

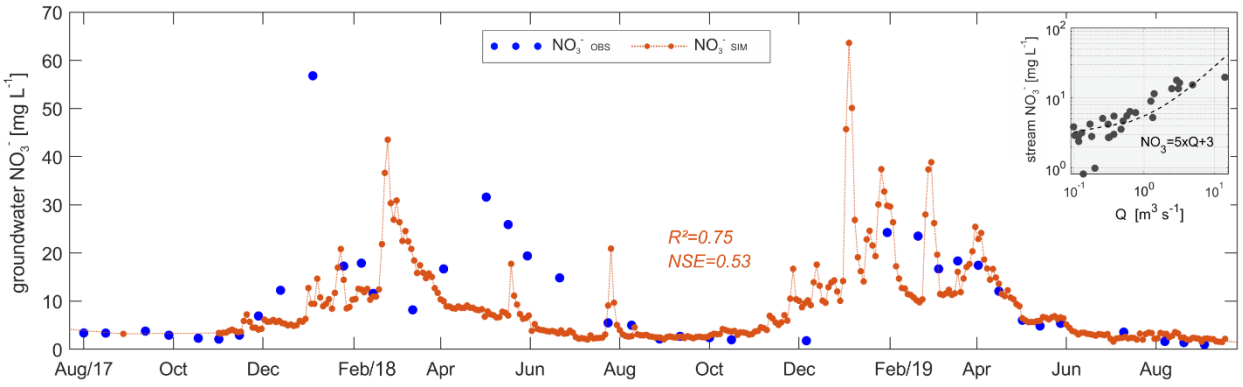

Figure S6: a) observed and simulated nitrate (NO_3^-) in the groundwater observation well F7. Simulations are based on field-data scenarios considering increasing initial NO_3^- concentrations with stream discharge (NO_3^- = 5xQ+3, inset plot), the transit-times extracted from the numerical flow model, and the application of the flow path-reaction model. The NSE and R^2 between simulated and observed groundwater NO_3^- concentrations are shown in the plot. Only biweekly measurements of NO_3^- were available for the simulation period.

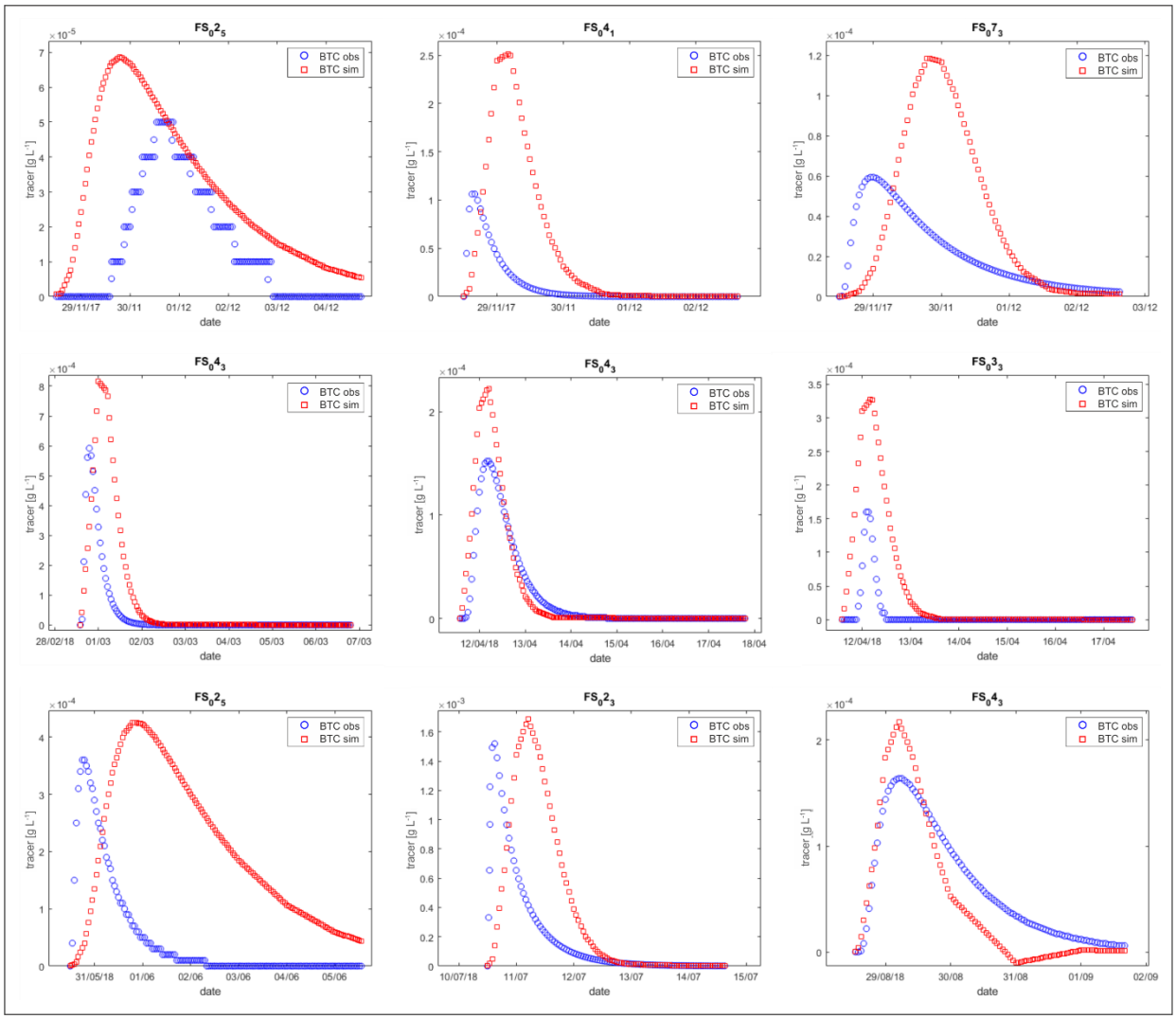

Figure S7: observed and simulated tracer breakthrough curves (BTC) (blue circles and red squares, respectively) from the well-to-well tracer-tests at the riparian zone of the Selke stream. Negative simulated concentrations on FS_04_3 are related to small numerical dispersions in the flow model. Observed BTC, relative metrics and other specific information from tracer-tests can be found through the provided repository link, as well as in Nogueira et al. (2021).

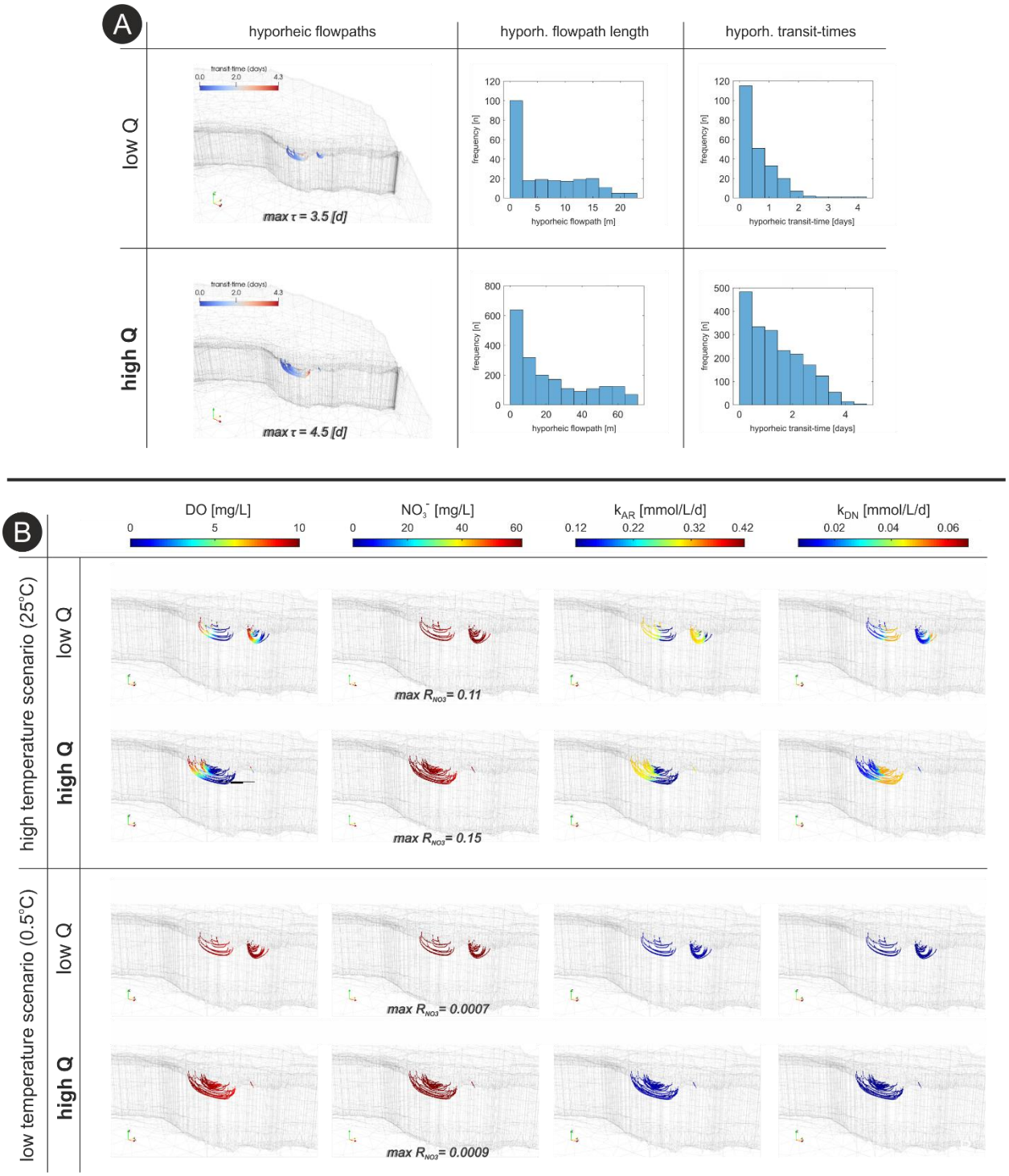

Figure S8: a) hyporheic flow paths with respective lengths and transit-times distribution for low Q (0.12 m^3/s) and high Q (12.0 m^3/s); **b)** hyporheic distribution of dissolved oxygen (DO), Nitrate (NO_3^-), aerobic respiration (k_{AR}), and denitrification (k_{DN}) for four different scenarios of stream discharges and water temperature. The maximum R_{NO3} (fraction of NO_3^- removed divided by NO_3^- influx) of each scenario is showed alongside the NO_3^- concentrations.

Chapter four

Spatio-temporal variations of water sources and mixing spots in a riparian zone

G. E. H. Nogueira[(1)], C. Schmidt[(1,2)], D. Partington[(3)], P. Brunner[(4)], J. H. Fleckenstein[(1,5)]

(1) Department of Hydrogeology, Helmholtz Centre for Environmental Research-UFZ, Leipzig, Germany.
(2) Department of Aquatic Ecosystem Analysis, Helmholtz Centre for Environmental Research-UFZ, Magdeburg, Germany
(3) National Centre for Groundwater Research and Training, & College of Science and Engineering, Flinders University, Adelaide, Australia
(4) Centre of Hydrogeology and Geothermics (CHYN), Neuchâtel, Switzerland
(5) Bayreuth Center of Ecology and Environmental Research, University of Bayreuth, Bayreuth, Germany

Submitted to Hydrology and Earth System Sciences XX(x), 2021, DOI: 10.5194/hess-2021-573

Abstract

Riparian zones are known to modulate water quality in stream-corridors. They can act as buffers for groundwater borne solutes before they enter the stream at harmful, high concentrations, or facilitate solute turnover and attenuation in zones where stream water (SW) and groundwater (GW) mix. This natural attenuation capacity is strongly controlled by the dynamic exchange of water and solutes between the stream and the adjoining aquifer, creating potential for mixing-dependent reactions to take place. Here, we couple a previously calibrated transient and fully-integrated 3D surface-subsurface, numerical flow model with a Hydraulic Mixing Cell (HMC) method to map the source composition of water along an overcall losing reach (900m) of the 4th-order Selke stream and track its spatio-temporal evolution. This allows us to define zones in the aquifer with similar fractions of surface- and groundwater per aquifer volume (called "mixing hot-spots"), which have a high potential to facilitate mixing-dependent reactions and in turn enhance solute turnover. We further evaluated the HMC results against hydrochemical monitoring data. Our results show that on average about 50% of the water in the alluvial aquifer consists of infiltrating SW. Within about 200m around the stream the aquifer is almost entirely made up of infiltrated SW with nearly no other water sources mixed in. On average, about 9% of the model domain could be characterized as "mixing hot-spots", which were mainly located at the fringe of the geochemical hyporheic zone rather than below the streambed. This percentage could rise to values nearly 1.5 times higher following large discharge events. Moreover, event intensity (magnitude of peak flow) was found to be more important for the increase of mixing than event duration. Our modelling results further suggest that discharge events more significantly increase mixing potential at greater distances from the stream. In contrast near and below the stream, the rapid increase of SW influx shifts the ratio between the water fractions to SW, reducing the potential for mixing and the associated reactions. With this easy-to-transfer framework we seek to show the applicability of the HMC method as a complementary approach for the identification of mixing hot-spots in stream corridors, while showing the spatio-temporal controls of the SW-GW mixing process and the implications for riparian biogeochemistry and mixing-dependent turnover processes.

4.1 Introduction

4.1.1 Importance of mixing at the riparian zone

The importance of riparian zones for regulating water quality in stream corridors has long been recognized (Bernhardt et al., 2017; Gu et al., 2012; Hill, 1996; Jencso et al., 2010; Mayer et al., 2006; McClain et al., 2003; Vidon et al., 2010). Their natural attenuation capacity is partly related to dynamic water and solute

exchanges between the stream and aquifer. Specifically, the mixing of stream water (SW) and groundwater (GW) within the riparian zone increases the potential for biogeochemical reactions by bringing different reactants in contact (Gassen et al., 2017; Hester et al., 2019, 2014; Sawyer, 2015; Sawyer et al., 2014; Trauth et al., 2015). For instance, riparian zones have shown large removal capacities for nitrate (NO_3^-) derived from nitrogen-based fertilizers leaking into groundwater below agricultural areas (Ocampo et al., 2006; Pinay et al., 2015; Ranalli and Macalady, 2010; Vidon and Hill, 2004). Particularly along losing stream sections, infiltrating SW can increase the availability of dissolved organic carbon (DOC) as an electron donor in the riparian aquifer and in turn enhance denitrification rates following oxygen depletion (Battin, 1999; Trauth et al., 2018; Zarnetske et al., 2011).

The transit of a stream water parcel after infiltration across the streambed into the riparian aquifer is followed by progressive mixing with ambient groundwater. Here, we refer to mixing at the macroscopic level, i.e. the colocation of different source waters within a defined volume of the aquifer (e.g. a numerical model cell or element), rather than pore-scale, physical-mixing, which leads to solute and molecules being present simultaneously in an overlapping area (Bear and Verruijt, 1987; Cirpka and Kitanidis, 2000; Dentz et al., 2011; Kitanidis, 1994). Increased macroscopic mixing, however, will in turn also lead to increased potential for physical mixing and associated reactions. In this sense, several studies have showed how macroscopic SW-GW mixing dynamics can control biogeochemical reactions within the riparian zone (Hester et al., 2013; McClain et al., 2003; Sawyer, 2015; Sawyer et al., 2014; Sawyer and Cardenas, 2009; Song et al., 2018; Stegen et al., 2016). For example, Hester et al. (2019) have demonstrated that increasing stream stage enhanced the mixing-dependent denitrification of upwelling NO_3^-, with a concomitant shift of the SW-GW mixing-interface to deeper parts of the hyporheic zone (HZ). Moreover, it has been proven that the highest potential for mixing-dependent turnover of groundwater-borne solutes is at the fringe of the HZ, where mixing between infiltrating SW and local flowing GW might develop to a larger degree (Hester et al., 2019, 2017, 2014; Sawyer and Cardenas, 2009; Trauth et al., 2015; Triska et al., 1989), Fig.1. These mixing-triggered processes could represent the last natural protection before harmful groundwater-borne solutes such as NO_3^- enter a stream. As SW-GW exchange (and subsequent SW-GW mixing) is a spatially and temporally dynamic process, identifying the different water sources within the riparian zone and their mixing dynamics can be helpful to advise adequate stream restoration plans to improve aquatic ecosystem health (Hester et al., 2017; Lawrence et al., 2013). However, to the best of our knowledge, the continuous spatio-temporal changes of SW-GW mixing degrees due to transient hydrological forces have rarely been assessed at the stream corridor scale (Berezowski et al., 2019; Gomez-Velez et al., 2017; Lessels et al., 2016; Liggett et al., 2015). This is partly due to the significant effort required to identify different water sources and their dynamics at high spatio-temporal resolution at the river corridor scale.

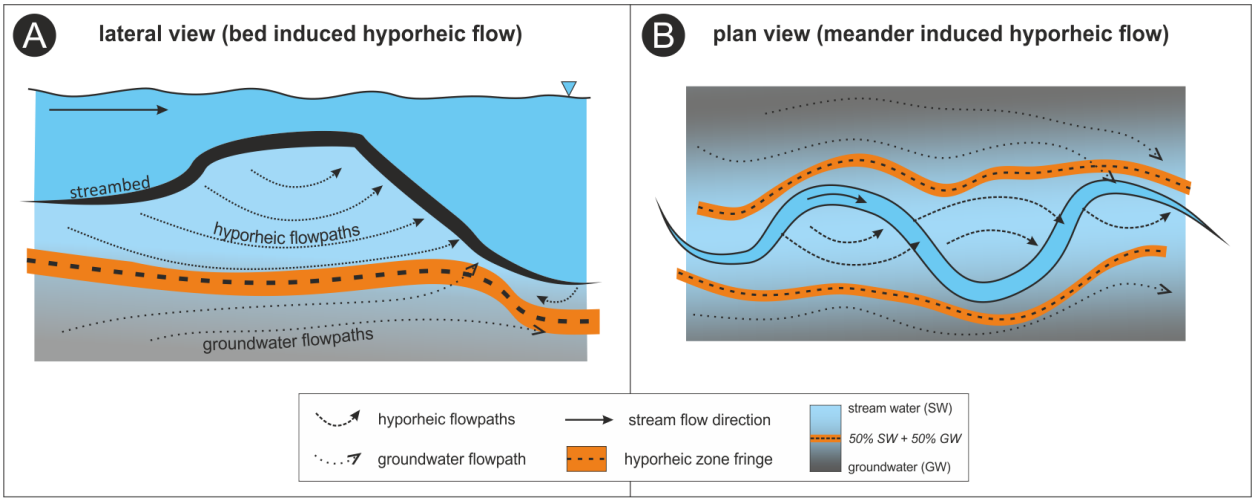

Fig.1: Scheme of two different hyporheic flow types and their flow paths. The orange area highlights the hyporheic zone fringe (Triska *et al.*, 1989), with highest turnover potential for groundwater-borne solutes.

4.1.2 Identification of water sources and their relative abundance in the riparian zone.

In order to map different water sources and assess the locations and temporal variations of SW-GW exchange processes at different scales within stream corridors, end-member mixing models (e.g., with Chloride, or other traceable chemical components or isotopes) have been used. They can reveal spatio-temporal patterns of mixing in the riparian zone and provide a quantitative estimate of mixing ratios (Appelo and Postma, 2005; Battin, 1999; Pinay et al., 1998; Schilling et al., 2017; Stigter et al., 1998), as long as it is possible to properly identify the system end-members (McCallum et al., 2010). Geostatistical methods have also been used to identify and understand the distribution of different water sources within riparian zones (Lessels et al., 2016). However, these approaches rely on intense water sampling for identifying the extent, to which different water sources mix (Biehler et al., 2020; Lessels et al., 2016; Schneider et al., 2011). Yet, such methods still have limitations in capturing the full spatio-temporal dynamics of SW-GW exchange and mixing in stream corridors. Assessing the spatio-temporal evolution of mixing zones and their implications for the biogeochemistry of stream corridors remains a significant challenge.

The use of hydrodynamic models can yield detailed insights into stream-riparian zone exchange dynamics (Broecker et al., 2021; Hester et al., 2017; Liu and Chui, 2018). In particular 3D fully-integrated surface-subsurface models that explicitly account for SW-GW exchange fluxes at high spatial and temporal resolution, such as HydroGeoSphere (HGS, Aquanty Inc., 2015) or ParFlow (Kollet and Maxwell, 2006) are well suited for this purpose. Still, most numerical models cannot quantify the extent of different water sources solely based on computed water fluxes and resulting water flow paths (Gomez-Velez et al., 2017). Such quantification usually requires additional solute transport routines, and in turn extra computational

resources, which can be facilitated via particle tracking techniques (Frei et al., 2012; Nogueira et al., 2021b). The Hydraulic Mixing-Cell (HMC) method (Partington et al., 2011) is one such approach that allows a quantification of mixing and can be applied to any hydrological model that provides an explicit fluid mass balance at sufficiently resolved spatial scale (e.g., at the scale of numerical model cells). The method was originally developed to identify the contribution of different water sources - namely surface water (e.g., surface runoff) and groundwater - to the total streamflow hydrograph (Gutiérrez-Jurado et al., 2019; Liggett et al., 2015; Partington et al., 2013, 2012), but it has also been applied to track water from different sources in other contexts such as groundwater abstraction (Schilling et al., 2017), or the spatio-temporal variation of mixing fronts (Berezowski et al., 2019).

4.1.3 Purpose of this study

In this study, we aim to map the different water sources and assess the dynamics of their macroscopic mixing within a riparian zone in order to evaluate the potential for biogeochemical turnover. To do so we use a state of the art numerical model and mixing cell routine. Rather than explicitly simulating the reactions induced by SW-GW mixing (Hester et al., 2019, 2014), our objectives are to:

1. quantify the different water sources within the riparian zone and their spatio-temporal evolution;
2. assess the relationship between flow dynamics and the degree of macroscopic mixing of these different waters; and
3. evaluate the formation and dynamics of mixing hot-spots within the riparian zone.

To reach our objectives we do not aim to produce a meticulously calibrated, complex model for the studied site, but rather to harness the insights that detailed field observations in conjunction with such numerical modelling of macroscopic mixing provide (i.e., an "hypothetical reality") (Mirus et al., 2011). We again emphasize that here "mixing" refers to the colocation of different source waters within a defined volume of aquifer (e.g., a numerical model cell). Mixing degrees were computed based on transient results of HMC, which does not require further solute transport simulations in order to track different water components in space and time. The HMC routine was coupled to a transient and fully-integrated 3D numerical flow model covering the riparian zone of a 4th-order stream. We evaluate the HMC results in the light of hydrochemical data, and further quantify distinct mixing hot-spots that have the potential to enhance mixing-dependent turnover processes (Hester et al., 2019, 2014; Trauth et al., 2014). With this easy-to-transfer framework we also seek to demonstrate the utility of the HMC method for the identification of mixing hot-spots at the river-corridor scale.

4.2 Methods

The steps followed in this study to assess the spatio-temporal variations of water sources and mixing within a riparian zone are summarized in Fig.2. In brief, following field data collection, a 3D numerical flow model was developed and calibrated against the collected data (Nogueira et al., 2021b). The HMC method is then coupled to the numerical model, whereas results are additionally evaluated according to additional hydrochemical data (i.e., water samples) for the further mapping of water sources and analysis of mixing degrees in the riparian zone. In the subsequent sections we detail each step and methods followed.

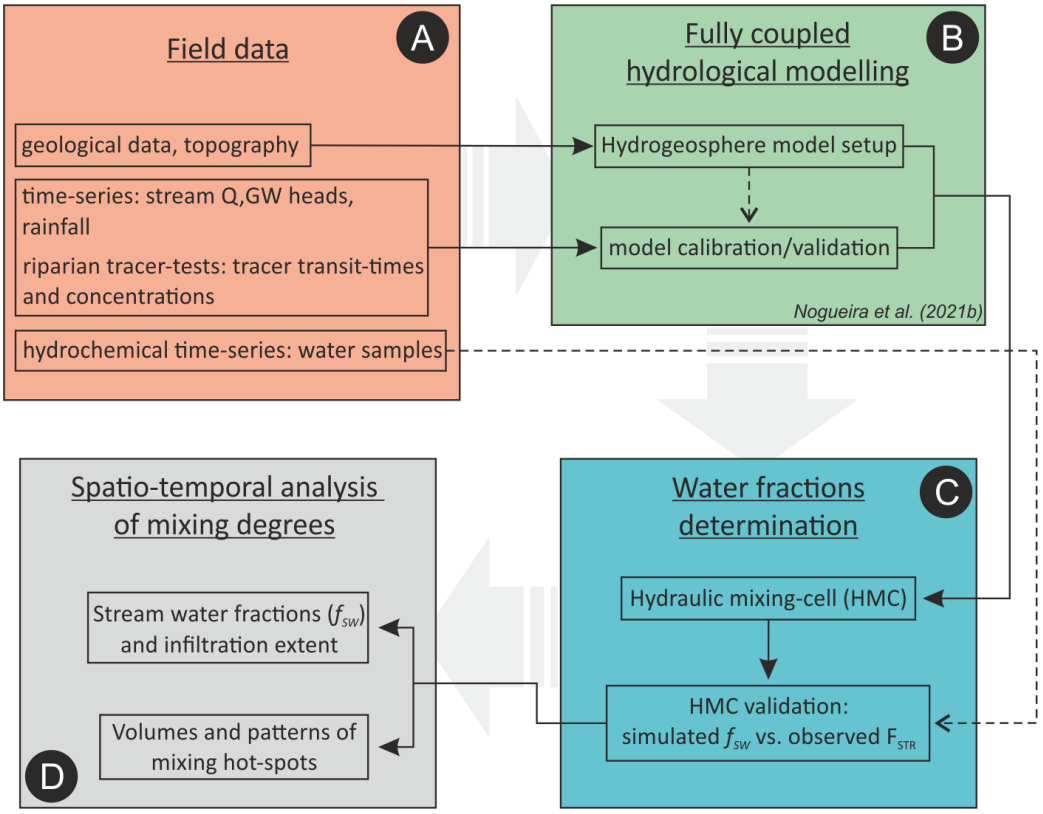

Fig.2: Flowchart of methods used to assess the spatio-temporal dynamics of the hyporheic zone and of the mixing degrees.

4.2.1 Study area and hydrological modelling

We coupled the HMC method to a previously calibrated numerical surface-subsurface flow model (Nogueira et al., 2021b) of a highly instrumented test-site of the TERENO observatory (Wollschläger et al., 2017). The study site is located within the catchment of the Selke Stream, a 4th-order perennial stream, in central Germany, Fig.3. The studied stream section (appx. 900 m) is characterized by predominantly losing conditions, which has been linked to enhanced turnover of groundwater-borne NO_3^- at the site due

to mixing with infiltrating stream-borne DOC and subsequent denitrification (Gassen et al., 2017; Lutz et al., 2020; Trauth et al., 2018). The alluvial aquifer consists of up to 8 m-thick fluvial sediments, with grain sizes ranging from medium sands to coarse gravels, underlain by less permeable clay-silt deposits forming its bottom. The numerical flow model presented in Nogueira *et al.*, 2021b, which is based on the code HydroGeoSphere (HGS), is used here for coupling the HMC method since HGS explicitly computes fluid mass balances at every model cell and in each time-step of the simulation. HGS provides a fully-integrated 3D solution for variably saturated subsurface flow (using Richards's equation) and a 2D depth-averaged solution for surface flows based on the diffusive wave approximation to the St. Venant equations (Therrien et al., 2010).

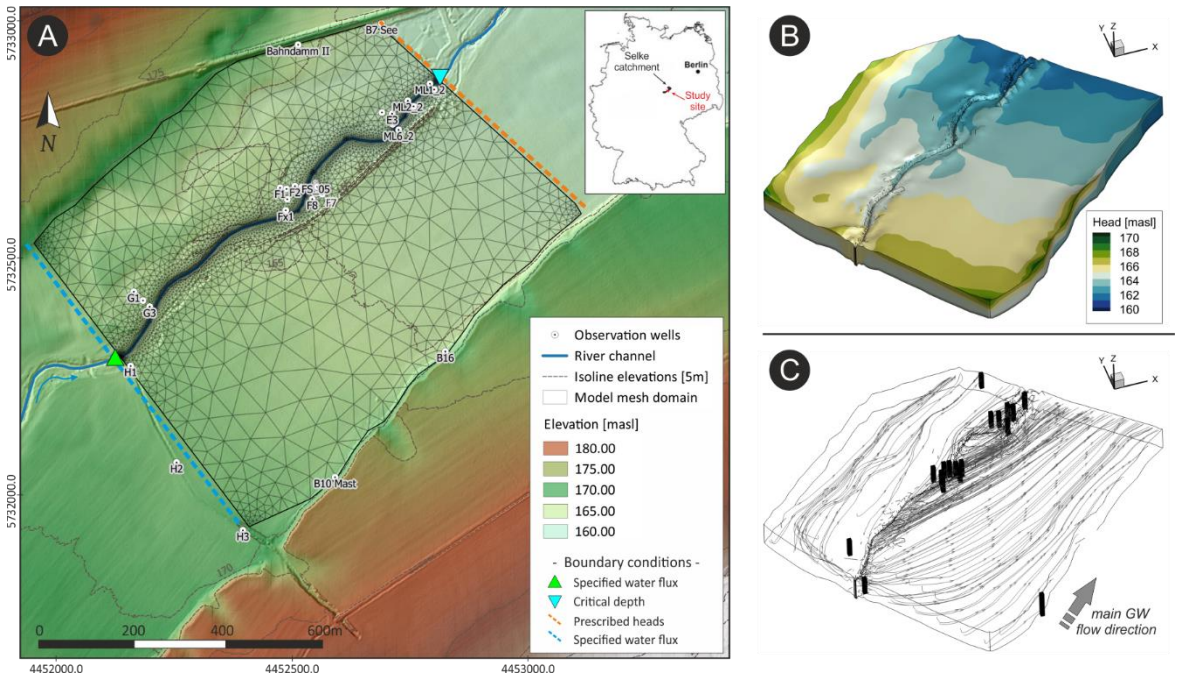

Fig.3: a) study area and model domain; **b)** simulated groundwater heads for a baseflow (Q=0.1 m^3/s) scenario; **c)** streamlines (grey lines) depicting main groundwater flow direction for the baseflow scenario. Black vertical lines in (c) depict some of the wells shown in (a). Note the vertical exaggeration of the 3D plots (10x).

The flow model parameterization is only briefly summarized here, as the model and its calibration are described in detail in Nogueira *et al.* 2021b). The simulated domain (900 × 770 × 10 m) was divided into four main hydrogeological units according to geophysical and borelog data, which further indicates the thinning of the alluvial aquifer with distance from the stream (Lutz et al., 2020; Trauth et al., 2018). Thus, the simulated domain covers most of the mapped alluvial aquifer present in the area. The bottom of the numerical model was set according to the less permeable clay-silt deposits. The boundary conditions (BCs)

on the model surface domain were defined as (i) groundwater recharge (as a fraction of daily precipitation) at the model top, (ii) specified water flux at the model stream inlet according to discharge values measured at a gauge station about 3000m upstream of the study site, and (iii) a critical depth BC at the model stream outlet (Fig.3a). The BCs on the subsurface model domain were defined as (iv) specified water flux representing ambient groundwater flow at the upstream side of the model, and (v) prescribed time-varying hydraulic heads at the downstream side of the model (Fig.3a). The other laterals and the bottom of the model domain were set as no-flow boundaries. The model was calibrated using the PEST software (Doherty, 2018) based on stream discharge values, multi-well groundwater heads, as well as multiple breakthrough curves from performed groundwater tracer-tests (Nogueira et al., 2021a, 2021b). Automatically calibrated parameters were within the literature ranges and the calibrated model showed a very good match between observed and simulated values, with coefficient of determination (R^2) and Kling-Gupta-Efficiency (KGE) (Gupta et al., 2009; Knoben et al., 2019) generally above 0.8 and 0.5, respectively. The flow model was previously calibrated for the period of 2017-2018 and here we have only implemented changes in the BCs, without any additional model calibration. We performed transient simulations using daily forcing inputs for the hydrological years 2013-2016 since this is the period with more hydrochemical data available to further validate the HMC results. The quality of the flow model was evaluated according to the water balance error, R^2 between observed and simulated groundwater heads and stream discharge for the period under analysis (2013-2016), as well as KGE.

4.2.2 The Hydraulic Mixing-Cell (HMC) method

The contribution of water sources (and subsequent mixing degrees) in each model cell was calculated with the HMC method (Partington et al., 2013, 2012, 2011). The different water sources have to be predefined in terms of their origin (e.g., stream water, groundwater, and rainfall), which are related to the BCs applied to the numerical model. HMC calculation depends only on computed nodal water fluxes and does not involve any extra parameters. The HMC method uses the ‘‘modified mixing rule’’, which simulates a mixing regime between perfect mixing and piston flow. Initially, all model cells have an artificial “initial” water fraction. In the subsequent time-steps, different water sources are mixed according to volumes of water flowing into and out of a cell accordingly (Partington et al., 2011):

$$f_{i(w)}^{t} = \left(\frac{V_i^{t-1}}{V_i^{t}} - \frac{Vbc_{out}^{t} + \sum_{j=1}^{m} V_{ij}|_{t-1}^{t}}{V_i^{t}} \right) f_{j(w)}^{t-1} + \frac{Vbc_{w}^{t} + \sum_{j=1}^{n} V_{ji}|_{t-1}^{t} \; f_{j(w)}^{t-1}}{V_i^{t}} \quad (1)$$

where $f_{i(w)}^{t}$ [-] is the computed water fraction *w* at time-step *t* in cell *i*, *n* and *m* are sources and sinks for cell *i*, $f_{j(w)}^{t-1}$ denotes the water fraction *w* at time *t-1* in a neighbouring cell *j*, *V* denotes the volume with the

superscript denoting time-step and subscript *i* denoting the cell, *ij* denoting volume into cell *j* from cell *i* over the time-step from *t-1* to t, *ji* denoting volume from neighbour cell *j* into cell *i*, and Vbc_w^t is a volume from the inflowing boundary condition associated with water fraction *w* and Vbc_{out}^t is a volume summed from all outflowing boundary conditions at cell *i*. Inflow from adjacent cells is assigned the computed water fractions from the upstream cell. The HMC has an independent sub-time-step routine to calculate water fractions between the adaptive HGS time-steps, which circumvents the need of extremely small time-steps in the HGS simulations (Partington et al., 2013). This sub-routine is required to avoid instability during the HMC calculations, which can occur if the volume of water leaving a cell over a time-step is greater than the volume in storage.

Within our simulations, we defined three main water sources to be tracked, namely stream water (f_{SW}), groundwater (f_{GW}), and floodplain water (f_{FW}). The f_{SW} represents any water parcel that infiltrates into the subsurface domain through streambed cells; the f_{GW} represents groundwater flowing into the domain through the upstream subsurface boundary; the f_{FW} represents water that percolates from soil top through the unsaturated zone (e.g., from rain or flood events). An additional water source named initial groundwater (f_{GWi}) was defined representing the "initial" water residing in the model cells at the beginning of the simulations. We carried out a warm-up period during the simulations in order to flush f_{GWi} and have a more realistic distribution of the three water fractions at the domain at the start of our analyses. The warm-up period consisted of a two-year simulation period using constant average BC values. Following this period, the f_{GWi} fraction was virtually zero, whereas the three remaining water fractions were the only fractions observed throughout the domain. Thus, in the remaining analyses we mainly consider the three remaining water fractions for our calculations.

The sum of all HMC fractions in each model cell is $[f_{SW}+f_{GW}+f_{FW}]=1$, for an error-free fluid mass balance. With that approach, we can evaluate the composition of the different water fractions at any time-step and location at the model domain. We further spatially aggregated the different HMC fractions to assess the temporal variation of their contribution to the total volume of the simulated domain with the *Integration* function in TecPlot 360 EX, Version 2019 R1 (TecPlot, Inc.) using the different HMC fractions as scalar variables and dividing the results by the total volume of the simulated domain. The function integrates the numerical cells within the simulated domain taking into account only the fraction of interest that comprises each cell volume. The calculation sums the resulting quantities over the domain to produce the integrated result, which is then normalized by the total volume of the simulated domain (V_{tot}). Thus, the resulting volume V_w represents a percentage of the total simulated domain:

$$V_w = \frac{\sum_{p=1}^{P} (V_p \, f_{w,p})}{V_{tot}} \times 100\% \quad (2)$$

where V_w is the percentage volume of a HMC fraction *w* within the model domain in a given time-step, V is the volume of a model cell, *p* is a cell (from *p*=1 to P) with a specific water fraction f_w (e.g., f_{SW}, f_{GW}, f_{FW}), and V_{tot} is the total volume of the simulated domain (4.63×10^6 m³).

A similar version of Eq.2 was used to assess the spatio-temporal evolution of the hyporheic zone (HZ). To do so, we employ the *geochemical definition* of the HZ, similar to the one proposed by Triska et al. (1989), where the HZ is the area within the riparian zone containing more than 50% of stream water ($f_{SW} \geq 0.5$) in the mixture of waters. Using Eq.2, we computed the total volume of the HZ (V_{HZ}) in each time-step by only aggregating cells presenting $f_{SW} \geq 0.5$ in the domain. This *geochemical definition* was preferred over the *hydrodynamic definition* (Gooseff, 2010; Trauth et al., 2013) because of its stronger relevance for biogeochemical transformations (Boano et al., 2010; Gomez-Velez et al., 2017). Besides, in strongly losing streams, the HZ definition based on hyporheic streamlines (i.e., *hydrodynamic definition*) would describe the HZ as a very narrow zone limited to the streambed and its immediate vicinity only, since most of the infiltrating SW does not immediately return to the stream.

4.2.3 HMC validation and stream water fraction calculation

In order to validate the HMC results, we compared the simulated stream water fractions (f_{SW}) with the calculated stream water fractions (F_{STR}) at riparian observation wells. The F_{STR} is based on a two end-member chloride (Cl^-) linear mixing model (Appelo and Postma, 2005). By assuming Cl^- as a conservative solute, mixing between two independent end-members occurs, namely stream water and groundwater farther away from the stream (not affected by infiltrating stream water). The fraction of stream water in the riparian groundwater was computed as:

$$F_{STR} = \frac{[Cl^-_{obs}] - [Cl^-_{GW}]}{[Cl^-_{SW}] - [Cl^-_{GW}]} \quad (3)$$

where $[Cl^-_{obs}]$, $[Cl^-_{GW}]$, and $[Cl^-_{SW}]$ indicates the Cl^- concentration measured in an observation well, in the groundwater distant from the stream, and in the stream at a given time, respectively. Calculations and measurements are based on biweekly collected water samples of 2014-2016. Groundwater was sampled with a peristaltic pump placed at the middle of the fully screened wells and surface water was collected as grab samples. Samples were stored and analysed in the lab following standard procedures (Trauth et al., 2018). The groundwater end-member $[Cl^-_{GW}]$ was assumed to be equal to values from the observation well

B10 (95 ± 5 mg L^{-1}, Fig.S1, supplementary material). To compare F_{STR} and f_{SW}, we extracted simulated f_{SW} values from the locations of the observation wells in the numerical model by averaging the f_{SW} values of all fully-saturated cells that comprises each well position. That was done to approximate how water samples were collected at the fully screened wells, which likely results in sampling of a mix of the whole saturated column rather than from a specific groundwater depth. In a perfect model $F_{STR}=f_{SW}$ independent of the other simulated HMC fractions. The quality of the results was evaluated for each well in terms of the coefficient of determination (R^2) and with the nonparametric Wilcoxon rank-sum test (Ziegel et al., 2011) between F_{STR} and f_{SW} datasets. With the test, a result of $h=0$ (null hypothesis) indicates the distributions of both populations are statistically equal. A value of $h=1$ (alternative hypothesis) indicates the distributions of both populations are not equal.

4.2.4 Calculation and analyses of mixing degrees

Mixing degree calculation

At this stage, the results enable us to track and assess the different water source compositions at different time-steps and locations of our domain. We further computed a mixing degree (d) to quantify the degree to which different water sources mix within a model cell similarly to Berezowski *et al.* (2019). We emphasize that the quantification of mixing here does not refer to true pore-scale mixing, but it rather gives an indication of how different water sources are "mixed" within a model cell in a given time-step based on neighbouring cells inflows and outflows. In that sense it provides a proxy for the potential for true pore-scale mixing to occur within that model cell.

For a three end-member mixing, where each end-member is a different water source (e.g., f_{SW}, f_{GW}, and f_{FW}), any three fractions combined could be represented by a vector in a 3D coordinate space: d=[f_{SW}, f_{GW}, f_{FW}], whereas a "perfect mixing" (e.g., equal fractions of different water sources) is represented by a vector d_p=[$^1/_3$, $^1/_3$, $^1/_3$] (Fig.S2, supplementary material). Thus, the resulting mixing degree d can be calculated as the Euclidean distance between the vectors d and d_p taking into account that a maximum value for a given fraction can only be 1, as well as that the fractions have to sum up to 1 within a cell (for an error-free fluid mass balance). A more general equation to quantify the mixing degree for three (or more) end-members (w) could be written as:

$$d = 1 - \left[\frac{\sqrt{\left(^1/_w - f_1\right)^2 + \left(^1/_w - f_2\right)^2 + \ldots + \left(^1/_w - f_w\right)^2}}{\left(\sqrt{2} \times \sqrt{w}/_w\right)} \right] \quad (4)$$

where f_1, f_2, and f_w represent HMC fractions. Based on preliminary results, we have observed that actual volumes of f_{FW} were very low in comparison to f_{GW} and f_{SW} in the fully saturated portion of the domain as

it will be demonstrated in section 3.2. This occurs because recharge from rainfall is very low locally (Nogueira et al., 2021b), and the percolation of water from the top of the model domain is further limited to only occasional episodes. Therefore, we have employed a simplified version of the Eq.4 considering a two end-member mixing only. To do so, we combined the two end-members f_{GW} and f_{FW} to a single one (e.g., [f_{GW}+ f_{FW}], Fig.S2, supplementary material), which reduces the mixing model to a 2D case. This streamlined two end-member mixing is the preferred one used throughout the manuscript because otherwise resulting *d* values would be consistently very low in the simulations, which would impair their further analyses. In this formulation, $d=1$ represents a perfect mixing within a cell at a given time-step (e.g., equal water fractions: f_{SW}=0.5 and f_{GW}+f_{FW}=0.5), while smaller values would indicate a disproportional contribution of one or another water sources to the mixture (e.g., too much of one water source and too few of another). By calculating *d* in every location and time-step, we can identify the model cells where the water sources of interest are mixed at equal proportions and assess its dynamics without depending on solute transport simulations.

To analyse the temporal variation of different mixing degrees, we spatially aggregated model cells presenting different *d* values (e.g., $d > 0$, $d \geq 0.25$, $d \geq 0.50$, and $d \geq 0.75$) in each time-step and compared them to the total volume of the simulated domain (Eq.5), as well as to the total HZ volume (Eq.6) to assess their relative percentage in each time-step:

$$\mathrm{V}_d = \frac{\sum_{p=1}^{\mathrm{P}} (V_p\, d)}{V_{tot}} \times 100\% \tag{5}$$

$$\mathrm{V}_{d\_HZ} = \frac{\sum_{p=1}^{\mathrm{P}} (V_p\, d)}{V_{HZ}} \times 100\% \tag{6}$$

where V_d and $\mathrm{V}_{d\_\mathrm{HZ}}$ are the percentage volumes of cells presenting a certain *d* value (e.g., $d > 0$, $d \geq 0.25$, $d \geq 0.50$, and $d \geq 0.75$) within the model domain and within the HZ, respectively, in a given time-step, V is the volume of a model cell, *p* is a cell (from p=1 to P) presenting a certain *d* value, V_{HZ} is the HZ volume according to Eq.2. Here, mixing hot-spots (d_h) are characterized by model cells presenting $d \geq 0.75$, as equally used in Berezowski *et al.* (2019) for delineating the active perirheic zone after the definition of Mertes (1997). We also assessed the temporal development of mixing hot-spots in the domain by comparing the peaks of d_h values from Eq.5 with the peak of discharge events observed in the simulation period. So we can evaluate when mixing hot-spots occur in relation to flow dynamics and their magnitude of occurrence. We computed the Spearman's rank correlation to rank the metrics of discharge events (e.g., peak prominence, event duration, time-to-peak) that control the increasing in d_h.

Transit-times within mixing hot-spots

The development of mixing hot-spots is a good indication of the locations and moments where and when mixing-dependent reactions such as the turnover of groundwater-borne NO_3^- due to pore-scale mixing with infiltrating SW can occur. However, since time is also a relevant variable for biogeochemical processes, it is equally important to know for how long a certain water parcel resides within mixing hot-spots. To quantify this time span, we defined exposure-time ($d_{h\text{-}\tau}$), as the time that a water parcel resides within defined mixing hot-spots along its transit through the riparian aquifer. We computed transit-times (τ) based on a transient particle tracking analyses according to HGS flow model results (Nogueira et al., 2021b). Flow paths were extracted from each HGS time-step based on massless particles released from streambed cells and from the top of the model domain. A total of around 1,300 particles were released in each HGS time-step, capturing main groundwater flow directions and infiltrating SW flow paths.

For this analysis, we differentiated the flow paths in two categories: flow paths of SW that infiltrates and subsequently exfiltrates back to the stream within the simulated domain (called hyporheic flow paths), and water flow paths that do not exfiltrate to the stream within the simulated domain (called floodplain flow paths). Each flow path is divided into smaller sub-sections, which were analysed in terms of HMC fractions, d_h, τ, and thus $d_{h\text{-}\tau}$. By carrying out these combined analyses, we can assess how $d_{h\text{-}\tau}$ is affected by transient hydrological conditions. Model visualization, integration and particle tracking analyses were performed in TecPlot 360 EX; additional calculations were carried out with MatLab® 2019b.

4.3 Results

In this section we will focus on the results of simulations for the years of 2013-2016 since it was the period used for the validation of HMC results. The results of the flow model are not detailed here, but only generalized for a better understanding of the SW-GW exchanges dynamics and overall characteristics of the flow system. Simulated groundwater heads and stream discharge matched the field values well, with a mean KGE of 0.73 for groundwater heads and 0.84 for stream discharge (Fig.S3, supplementary material). The stream reach was characterized by predominantly losing conditions with average water losses to the subsurface of around 40-50% of total discharge. This is higher than the 25% measured in the field by Schmadel *et al.* (2016) during a small discharge event in July 2014; however, our simulated water losses for the same period of their analyses were around 30%, indicating a good match to observed reach conditions during the discharge event.

A small gaining portion was observed for the simulated reach only at a localized deep pool downstream in the domain (representing only about 1% of the total infiltrating SW), whereas the majority of infiltrating SW exited the domain via the downstream subsurface boundary. During very high discharge and overbank flow (generally $Q \geq 7.0$ m^3s^{-1}) the near-stream riparian zone can be partially flooded. Moreover, groundwater flow paths are somewhat more parallel to the stream under low discharge and more divergent under high discharge conditions (Nogueira et al., 2021b).

4.3.1 Validation of HMC fractions

Before further assessment of the HMC results, the simulated stream water fractions (f_{SW}) were compared to observed stream water fractions (F_{STR}), which were calculated based on Cl^- measurements for a validation of model results (Sect. 2.3). The F_{STR} computed according to Eq.2, as well as the extracted f_{SW} for some observation wells are presented in Fig.4. The locations of the wells are presented in Fig.3.

For 70% of all groundwater samples the mixing model was applicable for the calculation of F_{STR}. For the other samples, Cl^- concentrations were temporally lower than in the stream water and they were excluded from further analyses (Fig.S1, supplementary material). In general, the observation wells had exhibited high F_{STR} values, indicating higher fractions of stream water than other components like groundwater, Fig.4. Calculated F_{STR} and simulated f_{SW} for wells presented similar ranges (between 0.7 and 1.0), while F_{STR} showed slightly larger variations in comparison to f_{SW} values. Despite that, correlating calculated F_{STR} with simulated f_{SW} showed reasonable coefficients of determination (R^2 values shown in Fig.4) indicating that the model generally captures the variations of stream water fractions in the riparian groundwater for most observation wells. Small differences between F_{STR} and f_{SW} existing in some of the wells (e.g., ML wells and well F2) can be related to localized processes and conditions not captured by the model as later discussed in the manuscript. The Wilcoxon-test performed between F_{STR} and f_{SW} datasets individually for each observation well also indicated that the populations were not statistically different for the majority (indicated by h=0 on Fig.4), reinforcing the good match between simulated and observed stream water fractions on riparian groundwater.

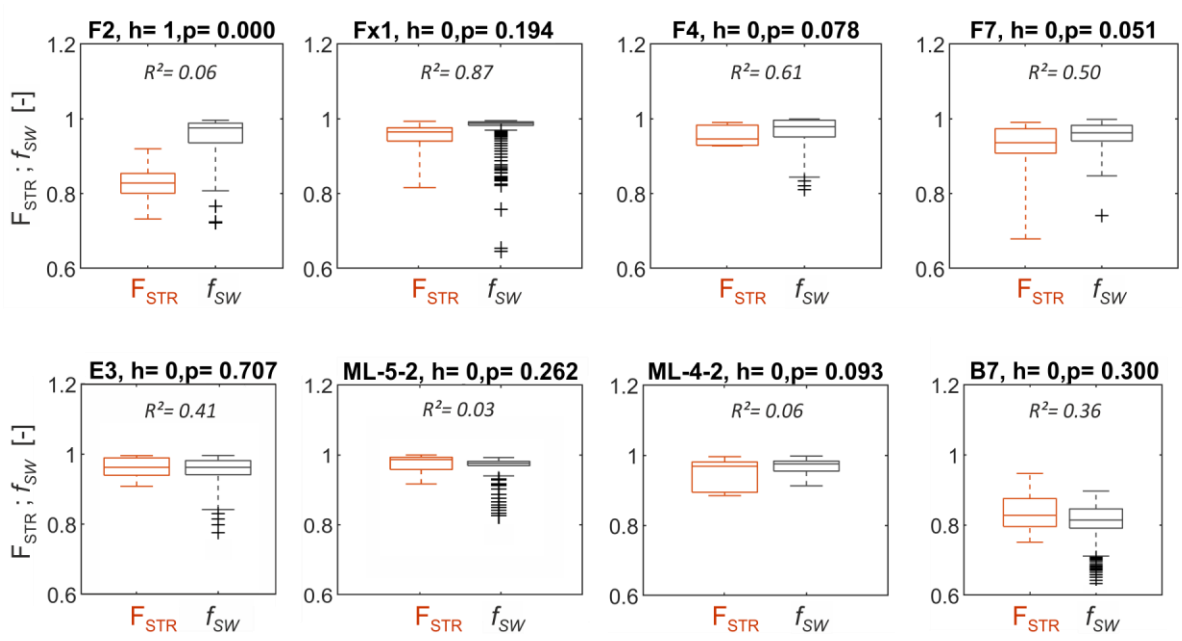

Fig.4: Observed and simulated stream water fractions (F_{STR} and f_{SW}, respectively) for some observation wells in the study area. The *h* values represent the results of the Wilcoxon-test between F_{STR} and f_{SW} datasets with respective *p-values* (p): h=0 indicates that the F_{STR} and f_{SW} groups are from continuous distributions with equal medians, while h=1 indicates the difference between the medians is statistically significant; The R values show the coefficient of determination between the F_{STR} and f_{SW} datasets**.** The names of the wells are shown at the top of each plot.

4.3.2 Spatio-temporal variation of simulated HMC fractions

The temporal variation of simulated HMC water fractions (here referred to as just "fraction(s)") is presented in Fig.5. A warm-up period required to flush the initial f_{GWi} was found to be around 2 years, which is an approximation to the time required to fill the aquifer with "new" water sources. From this point on throughout the manuscript, we focus only on the analyses of the three remaining fractions (i.e., f_{SW}, f_{GW} and f_{FW}).

Integrating the different fractions over time (Eq.2), on average 35% of the simulated domain comprised water originating from the stream (f_{SW}), whereas groundwater inflowing from the upstream subsurface boundary (f_{GW}) was around 35%, and 30% consisted of water originating from the soil surface (f_{FW}). Since the HMC results indicate the water-origin rather than the water content, we further evaluate the HMC results considering only the fully-saturated portion of the model domain using Eq.2, which we can then relate to total HMC water contents in the subsurface. In terms of stream water, nearly 80% of the saturated domain presented $f_{SW} \geq 0.1$, and about 20% presented $f_{SW} \geq 0.9$. Following the geochemical HZ definition ($f_{SW} \geq 0.5$),

this corresponded to around 50% of the fully-saturated domain (Fig.5b). Likewise, 50% of the fully-saturated domain consisted of surface water, followed by 40% consisting of groundwater and only 10% of floodplain water, Fig.5c. This indicates relatively small contributions of water originating from the top of the domain to the saturated portion of the aquifer for most of the simulated period.

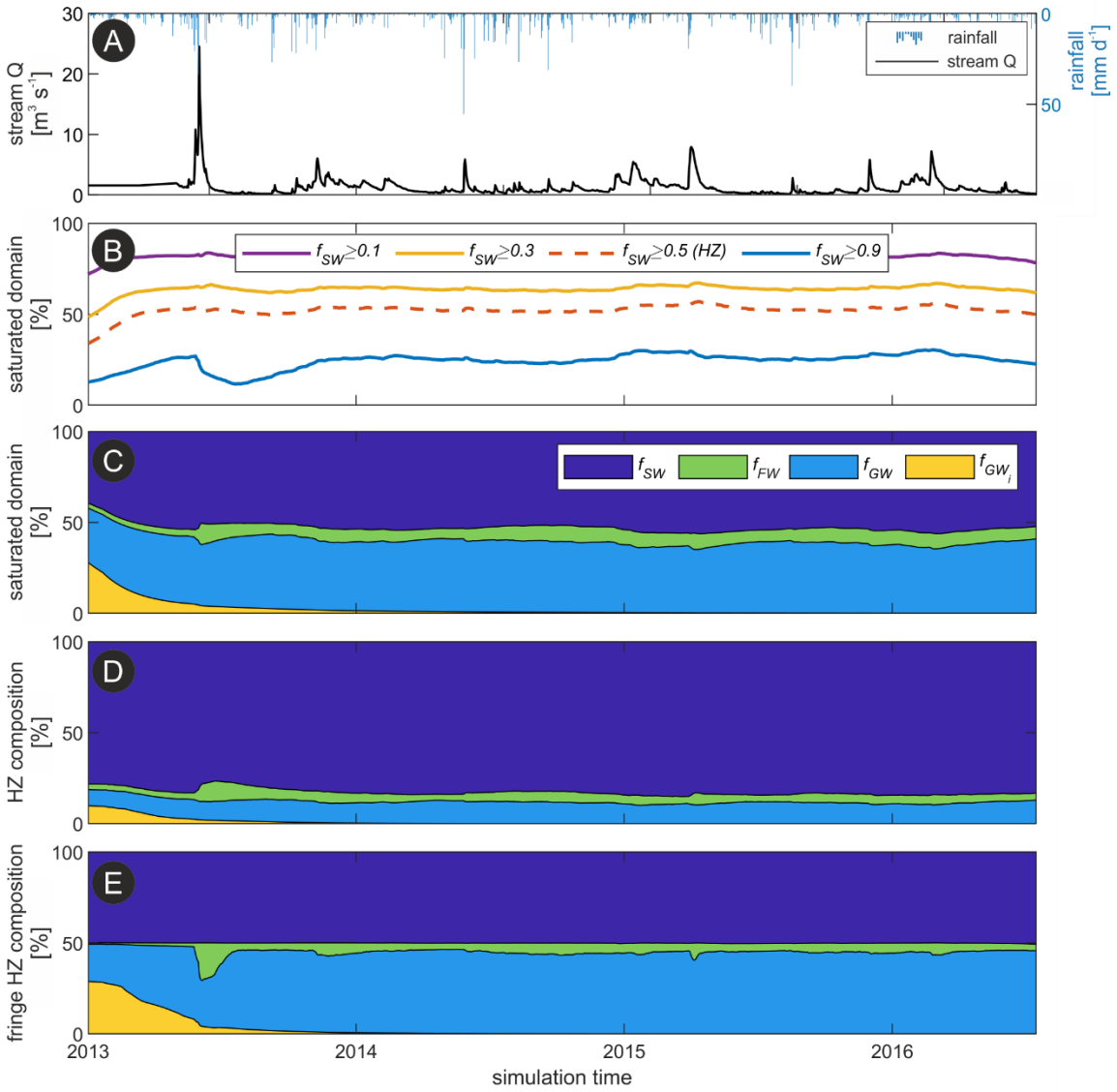

Fig.5: a) Stream discharge (Q) and rainfall time-series; **b)** temporal variation of the saturated domain consisting of at least a certain fraction (e.g., 0.1, 0.3, 0.5, and 0.9) of stream water (f_{SW}); **c)** contribution of different fractions to the saturated domain (stream water (f_{SW}), floodplain water (f_{FW}), groundwater (f_{GW}), and initial groundwater (f_{GWi})); **d)** composition of different fractions to the hyporheic zone (HZ, f_{SW}≥0.5); **e)** composition of different fractions at the fringe of the HZ (f_{SW}=0.5). Note that the start of the simulation (when f_{GWi}=100% and other water fractions are 0) is not shown in the plot.

Around 80% of the geochemical HZ volume consisted of water originating from the stream, with the rest being represented by groundwater (15%) and floodplain water (5%), Fig.5d. This already suggested that, despite the potential for subsurface biogeochemical processes and turnover of stream-borne solutes within hyporheic flow paths (Trauth et al., 2014; Zarnetske et al., 2011), there is limited potential for mixing-dependent reactions involving reactants from both water sources (SW and GW) due to the dominance of stream water in this zone. Differently, at the HZ fringe (where f_{SW}=0.5), f_{GW} and f_{FW} 40% and 10% respectively (Fig.5e), indicating a higher potential for mixing between the different water sources. The Fig.6 shows the spatial distribution of minimum, maximum and median values, as well as the standard deviation (σ) of each fraction within the domain for the entire simulation period. The plots indicate the minimum and maximum possible distributions of each water fraction in the domain, as well as their typical distribution throughout the simulation period. To better represent the maximum probable HMC water contents (and not only the proportions of the different sources) in each model cell, the fractions shown in the plot were multiplied by the maximum saturation value that was recorded in each model cell during the entire simulation period.

Throughout the simulation, f_{SW} was high around the stream and decreased with distance from the stream, Fig.6a-c, reaching values of 0.5 at around 150-200m from the stream channel, which defines the local geochemical HZ. This regularity was maintained by the continuous SW infiltration to the aquifer due to the overall losing conditions of the stream reach. The f_{SW} plume was slightly smaller at upstream areas due to boundary condition effects. There was also a large variation of f_{SW} values around the stream and at the groundwater-table interface (Fig.6d). High values of f_{GW} were only observed at the periphery of the simulated domain, as well as at the southern upstream face of the domain (boundary effect), Fig.6e-g. Lastly, high f_{FW} values were mainly observed above the groundwater-table. However, since absolute water content (i.e., saturation) is low at these areas, the total f_{FW} content is also relatively low in comparison to other HMC fractions, Fig.6i-k. Still, some high f_{FW} values were recorded in the subsurface (Fig.6j), when a considerable volume of water originating from the stream flows overbank and subsequently percolates through the riparian soils (e.g., following the high discharge event on Jun-2013, Fig.S4, supplementary material). Although the model indicates this is floodplain water, it is important to keep in mind that it is overbank flow of stream water that subsequently percolates into the subsurface after flooding.

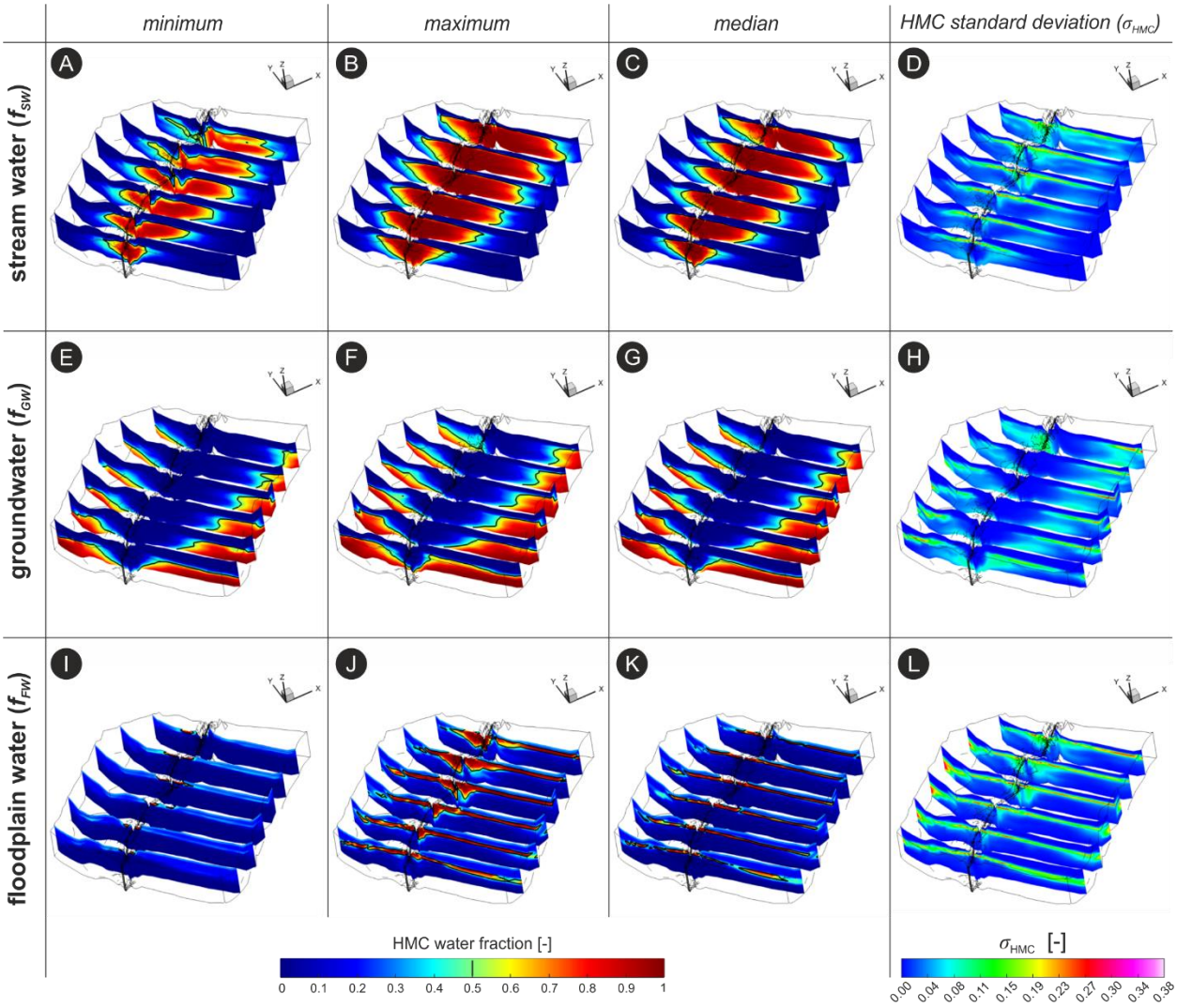

Fig.6: slices throughout the simulated 3D domain showing the minimum, maximum, median values, as well as standard deviations (σ_{HMC}) of stream water (f_{SW}) **(a-d)**, groundwater (f_{GW}) **(e-h)**, and floodplain water (f_{FW}) **(i-l)** fractions for the entire simulation period in different sections of the domain. The black line **(a-c, e-g, i-k)** indicates the HMC fractions of 0.5. Note the vertical exaggeration of the 3D plots (20x).

4.3.3 Spatial variation of mixing degrees

Despite the nearly constant spatial distribution of fractions throughout the domain (Fig.6), flow dynamics and stream stage fluctuations resulted in different mixing degrees between the different fractions. The plots in Fig.7 show the spatial distribution of minimum, maximum and the median values of mixing degree, as well as its standard deviations (σ_d) for the entire simulation period (2013-2016). The plots show the minimum and maximum possible distributions of the mixing degrees in the domain, as well as their average distribution for the entire simulation period.

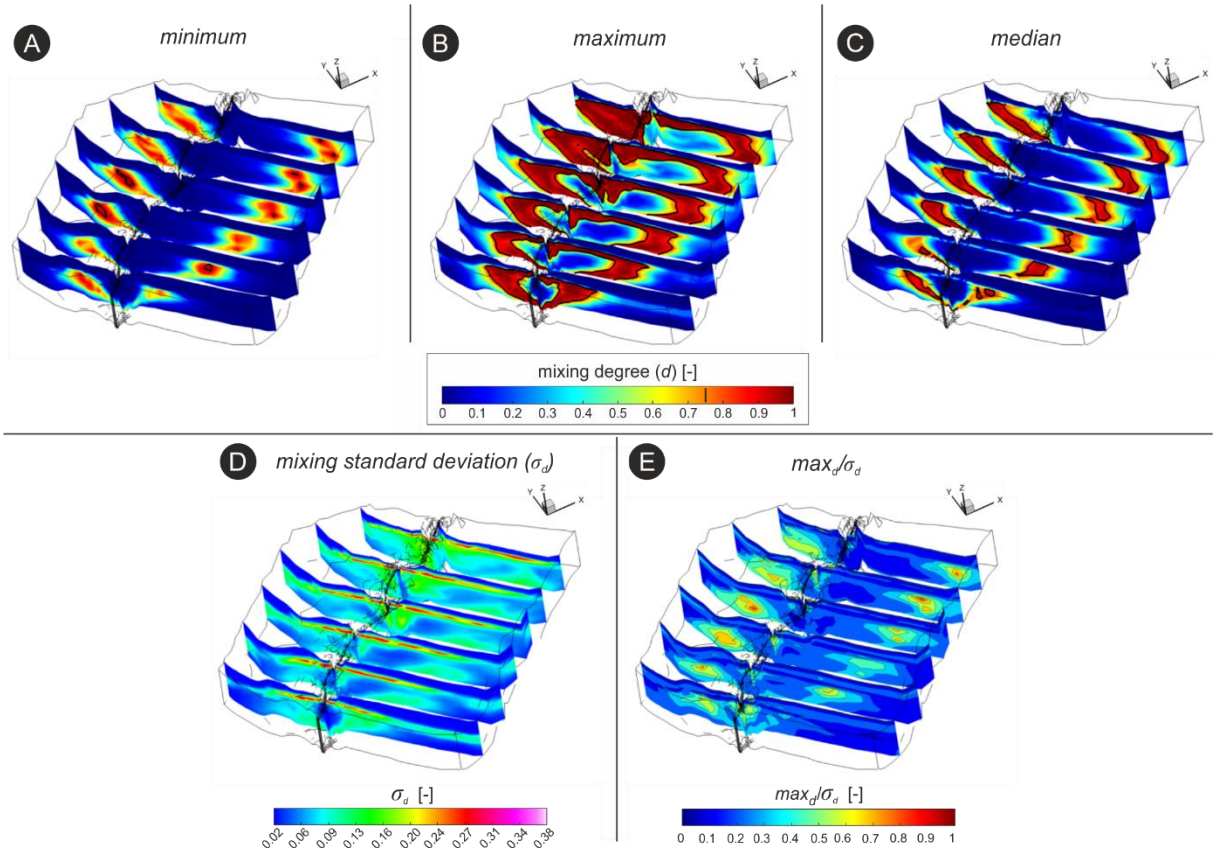

Fig.7: slices throughout the simulated 3D domain showing the minimum **(a)**, maximum **(b)**, median **(c)**, standard deviation (σ_d) **(d)**, and the normalized ratio max_d/σ_d **(e)** of mixing degrees for the entire simulation period in different segments of the domain. The black lines **(a-c)** indicate regions with $d=0.75$ (*mixing hot-spots*, d_h). Note the vertical exaggeration of the 3D plots (20x).

The relatively high f_{SW} within the HZ prevents high mixing degrees to occur near the stream. In contrast, regions at the fringe of the HZ presented the highest minimum *d* values over the entire simulation period (Fig.7a), which suggest constant high *d* values in those areas. Yet, larger *d* values also occurred near the stream at some points during the simulation (Fig.7b) throughout the simulation. These large *d* values near the stream followed discharge events with partial flooding of the riparian zone, which leads to large percolation of inundation water into the riparian aquifer, which then mixes with infiltrating SW and with ambient groundwater. Nevertheless, the computed median values of *d* indicate that *mixing hot-spots* (d_h) ($d \geq 0.75$) were indeed more persistent near the HZ fringe (Fig.7c). In comparison to regions near the groundwater-table interface, for example, these areas at the HZ fringe also presented slightly smaller σ_d (Fig.7d), showing smaller variation in time. We further quantified the persistence of *mixing hot-spots* in time by computing and normalizing the ratio of maximum *d* over their σ_d (max_d/σ_d) since a small σ_d alone

does not imply a persistent *mixing hot-spot* over time. A high value of this metric would indicate the occurrence and persistence of *mixing hot-spots* over the entire simulation period, as it can be observed near the HZ fringe for instance (Fig.7e) where max_d/σ_d are generally above 0.5. These areas comprise only around 5% of the total model domain.

4.3.4 Temporal variation of mixing degrees

Mixing degrees also varied in time, as could be concluded from the plots in Fig.7. Here, we further assessed how mixing degrees varied over time, as well as their relationship with flow dynamics. For that, we have integrated cells with at least a certain degree of mixing (e.g., $d > 0$, $d \geq 0.25$, $d \geq 0.50$, and $d \geq 0.75$) and compared them to the total volume of the domain (Eq.5). Around 80% of the domain presented some sort of mixing ($d > 0$), which strongly varied over time suggesting the activation of areas that do not present consistent mixing throughout the simulation, Fig.8b. Zones with $d \geq 0.25$ were on average 40% of the total domain. Only around 9% of the total domain presented $d \geq 0.50$, which was just slightly larger than d_h ($d \geq 0.75$). Moreover, d_h represented 7-12% of the total domain volume (Fig.8c). In relation to the geochemical HZ, *mixing hot-spots* were comparatively higher and represented on average 23% (between 15% and 30%) of the total HZ volume (Fig.8d).

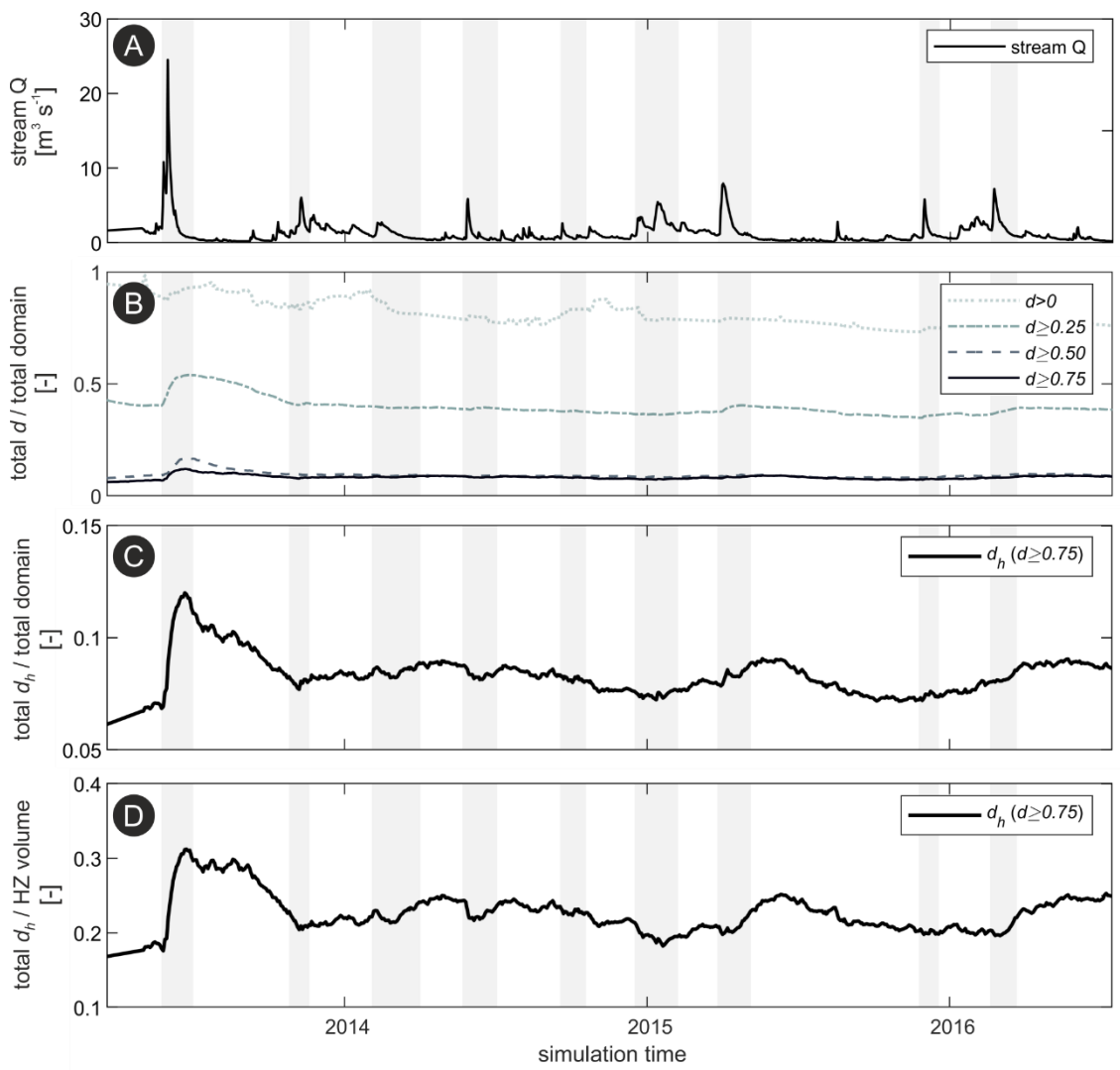

Fig.8: a) time-series of stream discharge for the period of 2013-2016; **b)** total volume of cells presenting a certain degree of mixing (*d>0*, *d≥0.25*, *d≥0.50*, and *d≥0.75*) in relation to total domain volume; **c)** total volume of mixing hot-spots (d_h, *d≥0.75*) in relation to total domain volume; and **d)** total volume of d_h in relation to total hyporheic zone (HZ) volume. Grey vertical bars indicate discharge events periods.

The impacts of discharge (Q) variations on *d* were also evident (Fig.8b). Concerning *mixing hot-spots*, discharge events increased d_h by 5-10% in comparison to conditions immediately before the start of the events (Fig.8c). Spearman's rank correlation (Table 1) showed that the discharge peak prominence (ΔQ) (in relation to Q value prior to the event) and the increase of d_h from the value immediately prior the event (Δd_h) were positively correlated (R_{spear}=0.96). Both the event duration and the time-to-peak were not strongly correlated to Δd_h (R_{spear}=0.09 and R_{spear}=0.30, respectively) (Fig.S5, supplementary material). In

our simulations, event duration and peak prominence were also not strongly correlated (R_{spear}=0.14, data not shown).

Moreover, the lag between the peak of the discharge events and the peak of d_h was 14 days on average, somewhat shorter for events presenting higher ΔQ, but the metrics showed only a weak correlation (R_{spear}=0.28). On the other hand, event duration and the lag between the peak of the discharge events and the peak of d_h showed a good correlation (R_{spear}=0.66), suggesting that longer events would lead to later developments of d_h. Due to the temporal lag between the peak of Q events and peak of d_h, mixing degrees were generally higher during the recession of discharge events.

Table 1: Overall Spearman's rank correlation between metrics of discharge events and the increasing of mixing hot-spots (d_h) at the riparian zone.

Discharge events metrics	**Correlation to Δd_h**
Event duration [days]	0.009
Time-to-peak [days]	0.305
Time-to-peak/event duration [-]	0.340
Peak prominence (ΔQ) [m^3 s^{-1}]	0.963
Lag between Q *peak-event* and following peak d_h [days]	
Min	1
Mean	14
Max	46
R_{spear} between ΔQ and lag to peak d_h: 0.28	
R_{spear} between event duration and lag to peak d_h: 0.66	

4.3.5 Exposure-times ($d_{h\text{-}\tau}$)

Since the time that a water parcel resides within *mixing hot-spots* also affects the potential for biogeochemical processes, for each flow path we computed exposure-time ($d_{h\text{-}\tau}$), as the share of water transit-times (τ) spent within *mixing hot-spots*. Overall, $d_{h\text{-}\tau}$ were generally smaller during the peak of discharge events since: i) groundwater velocities are higher during events, leading to relatively shorter τ (Fig.9a), and ii) d_h was relatively smaller during peak events (Fig.8c). Since transit-times are generally longer under baseflow conditions (Fig.S6, supplementary material), $d_{h\text{-}\tau}$ was equally longer during the recession of discharge events (Fig.9b).

Specifically, the median $d_{h\text{-}\tau}$ of floodplain flow paths (i.e., water parcels that do not exfiltrate through streambed cells within the model domain) was highly variable in time (3-12 days), on average 15% of the total flow path τ, Fig.9b. On the other hand, for the hyporheic flow paths (i.e., infiltrating SW that exfiltrates through streambed cells after infiltration and subsurface transit), $d_{h\text{-}\tau}$ were small (0-3 days), on average 5%

of the total hyporheic τ. The median τ of floodplain flow paths were slightly stronger correlated to Q variations than hyporheic flow paths, R_{spear}= -0.50 and R_{spear}= -0.45, respectively (Fig.9c).

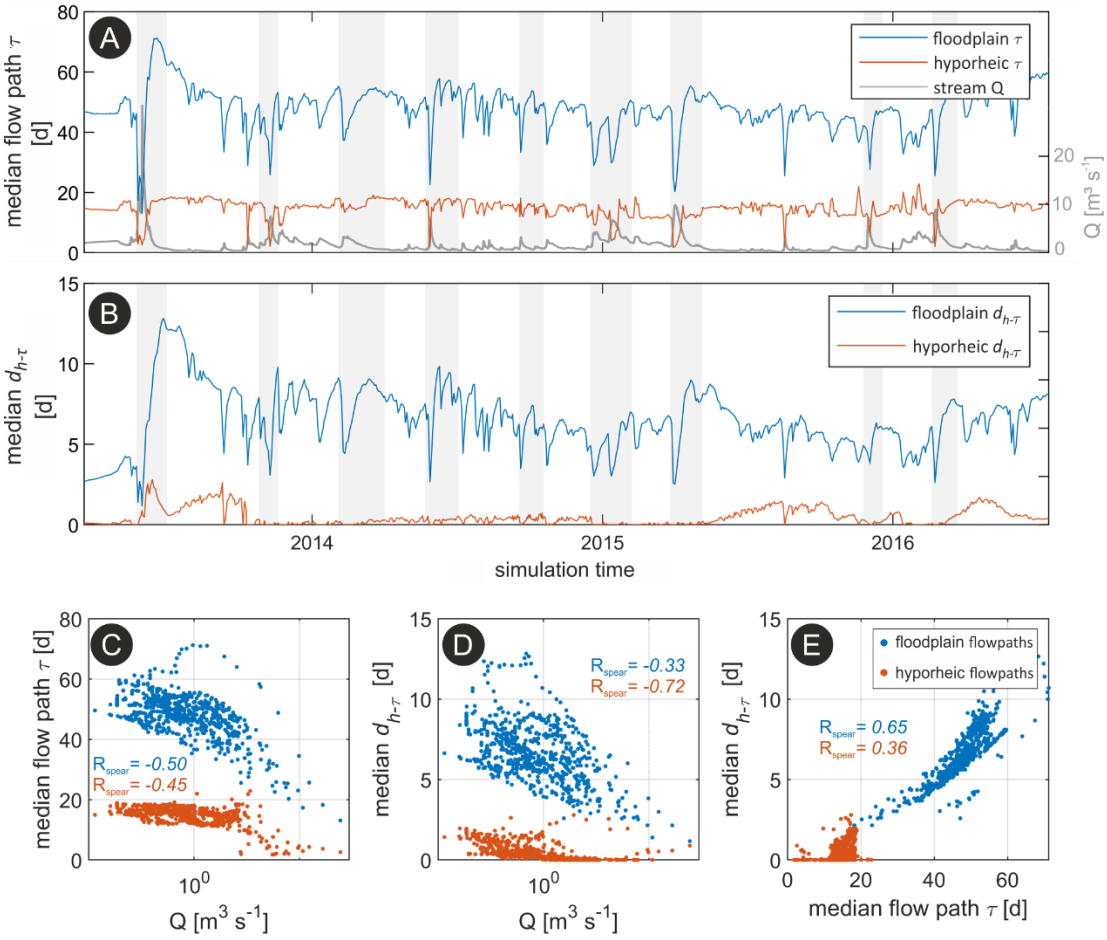

Fig.9: a) median transit-times (median flow path τ) alongside stream Q; **b)** median exposure-times (median $d_{h\text{-}\tau}$); **c)** median flow path *vs.* stream discharge (Q); **d)** median $d_{h\text{-}\tau}$ *vs.* Q; and **e)** median $d_{h\text{-}\tau}$ *vs.* median flow path τ. The Spearman's rank correlation (R_{spear}) between variables is showed in the scatter plots (c-e). Grey vertical bars (a-b) indicate discharge events periods. Note the log scale for Q values in (c-d).

The Fig.9b indicates that hyporheic $d_{h\text{-}\tau}$ increases under baseflow conditions relative to values during discharge events although hyporheic τ were somewhat constant over time (Fig.9a). Indeed, hyporheic $d_{h\text{-}\tau}$ were inversely correlated to stream discharge (R_{spear}= -0.72, Fig.9d), but only weakly correlated to variations of transit-times (R_{spear}= 0.36, Fig.9e). In contrast, for floodplain flow paths, $d_{h\text{-}\tau}$ was only slightly negative correlated with stream Q (R_{spear}= -0.33), whereas they showed a stronger correlation with flow path transit-times (R_{spear}= 0.65). Whereas both hyporheic and floodplain $d_{h\text{-}\tau}$ decrease with increasing Q due

to overall shorter water transit-times, the occurrence and controls of mixing hot-spots due to flow dynamics at these different regions are somewhat different, as it will be discussed in Sect. 4.3.

4.4 Discussion

4.4.1 Validation of the flow model and the HMC results

In this study, we coupled a previously calibrated numerical flow model with the HMC method (Partington et al., 2011) in order to assess the distribution of different water fractions in a stream corridor, using the riparian zone of the Selke stream as a study case. The numerical model used here had been calibrated based on another observation period (Nogueira et al., 2021b), but after implementation of correct hydrological BCs (e.g., stream inflow, groundwater heads at the boundary) showed good agreement with field data from the period investigated in this paper. This reinforces the quality of the original calibration and justifies the application of the numerical flow model to another time period after BC adjustments. Small mismatches between observations and simulated values in terms of groundwater heads and stream discharge could be related to the simplified geology within the numerical flow model, which can affect SW-GW dynamics and groundwater flow paths (Fleckenstein et al., 2006; Gianni et al., 2019; Savoy et al., 2017), as well as to the simplified streambed heterogeneity that can modify overall SW-GW exchange fluxes (Pryshlak et al., 2015; Tang et al., 2017).

Usually, numerical flow models are solely calibrated based on hydrological observations. Previous studies using the HMC method have rarely attempted to validate their results based on hydrochemical data, exceptions being the studies by Liggett *et al.* (2015) and Berezowski *et al.* (2019), for instance, while this could further enhance model reliability and parameterization (Partington et al., 2020; Schilling et al., 2017, 2019). Here, in addition to groundwater heads and stream discharge evaluation, we verified the HMC results by comparing simulated f_{SW} and calculated F_{STR}, the latter based on a Cl^- mixing model. The calculation of F_{STR} was possible for most of the water samples (70%), whereas a few of them presented unrealistic $F_{STR}>1$ due to Cl^- concentrations being temporally lower than in the stream water end-member. We attribute this to local variability in evaporation or the presence of geogenic Cl^- that can affect Cl^- concentrations (Delsman et al., 2013; Ong et al., 1995). Nevertheless, the simulated f_{SW} values matched the field F_{STR} values at the observation wells quite well, indicating a good performance of the HMC method for mapping water source composition despite model simplifications. The small differences between F_{STR} and f_{SW} were acceptable given that a calibration to hydrochemical data was not performed in this study, and that the model captured the main SW-GW dynamics and hydrochemical variations, well which is further discussed in Sect. 4.5.

These results suggest that the HMC method can be a valuable tool, complementary to more labour-intensive field sampling, for mapping patterns of water source composition and their temporal variation at the riparian zone and watershed scales (Berezowski et al., 2019; Schilling et al., 2017).

4.4.2 HMC fractions and HZ dynamics

In terms of water origin there was a nearly constant distribution of the different HMC fractions within the model domain (35% stream water, 35% groundwater, and 30% floodplain water). However, taking a look at the fully-saturated domain only (70-80% of the total simulated domain), reveals that at least 90% of the water in the saturated zone originates from the stream (comprising 50% of total saturated domain) and from groundwater flowing into the domain via the upstream boundary (40%), Fig.5b. This is manifested in a geochemical HZ (region presenting $f_{SW} \geq 0.5$) that extends up to 200 m into the riparian aquifer. While this may appear as a large percentage of stream water in the riparian aquifer, other studies of alluvial aquifers reported equally large percentages of stream water in the riparian aquifer at large distances from the stream (up to 250m), which were especially controlled by the permeability of the aquifer material (Schilling et al., 2017). Similarly, Poole *et al.* (2008) have found that alluvial aquifer water at the Minthorn study site (gravel-alluvial dominated aquifer) was essentially all derived from the main stream channel of the Umatilla River. They also found that the *geochemical* HZ penetrates to the entire local riparian zone (about 300m wide) (Jones et al., 2008). In contrast, Sawyer *et al.* (2009) estimated the HZ extent to be only up to 30 m from the banks of the Colorado River near the Hornsby Bend site. In their case, however, the hydraulic conductivity of the aquifer material was nearly one order of magnitude smaller than on the other sites and on ours (and the stream reach has not been predominantly losing). Those previous studies and our findings go in line with the propositions of Boulton *et al.* (1998) and Wondzell (2011) on the combined influence of hydrogeology and stream flow dynamics on the development of the hyporheic zone and exchanges around streams. Both studies have suggested that the cross-sectional area of the hyporheic zone relative to the stream channel are the highest for low-order streams, while unconstrained lowland streams present the greatest hyporheic zone cross-sectional area relative to wetted stream channel (Boulton et al., 1998).

Within the local HZ, most of the water was advected stream water (approximately 80%). This is also in line with previous studies highlighting the dominance of purely advected surface water within hyporheic zones (Hester et al., 2019, 2014). Within the simulated domain, most of the infiltrated stream water did not immediately return to the stream and may therefore be termed “groundwater” after some transit through the aquifer. However, the fact that it originated from the stream manifests in a different chemical composition compared to ambient groundwater. For instance, the infiltrated stream water will have higher contents of dissolved oxygen (DO) and dissolved organic carbon (DOC) compared to ambient groundwater (Trauth et

al., 2018). In turn, the mixing between the infiltrated SW and ambient GW, can deliver DOC as an electron donor to facilitate denitrification of groundwater-borne nitrate (Hester et al., 2019; Song et al., 2018; N. Trauth & Fleckenstein, 2017; Trauth et al., 2014).

4.4.3 Variations and controls of mixing degrees and mixing hot-spots

Only a few studies attempted to quantify the spatio-temporal variations of the mixing degrees resulting from SW-GW exchange process at the stream-corridor scale (Lessels et al., 2016), as well as their potential implications for biogeochemical processes. While some studies have relied on extensive field campaigns (Gassen et al., 2017; Jones et al., 2014), numerical simulations carried out by Trauth & Fleckenstein (2017) and Hester et al. (2019), suggested the importance of mixing zones for the denitrification of groundwater-borne nitrate. Here, on average, nearly 50% of the model domain presented $d \geq 0.25$ throughout the simulation period. About 9% of the domain (and roughly 20% of the HZ) could be defined as *mixing hot-spots* ($d \geq 0.75$), with most of them being located at the fringe of the HZ. The persistence of these mixing hot-spots in time could be illustrated with the metric $\max_d/\sigma_d$, which was consistently high at the fringe of the HZ. This is qualitatively consistent with previous smaller-scale studies showing that mixing hot-spots between SW-GW tend to occur in narrow zones at the fringe of the HZ (Hester et al., 2013; Sawyer and Cardenas, 2009; Trauth and Fleckenstein, 2017). Likewise, Berezowski *et al.* (2019) computed d_h values slightly above 6% of the total area of a larger basin in Poland following a large flood event, d_h that were also mainly located at the fringe of the HZ.

In our simulations, magnitudes of peak discharges during events were strongly correlated with increases of d_h over the event. This is in line with Trauth & Fleckenstein (2017), who found that for the same event duration, discharge events with higher peaks increased denitrification of groundwater-borne nitrate by a factor of up to 7x due to enhanced mixing with stream-borne DOC. In the same way, Hester et al. (2019) showed that the size of the SW-GW mixing zone below a streambed dune increased and shifted with increasing SW depth (analogous to increasing stream discharge in this study). While our results indicated a similar expansion of the mixing zones following discharge events (Fig.8c), we could also observe and quantify the temporal shift of d_h peaks (e.g., counter-clockwise hysteresis with a peak of stream discharge events) alongside the shift of their locations within the riparian zone.

Water transit-times are usually used as a metric to assess the HZ reactive potential since the longer the transit-time, the higher the potential for solute transformations (Boano et al., 2010; Zarnetske et al., 2011). To evaluate this potential in relation to reactive mixing zones we defined the exposure-time ($d_{h\text{-}\tau}$), as the time water resides within model cells classified as mixing hot-spots. Our results show that the hyporheic $d_{h\text{-}\tau}$ were generally smaller than (non-hyporheic) floodplain $d_{h\text{-}\tau}$ and more negatively correlated with stream

discharge (Fig.9d). This is mainly because hyporheic transit-times are generally shorter than floodplain water transit-times. Besides, under low stream discharge conditions, ambient groundwater flow is somewhat more parallel to the stream (Nogueira et al., 2021b), while groundwater flow towards the stream increases due to a decrease in SW depth (Buffington and Tonina, 2009). This and the slightly stronger gaining conditions at the pool located further downstream in the model domain (Fig.S4, supplementary material) result in a greater SW-GW mixing near the stream region, hence increasing the hyporheic $d_{h\text{-}\tau}$. With increasing stream discharge, however, SW influx into the riparian aquifer increases, which shifts the SW-GW mixing front to regions farther from the stream (Hester et al., 2019) and hyporheic $d_{h\text{-}\tau}$ decreases.

In contrast, with distance from the stream, $d_{h\text{-}\tau}$ is mainly controlled by variations in water transit-times. This is because mixing far from the stream is mainly enhanced by increasing stream discharge, which brings SW to farther distances within the aquifer where it can mix with ambient groundwater. In line with our results, Trauth et al. (2015) found the total consumption of groundwater-borne nitrate within an instream gravel bar to be higher under neutral and slightly gaining ambient groundwater conditions (i.e., low stream discharge). This is when the total influx of solutes from the stream is low, but consumption of groundwater-borne nitrate is high due to enhanced SW-GW mixing. Likewise, our results suggest that discharge events can enhance turnover of groundwater-borne solutes in the riparian zone at locations farther from the stream more than in the hyporheic regions near the stream. Conversely, under low discharge conditions, hyporheic $d_{h\text{-}\tau}$ increase due to slightly increasing GW upwelling and subsequent SW-GW mixing. Nevertheless, in strongly gaining stream reaches with a dominance of GW-seepage to the stream (e.g., limited or absent hyporheic flow paths), hyporheic transit-times (Cardenas, 2009; Trauth et al., 2014, 2013), as well as SW-GW mixing (e.g., in terms of flux magnitude) (Hester et al., 2013; Sawyer et al., 2009) would be smaller, and consequently the potential for turnover of groundwater-borne solutes would be smaller too (Hester et al., 2019). On the top of other modelling works mainly carried in 1D or 2D setups and focusing on biogeochemical processes below the streambed (Hester et al., 2014, 2019; Newcomer et al., 2018), our larger scale 3D model consider lateral SW-GW exchange and long-term mixing processes. In line with results from Nogueira et al. (2021b) and Trauth et al. (2018), results from our 3D model coupled with the HMC method reinforce that such larger scale and long-term processes are important around losing streams for the creation of biogeochemical mixing hot-spots. In such environments, SW-GW mixing, and thus mixing-triggered biogeochemical reactions take place mostly with distance from the stream channel, and their potential to the turnover of groundwater-borne solutes might not have been detected in small scale studies.

4.4.4 Mixing hot-spots and biogeochemical implications

In order to further show the implications of mixing for local biogeochemical processes, we compared our HMC results with hydrochemical analyses from Gassen et al. (2017), who monitored water quality across the groundwater-table interface using a local multilevel piezometer that can be sampled at highly resolved depth intervals in the variably saturated vadose and fully saturated groundwater zones (Fig.S7, supplementary material).

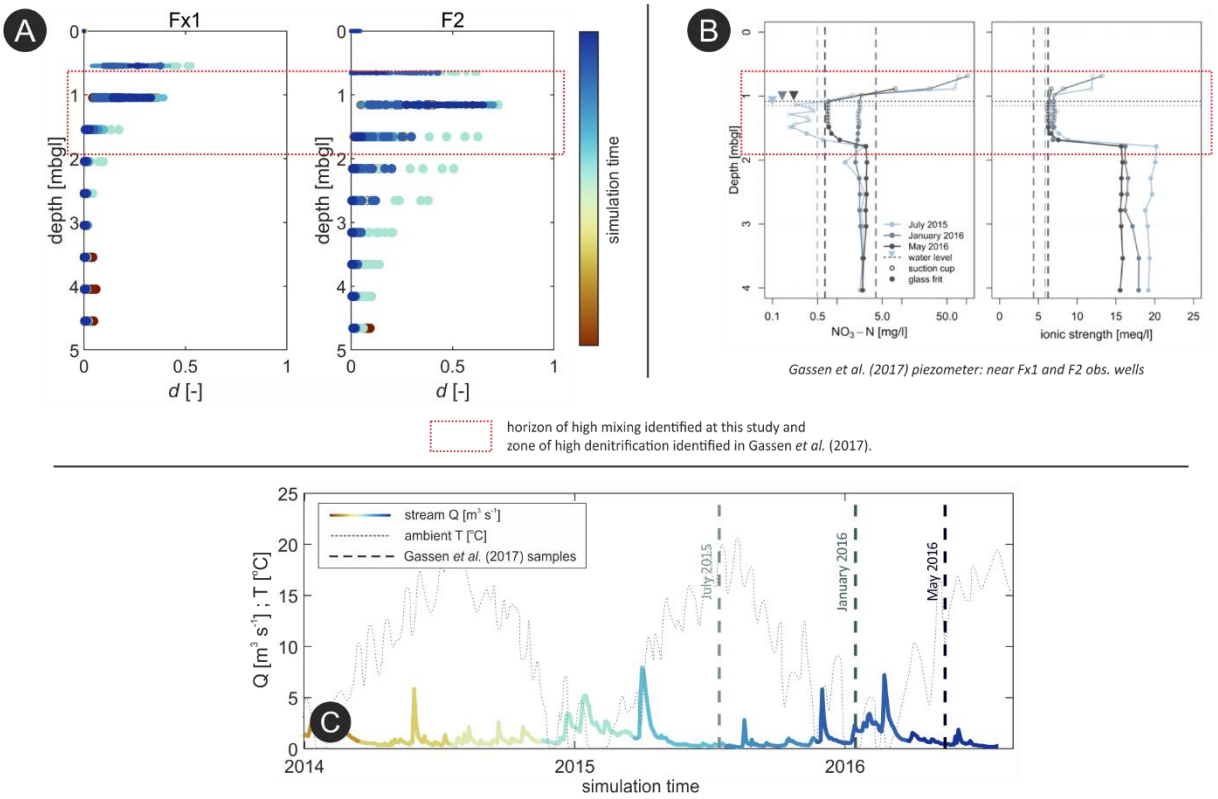

Fig.10: a) mixing degrees with depth for two observation wells. Colours indicate simulation time; **b)** measurements of NO3−N concentrations and ionic strength in a multilevel piezometer for three different sampling dates. Vertical dashed lines represent NO3−N concentrations/ionic strength of the stream water, horizontal dotted lines represent the groundwater-table at the corresponding sampling date (reprinted (adapted) with permission from Gassen et al. (2017), Copyright (2017), American Chemical Society); and **c)** ambient temperature alongside stream Q coloured according to simulation time. Vertical dashed lines indicate the sampling dates from Gassen et al. (2017).

The HMC-simulated vertical variations of mixing degrees at the near stream observation wells show strong similarity with observed vertical variations in nitrate concentrations and a denitrification fringe around the

water table separating high concentrations in the vadose zone form significantly lower concentrations in the saturated zone as highlighted by the red rectangle in Fig.10a and Fig.10b. Our simulations revealed generally higher mixing degrees ($d \geq 0.5$) over the top 1-2m of the saturated zone, while Gassen et al. (2017) observed high nitrate concentrations above the groundwater table (up to 70 mg L^{-1}),which exponentially decreased across the uppermost saturated zone to values below 3 mg L^{-1}. Besides seasonal temperature effects on denitrification rates (Fig.10c) (Nogueira et al., 2021; Widdowson et al., 1988; Zheng et al., 2016), mixing with stream-borne DOC and subsequent denitrification is most likely the processes responsible for the observed high denitrification rates at the vadose zone-groundwater interface in the uppermost parts of the saturated zone. This reinforces the importance of mixing hot-spots for biogeochemical processes in riparian zones and highlights the importance of mapping different water sources and their mixing dynamics.

4.4.5 Limitations of the employed method and recommendations for future studies

Even though the numerical model matched well the field observations, the employed model represents a simplification of the reality, which in turn result in limitations and uncertainties. For instance, based on available geophysical data we have assumed the clay-silt formation as the bottom of the alluvial aquifer and impermeable in the model. Likewise, we assumed that the alluvial aquifer presents a limited lateral extention (Lutz et al., 2020; Trauth et al., 2018). These assumptions and the model geometry can lead to misconception on larger scale hydrological processes, which are inherent to nested SW-GW systems. For instance, as showed by Flipo et al. (2014) and by other studies (Boulton et al., 1998; Magliozi et al., 2018; Toth 1963), SW-GW system are connected interfaces, which are linked to each other through different spatio-temporal processes. For instance, longer and deeper flowpaths that might have been not represented in our numerical model could lead to the development of additional mixing spots at greater depths or distances from the stream (Lessels et al., 2016). This could further emphasize and explain how alluvial aquifers and riparian zones act as buffer zones connecting low-frequency processes occurring at regional scale and high-frequency processes occurring in the stream network (Ebeling et al., 2021; Flipo et al., 2014; Rivett et al., 2008; Sun et al. 2017). Equally, lateral influx of groundwater through the laterals of the model domain could also effect the dynamics and main directions of GW flow paths and therefore SW-GW mixing spots development. At a larger scale, longer and deeper flow paths could influence the exchanges between the alluvial aquifer and the regional aquifer underneath depending on their connectivity, which could explain some of observed relations between stream discharge and solute loads in the catchment outlet (Winter et al., 2021; Zhang et al., 2021).

Despite good agreement with field F_{STR} values, simulated HMC water fractions such as f_{SW} were not included in the calibration of the numerical model. In a more rigorous calibration, this could have been

done, which might further minimize mismatches between simulated and observed HMC fractions, while still respecting the parameter range. It is a trade-off with computation time since model calibration can largely increase with sub-routines for the calculation of observations/parameters of interest. Since the numerical model used here was previously calibrated based on both conventional and more unconventional oservations, and since the goal of this study was not to reproduce all details at the field site, we did not carry out additional model calibration. However, the addition of unconventional observation-types to model calibration (on the top of commonly used groundwater heads and stream stage/discharge measurements) tends to lead to a more robust calibration reducing equifinality in the parameter sets (Nogueira *et al.*, 2021b; Schilling *et al.*, 2017, 2019; Partington *et al.*, 2020), and should be considered in future studies.

We intentionally did not conduct explicit simulations of reactive transport in this study since our main goal here was to explore the HMC method (coupled to a flow model) in order to assess the development of mixing spots on the riparian zone and their relation to hydrological variations. We additionally showed the importance of such macroscopic mixing spots for groundwater-borne NO3- turnover by comparing the quantitative mixing results of the HMC method with previous biogeochemical assessments carried out in the study area. For a direct quantification of nitrate removal rates, however, the use of reactive-transport models or other data-driven analyses would be indispensable. Such simulations would have allowed a comparison of observed and simulated concentration values and their dynamics for a more rigorous evaluation of model performance (Nogueira et al., 2021b). However, our model results could match patterns of mixing degrees estimated from field observations very well and the simulated patterns allowed an improved interpretation of observed processes. Furthermore our results were well in line with other studies on biogeochemical processes related to SW-GW mixing at comparable sites. The identification of hot-spots for macroscopic mixing between SW-GW with the HMC method can provide a good proxy for the occurrence of potential biogeochemical hot-spots for mixing-dependent turnover of groundwater-borne solutes in river corridors. However, care should be taken in interpreting such results as this “potential” may not be realized if stream-borne reactants (like DOC) have been exhausted before reaching the mixing hot-spots.

Finally, the HMC method is based on water fluxes computed between model cells and therefore assumes that all HMC fractions are perfectly mixed within a model cell at every time-step (Partington et al., 2011). This condition may be violated, if stratification of different waters exist over the vertical extent of a model cell (Karan et al., 2013; Kolbe et al., 2019). Although the vertical extent of the model cells in our study is much smaller than the extent over which significant stratification would commonly be assumed to occur, high-resolution local observations (e.g., of vertical concentration variations) may not be captured with our approach, which integrates over the scale of larger model cells.

4.5 Conclusion

Riparian zones contain waters from different sources, which can mix with each other and in turn enable mixing-dependent biogeochemical processing. In this study, we coupled a hydraulic mixing cell (HMC) method with a previously-calibrated transient and fully-integrated 3D numerical flow model to assess the distribution of different water sources in a riparian aquifer, as well as their mixing dynamics. The simulated mixing degrees matched estimated values based on natural chloride tracer data well. A qualitative comparison of HMC based mixing patterns with concentration patterns from additional, hydrochemical data generally confirmed the robustness of the method, which is computationally comparably cheap, as it does not require explicit solute transport simulations to track different water sources in space and time.

Our estimations indicated that along the simulated stream reach, about 50% of the water in the riparian aquifer originates from the stream, whereas about 40% is groundwater and the remaining 10% is floodplain water (e.g., from rainfall or flooding from top soil). This overall composition was relatively steady over time, but it was episodically affected by larger stream discharge events, which deliver larger volumes of stream water to the riparian aquifer via infiltration or overbank flow. Similarly, macroscopic mixing, evaluated in terms of the mixing-degrees, was observed at least in 80% of the domain ($d > 0$), but it was spatially and temporally variable within the riparian zone. On average, about 9% of the aquifer volume could be characterized as mixing hot-spots ($d \geq 0.75$), but this percentage could be nearly 1.5 times higher following large discharge events. Moreover, event intensity (event peak magnitude) was found to be more important for the increase of the spatial extent of mixing hot-spots than event duration. Our modelling results also indicate that event-driven changes in the fluxes and velocity of infiltrating stream water, affect exposure-times (i.e., time of a water parcel residing within a *mixing hot-spot*) along hyporheic flow paths to a larger extent than the exposure-times of water flowing far from the stream. With distance from the stream, exposure-times become increasingly controlled by variations in general water transit-times. In contrast, in the near stream zone, the rapid increase of SW influx during events shifts the ratio between the water fractions to SW, reducing the extent of potential mixing zones inhibiting mixing dependent reactions. At the same time increasing stream water infiltration at higher flow velocities delivers stream water further into the riparian aquifer, shifting the zones with significant macroscopic mixing between SW and GW away from the near stream zone.

The analysis of water source dynamics, and of the relationship between the mixing of different water sources and flow dynamics in a riparian zone presented in this study provides an easy-to-transfer approach for the mapping of water sources and the identification of *mixing hot-spots* within riparian zones. Understanding the patterns and dynamics of macroscopic mixing between SW and GW in riparian zones can help to better understand patterns of reactive turnover or the redistribution of other, non-reactive solutes

or small particulate substances (e.g., micro plastic particles) in the riparian zone. Future assessments could also focus on smaller scale streambed mixing processes, considering, for instance, (1) more heterogeneous hydraulic conductivity fields at the streambed and at the riparian aquifer, as well as (2) different events duration and peak magnitudes.

4.6 Data availability

The field data, and the numerical model files are publically available and can be assessed through: http://www.hydroshare.org/resource/a0dc51142fe249f89877c4005e0b6947.

4.7 Author contributions

GN performed the formal analysis, the investigation and wrote the original draft of the manuscript; all the authors contributed to review, final writing and editing; GN, CS, and JF conceptualized the study; GN, DP, PB, and JF conceived the methodology; GN, CS, DP, and JF worked on the validation of the study; CS and JF were responsible for supervision; JF was responsible for funding acquisition, resources and project administration.

4.8 Acknowledgment

This research was financially supported by the ENIGMA-ITN project within the European Union's Horizon 2020 research and innovation programme under the Marie Sklodowska-Curie Grant Agreement No.722028, as well as the Collaborative Research Centre 1357 MICROPLASTICS funded by the German Research Foundation (DFG) Project Number 391977956 – SFB 1357 and the Research Program of the Helmholtz Association. Special thanks to Tomasz Berezowski for his support in the study, as well as to two anonymous reviewers for their comments that helped on increasing the quality of the manuscript

4.9 References

Appelo, C. A. J. and Postma, D.: Geochemistry, Groundwater and Pollution - 2nd Edition, A.A. BALKEMA PUBLISHERS, Amsterdam., 2005.

Aquanty Inc.: HydroGeoSphere Reference Manual, Waterloo. [online] Available from: https://www.aquanty.com/hgs-download, 2015.

Battin, T. J.: Hydrologic flow paths control dissolved organic carbon fluxes and metabolism in an alpine stream hyporheic zone, , 35(10), 3159–3169, 1999.

Bear, J. and Verruijt, A.: Modeling Groundwater Flow and Pollution, 1st ed., edited by J. Bear, D. Reidel Publishing Company, Dordrecht., 1987.

Berezowski, T., Partington, D., Chormański, J. and Batelaan, O.: Spatiotemporal Dynamics of the Active Perirheic Zone in a Natural Wetland Floodplain, Water Resour. Res., 55(11), 9544–9562, doi:10.1029/2019WR024777, 2019.

Bernhardt, E. S., Blaszczak, J. R., Ficken, C. D., Fork, M. L., Kaiser, K. E. and Seybold, E. C.: Control Points in Ecosystems: Moving Beyond the Hot Spot Hot Moment Concept, Ecosystems, 20(4), 665–682, doi:10.1007/s10021-016-0103-y, 2017.

Biehler, A., Chaillou, G., Buffin-Bélanger, T. and Baudron, P.: Hydrological connectivity in the aquifer–river continuum: Impact of river stages on the geochemistry of groundwater floodplains, J. Hydrol., 590, 125379, doi:10.1016/j.jhydrol.2020.125379, 2020.

Boano, F., Demaria, A., Revelli, R. and Ridolfi, L.: Biogeochemical zonation due to intrameander hyporheic flow, Water Resour. Res., 46(2), 1–13, doi:10.1029/2008WR007583, 2010.

Boulton, A. J., Findlay, S., Marmonier, P., Stanley, E. H. and Valett, H. M.: The Functional Significance of the Hyporheic Zone in Streams and Rivers, Annu. Rev. Ecol. Syst., 29(1), 59–81, doi:10.1146/annurev.ecolsys.29.1.59, 1998.

Broecker, T., Sobhi Gollo, V., Fox, A., Lewandowski, J., Nützmann, G., Arnon, S. and Hinkelmann, R.: High-Resolution Integrated Transport Model for Studying Surface Water–Groundwater Interaction, Groundwater, 1–15, doi:10.1111/gwat.13071, 2021.

Buffington, J. M. and Tonina, D.: Hyporheic exchange in mountain rivers II: Effects of channel morphology on mechanics, scales, and rates of exchange, Geogr. Compass, 3(3), 1038–1062, doi:10.1111/j.1749-8198.2009.00225.x, 2009.

Cardenas, M. B.: Stream-aquifer interactions and hyporheic exchange in gaining and losing sinuous streams, Water Resour. Res., 45(6), 1–13, doi:10.1029/2008WR007651, 2009.

Cirpka, O. A. and Kitanidis, P. K.: Characterization of mixing and dilution in heterogeneous aquifers by means of local temporal moments, Water Resour. Res., 36(5), 1221–1236, doi:10.1029/1999WR900354, 2000.

Delsman, J. R., Essink, G. H. P. O., Beven, K. J. and Stuyfzand, P. J.: Uncertainty estimation of end-member mixing using generalized likelihood uncertainty estimation (GLUE), applied in a lowland catchment, Water Resour. Res., 49(8), 4792–4806, doi:10.1002/wrcr.20341, 2013.

Dentz, M., Le Borgne, T., Englert, A. and Bijeljic, B.: Mixing, spreading and reaction in heterogeneous media: A brief review, J. Contam. Hydrol., 120–121(C), 1–17, doi:10.1016/j.jconhyd.2010.05.002, 2011.

Doherty, J.: PEST: Model-independent parameter estimation. User Manual, , 368, 2018.

Ebeling, P., Dupas, R., Abbott, B., Kumar, R., Ehrhardt, S., Fleckenstein, J.H., Musolff, A.: Long-Term Nitrate Trajectories Vary by Season in Western European Catchments. Global Biogeochem. Cycles 35, 1–19. https://doi.org/10.1029/2021GB007050, 2021.

Fleckenstein, J. H., Niswonger, R. G. and Fogg, G. E.: River-aquifer interactions, geologic heterogeneity, and low-flow management, Ground Water, 44(6), 837–852, doi:10.1111/j.1745-6584.2006.00190.x, 2006.

Flipo, N., Mouhri, A., Labarthe, B., Biancamaria, S., Rivière, A., Weill, P.: Continental hydrosystem modelling: The concept of nested stream–aquifer interfaces. Hydrol. Earth Syst. Sci. 18, 3121–3149. https://doi.org/10.5194/hess-18-3121-2014, 2014.

Gassen, N., Griebler, C., Werban, U., Trauth, N. and Stumpp, C.: High Resolution Monitoring Above and Below the Groundwater Table Uncovers Small-Scale Hydrochemical Gradients, Environ. Sci. Technol., 51, 9, doi:10.1021/acs.est.7b03087, 2017.

Gianni, G., Doherty, J. and Brunner, P.: Conceptualization and Calibration of Anisotropic Alluvial Systems: Pitfalls and Biases, Groundwater, 57(3), 409–419, doi:10.1111/gwat.12802, 2019.

Gomez-Velez, J. D., Wilson, J. L., Cardenas, M. B. and Harvey, J. W.: Flow and Residence Times of Dynamic River Bank Storage and Sinuosity-Driven Hyporheic Exchange, Water Resour. Res., 53(10), 8572–8595, doi:10.1002/2017WR021362, 2017.

Gooseff, M. N.: Defining hyporheic zones - advancing our conceptual and operational definitions of where stream water and groundwater meet, Geogr. Compass, 4(8), 945–955, doi:10.1111/j.1749-8198.2010.00364.x, 2010.

Gu, C., Anderson, W. and Maggi, F.: Riparian biogeochemical hot moments induced by stream fluctuations, Water Resour. Res., 48(9), 1–17, doi:10.1029/2011WR011720, 2012.

Gupta, H. V., Kling, H., Yilmaz, K. K. and Martinez, G. F.: Decomposition of the mean squared error and NSE performance criteria: Implications for improving hydrological modelling, J. Hydrol., 377(1–2), 80–91, doi:10.1016/j.jhydrol.2009.08.003, 2009.

Gutiérrez-Jurado, K. Y., Partington, D., Batelaan, O., Cook, P. and Shanafield, M.: What Triggers Streamflow for Intermittent Rivers and Ephemeral Streams in Low-Gradient Catchments in Mediterranean Climates, Water Resour. Res., 55(11), 9926–9946, doi:10.1029/2019WR025041, 2019.

Hester, E. T., Young, K. I. and Widdowson, M. A.: Mixing of surface and groundwater induced by riverbed dunes: Implications for hyporheic zone definitions and pollutant reactions, Water Resour. Res., 49(9), 5221–5237, doi:10.1002/wrcr.20399, 2013.

Hester, E. T., Young, K. I. and Widdowson, M. A.: Controls on mixing-dependent denitrification in hyporheic zones induced by riverbed dunes: A steady state modeling study, Water Resour. Res., 50(11), 9048–9066, doi:10.1002/2014WR015424, 2014.

Hester, E. T., Cardenas, M. B., Haggerty, R. and Apte, S. V.: The importance and challenge of hyporheic mixing, Water Resour. Res., 53(5), 3565–3575, doi:10.1002/2016WR020005, 2017.

Hester, E. T., Eastes, L. A. and Widdowson, M. A.: Effect of Surface Water Stage Fluctuation on Mixing-Dependent Hyporheic Denitrification in Riverbed Dunes, Water Resour. Res., 55(6), 4668–4687, doi:10.1029/2018WR024198, 2019.

Hill, A. R.: Nitrate Removal in Stream Riparian Zones, J. Environ. Qual., 25(4), 743–755, doi:10.2134/jeq1996.00472425002500040014x, 1996.

Jencso, K. G., McGlynn, B. L., Gooseff, M. N., Bencala, K. E. and Wondzell, S. M.: Hillslope hydrologic connectivity controls riparian groundwater turnover: Implications of catchment structure for riparian buffering and stream water sources, Water Resour. Res., 46(10), 1–18, doi:10.1029/2009WR008818, 2010.

Jones, C. N., Scott, D. T., Edwards, B. L. and Keim, R. F.: Perirheic mixing and biogeochemical processing in flow-through and backwater floodplain wetlands, Water Resour. Res., 50(9), 7394–7405, doi:10.1002/2014WR015647, 2014.

Jones, K. L., Poole, G. C., Woessner, W. W., Vitale, M. V., Boer, B. R., O'Daniel, S. J., Thomas, S. A. and Geffen, B. A.: Geomorphology, hydrology, and aquatic vegetation drive seasonal hyporheic flow patterns across a gravel-dominated floodplain, Hydrol. Process., 22(13), 2105–2113, doi:10.1002/hyp.6810, 2008.

Karan, S., Engesgaard, P., Looms, M. C., Laier, T. and Kazmierczak, J.: Groundwater flow and mixing in a wetland-stream system: Field study and numerical modeling, J. Hydrol., 488, 73–83, doi:10.1016/j.jhydrol.2013.02.030, 2013.

Kitanidis, K.: The concept of the dilution index, , 30(7), 2011–2026, doi:https://doi.org/10.1029/94WR00762, 1994.

Knoben, W. J. M., Freer, J. E. and Woods, R. A.: Technical note: Inherent benchmark or not? Comparing Nash-Sutcliffe and Kling-Gupta efficiency scores, Hydrol. Earth Syst. Sci. Discuss., (July), 1–7, doi:10.5194/hess-2019-327, 2019.

Kolbe, T., de Dreuzy, J.-R., Abbott, B. W., Aquilina, L., Babey, T., Green, C. T., Fleckenstein, J. H., Labasque, T., Laverman, A. M., Marçais, J., Peiffer, S., Thomas, Z. and Pinay, G.: Stratification of reactivity determines nitrate removal in groundwater, Proc. Natl. Acad. Sci., 116(7), 2494–2499, doi:10.1073/pnas.1816892116, 2019.

Kollet, S. J. and Maxwell, R. M.: Integrated surface-groundwater flow modeling: A free-surface overland flow boundary condition in a parallel groundwater flow model, Adv. Water Resour., 29(7), 945–958, doi:10.1016/j.advwatres.2005.08.006, 2006.

Lawrence, J. E., Skold, M. E., Hussain, F. A., Silverman, D. R., Resh, V. H., Sedlak, D. L., Luthy, R. G. and McCray, J. E.: Hyporheic zone in urban streams: A review and opportunities for enhancing water quality and improving aquatic habitat by active management, Environ. Eng. Sci., 30(8), 480–501, doi:10.1089/ees.2012.0235, 2013.

Lessels, J. S., Tetzlaff, D., Birkel, C., Dick, J. and Soulsby, C.: Water sources and mixing in riparian wetlands revealed by tracers and geospatial analysis, Water Resour. Res., 52(1), 456–470, doi:10.1002/2015WR017519, 2016.

Liggett, J. E., Partington, D., Frei, S., Werner, A. D., Simmons, C. T. and Fleckenstein, J. H.: An exploration of coupled surface-subsurface solute transport in a fully integrated catchment model, J. Hydrol., 529, 969–979, doi:10.1016/j.jhydrol.2015.09.006, 2015.

Liu, S. and Chui, T. F. M.: Impacts of different rainfall patterns on hyporheic zone under transient conditions, J. Hydrol., 561(April), 598–608, doi:10.1016/j.jhydrol.2018.04.019, 2018.

Lutz, S.R., Trauth, N., Musolff, A., Van Breukelen, B.M., Knöller, K., Fleckenstein, J.H.: How Important is Denitrification in Riparian Zones? Combining End-Member Mixing and Isotope Modeling to Quantify Nitrate Removal from Riparian Groundwater. Water Resour. Res. 56. https://doi.org/10.1029/2019WR025528, 2020.

Magliozzi, C., Grabowski, R.C., Packman, A.I., Krause, S.: Toward a conceptual framework of hyporheic exchange across spatial scales. Hydrol. Earth Syst. Sci. 22, 6163–6185. https://doi.org/10.5194/hess-22-6163-2018, 2018.

Mayer, P. M., Reynolds, S. K. and Canfield, T. J.: Riparian buffer width, vegetative cover, and nitrogen removal effectiveness: a review of current science and regulations., Epa/600/R-05/118, 1–40 [online] Available from: http://nepis.epa.gov/Exe/ZyPDF.cgi/2000O182.PDF?Dockey=2000O182.PDF, 2006.

McCallum, J. L., Cook, P. G., Brunner, P. and Berhane, D.: Solute dynamics during bank storage flows and implications for chemical base flow separation, Water Resour. Res., 46(7), 1–11, doi:10.1029/2009WR008539, 2010.

McClain, M. E., Boyer, E. W., Dent, C. L., Gergel, S. E., Grimm, N. B., Groffman, P. M., Hart, S. C., Harvey, J. W., Johnston, C. A., Mayorga, E., McDowell, W. H. and Pinay, G.: Biogeochemical Hot Spots and Hot Moments at the Interface of Terrestrial and Aquatic Ecosystems, Ecosystems, 6(4), 301–312, doi:10.1007/s10021-003-0161-9, 2003.

Mertes, L. A. K.: Documentation and significance of the perirheic zone on inundated floodplains, Water Resour. Res., 33(7), 1749–1762, doi:10.1029/97WR00658, 1997.

Mirus, B. B., Ebel, B. A., Heppner, C. S. and Loague, K.: Assessing the detail needed to capture rainfall-runoff dynamics with physics-based hydrologic response simulation, Water Resour. Res., 47(6), 1–18, doi:10.1029/2010WR009906, 2011.

Newcomer, M.E., Hubbard, S.S., Fleckenstein, J.H., Maier, U., Schmidt, C., Thullner, M., Ulrich, C., Flipo, N., Rubin, Y.: Influence of Hydrological Perturbations and Riverbed Sediment Characteristics on Hyporheic Zone Respiration of CO2 and N2. J. Geophys. Res. Biogeosciences 123, 902–922. https://doi.org/10.1002/2017JG004090, 2018.

Nogueira, G. E. H., Schmidt, C., Trauth, N. and Fleckenstein, J. H.: Seasonal and short-term controls of riparian oxygen dynamics and the implications for redox processes, Hydrol. Process., 35(2), 16, doi:10.1002/hyp.14055, 2021a.

Nogueira, G. E. H., Schmidt, C., Brunner, P., Graeber, D. and Fleckenstein, J. H.: Transit-time and temperature control the spatial patterns of aerobic respiration and denitrification in the riparian zone, Water Resour. Res., doi:10.1029/2021WR030117, 2021b.

Ocampo, C. J., Oldham, C. E. and Sivapalan, M.: Nitrate attenuation in agricultural catchments: Shifting balances between transport and reaction, Water Resour. Res., 42(1), 1–16, doi:10.1029/2004WR003773, 2006.

Ong, C. G., Tanji, K. K., Dahlgren, R. A., Smith, G. R. and Quek, A. F.: Water Quality and Trace Element Evapoconcentration in Evaporation Ponds for Agricultural Waste Water Disposal, J. Agric. Food Chem., 43(7), 1941–1947, doi:10.1021/jf00055a034, 1995.

Partington, D., Brunner, P., Simmons, C. T., Therrien, R., Werner, A. D., Dandy, G. C. and Maier, H. R.: A hydraulic mixing-cell method to quantify the groundwater component of streamflow within spatially distributed fully integrated surface water-groundwater flow models, Environ. Model. Softw., 26(7), 886–898, doi:10.1016/j.envsoft.2011.02.007, 2011.

Partington, D., Brunner, P., Simmons, C. T., Werner, A. D., Therrien, R., Maier, H. R. and Dandy, G. C.: Evaluation of outputs from automated baseflow separation methods against simulated baseflow from a physically based, surface water-groundwater flow model, J. Hydrol., 458–459, 28–39, doi:10.1016/j.jhydrol.2012.06.029, 2012.

Partington, D., Brunner, P., Frei, S., Simmons, C. T., Werner, A. D., Therrien, R., Maier, H. R., Dandy, G. C. and Fleckenstein, J. H.: Interpreting streamflow generation mechanisms from integrated surface-subsurface flow models of a riparian wetland and catchment, Water Resour. Res., 49(9), 5501–5519, doi:10.1002/wrcr.20405, 2013.

Partington, D., Knowling, M. J., Simmons, C. T., Cook, P. G., Xie, Y., Iwanaga, T. and Bouchez, C.: Worth of hydraulic and water chemistry observation data in terms of the reliability of surface water-groundwater exchange flux predictions under varied flow conditions, J. Hydrol., 590(November 2019), 125441, doi:10.1016/j.jhydrol.2020.125441, 2020.

Pinay, G., Ruffinoni, C., Wondzell, S. and Gazelle, F.: Change in groundwater nitrate concentration in a large river floodplain: Denitrification, uptake, or mixing?, J. North Am. Benthol. Soc., 17(2), 179–189, doi:10.2307/1467961, 1998.

Pinay, G., Peiffer, S., Dreuzy, J. De, Krause, S., Hannah, D. M., Fleckenstein, J. H., Sebilo, M., Bishop, K. and Hubert-moy, L.: Upscaling Nitrogen Removal Capacity from Local Hotspots to Low Stream Orders ' Drainage Basins, Ecosystems, 18(6), 1101–1120, doi:10.1007/s10021-015-9878-5, 2015.

Poole, G. C., O'Daniel, S. J., Jones, K. L., Woessner, W. W., Bernhardt, E. S., Helton, A. M., Stanford, J. A., Boer, B. R. and Beechie, T. J.: Hydrologic spiralling: the role of multiple interactive flow paths in stream ecosystems, River Res. Appl., 24(7), 1018–1031, doi:10.1002/rra.1099, 2008.

Pryshlak, T. T., Sawyer, A. H., Stonedahl, S. H. and Soltanian, M. R.: Multiscale hyporheic exchange through strongly heterogeneous sediments, Water Resour. Res., 51(11), 9127–9140, doi:10.1002/2015WR017293, 2015.

Ranalli, A. J. and Macalady, D. L.: The importance of the riparian zone and in-stream processes in nitrate attenuation in undisturbed and agricultural watersheds - A review of the scientific literature, J. Hydrol., 389(3–4), 406–415, doi:10.1016/j.jhydrol.2010.05.045, 2010.

Rivett, M.O., Buss, S.R., Morgan, P., Smith, J.W.N., Bemment, C. D.: Nitrate attenuation in groundwater: A review of biogeochemical controlling processes. Water Res. 42, 4215–4232. https://doi.org/10.1016/j.watres.2008.07.020, 2008.

Savoy, H., Kalbacher, T., Dietrich, P. and Rubin, Y.: Geological heterogeneity: Goal-oriented simplification of structure and characterization needs, Adv. Water Resour., 109, 1–13, doi:10.1016/j.advwatres.2017.08.017, 2017.

Sawyer, A. H.: Enhanced removal of groundwater-borne nitrate in heterogeneous aquatic sediments, Geophys. Res. Lett., 42(2), 403–410, doi:10.1002/2014GL062234, 2015.

Sawyer, A. H. and Cardenas, M. B.: Hyporheic flow and residence time distributions in heterogeneous cross-bedded sediment, Water Resour. Res., 45(8), 1–12, doi:10.1029/2008WR007632, 2009.

Sawyer, A. H., Cardenas, M. B., Bomar, A. and Mackey, M.: Impact of dam operations on hyporheic exchange in the riparian zone of a regulated river, Hydrol. Process., 23(15), 2129–2137, doi:10.1002/hyp.7324, 2009.

Sawyer, A. H., Kaplan, L. A., Lazareva, O. and Michael, H. A.: Hydrologic dynamics and geochemical responses within a floodplain aquifer and hyporheic zone during Hurricane Sandy, Water Resour. Res., 50(6), 4877–4892, doi:10.1002/2013WR015101, 2014.

Schilling, O. S., Gerber, C., Partington, D. J., Purtschert, R., Brennwald, M. S., Kipfer, R., Hunkeler, D. and Brunner, P.: Advancing Physically-Based Flow Simulations of Alluvial Systems Through Atmospheric Noble Gases and the Novel37Ar Tracer Method, Water Resour. Res., 53(12), 10465–10490, doi:10.1002/2017WR020754, 2017.

Schilling, O. S., Cook, P. G. and Brunner, P.: Beyond Classical Observations in Hydrogeology: The Advantages of Including Exchange Flux, Temperature, Tracer Concentration, Residence Time, and Soil

Moisture Observations in Groundwater Model Calibration, Rev. Geophys., 57(1), 146–182, doi:10.1029/2018RG000619, 2019.

Schmadel, N. M., Ward, A. S., Kurz, M. J., Fleckenstein, J. H., Zarnetske, J. P., Hannah, D. M., Blume, T., Vieweg, M., Blaen, P. J., Schmidt, C., Knapp, J. L. A., Klaar, M. J., Romeijn, P., Datry, T., Keller, T., Folegot, S., Arricibita, A. I. M. and Krause, S.: Stream solute tracer timescales changing with discharge and reach length confound process interpretation, Water Resour. Res., 52(4), 3227–3245, doi:10.1002/2015WR018062, 2016.

Schneider, P., Vogt, T., Schirmer, M., Doetsch, J., Linde, N., Pasquale, N., Perona, P. and Cirpka, O. A.: Towards improved instrumentation for assessing river-groundwater interactions in a restored river corridor, Hydrol. Earth Syst. Sci., 15(8), 2531–2549, doi:10.5194/hess-15-2531-2011, 2011.

Song, X., Chen, X., Stegen, J., Hammond, G., Song, H., Dai, H., Graham, E. and Zachara, J. M.: Drought Conditions Maximize the Impact of High-Frequency Flow Variations on Thermal Regimes and Biogeochemical Function in the Hyporheic Zone, Water Resour. Res., 54(10), 7361–7382, doi:10.1029/2018WR022586, 2018.

Stegen, J. C., Fredrickson, J. K., Wilkins, M. J., Konopka, A. E., Nelson, W. C., Arntzen, E. V., Chrisler, W. B., Chu, R. K., Danczak, R. E., Fansler, S. J., Kennedy, D. W., Resch, C. T. and Tfaily, M.: Groundwater-surface water mixing shifts ecological assembly processes and stimulates organic carbon turnover, Nat. Commun., 7, doi:10.1038/ncomms11237, 2016.

Stigter, T. Y., Van Ooijen, S. P. J., Post, V. E. A., Appelo, C. A. J. and Carvalho Dill, A. M. M.: A hydrogeological and hydrochemical explanation of the groundwater composition under irrigated land in a Mediterranean environment, Algarve, Portugal, J. Hydrol., 208(3–4), 262–279, doi:10.1016/S0022-1694(98)00168-1, 1998.

Sun, X., Bernard-Jannin, L., Sauvage, S., Garneau, C., Arnold, J.G., Srinivasan, R., Sánchez-Pérez, J.M.: Assessment of the denitrification process in alluvial wetlands at floodplain scale using the SWAT model. Ecol. Eng. 103, 344–358. https://doi.org/10.1016/j.ecoleng.2016.06.098, 2017.

Tang, Q., Kurtz, W., Schilling, O. S., Brunner, P., Vereecken, H. and Hendricks Franssen, H. J.: The influence of riverbed heterogeneity patterns on river-aquifer exchange fluxes under different connection regimes, J. Hydrol., 554, 383–396, doi:10.1016/j.jhydrol.2017.09.031, 2017.

Therrien, R., McLaren, R. G., Sudicky, E. A. and Panday, S. M.: HydroGeoSphere. A three-dimensional numerical model describing fully-integrated subsurface and surface flow and solute transport, Groundw. Simulations Gr., 457, doi:10.5123/S1679-49742014000300002, 2010.

Tóth, J.: A theoretical analysis of groundwater flow in small drainage basins. J. Geophys. Res. 68, 4795–4812. https://doi.org/10.1029/JZ068i016p04795, 1963.

Trauth, N. and Fleckenstein, J. H.: Single discharge events increase reactive efficiency of the hyporheic zone, Water Resour. Res., 53(Jan), 779–798, doi:10.1111/j.1752-1688.1969.tb04897.x, 2017.

Trauth, N., Schmidt, C., Maier, U., Vieweg, M. and Fleckenstein, J. H.: Coupled 3-D stream flow and hyporheic flow model under varying stream and ambient groundwater flow conditions in a pool-riffle system, Water Resour. Res., 49(9), 5834–5850, doi:10.1002/wrcr.20442, 2013.

Trauth, N., Schmidt, C., Vieweg, M., Maier, U. and Fleckenstein, J. H.: Hyporheic transport and biogeochemical reactions in pool-riffle systems under varying ambient groundwater flow conditions, J. Geophys. Res. Biogeosciences, 119(5), 910–928, doi:10.1002/2013JG002586, 2014.

Trauth, N., Schmidt, C., Vieweg, M., Oswald, S. E. and Fleckenstein, J. H.: Hydraulic controls of in-stream gravel bar hyporheic exchange and reactions, Water Resour. Res., 51(4), 2243–2263, doi:10.1002/2014WR015857, 2015.

Trauth, N., Musolff, A., Knöller, K., Kaden, U. S., Keller, T., Werban, U. and Fleckenstein, J. H.: River water infiltration enhances denitrification efficiency in riparian groundwater, Water Res., 130, 185–199, doi:10.1016/j.watres.2017.11.058, 2018.

Triska, F. J., Kennedy, V. C., Avanzino, R. J., Zellweger, G. W. and Bencala, K. E.: Retention and transport of nutrients in a third-order stream: channel processes, Ecology, 70(6), 1877–1892, doi:10.2307/1938119, 1989.

Vidon, P., Allan, C., Burns, D., Duval, T. P., Gurwick, N., Inamdar, S., Lowrance, R., Okay, J., Scott, D. and Sebestyen, S.: Hot spots and hot moments in riparian zones: Potential for improved water quality management, J. Am. Water Resour. Assoc., 46(2), 278–298, doi:10.1111/j.1752-1688.2010.00420.x, 2010.

Vidon, P. G. F. and Hill, A. R.: Landscape controls on nitrate removal in stream riparian zones, Water Resour. Res., 40(3), 1–14, doi:10.1029/2003WR002473, 2004.

Widdowson, M. A., Molz, F. J. and Benefield, L. D.: A numerical transport model for oxygen- and nitrate-based respiration linked to substrate and nutrient availability in porous media, Water Resour. Res., 24(9), 1553–1565, doi:10.1029/WR024i009p01553, 1988.

Winter, C., Lutz, S.R., Musolff, A., Kumar, R., Weber, M., Fleckenstein, J.H.: Disentangling the Impact of Catchment Heterogeneity on Nitrate Export Dynamics From Event to Long-Term Time Scales. Water Resour. Res. 57, 1–24. https://doi.org/10.1029/2020WR027992, 2021.

Wollschläger, U., Attinger, S., Borchardt, D., Brauns, M., Cuntz, M., Dietrich, P., Fleckenstein, J. H., Friese, K., Friesen, J., Harpke, A., Hildebrandt, A., Jäckel, G., Kamjunke, N., Knöller, K., Kögler, S., Kolditz, O., Krieg, R., Kumar, R., Lausch, A., Liess, M., Marx, A., Merz, R., Mueller, C., Musolff, A., Norf, H., Oswald, S. E., Rebmann, C., Reinstorf, F., Rode, M., Rink, K., Rinke, K., Samaniego, L., Vieweg, M., Vogel, H.-J., Weitere, M., Werban, U., Zink, M. and Zacharias, S.: The Bode hydrological observatory: a platform for integrated, interdisciplinary hydro-ecological research within the TERENO Harz/Central German Lowland Observatory, Environ. Earth Sci., 76(1), 29, doi:10.1007/s12665-016-6327-5, 2017.

Wondzell, S. M.: The role of the hyporheic zone across stream networks, Hydrol. Process., 25(22), 3525–3532, doi:10.1002/hyp.8119, 2011.

Zarnetske, J. P., Haggerty, R., Wondzell, S. M. and Baker, M. A.: Dynamics of nitrate production and removal as a function of residence time in the hyporheic zone, J. Geophys. Res., 116(G1), G01025, doi:10.1029/2010JG001356, 2011.

Zhang, Z., Schmidt, C., Nixdorf, E., Kuang, X., Fleckenstein, J.H.: Effects of Heterogeneous Stream-Groundwater Exchange on the Source Composition of Stream Discharge and Solute Load. Water Resour. Res. 57, 1–19. https://doi.org/10.1029/2020WR029079, 2021.

Zheng, L., Cardenas, M. B. and Wang, L.: Temperature effects on nitrogen cycling and nitrate removal-production efficiency in bed form-induced hyporheic zones, J. Geophys. Res. G Biogeosciences, 121(4), 1086–1103, doi:10.1002/2015JG003162, 2016.

Ziegel, E. R., Gibbons, J. and Chakraborti, S.: Nonparametric Statistical Inference, 5th ed., CRC Press, Boca Raton., 2011.

Supplementary Material

Spatio-temporal variations of water sources and mixing spots in a riparian zone

Guilherme E. H. Nogueira[1]; Christian Schmidt [2]; Daniel Partington [3]; Philip Brunner [4]; Jan H. Fleckenstein[1,5]

[1] Department of Hydrogeology, Helmholtz-Centre for Environmental Research - UFZ, Leipzig, Germany.
[2] Department of Aquatic Ecosystem Analysis, Helmholtz-Centre for Environmental Research - UFZ, Magdeburg, Germany.
[3] National Centre for Groundwater Research and Training, & College of Science and Engineering, Flinders University, Adelaide, Australia

[4] Centre for Hydrogeology and Geothermics, University of Neuchâtel, Neuchâtel, Switzerland.

[5] Bayreuth Centre of Ecology and Environmental Research, University of Bayreuth, Bayreuth, Germany

Correspondence to: Guilherme E. H. Nogueira (*guilherme.nogueira@ufz.de*)

Contents of this file: Figures S1-S6

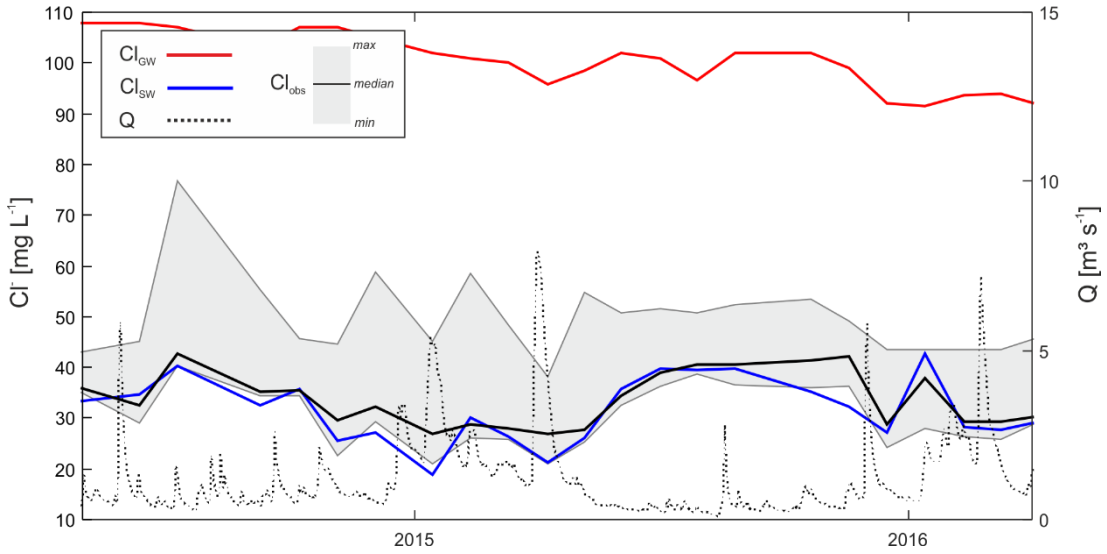

Fig.S1: Measured Cl^- concentrations on groundwater end-member well (Cl_{GW}), on stream water end-member (Cl_{SW}), and on other observation wells at the area (Cl_{obs}) alongside stream discharge (Q). Cl^- measurements were used to calculate the stream water fraction (F_{STR}) present on the riparian groundwater in the observation wells (Eq.3).

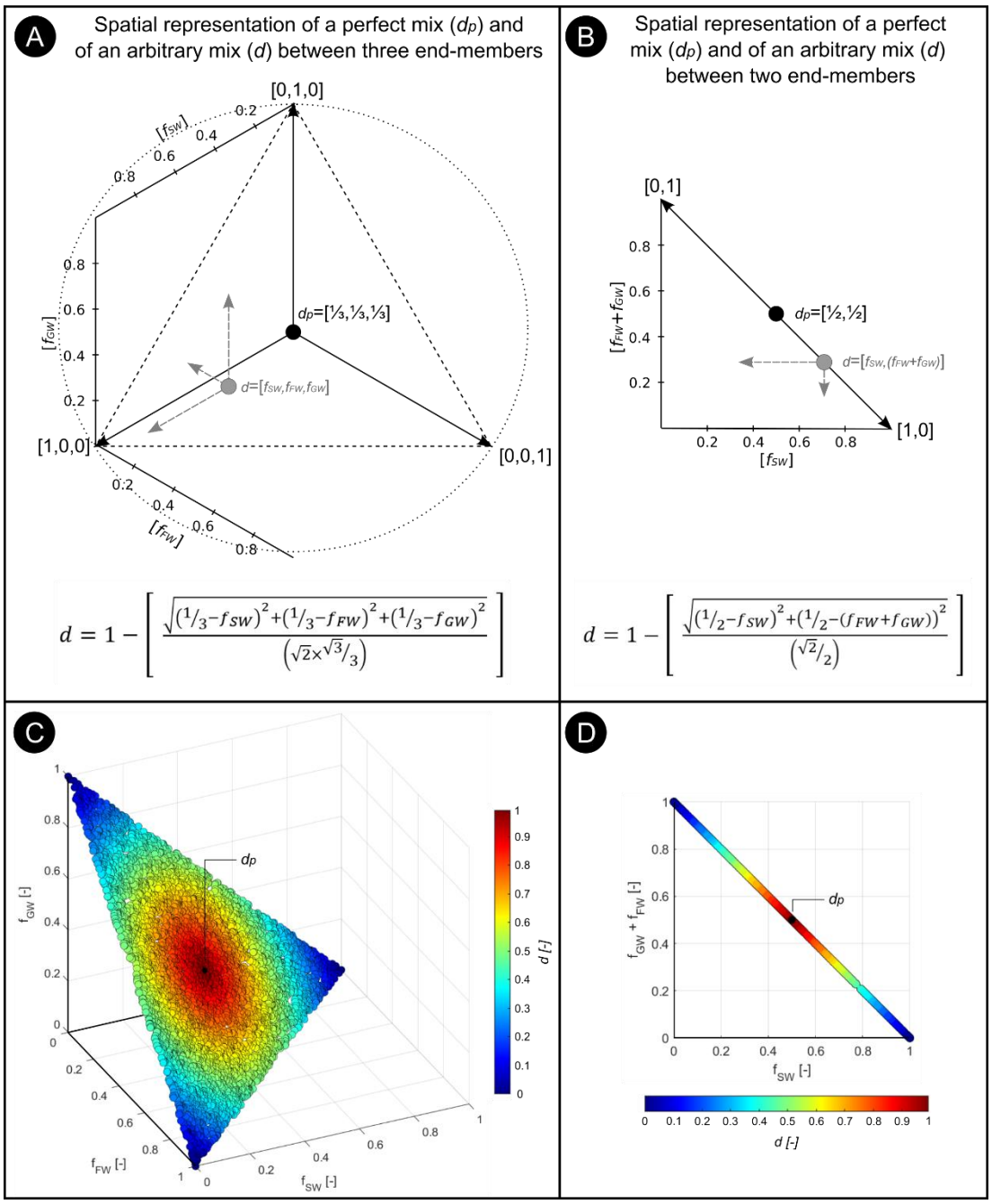

Fig.S2: Spatial representation of a perfect mixing (d_p) and of and arbitrary mixing (d) for the cases of three **(a)** and two **(b)** end-members mixing. The final mixing d can be calculated as the Euclidean distance between points d_p and d. For a three end-members mixing (3D case), any combination of fractions can be represented as a point d in a 3D coordinate space, in which the maximum distance is a radius of a circle (centred at [1/3, 1/3, 1/3]) escribed on an equilateral triangle (side length of $\sqrt{2}$). Thus, the maximum distance between d_p and d is $(\sqrt{2} \times \sqrt{3}/3)$ For a two end-members mixing (2D case), the maximum segment is the diameter of a circle (centred at [0.5, 0.5]), whereas the maximum distance between dp and d is $(\sqrt{2}/2)$. The long-dashed lines in (a) delimit the solution space for any possible mixing d where fractions sum up to 1. In (b) final mixing d values would fall over the solid line passing through d_p. Example of theoretical mixings between three **(c)** and two **(d)** end-members coloured according to

computed *d* values (warmer colours indicate a more homogenous mixing); d_p is indicated as a black circle. The theoretical mixings were generated with 10000 random combinations of HMC fractions that sum to up 1. For a four (or more) end-members mixing a spatial representation is not possible but the general Eq.4 would equally work.

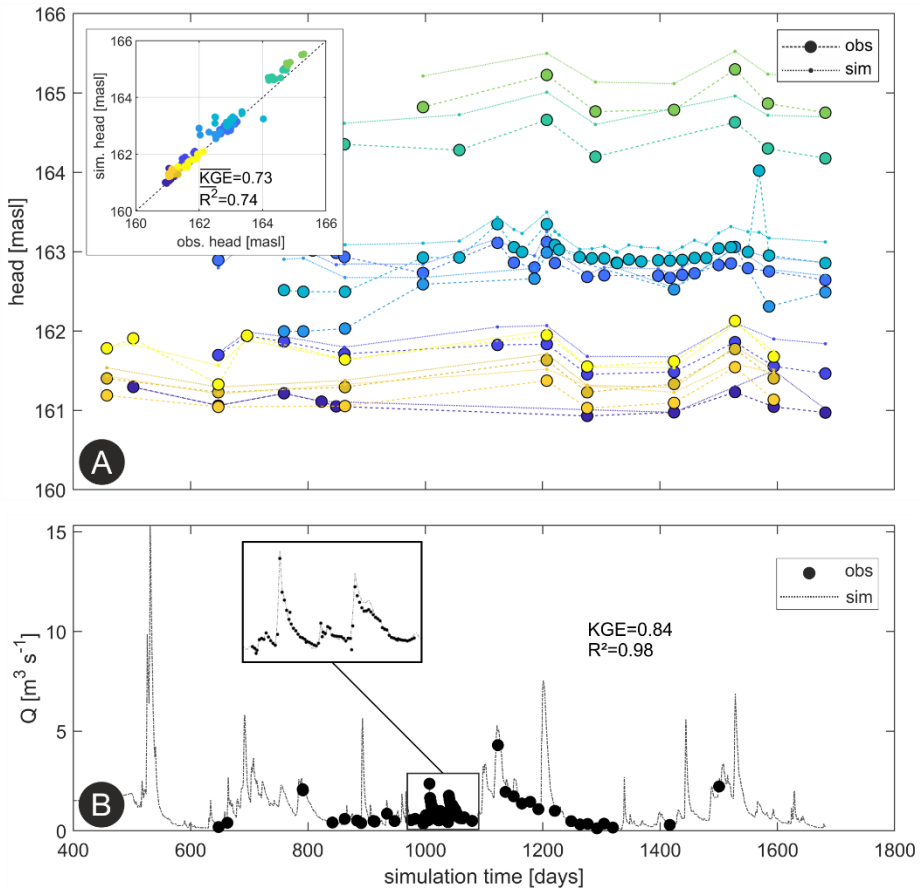

Fig.S3: Observed and simulated hydraulic heads **(a)** and stream discharge (Q) **(b)** for the simulated period. The inset scatter plot in (a) shows the observed versus simulated hydraulic heads alongside the mean coefficient of determination (R^2) and mean Kling-Gupta Efficiency (KGE). Each observation well is presented with a different colour.

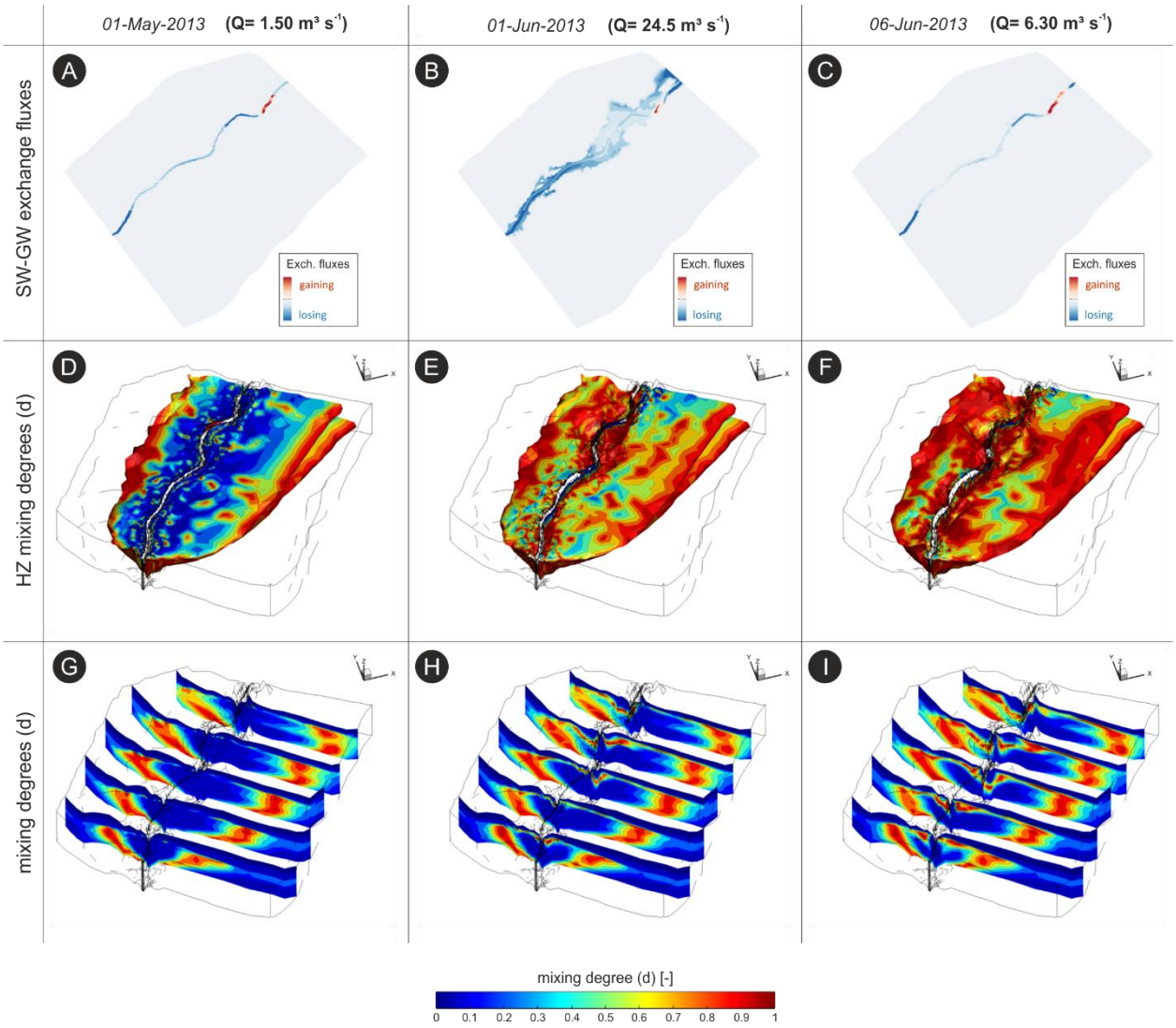

Fig.S4: Three snapshots showing conditions before, at the peak, and during the falling limb of the largest discharge event observed during the simulation period (2013-2016). **a-c)** SW-GW exchange fluxes in terms of gaining and losing conditions (the inverse relation between stream gaining conditions and stream discharge can be depicted); **d-f)** geochemical hyporheic zone (HZ, $f_{SW} \geq 0.5$) around the stream channel coloured according to computed mixing degrees (*d*); and **g-i)** mixing degrees for the entire domain. Warmer colours indicate higher mixing degrees. Note the vertical exaggeration of the 3D plots (20x).

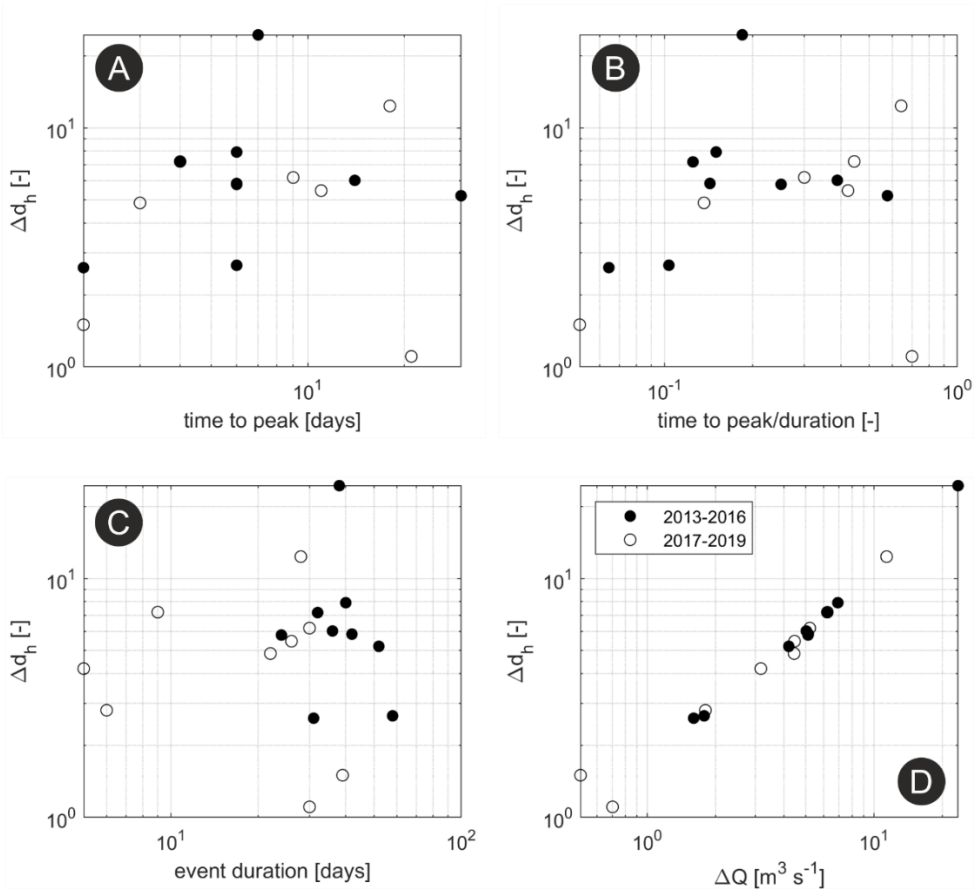

Fig.S5: Metrics of the stream discharge events and the resulting changes in d_h (Δd_h) from conditions immediately prior to the rising limb of the discharge event. The ΔQ represents the peak prominence of the different discharge events. Note that two set of simulations (2013-2016 and 2017-2019) were carried out for the analyses in order to comprise a large number of discharge events under evaluation.

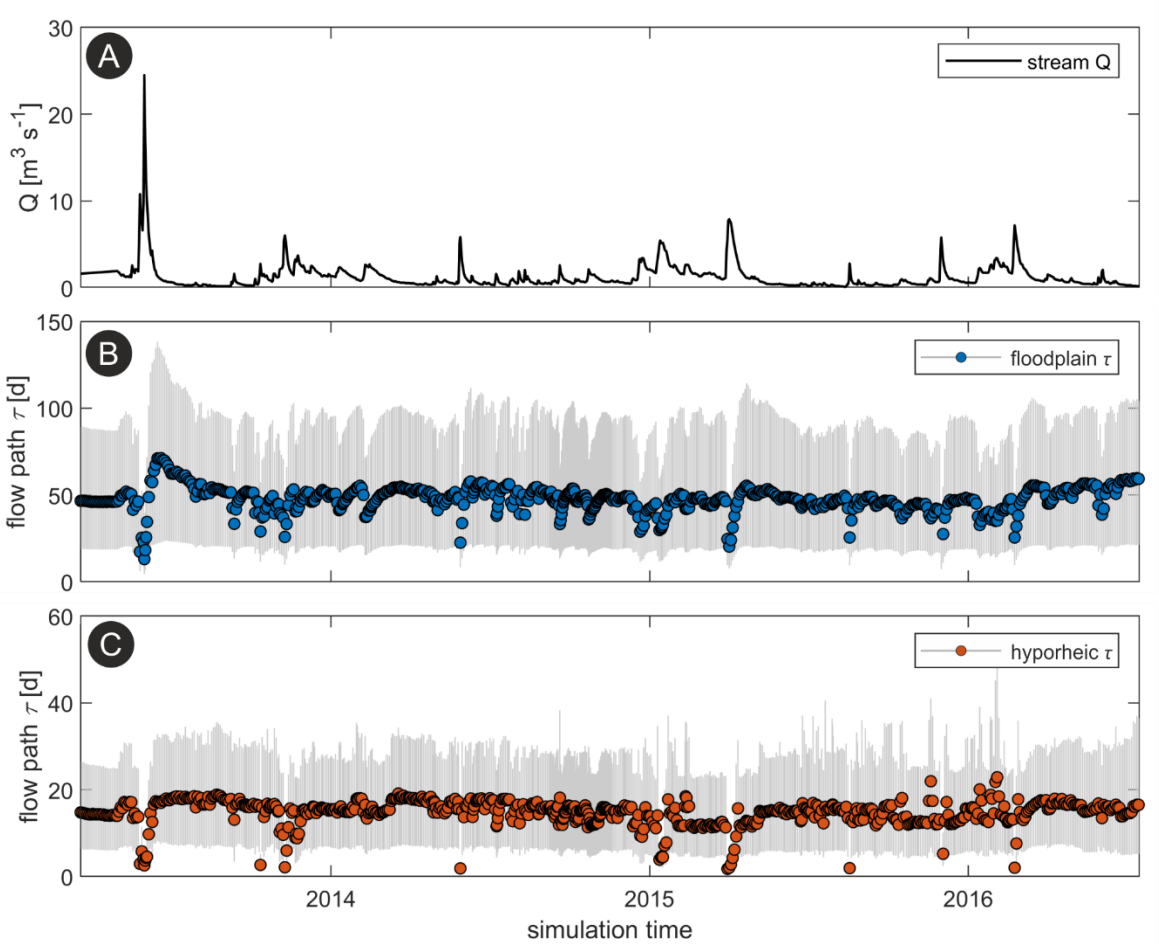

Fig.S6: a) time-series of stream discharge (Q); and variation of water transit-times (τ) for floodplain **(b)** and for hyporheic flow paths **(c)**. Hyporheic flow paths are defined as infiltrating SW that exfiltrates at streambed cells after subsurface transit. The grey bars indicate the interval between 0.25 and 0.75 quantiles of transit-times, whereas the large symbols indicate their median values.

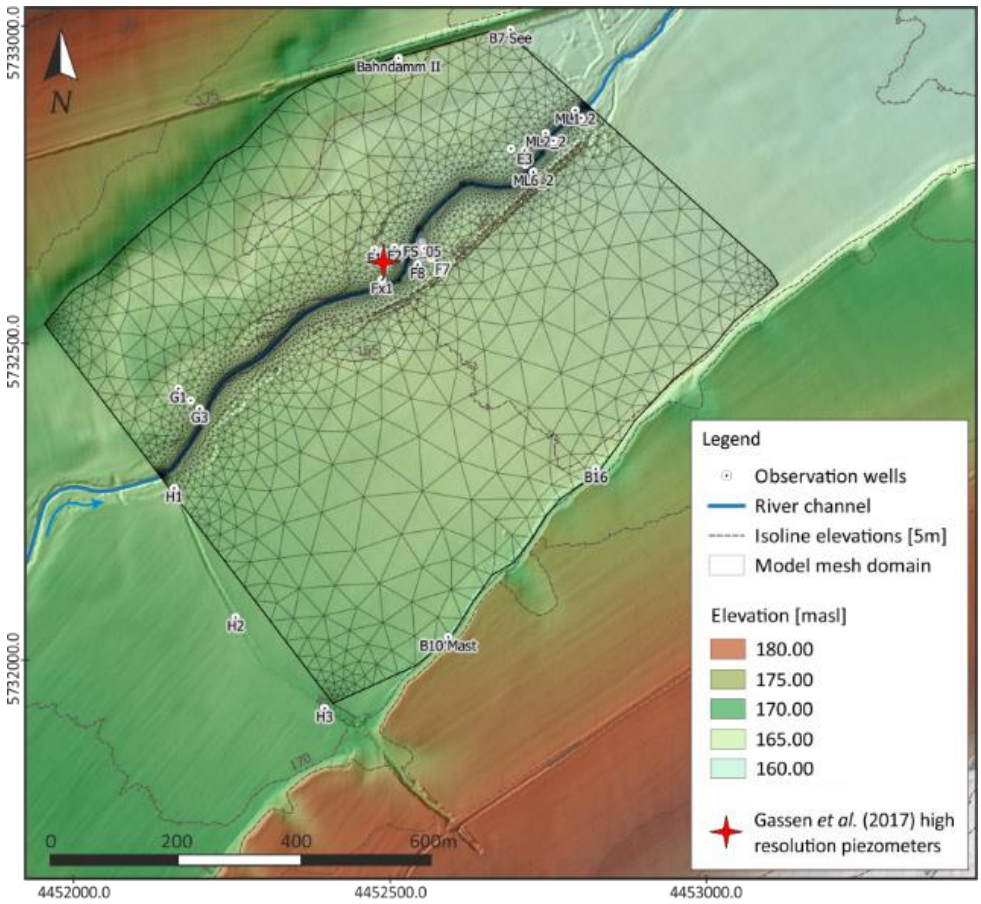

Fig.S7: Location of the multilevel piezometers monitored in Gassen et al. (2017). They are located somewhat between the observation wells F2 and Fx1.

List of peer-reviewed publications

Publications included in the thesis

- **Nogueira, G.E.H.**, Schmidt, C., Partington, D., Brunner, P., Fleckenstein, J. H.., (*2021*):
  Spatio-temporal variations of water sources and mixing spots in a riparian zone, *Hydrology and Earth System Sci.*, under review, https://doi.org/10.5194/hess-2021-573.

- **Nogueira, G.E.H.**, Schmidt, C., Brunner, P., Graeber, D., Fleckenstein, J. H., (*2021*):
  Transit-time and temperature control the spatial patterns of aerobic respiration and denitrification in the riparian zone, *Water Resources Res.* 57, e2021WR030117, https://doi.org/10.1029/2021WR030117.

- **Nogueira, G.E.H.**, Schmidt, C., Trauth, N., Fleckenstein, J. H., (*2021*):
  Seasonal and short-term controls of riparian oxygen dynamics and the implications for redox processes, *Hydrol. Process.* 35 (2), e14055, http://dx.doi.org/10.1002/hyp.14055.

Other publications

- **Nogueira, G.E.H.**, Gonçalves, R., (*2021*):
  Groundwater recharge in phreatic aquifers, a case study: modeling unsaturated zone and recharge rates of the Rio Claro Aquifer using HYDRUS-1D, *HOLOS Environ. 21*, 402 – 422, https://doi.org/10.14295/holos.v21i3.12455.

- Fathi, S., Sjåstad Hagen, J., Matanó, A., **Nogueira, G.E.H.**, (*2021*):
  Review of GIS multi-criteria decision analysis for managed aquifer recharge in semi-arid regions
  In: Pande, C.B., Moharir, K.N., (eds.), *Groundwater resources development and planning in the semi-arid region*, Springer, Cham., p. 19 – 52, https:/doi.org/10.1007/978-3-030-68124-1_2.

- Cendón, D.I., Haldorsen, S., Chen, J., Hankin, S., **Nogueira, G.E.H.**, Momade, F., Achimo, M., Muiuane, E., Mugabe, J., Stigter, T.Y., (*2020*):
  Hydrogeochemical aquifer characterization and its implication for groundwater development in the Maputo district, Mozambique, *Quat. Int.* 547, 113 – 126, http://dx.doi.org/10.1016/j.quaint.2019.06.024.

- **Nogueira, G.**, Stigter, T.Y., Zhou, Y., Mussa, F., Juizo, D., (*2019*):
  Understanding groundwater salinization mechanisms to secure freshwater resources in the water-scarce city of Maputo, Mozambique, *Sci. Total Environ.* 661, 723 – 736, http://dx.doi.org/10.1016/j.scitotenv.2018.12.343.

- **Nogueira, G.**, Chang, H. K., (*2015*):
  Simulação Numérica de Fluxo de Águas Subterrâneas do Aquífero Rio Claro, na Porção Nordeste do Município de Rio Claro, SP. *Associação Brasileira de Águas Subterrâneas*, https://doi.org/10.14295/ras.v29i2.28304.

- Teramoto, E. H, Chang, H. K., Dias, R., **Nogueira, G.**, Kiang, C. H., (*2015*):
  Correções Empíricas para o Aprimoramento da Classificação de Coberturas Impermeáveis Empregando Imagens de Satélite de Média Resolução, *Associação Brasileira de Águas Subterrâneas*, https://doi.org/10.14295/ras.v29i1.27933.

(Eidesstattliche) Versicherungen und Erklärungen

(§ 8 Satz 2 Nr. 3 PromO Fakultät)

Hiermit versichere ich eidesstattlich, dass ich die Arbeit selbstständig verfasst und keine anderen als die von mir angegebenen Quellen und Hilfsmittel benutzt habe (vgl. Art. 64 Abs. 1 Satz 6 BayHSchG).

(§ 8 Satz 2 Nr. 3 PromO Fakultät)

Hiermit erkläre ich, dass ich die Dissertation nicht bereits zur Erlangung eines akademischen Grades eingereicht habe und dass ich nicht bereits diese oder eine gleichartige Doktorprüfung endgültig nicht bestanden habe.

(§ 8 Satz 2 Nr. 4 PromO Fakultät)

Hiermit erkläre ich, dass ich Hilfe von gewerblichen Promotionsberatern bzw. –vermittlern oder ähnlichen Dienstleistern weder bisher in Anspruch genommen habe noch künftig in Anspruch nehmen werde.

(§ 8 Satz 2 Nr. 7 PromO Fakultät)

Hiermit erkläre ich mein Einverständnis, dass die elektronische Fassung der Dissertation unter Wahrung meiner Urheberrechte und des Datenschutzes einer gesonderten Überprüfung unterzogen werden kann.

(§ 8 Satz 2 Nr. 8 PromO Fakultät)

Hiermit erkläre ich mein Einverständnis, dass bei Verdacht wissenschaftlichen Fehlverhaltens Ermittlungen durch universitätsinterne Organe der wissenschaftlichen Selbstkontrolle stattfinden können.

…….
Ort, Datum, Unterschrift